Dissertation

Submitted to the
Combined Faculty of Natural Sciences and Mathematics
of Heidelberg University, Germany
for the Degree of
Doctor of Natural Sciences

Put forward by
M.Sc. Andreas Weu
Born in Rostock, Germany

Oral examination: 10th December 2019

Investigating the Photophysics and Stability of Organic Photovoltaics Using Ultrafast Spectroscopy

Referees: Prof. Dr. Yana Vaynzof
Prof. Dr. Annemarie Pucci

Untersuchung der Photophysik und Stabilität von organischer Photovoltaik mithilfe von Ultrakurzzeit-Spektroskopie

Ungeachtet enormer Fortschritte in der Leistungssteigerung organischer Solarzellen vergangener Jahre, sind grundlegende Prozesse der Ladungsträgererzeugung weiterhin ungelöst. Ferner ist die Umweltstabilität organischer Solarzellen eine wesentliche Grundvoraussetzung für den erfolgreichen Übergang vom Labor in die Praxis, welche oftmals nur ungenügend charakterisiert ist. Die vorliegende Arbeit widmet sich diesen dringenden und komplexen Herausforderungen, indem die Photophysik und die Langzeitstabilität in zwei modernen Materialsystemen mittels Ultrakurzzeit-Spektroskopie untersucht wird. Zunächst wird die Ladungsträgererzeugung in PffBT4T-2OD:PC$_{70}$BM analysiert, welches als Modellsystem für eine neuartige Klasse von Solarzellenmaterialien gilt. Es zeigt sich, dass die Trennung von Elektron-Loch-Paaren feldabhängig ist, was weitreichende Folgen für die Erforschung organischer Solarzellen hat. Auf dieser Grundlage befasst sich der zweite Teil der Arbeit mit der Umweltstabilität der zuvor genannten Materialien, welche ungewöhnlich stark unter dem Einfluss von Sauerstoff leiden. Hierbei wird gezeigt, dass dieses Verhalten durch p-Dotierung der aktiven Schicht hervorgerufen wird, welches zu einem schnellen Verlust der Solarzellenleistung führt. Zuletzt werden die photophysikalischen Eigenschaften und die Stabilität des Moleküls DRCN5T, stellvertretend für einen neuen Trend in der Solarzellenforschung, charakterisiert. Dieses System zeigt erstaunliche Resistenzen gegen Umwelteinflüsse, was auf einen effizienten Energietransfer von den instabilen zu den stabilen Komponenten zurückzuführen ist. Dieses Ergebnis hat das Potenzial die Erforschung organischer Solarzellen nachhaltig zu beeinflussen. Somit leistet diese Arbeit einen substanziellen Beitrag zum Verständnis der Physik auf kurzen Zeitskalen und der Stabilität organischer Komponenten, mit enormer Relevanz für das Forschungsfeld.

Investigating the Photophysics and Stability of Organic Photovoltaics Using Ultrafast Spectroscopy

Despite recent advances leading to unprecedented performance in organic photovoltaic devices, the underlying processes of charge generation in these semiconductors are still unclear. Furthermore, the operational stability of organic solar cells – a key requirement for successful application outside the laboratory – is often neglected. This thesis addresses these urgent and complex challenges by investigating the photophysics and degradation mechanisms of two high-efficiency material systems by employing ultrafast transient spec-

troscopy. The first part is devoted to the understanding of charge generation in PffBT4T-2OD:PC$_{70}$BM which acts as a model system for a new class of organic photovoltaic materials. It is unambiguously shown that the separation of electron-hole pairs is field-dependent, with significant implications for the research of novel combinations of materials with low energy offsets. Based on these results, the second part of this thesis focuses on the environmental stability of the aforementioned system which is shown to be exceptionally sensitive to the influence of oxygen. The observed results can be comprehended by oxygen-induced p-doping of the active layer, resulting in rapid deterioration of the device properties. Finally, the photophysics and degradation of solar cells based on the small molecule donor DRCN5T, representative of a new trend in solar cell design, are addressed. These devices display remarkable stability which is accredited to an ultrafast energy transfer from the unstable to the stable components. This insight can potentially influence design rules for future research on organic solar cells. Therefore, this work contributes substantially to the understanding of the photophysics at short timescales and the stability of organic solar cells with high relevance for the field.

Contents

IV   Results   119

6   Field-assisted charge generation   121

7   Degradation through oxygen-doping   145

8   Photoprotection by small molecules   167

List of publications

Publications included in this thesis

1. **A. Weu**, T. R. Hopper, V. Lami, J. A. Kreß, A. A. Bakulin, and Y. Vaynzof, Field-assisted exciton dissociation in highly efficient PffBT4T-2OD:fullerene organic solar cells. *Chem. Mater.* **2018**, 30, 8, 2660-2667

2. **A. Weu**, J. A. Kress, F. Paulus, D. Becker-Koch, V. Lami, A. A. Bakulin, and Y. Vaynzof, Oxygen-Induced Doping as a Degradation Mechanism in Highly Efficient Organic Solar Cells. *ACS Appl. Energy Mater.* **2019**, 2, 3, 1943-1950

3. **A. Weu**, R. Kumar, J. F. Butscher, V. Lami, F. Paulus, A. A. Bakulin, and Y. Vaynzof, Energy Transfer to a Stable Donor Suppresses Degradation in Organic Solar Cells. *Manuscript submitted for publication.* **2019**

Additional publications

1. V. Lami, **A. Weu**, J. Zhang, Y. Chen, Z. Fei, M. Heeney, R. H. Friend and Y. Vaynzof, Visualising the Vertical Energetic Landscape in Organic Photovoltaics. *Joule* **2019**, In Press

2. Qingzhi An, Qing Sun, **A. Weu**, D. Becker-Koch, F. Paulus, S. Arndt, F. Stuck, A. S. K. Hashmi, N. Tessler, and Y. Vaynzof, Enhancing the Open-Circuit Voltage of Perovskite Solar Cells by up to 120 mV Using π-Extended Phosphoniumfluorene Electrolytes as Hole Blocking Layers. *Adv. Energ. Mater.* **2019**, 9, 33, 1901257

3. D. Leibold, V. Lami, Y. J. Hofstetter, D. Becker-Koch, **A. Weu**, P. Biegger, F. Paulus, U. H. F. Bunz, P. E. Hopkinson, A. A. Bakulin,

and Y. Vaynzof, Triptycenyl-phenazino-thiadiazole as acceptor in organic bulk-heterojunction solar cells. *Organic Electronics* **2018**, 57, 285-291

Conference contributions

1. **A. Weu**, T. R. Hopper, V. Lami, J. A. Kreß, A. A. Bakulin, and Y. Vaynzof, Field-Assisted Exciton Dissociation in Highly Efficient PffBT4T-2OD:fullerene Organic Solar Cells. Oral presentation - DPG Spring Meeting 2018, Berlin, Germany

2. **A. Weu**, J. A. Kress, F. Paulus, D. Becker-Koch, V. Lami, A. A. Bakulin, and Y. Vaynzof, Oxygen-induced doping as a degradation mechanism in highly efficient polymer organic solar cells. Poster presentation - DPG Spring Meeting 2019, Regensburg, Germany

3. **A. Weu**, J. A. Kress, F. Paulus, D. Becker-Koch, V. Lami, A. A. Bakulin, and Y. Vaynzof, Oxygen-Induced Doping as a Degradation Mechanism in PCE-11 Organic Solar Cells. Poster presentation - EMRS 2019, Nice, France

Abbreviations

Ag	silver
Al	aluminium
AM	air mass factor
as	attosecond
Au	gold
BBO	beta barium borate
BCB	bisbenzocyclobutene
BHJ	bulk heterojunction
bisPC$_{60}$BM	bis-substituted [6,6]-phenyl C61-butyric acid methyl ester
BPO	4,4'-biphenol
Ca	calcium
CdTe	cadmium telluride
CELIV	current extraction by linearly increasing voltage
CIGS	copper indium gallium selenide
CPA	chirped pulse amplification
CT	charge transfer
CTC	charge-transfer-complex
cw	continuous wave
DFT	density field theory
DIO	1,8-diiodooctane
DOS	density of states

DRCN5T	2,2'-[(3,3"',3"",4'-tetraoctyl [2,2':5',2":5",2"':5"',2""-quinquethiophene]-5,5""-diyl)bis[(Z)-methylidyne(3-ethyl-4-oxo-5,2-thiazolidinediylidene)]]bis-propanedinitrile
EQE	external quantum efficiency
ESA	excited state absorption
ETL	electron transport layer
FF	fill factor
FRET	Förster resonant energy transfer
fs	femtosecond
GaAs	gallium arsenide
GSB	ground state bleach
HOMO	highest occupied molecular orbital
HTL	hole transport layer
IC	internal conversion
ICS	intersystem crossing
IDIC	2,2'-((2Z,2'Z)-((4,4,9,9-tetrahexyl-4,9-dihydro-s-indaceno[1,2-b:5,6-b']dithiophene-2,7-diyl)bis(methanylylidene))bis(3-oxo-2,3-dihydro-1H-indene-2,1-diylidene))dimalononitrile
IR	infrared
IRF	instrument response function
ITIC	3,9-bis(2-methylene-(3-(1,1-dicyanomethylene)-indanone))-5,5,11,11-tetrakis(4-hexylphenyl)-dithieno[2,3-d:2',3'-d']-s-indaceno[1,2-b:5,6-b']dithiophene
ITO	indium tin oxide
$\mathbf{J_{SC}}$	short-circuit current
KLM	Kerr lens mode-locking

LBIC	laser beam induced current
LUMO	lowest unoccupied molecular orbital
MoO$_3$	molybdenum trioxide
MPP	maximum power point
Nd:glass	neodymium doped laser glass
NFA	non-fullerene acceptor
NIR	near-infrared
OFET	organic field effect transistor
OLED	organic light emitting diode
OPA	optical parametric amplification
OPV	organic photovoltaic
OSC	organic solar cell
P3HT	poly(3-hexyl thiophene)
PBDB-T-2Cl	Poly[(2,6-(4,8-bis(5-(2-ethylhexyl-3-chloro)thiophen-2-yl)-benzo[1,2-b:4,5-b']dithiophene))-alt-(5,5-(1',3'-di-2-thienyl-5',7'-bis(2-ethylhexyl)benzo[1',2'-c:4',5'-c']dithiophene-4,8-dione)]
PBDTTT-C	Poly[(4,8-bis-(2-ethylhexyloxy)-benzo(1,2-b:4,5-b')dithiophene)-2,6-diyl-alt-(4-(2-ethylhexanoyl)-thieno[3,4-b]thiophene-)-2-6-diyl)]
PC$_{60}$BM	[6,6]-phenyl C61-butyric acid methyl ester
PC$_{70}$BM	[6,6]-phenyl C71-butyric acid methyl ester
PCDTBT	poly[N-9'-heptadecanyl-2,7-carbazole-alt-5,5-(4',7'-di-2-thienyl-2',1',3'-benzothiadiazole)]
PCE	power conversion efficiency
PCPDTBT	poly[2,6-(4,4-bis-(2-ethylhexyl)-4H-cyclopenta [2,1-b;3,4-b']dithiophene)-alt-4,7(2,1,3-benzothiadiazole)]
PDS	photo-thermal deflection spectroscopy
PEDOT:PSS	poly(3,4-ethylenedioxythiophene):poly(styrenesulfonate)
PES	photoelectron emission spectroscopy

PffBT4T-2OD	poly[(5,6-difluoro-2,1,3-benzothiadiazol-4,7-diyl)-alt-(3,3'''-di(2-octyldodecyl)-2,2',5',2'',5'',2'''-quaterthiophen-5,5'''-diyl)]
PL	photoluminescence
ppm	parts per million
PPPC	pump-push photocurrent
PPV	poly(phenylenevinylene)
ps	picosecond
PSS	poly(styrenesulfonate)
PTB7	poly[[4,8-bis[(2-ethylhexyl)oxy]benzo[1,2-b:4,5-b']dithiophene-2,6-diyl][3-fluoro-2-[(2-ethylhexyl)carbonyl]thieno[3,4-b]thiophenediyl]]
PTB7-Th	poly[[4,8-bis[5-(2-ethylhexyl)thiophen-2-yl]benzo[1,2-b:4,5-b']dithiophene-2,6-diyl][3-fluoro-2-[(2-ethylhexyl)carbonyl]thieno[3,4-b]thiophenediyl]]
rpm	rotations per minute
Si	silicon
Si-PCPDTBT	(poly[(4,4'-bis(2-ethylhexyl)dithieno[3,2-b:2',3'-d]silole)-2,6-diyl-alt-(4,7-bis(2-thienyl)-2,1,3-benzothiadiazole)-5,5'-diyl]
SM	small molecule
SMU	source measure unit
SVD	singular value decomposition
T$_g$	glass transition temperature
TA	transient absorption
TCSPC	time-correlated single photon counting
Ti:sapphire	titanium-doped aluminium oxide
TiO$_2$	titanium dioxide
TOF	time-of-flight
TOF-SIMS	time-of-flight secondary ion mass spectrometry
TPC	transient photocurrent

UPS	ultra-violet photoelectron spectroscopy
UV	ultra-violet
UV-Vis	ultraviolet–visible
V$_{OC}$	open-circuit voltage
VIS	visible
WO$_3$	tungsten trioxide
XPS	X-ray photoelectron spectroscopy
XRD	X-ray diffraction
ZnO	zinc oxide

"When you have eliminated all which is impossible, then whatever remains, however improbable, must be the truth."

– Sherlock Holmes

Part I

Introduction

Introduction

The global energy demand is steadily rising. In 2018, the primary energy consumption reached ~166,000 TWh which is expected to increase by 27% until the year 2040.[1,2] This evolution is substantially driven by growing energy requirements in developing countries, including China and India. Currently, 80% of this energy is provided by combustion of fossil fuels and, consequently, the CO_2 concentration in the atmosphere reached average values of 407 ppm (parts per million) today - the highest it has been in at least 800,000 years.[3–5] A continued emission of CO_2 and other greenhouse gases will have devastating consequences for our planet.[6–11] Limiting the global warming to 1.5°C above pre-industrial levels is required to mitigate these changes, according to IPCC (Intergovernmental Panel on Climate Change) climate models.[12] Therefore, arguably the greatest challenge the global community is facing today is to reduce the impact of climate change on the planet.[13–15] A possible way to mitigate emissions is an increased use of renewable energy sources.[12,16,17]

Among the various possible renewable energy technologies, photovoltaics are the fastest growing and most promising concepts for a scalable and decentralised power generation in the future.[1,2,18] The sun is a vast source of energy, with almost 90,000 TW of solar power reaching the earth's surface.[19] This is more energy every two hours than the global energy demand in the entire year 2018.[1] Thus, immense research has been dedicated during the last decades to bring the efficiency of photovoltaic devices to the theoretical limit (see Figure 1).[20] The most widespread technologies today include crystalline silicon (Si), cadmium telluride (CdTe), or copper indium gallium selenide (CIGS) solar cells, providing around 480 GW of worldwide photovoltaic capacity.[21] These conventional devices exhibit high efficiencies and long lifetimes, and their production benefits from existing semiconductor industries.[22] However, their fabrication requires expensive and energy-intensive processes for crystal growth, e.g. the Czochralski method. Furthermore, traditional solar cells are often incompatible with modern applications like transparent, flexible, or wearable
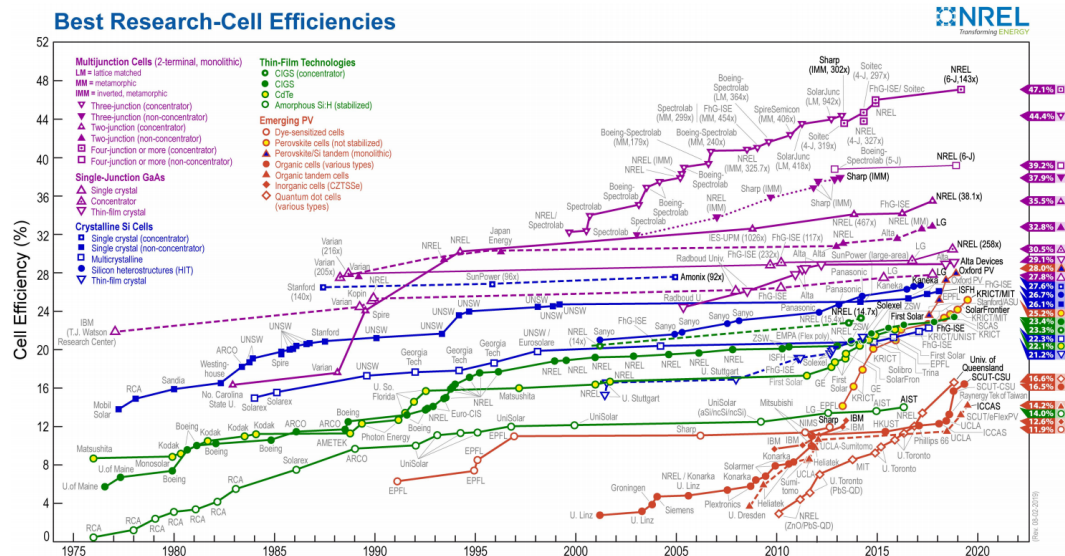
Figure 1: Highest confirmed conversion efficiencies for research cells for a range of photovoltaic technologies, plotted from 1976 to the present. Organic photovoltaics show a remarkable trend in the last years. Figure courtesy of NREL.[34]

devices.[23]

In the last two decades, the field of organic photovoltaics (OPVs) has emerged as an alternative technology, presenting an enormous variety of new compounds for solar cell research due to the chemical tunability of their properties.[24–26] This approach uses the semiconducting properties of polymers and small molecules which, due to their high absorption coefficients, can be used for thin film applications, offering low-cost, high-throughput fabrication (solution-processable, no high-temperature steps required, using roll-to-roll manufacturing[27–29]) and novel applications (semi-transparent and flexible devices,[30–32] efficient operation at low light intensities[33]). Within the next few years, OPV modules are expected to be fabricated at lower prices per Watt than commercially available technologies.[27]

The research on organic electronics has progressed at a remarkable rate. The first organic solar cells consisted of a simple metal/organic/metal structure.[35,36] However, these devices exhibited extremely low efficiencies, as they relied only on the built-in electric field provided by the potential difference of the electrodes to separate the electron-hole pairs, which typically have much larger binding energies.[37] This limitation was overcome by the introduction

of the donor:acceptor heterojunction, in which the energetic offset between the energy levels of two adjacent materials drives dissociation of the bound pair. This major breakthrough enabled the first organic solar cells with a power conversion efficiency (PCE) over 1%.[38] The development of the bulk heterojunction (BHJ), in which the active materials are intimately mixed, was a further milestone in the progress of organic solar cells and is an essential concept for modern-day organic devices.[39] Early research focussed on PPV derivatives and later shifted to poly-thiophenes, most notably P3HT, with efficiencies over 5%.[40] The usage of donor-acceptor co-polymers, such as PTB7, PTB7-Th, or PffBT4T-2OD, lead to impressive performances with efficiencies of more than 10%.[40–43] Todays' high-performance systems convert more than 16% of the sunlight into electrical power.[44]

Traditionally, fullerene derivatives such as $PC_{60}BM$ and $PC_{70}BM$ have been used as acceptor molecules in OPVs, due to their unique electron accepting properties enabling efficient charge generation.[45,46] However, these molecules do not exhibit strong absorption in the visible part of the solar spectrum, and, therefore, efficiencies of devices based on fullerene acceptors are limited. More recently, the class of non-fullerene acceptors (NFAs), which are used in current record devices, emerged as a new alternative to overcome those limitations.[44,47–49] Modern research also focusses on more complex structures, such as ternary blends[50–52] or tandem cells[53–55], to boost performance by harvesting a broader spectrum of the sunlight. Simultaneously to organic solar cells based on polymers or small molecules, the development of perovskite materials progresses in an unprecedented form, already surpassing some conventional technologies.[56–58]

Unsurprisingly, most research has focussed on improving the efficiency of organic solar cells, leading to a remarkable increase in performance from 12% to over 16% in the past 3 years.[44] While these efficiencies are approaching the range of conventional consumer modules[59], the upscaling of lab-sized cells (typically ~ 1 cm^2) to large-area modules is still a challenge.[60–62] Furthermore, while efficiencies are rising, the environmental stability, which limits the lifetime of polymer- and small molecule-based solar cells, remains a problem that is still insufficiently addressed. Understanding the processes involved in the device degradation, therefore, is of paramount importance for the transition from laboratory cells to commercial applications.[63]

This thesis addresses this urgent topic by investigating the operational stability of two high-efficiency OPV systems in ambient conditions. Particular focus is given to the photophysics on the picosecond (ps) timescales during

which the relevant processes of charge generation occur. An improved comprehension of the early charge carrier dynamics of novel material systems not only provides valuable information for the research on more efficient compounds; it also gives important insights into how these processes are affected during degradation which is a prerequisite for the development of efficient mitigation strategies. The ultrafast physics of such systems is investigated by transient absorption (TA) spectroscopy which is based on femtosecond (fs) laser pulses and has led to a range of remarkable discoveries.[64,65]

This thesis starts with a brief introduction into the physical principles of organic solar cells (Chapter 1), followed by a review of the processes occurring during device degradation (Chapter 2), and the fundamentals of ultrafast laser spectroscopy (Chapter 3). Following necessary details on the used materials and methods (Chapters 4 and 5), the unusual photophysics of the polymer:fullerene system PffBT4T-2OD:$PC_{70}BM$ is investigated (Chapter 6). In Chapter 7 the stability of this material system under light and oxygen exposure is studied, and, subsequently, results of the investigation of the small molecule DRCN5T are presented in Chapter 8. Finally, the obtained results are concluded in the context of the development of novel high-efficiency and stable devices for future research and application.

Bibliography

[1] IEA, Global Energy & CO2 Status Report - Renewables. 2019; https://www.iea.org/geco/data/.

[2] International Energy Agency, *World Energy Outlook 2018*; 2018.

[3] Le Quéré, C. et al. Global Carbon Budget 2018. *Earth System Science Data* **2018**, *10*, 2141–2194.

[4] Lüthi, D.; Le Floch, M.; Bereiter, B.; Blunier, T.; Barnola, J.-M.; Siegenthaler, U.; Raynaud, D.; Jouzel, J.; Fischer, H.; Kawamura, K.; Stocker, T. F. High-resolution carbon dioxide concentration record 650,000-800,000 years before present. *Nature* **2008**, *453*, 379–382.

[5] Fleurbaey, M.; Kartha, S.; Bolwig, S.; Chee, Y. L.; Chen, Y.; Corbera, E.; Lecocq, F.; Lutz, W.; Muylaert, M. S.; Norgaard, R. B.; Okereke, C.; Sagar, A. In *Climate Change 2014: Mitigation of Climate Change*; Edenhofer, O. et al. , Eds.; Cambridge University Press: United Kingdom, 2014.

[6] Rosenzweig, C.; Parry, M. L. Potential impact of climate change on world food supply. *Nature* **1994**, *367*, 133–138.

[7] Parmesan, C.; Yohe, G. A globally coherent fingerprint of climate change impacts across natural systems. *Nature* **2003**, *421*, 37–42.

[8] Hoegh-Guldberg, O.; Bruno, J. F. The impact of climate change on the world's marine ecosystems. *Science (New York, N.Y.)* **2010**, *328*, 1523–8.

[9] Edwards, M.; Richardson, A. J. Impact of climate change on marine pelagic phenology and trophic mismatch. *Nature* **2004**, *430*, 881–884.

[10] Morton, J. F. The impact of climate change on smallholder and subsistence agriculture. *Proceedings of the National Academy of Sciences* **2007**, *104*, 19680–19685.

[11] Patz, J. A.; Campbell-Lendrum, D.; Holloway, T.; Foley, J. A. Impact of regional climate change on human health. *Nature* **2005**, *438*, 310–317.

[12] IPCC, *Summary for Policymakers. In: Global Warming of 1.5°C. An IPCC Special Report on the impacts of global warming of 1.5°C above pre-industrial levels*; 2018; p32.

[13] Bastin, J.-F.; Finegold, Y.; Garcia, C.; Mollicone, D.; Rezende, M.; Routh, D.; Zohner, C. M.; Crowther, T. W. The global tree restoration potential. *Science (New York, N.Y.)* **2019**, *365*, 76–79.

[14] Figueres, C.; Quéré, C. L.; Mahindra, A.; Bäte, O.; Whiteman, G.; Peters, G.; Guan, D. Emissions are still rising: ramp up the cuts. *Nature* **2018**, *564*, 27–30.

[15] Mysiak, J.; Surminski, S.; Thieken, A.; Mechler, R.; Aerts, J. Brief communication: Sendai framework for disaster risk reduction – success or warning sign for Paris? *Natural Hazards and Earth System Sciences* **2016**, *16*, 2189–2193.

[16] United Nations, Paris Agreement. 2015; https://treaties.un.org/pages/ViewDetails.aspx?src=TREATY{&}mtdsg{_}no=XXVII-7-d{&}chapter=27{&}clang={_}en.

[17] Friedlingstein, P.; Andrew, R. M.; Rogelj, J.; Peters, G. P.; Canadell, J. G.; Knutti, R.; Luderer, G.; Raupach, M. R.; Schaeffer, M.; van Vuuren, D. P.; Le Quéré, C. Persistent growth of CO2 emissions and implications for reaching climate targets. *Nature Geoscience* **2014**, *7*, 709–715.

[18] Chen, S.; Lu, X.; Miao, Y.; Deng, Y.; Nielsen, C. P.; Elbot, N.; Wang, Y.; Logan, K. G.; McElroy, M. B.; Hao, J. The Potential of Photovoltaics to Power the Belt and Road Initiative. *Joule* **2019**, *3*, 1895–1912.

[19] Perez, R.; Perez, M. A fundamental look at supply side energy reserves for the planet. *Int. Energy Agency SHC Program.* **2015**, *62*, 4–6.

[20] Shockley, W.; Queisser, H. J. Detailed balance limit of efficiency of p-n junction solar cells. *Journal of Applied Physics* **1961**, *32*, 510–519.

[21] International Renewable Energy Agency, *Renewable Capacity Statistics 2019*; 2019.

[22] Mints, P. Global photovoltaic shipments jump 15% in 2014. 2015; https://www.idtechex.com/en/research-article/global-photovoltaic-shipments-jump-15-in-2014/7454.

[23] Aberle, A. G. Thin-film solar cells. *Thin Solid Films* **2009**, *517*, 4706–4710.

[24] Zhang, J.; Zhu, L.; Wei, Z. Toward Over 15% Power Conversion Efficiency for Organic Solar Cells: Current Status and Perspectives. *Small Methods* **2017**, *1*, 1700258.

[25] Rand, B. P., Richter, H., Eds. *Organic solar cells : fundamentals, devices, and upscaling*, 1st ed.; Jenny Standford Publishing, 2014; p810.

[26] Brabec, C.; Scherf, U.; Dyakonov, V. *Organic Photovoltaics : Materials, Device Physics, and Manufacturing Technologies*.; Wiley, 2014; p638.

[27] Gambhir, A.; Sandwell, P.; Nelson, J. The future costs of OPV – A bottom-up model of material and manufacturing costs with uncertainty analysis. *Solar Energy Materials and Solar Cells* **2016**, *156*, 49–58.

[28] Machui, F. et al. Cost analysis of roll-to-roll fabricated ITO free single and tandem organic solar modules based on data from manufacture. *Energy & Environmental Science* **2014**, *7*, 2792.

[29] Hoppe, H.; Sariciftci, N. S. Organic solar cells: An overview. *Journal of Materials Research* **2004**, *19*, 1924–1945.

[30] Chang, S.-Y.; Cheng, P.; Li, G.; Yang, Y. Transparent Polymer Photovoltaics for Solar Energy Harvesting and Beyond. *Joule* **2018**, *2*, 1039–1054.

[31] Li, Y.; Lin, J.-D.; Che, X.; Qu, Y.; Liu, F.; Liao, L.-S.; Forrest, S. R. High Efficiency Near-Infrared and Semitransparent Non-Fullerene Acceptor Organic Photovoltaic Cells. *Journal of the American Chemical Society* **2017**, *139*, 17114–17119.

[32] Li, G.; Zhu, R.; Yang, Y. Polymer solar cells. *Nature Photonics* **2012**, *6*, 153–161.

[33] Cui, Y.; Wang, Y.; Bergqvist, J.; Yao, H.; Xu, Y.; Gao, B.; Yang, C.; Zhang, S.; Inganäs, O.; Gao, F.; Hou, J. Wide-gap non-fullerene acceptor enabling high-performance organic photovoltaic cells for indoor applications. *Nature Energy* **2019**, *4*, 768–775.

[34] National Renewable Energy Laboratory, Best Research-Cell Efficiency Chart. 2019; https://www.nrel.gov/pv/cell-efficiency.html.

[35] Kearns, D.; Calvin, M. Photovoltaic Effect and Photoconductivity in Laminated Organic Systems. *The Journal of Chemical Physics* **1958**, *29*, 950–951.

[36] Tang, C. W.; Albrecht, A. C. Photovoltaic effects of metal-chlorophyll-a-metal sandwich cells. *The Journal of Chemical Physics* **1975**, *62*, 2139–2149.

[37] Głowacki, E. D.; Sariciftci, N. S.; Tang, C. W. *Solar Energy*; Springer New York: New York, NY, 2013; pp 97–128.

[38] Tang, C. W. Two-layer organic photovoltaic cell. *Applied Physics Letters* **1986**, *48*, 183–185.

[39] Kraabel, B.; Lee, C.; McBranch, D.; Moses, D.; Sariciftci, N.; Heeger, A. Ultrafast photoinduced electron transfer in conducting polymer—buckminsterfullerene composites. *Chemical Physics Letters* **1993**, *213*, 389–394.

[40] Lu, L.; Zheng, T.; Wu, Q.; Schneider, A. M.; Zhao, D.; Yu, L. Recent Advances in Bulk Heterojunction Polymer Solar Cells. *Chemical Reviews* **2015**, *115*, 12666–12731.

[41] Brus, V. V.; Lee, J.; Luginbuhl, B.; Ko, S.-J.; Bazan, G. C.; Nguyen, T.-Q. Solution-Processed Semitransparent Organic Photovoltaics: From Molecular Design to Device Performance. *Advanced Materials* **2019**, *31*, 1900904.

[42] Ye, L.; Zhang, S.; Zhao, W.; Yao, H.; Hou, J. Highly Efficient 2D-Conjugated Benzodithiophene-Based Photovoltaic Polymer with Linear Alkylthio Side Chain. *Chemistry of Materials* **2014**, *26*, 3603–3605.

[43] Liu, Y.; Zhao, J.; Li, Z.; Mu, C.; Ma, W.; Hu, H.; Jiang, K.; Lin, H.; Ade, H.; Yan, H. Aggregation and morphology control enables multiple cases of high-efficiency polymer solar cells. *Nature Communications* **2014**, *5*, 5293.

[44] Cui, Y.; Yao, H.; Zhang, J.; Zhang, T.; Wang, Y.; Hong, L.; Xian, K.; Xu, B.; Zhang, S.; Peng, J.; Wei, Z.; Gao, F.; Hou, J. Over 16% efficiency organic photovoltaic cells enabled by a chlorinated acceptor with increased open-circuit voltages. *Nature Communications* **2019**, *10*, 2515.

[45] Liu, T.; Troisi, A. What Makes Fullerene Acceptors Special as Electron Acceptors in Organic Solar Cells and How to Replace Them. *Advanced Materials* **2013**, *25*, 1038–1041.

[46] Zhang, F.; Zhuo, Z.; Zhang, J.; Wang, X.; Xu, X.; Wang, Z.; Xin, Y.; Wang, J.; Wang, J.; Tang, W.; Xu, Z.; Wang, Y. Influence of PC60BM or PC70BM as electron acceptor on the performance of polymer solar cells. *Solar Energy Materials and Solar Cells* **2012**, *97*, 71–77.

[47] Hou, J.; Inganäs, O.; Friend, R. H.; Gao, F. Organic solar cells based on non-fullerene acceptors. *Nature Materials* **2018**, *17*, 119–128.

[48] Cui, Y.; Yao, H.; Hong, L.; Zhang, T.; Xu, Y.; Xian, K.; Gao, B.; Qin, J.; Zhang, J.; Wei, Z.; Hou, J. Achieving Over 15% Efficiency in Organic Photovoltaic Cells via Copolymer Design. *Advanced Materials* **2019**, *31*, 1808356.

[49] Yuan, J.; Zhang, Y.; Zhou, L.; Zhang, G.; Yip, H.-L.; Lau, T.-K.; Lu, X.; Zhu, C.; Peng, H.; Johnson, P. A.; Leclerc, M.; Cao, Y.; Ulanski, J.; Li, Y.; Zou, Y. Single-Junction Organic Solar Cell with over 15% Efficiency Using Fused-Ring Acceptor with Electron-Deficient Core. *Joule* **2019**, *3*, 1140–1151.

[50] Gasparini, N.; Salleo, A.; McCulloch, I.; Baran, D. The role of the third component in ternary organic solar cells. *Nature Reviews Materials* **2019**, *4*, 229–242.

[51] Baran, D. et al. Reducing the efficiency–stability–cost gap of organic photovoltaics with highly efficient and stable small molecule acceptor ternary solar cells. *Nature Materials* **2017**, *16*, 363–369.

[52] Gasparini, N.; Lucera, L.; Salvador, M.; Prosa, M.; Spyropoulos, G. D.; Kubis, P.; Egelhaaf, H.-J.; Brabec, C. J.; Ameri, T. High-performance ternary organic solar cells with thick active layer exceeding 11% efficiency. *Energy & Environmental Science* **2017**, *10*, 885–892.

[53] Meng, L.; Zhang, Y.; Wan, X.; Li, C.; Zhang, X.; Wang, Y.; Ke, X.; Xiao, Z.; Ding, L.; Xia, R.; Yip, H.-L.; Cao, Y.; Chen, Y. Organic and solution-processed tandem solar cells with 17.3% efficiency. *Science (New York, N.Y.)* **2018**, *361*, 1094–1098.

[54] Che, X.; Li, Y.; Qu, Y.; Forrest, S. R. High fabrication yield organic tandem photovoltaics combining vacuum- and solution-processed subcells with 15% efficiency. *Nature Energy* **2018**, *3*, 422–427.

[55] Cui, Y.; Yao, H.; Gao, B.; Qin, Y.; Zhang, S.; Yang, B.; He, C.; Xu, B.; Hou, J. Fine-Tuned Photoactive and Interconnection Layers for Achieving over 13% Efficiency in a Fullerene-Free Tandem Organic Solar Cell. *Journal of the American Chemical Society* **2017**, *139*, 7302–7309.

[56] Yang, W. S.; Park, B.-W.; Jung, E. H.; Jeon, N. J.; Kim, Y. C.; Lee, D. U.; Shin, S. S.; Seo, J.; Kim, E. K.; Noh, J. H.; Seok, S. I. Iodide management in formamidinium-lead-halide-based perovskite layers for efficient solar cells. *Science (New York, N.Y.)* **2017**, *356*, 1376–1379.

[57] Jeon, N. J.; Noh, J. H.; Yang, W. S.; Kim, Y. C.; Ryu, S.; Seo, J.; Seok, S. I. Compositional engineering of perovskite materials for high-performance solar cells. *Nature* **2015**, *517*, 476–480.

[58] Yin, W.-J.; Yang, J.-H.; Kang, J.; Yan, Y.; Wei, S.-H. Halide perovskite materials for solar cells: a theoretical review. *Journal of Materials Chemistry A* **2015**, *3*, 8926–8942.

[59] Green, M. A.; Hishikawa, Y.; Dunlop, E. D.; Levi, D. H.; Hohl-Ebinger, J.; Yoshita, M.; Ho-Baillie, A. W. Solar cell efficiency tables (Version 53). *Progress in Photovoltaics: Research and Applications* **2019**, *27*, 3–12.

[60] Burgués-Ceballos, I.; Stella, M.; Lacharmoise, P.; Martínez-Ferrero, E. Towards industrialization of polymer solar cells: material processing for upscaling. *J. Mater. Chem. A* **2014**, *2*, 17711–17722.

[61] Krebs, F. C.; Tromholt, T.; Jørgensen, M. Upscaling of polymer solar cell fabrication using full roll-to-roll processing. *Nanoscale* **2010**, *2*, 873.

[62] Lungenschmied, C.; Dennler, G.; Neugebauer, H.; Sariciftci, S. N.; Glatthaar, M.; Meyer, T.; Meyer, A. Flexible, long-lived, large-area, organic solar cells. *Solar Energy Materials and Solar Cells* **2007**, *91*, 379–384.

[63] Jean, J.; Woodhouse, M.; Bulović, V. Accelerating Photovoltaic Market Entry with Module Replacement. *Joule* **2019**, *0*.

[64] Zewail, A. H. Femtochemistry: Atomic-Scale Dynamics of the Chemical Bond Using Ultrafast Lasers (Nobel Lecture). *Angewandte Chemie International Edition* **2000**, *39*, 2586–2631.

[65] Di Donato, M.; Groot, M. L. Ultrafast infrared spectroscopy in photosynthesis. *Biochimica et Biophysica Acta (BBA) - Bioenergetics* **2015**, *1847*, 2–11.

Part II

Theoretical Background

Chapter 1

Organic solar cells

A better understanding of the working principle of organic photovoltaics (OPVs) can help to develop novel devices with optimised performance and longer lifetimes. Therefore, in this chapter the principles of OPVs are presented, introducing the concept of the bulk heterojunction (BHJ), the device structure, and the current-voltage characteristics (Section 1.1). Particular focus is given to the specific processes which lead to generation of free charges in the devices (Section 1.2).

1.1 Organic photovoltaics

1.1.1 Active layer

In an OPV device, incident photons are converted into charge carriers which can be extracted by electrodes and then used to power an external circuit. The elemental processes leading to charge generation are illustrated in Figure 1.1. In contrast to inorganic solar cells, in which free charge carriers are directly created and separated in a pn-junction, strongly bound electron-hole pairs (*excitons*) are formed after light absorption in organic films. Those excitons do not readily dissociate in a single organic semiconductor at room temperatures, as their Coulomb attraction is on the order of several hundred meV.[1,2] Instead a second material with different electron affinity or ionisation potential is needed to separate the pairs at an interface through charge transfer between the two components which are referred to as *donor* and *acceptor*. Absorption of light and subsequent charge transfer between the components occurs in both, the donor and the acceptor materials.

Figure 1.1: Schematic representation of the BHJ and the processes involved in charge generation. After light absorption an exciton is create which diffuses through the active layer. After arriving at an interface to the acceptor charge transfer dissociates the exciton into free charges. Reproduced with permission from Ref.[3] Copyright 2018, The Royal Society of Chemistry.
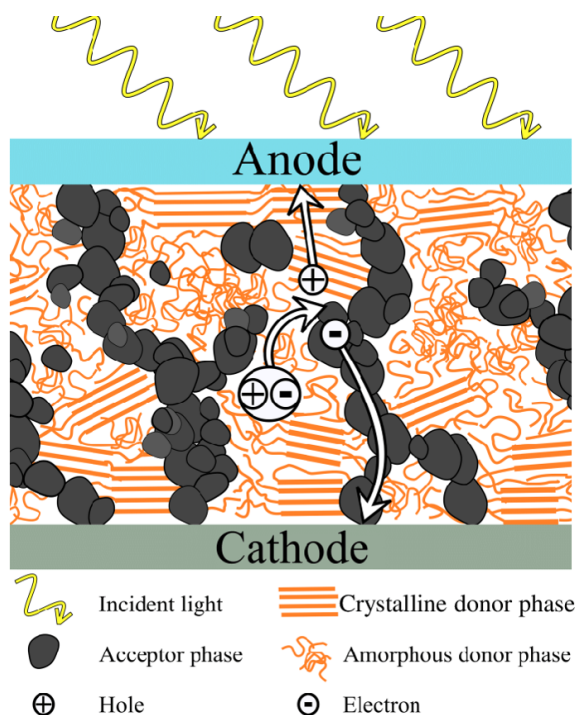
Since the exciton has a limited lifetime and thus a certain diffusion length (typically on the order of $\sim$10 nm[4–7]), an optimal morphology provides interfaces for exciton dissociation on the nanometer scale. Furthermore, continuous percolation pathways for the separated charges to the extracting electrodes must exist. The best practical solution to these conditions is a blend mixture of the two active components in a *bulk heterojunction (BHJ)* which provides both crystalline domains and pathways for charge transport, and intimately mixed regions for efficient charge separation.

1.1.2   Device structure

In order to extract and use the charges which are created in the above mentioned active layer, the BHJ of an OPV is sandwiched between several layers and contacts (Figure 1.2). After separation of the exciton, the charges are transported energetically downwards through the layers and extracted at the electrodes (Figure 1.2b). One contact is transparent and permits the light to enter the device through this side, while the other contact is highly reflective to increase the optical path through the BHJ and ensure efficient absorption.
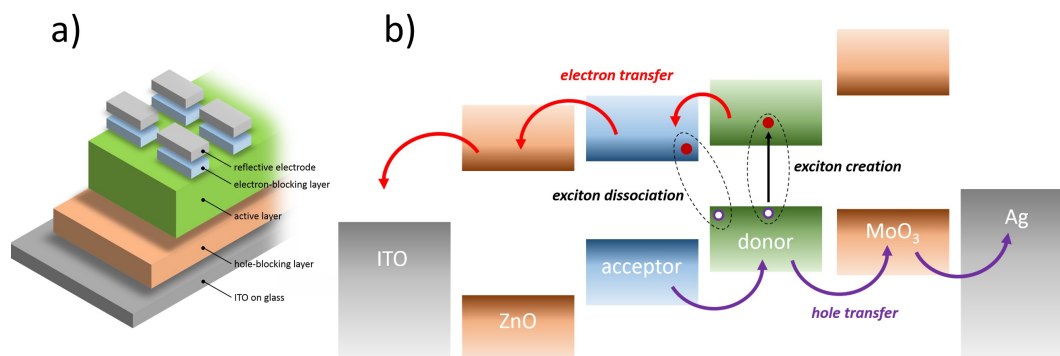
Figure 1.2: (a) Typical device architecture with the active layer sandwiched between the transport layers and the electrodes. (b) Energy level diagram of a typical inverted OPV cell. Indicated are the formation of excitons, exciton diffusion to an interface, charge transfer, and subsequent transport through the charge-transport layers and extraction at the electrodes. Absorption of photons can occur in both active layer materials.

The common choice for the transmissive electrode are conductive oxides, such as indium tin oxide (ITO). ITO has a work function of 4.8 ± 0.5 eV which makes it suitable for charge extraction or injection at the metal-semiconductor interface. Depending on the specific device architecture aluminium, silver, or gold is used as reflective back contact. OPVs can be fabricated in the normal (standard) geometry or in the inverted geometry. In the former, light enters through the transparent anode, while the reflective back contact serves as the cathode. This architecture is commonly used for high-efficiency devices, however, the low work function metal electrodes have several disadvantages concerning ease of fabrication and device stability which will be discussed in detail in Chapter 2.[8,9] In the inverted architecture, light enters through the transparent cathode and is reflected at the high work function anode.

To spatially separate electrons and holes after exciton dissociation and to reduce recombination at the electrodes, additional blocking layers are inserted that promote transport of one charge type, but block the other. Common hole-transport/electron-blocking layers hole transport layers (HTLs) are PEDOT:PSS, molybdenum trioxide (MoO_3), or tungsten trioxide (WO_3), whereas zinc oxide (ZnO) or titanium dioxide (TiO_2) are often used as electron-transport/hole-blocking layer electron transport layer (ETL). Another purpose is to block the excitons at the interface which prevents them from reaching the electrode

where they can recombine.[10]

1.1.3   Current-voltage characteristics

Organic solar cells (OSCs) follow the characteristics of diodes with additional photocurrent (Figure 1.3a). When the above-mentioned stack is operated under reverse-bias conditions (i.e. the anode is at a negative potential with respect to the cathode), photogenerated charges are extracted from the device by the increased built-in electric field, which is provided by the Fermi levels of the electrodes. This region is marked by a quasi-voltage-independent, negative current (electrons flow towards the cathode, while hole drift towards the anode). Under forward-bias conditions, the applied voltage reduces the magnitude of the built-in electric field. Consequently, current flow in the opposite direction is promoted which increases exponentially with increasing forward-bias.

In order to generate electrical power P_{out}, the charges must be extracted from the solar cell with a potential difference, according to $P_{out} = J \cdot V$, where J is the current density and V the voltage. This power is generated when the product of current density and voltage is negative, i.e. when the J-V curve passes through quadrant IV in Figure 1.3a. An analytical expression for $J(V)$ in the sense of the Shockley equation for pn-junctions is difficult to obtain for organic solar cells, due to the fundamentally different working principle and conditions concerning charge carrier density, mobility, or diffusivity, and is indeed a current topic of research. An approximation for a bi-layer device at low biases, neglecting geminate recombination, leakage, and charge accumulation is reported by Giebink et al.[11]

$$J = J_S \left[\exp\left(\frac{eV}{k_B T} \right) - \frac{k_d}{k_{d,thermal}} \right] - e\eta_d J_{ex} \qquad (1.1)$$

where $k_{d,thermal}$ is the exciton dissociation rate in the absence of bias or illumination, $\eta_d = k_d/(k_d + k_f)$ the probability of exciton dissociation with the recombination rate k_f, J_S the dark saturation current, and J_{ex} the flux of exciton diffusion towards a donor-acceptor interface.

The most important metric describing the performance of a solar cell is the *power conversion efficiency (PCE)* which is given by the maximum electrical power $P_{out,max}$ divided by the incident light power P_{in}

$$PCE = \frac{P_{out,max}}{P_{in}} \qquad (1.2)$$
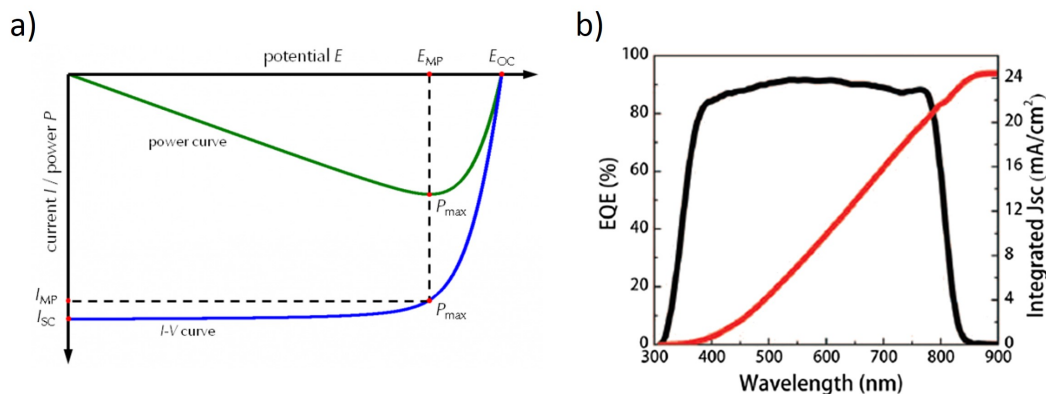
Figure 1.3: (a) Schematic JV-curve and power output of an inverted solar cell. Included are short-circuit current (J_{SC}) and open-circuit voltage (V_{OC}) (here denoted as E_{OC}). The JV-curve dictates the maximum power point (MPP), where the generated power is maximal. Figure courtesy of Gamry Instruments. (b) Example EQE spectrum of a perovskite solar cell. Integrating the curve over the solar spectrum yields the photo-current which can be extracted. Reproduced with permission from Ref.[14] Copyright 2016, SPIE.

The maximum achievable power conversion efficiency of a general solar cell is given by the Shockley-Queisser limit which was derived in 1961 for inorganic pn-junctions.[12] It states that the PCE depends on the optical bandgap of the material and has a maximal value of 33.7% for a single junction device, based on the assumptions that photons below the bandgap are not absorbed and excess energy from high-frequency photons is lost by rapid conversion to heat. In organic solar cells the efficiency limit depends also on the exciton binding energy which can be neglected for inorganic semiconductors. Consequently, the maximum PCE is reduced to <30% in organic devices.[13]

From the JV-characteristics in Equation 1.1 follows that $P_{out,max}$ assumes a maximum (the *maximum power point (MPP)*) between open-circuit conditions, where the current flow is zero, and short-circuit conditions, where the voltage is zero. The corresponding maximum photocurrent and photovoltage values are denoted *short-circuit current (J_{SC})* and *open-circuit voltage (V_{OC})*, respectively. These values define the *fill factor (FF)* which is a geometrical factor, given by the ratio of the maximum electrical power of the device and the theoretical power determined by J_{SC} and V_{OC}

$$FF = \frac{P_{out,max}}{J_{SC} \cdot V_{OC}} \tag{1.3}$$

The FF is a measure for how 'rectangular' the J-V curve looks in quadrant IV. With this definition the power conversion efficiency assumes the simple and common form

$$PCE = \frac{J_{SC} \cdot V_{OC} \cdot FF}{P_{in}} \tag{1.4}$$

The characteristic solar cell parameters J_{SC}, V_{OC} and FF allow a practical description of the solar cell performance. The J_{SC} is related to the amount of charges that are extracted and is thus influenced by the absorption properties of the materials, the charge generation process, transport to the electrodes, and recombination during these steps. The V_{OC} is determined by the energy levels of the materials and recombination losses, while the FF is, among others, influenced by transport properties in the bulk and at the interfaces. For improved solar cell operation, all three of these parameters need to be increased.

Since the efficiency is a function of the wavelength of the incident light, the $PCE(\lambda)$ has to be integrated over the entire spectrum of the light source. To ensure comparability between different laboratories, standard conditions have been defined, which fix the temperature (25°C), the intensity (100 mW cm^{-2}), and spectral profile (air mass factor (AM) 1.5) of the light. The latter corresponds to the emission spectrum of the sun after passing the earth's atmosphere 1.5 times (i.e. incident at an angle of 48.2° with respect to the vertical). Those conditions are referred to as *1 sun* illumination.

To quantify the wavelength-dependent efficiency of the OPV, the *external quantum efficiency (EQE)* is measured which is given by the ratio of charge pairs that are extracted j_e and the incident photon flux f_{ph} per wavelength (Figure 1.3b). It can be calculated by measuring the J_{SC} and light intensity I at every wavelength.

$$EQE = \frac{j_e}{j_{ph}} = \frac{J_{SC}(\lambda)}{I(\lambda)} \frac{hc}{\lambda e} \tag{1.5}$$

where h is Planck's constant, c the speed of light, and e the elementary charge. From the spectrum one can infer which parts of the material system efficiently contribute to the photocurrent generation. The overall photocurrent that the cell produces is given by the integral of the quantum efficiency over the entire spectrum.

$$J_{SC} = \frac{e}{hc} \int \text{EQE}(\lambda) \cdot S(\lambda) \cdot \lambda \, d\lambda \tag{1.6}$$

with the solar spectrum $S(\lambda)$ in units of $\text{Wm}^{-2}\text{nm}^{-1}$. The integrated photocurrent from Equation 1.6 is usually larger than the actual J_{SC} measured under 1 sun conditions, due to non-linear intensity dependences of the devices (see next Section for details). This intensity dependence leads to optimal operation in low intensity environments which makes this technology suitable for indoor applications.[15,16] The EQE is limited by the absorption of photons and recombination losses. Note that through multiple exciton generation processes, such as singlet fission, the EQE for high energy photons can surpass 100%, meaning that more than one charge pair is created and collected per incident photon.[17,18]

1.2 Charge generation

In this section the processes of charge generation are explained in detail which will be a basis for the results of this thesis. The principle processes are the formation of a tightly bound exciton upon light absorption, subsequent diffusion to a donor:acceptor interface, charge transfer to form a meta-stable charge transfer (CT) state, and dissociation of this state to yield free charge carriers that can be extracted by the electrodes (Figure 1.4).

1.2.1 Exciton creation and diffusion

When light is absorbed in an organic semiconductor usually singlet excited states are created. The excitation can occur by absorption of a single photon, the sequential absorption of multiple photons, or the simultaneous absorption of multiple photons where for the last case high intensities are required. The resulting electron-hole pair is localised (*Frenkel exciton*) and tightly bound by the Coulomb attraction with potential

$$V = \frac{e^2}{4\pi\epsilon_r\epsilon_0 r} \tag{1.7}$$

where e is the elementary charge, ϵ the dielectric constant, and r the electron-hole separation. Due to the low dielectric constant of organic materials ($\epsilon_r = 2-4$) compared to inorganic matter (e.g. $\epsilon_r = 11$ for GaAs) the binding energy
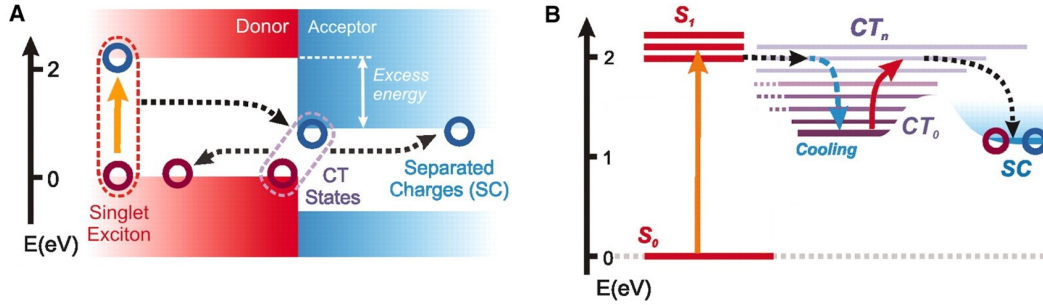
Figure 1.4: (a) Band diagram and (b) free-energy state diagram of a typical OPV system. Singlet, CT (lowest-lying CT_0; band states, CT_n) and separated-charges (SC) states are shown. Adapted with permission from Ref.[19] Copyright 2012, American Association for the Advancement of Science.

of the exciton ($E_b \sim 0.5$ - 1 eV) is much larger than the thermal energy at room temperature, and thus it is not easily dissociated.

During its lifetime the exciton diffuses through the rough energy landscape of the disordered semiconductor by thermally activated hopping. The simplest treatment uses a random-walk model of hopping events to describe this diffusion.[20] This hopping is facilitated by Dexter energy transfer and Förster resonant energy transfer (FRET) by which the exciton is transferred from one molecule to another molecule (Figure 1.5). In the former process, electrons are exchanged and it thus requires an overlap of the molecular orbitals of neighbouring molecules. Dexter energy transfer therefore dominates for short distances ($k_{Dexter} \sim e^{-r}$) and triplet states. The FRET mechanism relies on dipole-dipole interactions and prevails for singlet states and distances exceeding 1 nm.[5,21–23] Energy transfer requires a spectral overlap between emission of the donating molecule and absorption of the accepting molecule. For the approximation of point dipoles, the energy transfer rate can be expressed by

$$k_{\text{Förster}} = \frac{1}{\tau} \left(\frac{R_0}{r} \right)^6 \tag{1.8}$$

with the lifetime of the donor in the absence of an acceptor τ, the Förster radius R_0, and the separation between donor and acceptor r. The Förster radius depends mainly on the spectral overlap between emission and absorption of the two components, and is usually in the range of 1 - 10 nm.[5,22–24] Equation 1.8 is valid for the assumption of dipole-dipole interactions; for dipole-sheet or dipole-bulk interactions, which are more realistic conditions in a BHJ, the
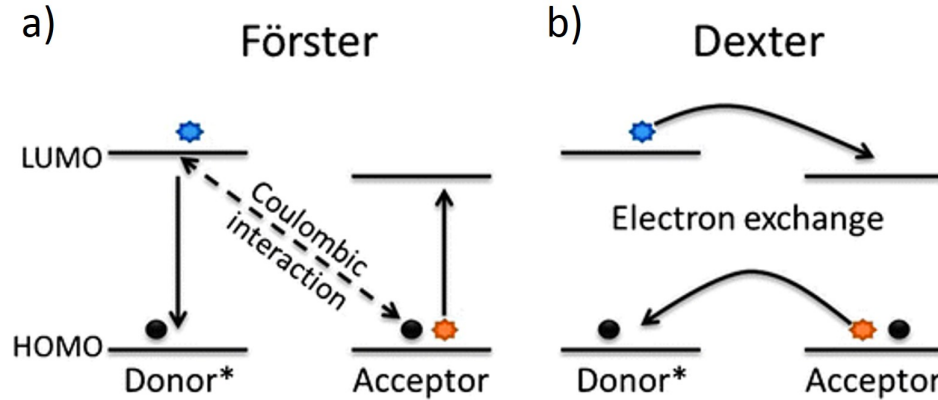
Figure 1.5: Illustration of two energy transfer processes. (a) Dipole-dipole interaction facilitates Förster resonant energy transfer (FRET) over long distances. (b) Electron-exchange interactions lead to Dexter-type energy transfer for short distances. Reproduced with permission from Ref.[26] Copyright 2011, The Royal Society of Chemistry.

separation-dependence changes to $\sim r^{-4}$ and $\sim r^{-3}$, respectively.[25]

For nearest neighbour interactions, these nanoscopic energy transfer rates relate to mesoscopic transport via the diffusion coefficient D

$$D = A\, r^2 k_{ET} \tag{1.9}$$

where r is the distance between the two hopping sites, A is a factor accounting for the disorder in the film, and k_{ET} the energy transfer rate.[5,27] The exciton diffusion length in the usually reported one-dimensional case then depends on its lifetime τ and its diffusion coefficient D by

$$L = \sqrt{D\tau} \tag{1.10}$$

It is typically determined by measuring the photoluminescence (PL) quenching or micro-wave conductivity, and is in the range of $L \approx 10$ - 30 nm.[4,5] Improving the crystallinity of the materials, for example by thermal annealing, increases the exciton diffusivity.[6,28] The diffusion length is therefore an upper limit for the optimal nano-morphology of the BHJ, since the charge pairs must diffuse to an interface with an acceptor within their lifetime before they decay. The diffusive motion of the excitons after generation is then described by the diffusion equation
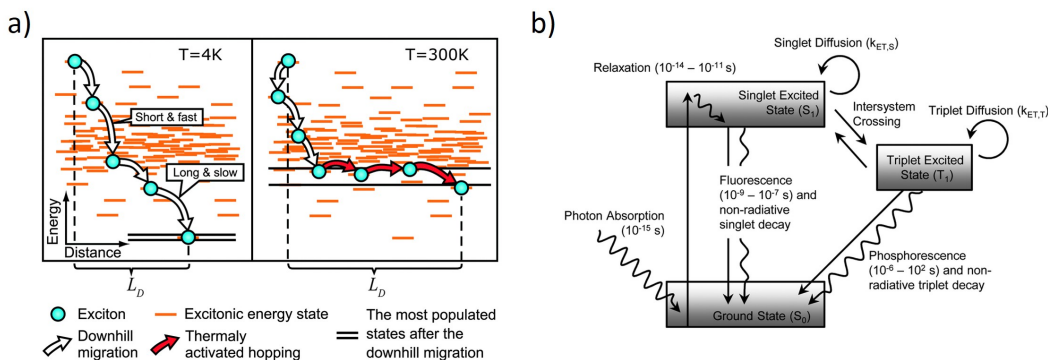
Figure 1.6: (a) Exciton diffusion process at low and room temperatures. The excitonic Gaussian density of states is represented by the distribution of the excitonic energies. Reproduced with permission.[29] Copyright 2008, American Chemical Society. (b) Schematic illustration of the processes in organic semiconductors after light absorption with typical timescales. Reproduced with permission from Ref.[5] Copyright 2014, The Royal Society of Chemistry.

$$\frac{dn}{dt} = D\nabla^2 n - \frac{n}{\tau} \tag{1.11}$$

Here n is the exciton concentration. Figure 1.6a shows the diffusion of excitons at different temperature regimes. At room temperature, thermally activated jumps are promoted; the equilibrium energy for excitons is proportional to the temperature.

The decay of singlet excitons proceeds via non-radiative (internal conversion (IC), intersystem crossing (ICS)) or radiative (photoluminescence) transitions (schematic Jablonski diagram in Figure 1.6b). The latter leads to a mono-exponential decay to the ground state which can be measured with time-resolved techniques, such as time-correlated single photon counting (TCSPC). A notable case of ICS is the singlet-fission process in which a singlet state with sufficient energy decays into two triplet states. This process is of great interest for OPVs as it can in principle double the number of charge carriers per absorbed photon.[17,18,30] At high exciton concentrations, for example in pump-probe experiments involving pulsed lasers with high intensities, two singlet excitons can collide which leads to singlet-singlet-annihilation and fast initial decay. If the concentration of triplet excitons is high, for example due to singlet-fission or in OLEDs, additional bimolecular triplet-annihilation processes occur.

1.2.2 Charge transfer to acceptor

When an exciton is able to reach an interface between the two materials in the BHJ, it can dissociate by transferring a charge between the molecules. In traditional OPVs, the excitons are mainly created on the polymer or small molecule with lower electron affinity, and charge transfer proceeds by donating an electron from its lowest unoccupied molecular orbital (LUMO) level to the LUMO level of the more electronegative molecule, e.g. a fullerene derivative. Simultaneously, the hole transfer between the highest occupied molecular orbital (HOMO) levels is possible, particularly in OPVs employing non-fullerene acceptors where light is strongly absorbed in both components. Alternatively to the diffusion of the donor exciton and subsequent charge transfer to the acceptor, long range Förster-type energy transfer according to Equation 1.8 can directly excite the acceptor, followed by charge transfer from acceptor to donor.[31–33]

The resulting meta-stable state is called *charge transfer (CT) state* or *geminate pair*. Its energy is lower than the excited states of either donor or acceptor, hence its absorption and emission are red-shifted with respect to the individual components.[34,35] The charge transfer itself typically occurs on the sub-ps timescale and can be observed with time-resolved pump-probe spectroscopy (see Chapter 3).[36–39] In systems with enhanced phase separation between the donor and acceptor domains, formation of CT states is thus determined by ultrafast charge transfer from excitons created in close proximity to an interface and by a diffusion-limited component, usually in the ps-regime.[40] The rate of charge transfer is often considered with classical Marcus theory,[41] which entails an optimum driving force ΔG^0 between the energy of the relaxed donor exciton and the CT state which is typically in the range of 0.3 - 0.6 eV.[42] In this formalism the rate k_{CT} for charge transfer between donor and acceptor is of the form

$$k_{CT} = \frac{H_{DA}^2}{\hbar} \sqrt{\frac{\pi}{\lambda k_B T}} \exp\left[-\frac{(\lambda + \Delta G^0)^2}{4\lambda k_B T}\right] \tag{1.12}$$

with the electronic coupling between donor and acceptor H_{DA} and the reorganisation energy λ. Both H_{DA} and λ depend on the distance between donor and acceptor molecule.[43–45] Figure 1.7 shows the driving force dependence of the electron transfer rate which gives rise to three distinct regimes. In the *normal region* k_{ET} increases with increasing driving force by lowering of the activation barrier which forms at small energy offsets. The *activationless region* is characterised by a temperature- and field-independent charge transfer,
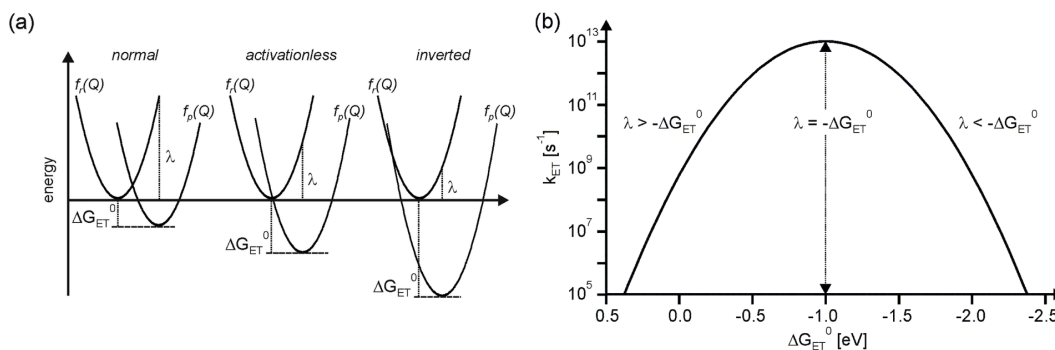
Figure 1.7: (a) The driving force in Equation 1.12 gives rise to three separate charge transfer regimes: normal, activationless, and inverted region. (b) The dependence of the electron transfer rate on the driving force provided by the energy offsets of excited and CT state. Adapted with permission from Ref.[48] Copyright 2016, The Royal Society of Chemistry.

due to the vanishing potential barrier between excited state and CT state. Increasing ΔG^0 further leads to the re-appearance of an activation barrier in the *inverted region*. The latter, though predicted by theory, was only much later unambiguously verified.[46,47] For his work on electron transfer in chemical reactions, Marcus was awarded with the Nobel prize for Chemistry in 1992.

The electron and hole remain bound across the interface by the Coulomb potential (Equation 1.7), with binding energies of 0.1 - 0.5 eV.[49–51] The excited ('hot') CT state (CT_n) undergoes electronic relaxation and vibrational cooling to the groundstate (CT_1) in ≈ 1 ps.[38,52] The dissociation of the CT exciton into free charges competes with several loss mechanisms. If electron-hole pairs cannot escape their mutual Coulomb attraction, they eventually recombine and decay radiatively or non-radiatively to the groundstate which is referred to as *geminate recombination*. It can be identified by pump-probe measurements as an intensity-independent decay.[53,54] Depending on the energy levels of donor and acceptor, thermally activated back transfer to the singlet exciton is possible in a process called *exciton-recycling*.[55] In systems with large electrical gap containing $PC_{60}BM$, energy transfer can lead to triplet formation on the fullerene.[56] However, if the electron-hole pair is spatially separated and loosely bound, it can dissociate into free, unbound charges, which will be discussed in the next section.

1.2.3 Charge separation

The separation of bound CT states into free charge carriers can be observed with ultrafast pump-probe techniques. In the model system P3HT:PC$_{60}$BM free charges are generated after a few ps[54,57], in PTB7:PC$_{70}$BM between 100 - 300 fs,[58] and in PCPDTBT:PC$_{60}$BM films after 50 fs.[37]

The mechanisms behind the dissociation of bound CT states into free charge carriers are still actively debated (Figure 1.8). It has been suggested that the excess energy of hot CT states after charge transfer leads to ultrafast dissociation of the electron-hole pair if it can outcompete relaxation.[37,52,60] In this case, the process is facilitated by the formation of delocalised band states, rather than energy-driven hopping.[19] However, other studies have shown that the yield of charge carriers in high-efficiency systems is independent of the photon energy, and that even after direct excitation of the lowest CT state, efficient charge separation occurs.[61–63] These findings show that in these cases relaxed inter-molecular charge pairs are the precursors for free charges, while the driving force for this process is still unclear. The processes leading to the spatial separation of the relaxed states are often rationalised by incoherent hopping through energy cascades.[58,64,65] Charge separation through relaxed states depends usually only weakly on the applied electric field,[62,63,66] and is enhanced by high mobilities[65] or by disorder.[67] Furthermore, the role of delocalisation of electron and hole on the acceptor and donor domains, respectively, has been suggested as a possible cause for CT dissociation.[59,68]

The classic formalism to describe the dissociation of electron-hole pairs in their mutual Coulomb potential and in the presence of an external field is the Onsager-Braun model. It assumes localised point charges in donor-acceptor systems. The dissociation rate is given by

$$k_d = \frac{3Dr_c}{r^3} \exp\left(-\frac{r_c}{r}\right) \frac{J_1(2\sqrt{-2b})}{\sqrt{-2b}} \text{ with } b = \frac{e^3 F}{8\pi\epsilon_0\epsilon_r k_B^2 T^2} \qquad (1.13)$$

where D is the sum of the diffusion coefficients, $r_c = \dfrac{e^2}{4\pi\epsilon_0\epsilon_r k_B T}$ the Coulomb radius, r the initial separation of electron and hole, and J_1 the first order Bessel function. It was extensively used to model charge dissociation in moderate fields, but requires several unrealistic assumptions about the CT lifetime or the mobility. A more realistic approach, taking into account the delocalisation of the hole over several repeat units in conjugated polymers, was suggested by Arkhipov and Nenashev.[69,70] By solving the Schrödinger equation for charges
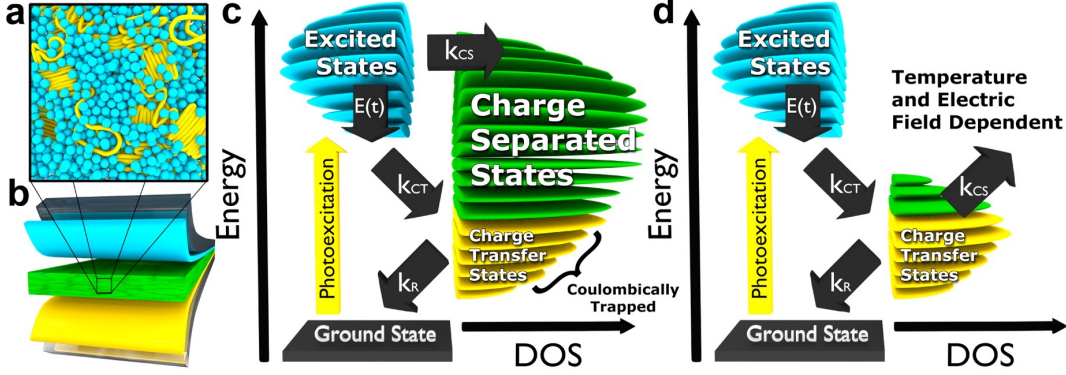
Figure 1.8: Fundamental charge generation processes, morphology, and device configuration in bulk-heterojunction organic photovoltaics. (a) Schematic depiction of the BHJ. (b) Typical device configuration with the active layer sandwiched between metallic and transparent electrodes. The states relevant to charge generation in (c) through 'hot' channel and (d) relaxed CT states. Reproduced with permission from Ref.[59] Copyright 2014, American Chemical Society.

in Coulomb and external fields, they calculated the dissociation rate to be

$$k_d = \sum_{n=1}^{N-1} a_{n \to n+1} \exp\left(-\frac{E_n - E_1}{k_B T}\right) \qquad (1.14)$$

where n is the distance of the hole to the interface in repeat units of the polymer chains, E_n is the energy of the hole at site n, and the Miller-Abrahams hopping rate of the hole

$$a_{n \to n+1} = \nu_0 e^{-2\gamma r} \begin{cases} \exp\left(-\dfrac{E_{n+1} - E_n}{k_B T}\right) & E_{n1} > E_n \\ 1 & E_{n+1} \le E_n \end{cases} \qquad (1.15)$$

Here ν_0 is the attempt-to-hop frequency and γ a measure for the electronic coupling. For more advanced theories I refer to general textbooks and reviews.[22,71] Once the charges are separated, they drift and diffuse through the active layer and are collected by the respective electrodes.

1.2.4 Charge transport and extraction

The current flow j (for electrons or holes) inside an organic semiconductor device is described by a drift and a diffusive term in the drift-diffusion-equation

$$j = en\mu\nabla\Phi - eD\nabla n \qquad (1.16)$$

where e is the elementary charge, μ the mobility of the charges, $\nabla\Phi$ the potential difference between the electrodes, D the diffusion coefficient and n charge carrier density. In contrast to inorganic pn-junctions, where the dynamics are typically dominated by the diffusion of the charges, in OSCs the drift term dominates. The diffusion coefficient is related to the charge carrier mobility *via* the Einstein-Smoluchowski equation

$$\mu = \frac{eD}{k_B T} \qquad (1.17)$$

where k_B is the Boltzmann constant and T the temperature. The charge carrier mobility can be determined experimentally, e.g. by time-of-flight (TOF) measurements[72], extracted from field-effect transistors[73], or by measuring space-charge-limited current in a diode.[74] The mobility generally depends on various parameters such as the temperature, the applied electrical field, amount of disorder and impurities, or charge carrier density.[75] There are several approaches to describe the mechanism by which the charges can be transported in organic semiconductors, and understanding the charge transport is still an open question in terms of theoretical concepts and experimental validation.[22] Under nearly ideal conditions, i.e. when the interaction energy between neighbouring sites is strong compared to the energetic disorder in the system, transport of charges can be described in terms of delocalised Bloch waves in a band-type motion.[76] However, those conditions usually only apply in pure molecular crystals at low temperature. Another successful approach is the description with a polaron model where the transport proceeds via inter-site polaron hopping, but this is typically only valid for temperatures above 600 - 1500 K.[71] In typical amorphous organic semiconductors at room temperature the charges scatter at every site and transport is often described by a disorder model where the charges are localised and diffuse through the DOS by incoherent hopping between the interacting molecules.[76] For a Gaussian DOS with (disorder) width σ this process is illustrated in Figure 1.9a.

The hopping rate in literature is usually described either with the Miller-Abrahams formalism or with Marcus theory (see above). In the disorder model, the temperature dependence of the mobility follows an Arrhenius law
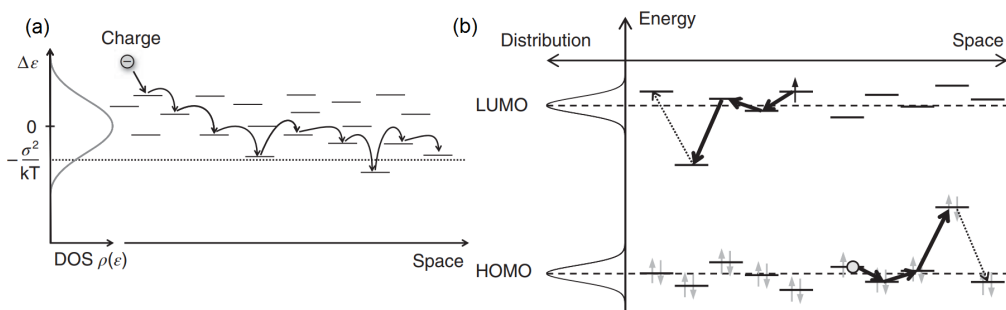
Figure 1.9: Illustration of a charge carrier that hops within a Gaussian DOS. The dotted horizontal line is the energy at which the charge carriers equilibrate. Reproduced with permission from Ref.[71] Copyright 2015, Wiley.

$$\mu = \mu_0 \exp\left[-\left(\frac{2\sigma}{3k_B T}\right)^2\right] \tag{1.18}$$

meaning that the transport is thermally activated and mobility increases with temperature.[71] Within an electric field, the mobility follows a Poole-Frenkel behaviour $\ln\mu \sim \sqrt{F}$.[77]

Due to structural faults or impurities, e.g. caused by degradation of the materials, the transport is affected by trapping effects. Depending on their concentration and energetic depth, a significant amount of charge carriers is captured and subsequent release requires thermal activation so that the transport is retarded. At 295 K with a trap depth of 40 meV at a concentration of 10^{-7} mol/mol the mobility is already reduced by a factor of 2.[71] The energetic depth is determined by the relative offset between the HOMO energies (for holes), or the distance between the LUMO energies (for electrons), as depicted in Figure 1.9b. The rate of trapping k_t is proportional to the density of traps N_T, a critical radius at which trapping occurs (R_T), and the diffusion coefficient:

$$k_t = 4\pi R_T D N_T \tag{1.19}$$

This trap-assisted recombination mechanism is often referred to as *Shockley-Read-Hall recombination*. In addition to monomolecular recombination via trap states, recombination of free charge carriers also occurs bimolecularly, depending on the density of free carriers. The rate for this bimolecular recombination k_L is given by the *Langevin formalism* as

$$k_L = -\gamma n p = -\frac{e}{\epsilon_0 \epsilon_r}(\mu_- + \mu_+)np \tag{1.20}$$

with n and p the concentrations of electrons and holes, ϵ the permittivity, and μ_- and μ_+ the mobilities of electrons and holes.[78] Although commonly employed, the Langevin model consistently overpredicts experimental recombination rates.[79] It assumes that once electron and hole meet, they rapidly recombine and two neutral molecules are recovered.[80] More recent theoretical treatments of recombination dynamics consider interfacial CT states between donor and acceptor as the result of the encounters of charge carriers. These either recombine to the neutral groundstate or dissociate again to yield free charges.[81] The charges that remain after bimolecular and trap-assisted recombination are extracted through the transport layers at the electrodes.

To summarise, after absorption of light in the active layer, strongly bound excitons are created. These excitons undergo diffusive motion by energy transfer through the BHJ until they reach a donor:acceptor interface or recombine. At an interface, the energetic offset between the molecular orbitals of the two active components provides a driving force for charge transfer which is described by Markus theory. The resulting intermolecular, meta-stable CT state dissociates by spatially separating electron and hole which yields free charge carriers. These charges drift through the active layer towards the electrodes where they are extracted. Their lifetime is limited by trap-assisted- and bimolecular recombination.

Bibliography

[1] Clarke, T. M.; Durrant, J. R. Charge Photogeneration in Organic Solar Cells. *Chemical Reviews* **2010**, *110*, 6736–6767.

[2] Gélinas, S.; Paré-Labrosse, O.; Brosseau, C.-N.; Albert-Seifried, S.; McNeill, C. R.; Kirov, K. R.; Howard, I. A.; Leonelli, R.; Friend, R. H.; Silva, C. The Binding Energy of Charge-Transfer Excitons Localized at Polymeric Semiconductor Heterojunctions. *The Journal of Physical Chemistry C* **2011**, *115*, 7114–7119.

[3] Radchenko, E. S.; Anokhin, D. V.; Gerasimov, K. L.; Rodygin, A. I.; Rychkov, A. A.; Shabratova, E. D.; Grigorian, S.; Ivanov, D. A. Impact of the solubility of organic semiconductors for solution-processable electronics on the structure formation: a real-time study of morphology and electrical properties. *Soft Matter* **2018**, *14*, 2560–2566.

[4] Lin, J. D. A.; Mikhnenko, O. V.; Chen, J.; Masri, Z.; Ruseckas, A.; Mikhailovsky, A.; Raab, R. P.; Liu, J.; Blom, P. W. M.; Loi, M. A.; García-Cervera, C. J.; Samuel, I. D. W.; Nguyen, T.-Q. Systematic study of exciton diffusion length in organic semiconductors by six experimental methods. *Mater. Horiz.* **2014**, *1*, 280–285.

[5] Menke, S. M.; Holmes, R. J. Exciton diffusion in organic photovoltaic cells. *Energy Environ. Sci.* **2014**, *7*, 499–512.

[6] Lunt, R. R.; Benziger, J. B.; Forrest, S. R. Relationship between Crystalline Order and Exciton Diffusion Length in Molecular Organic Semiconductors. *Advanced Materials* **2010**, *22*, 1233–1236.

[7] Shaw, P. E.; Ruseckas, A.; Samuel, I. D. W. Exciton Diffusion Measurements in Poly(3-hexylthiophene). *Advanced Materials* **2008**, *20*, 3516–3520.

[8] Li, G.; Shrotriya, V.; Huang, J.; Yao, Y.; Moriarty, T.; Emery, K.; Yang, Y. High-efficiency solution processable polymer photovoltaic cells by self-organization of polymer blends. *Nature Materials* **2005**, *4*, 864–868.

[9] Zhou, Y. et al. A Universal Method to Produce Low-Work Function Electrodes for Organic Electronics. *Science* **2012**, *336*, 327–332.

[10] Peumans, P.; Bulović, V.; Forrest, S. R. Efficient photon harvesting at high optical intensities in ultrathin organic double-heterostructure photovoltaic diodes. *Applied Physics Letters* **2000**, *76*, 2650–2652.

[11] Giebink, N. C.; Wiederrecht, G. P.; Wasielewski, M. R.; Forrest, S. R. Ideal diode equation for organic heterojunctions. I. Derivation and application. *Physical Review B* **2010**, *82*, 155305.

[12] Shockley, W.; Queisser, H. J. Detailed balance limit of efficiency of p-n junction solar cells. *Journal of Applied Physics* **1961**, *32*, 510–519.

[13] Giebink, N. C.; Wiederrecht, G. P.; Wasielewski, M. R.; Forrest, S. R. Thermodynamic efficiency limit of excitonic solar cells. *Physical Review B* **2011**, *83*, 195326.

[14] Song, Z.; Watthage, S. C.; Phillips, A. B.; Heben, M. J. Pathways toward high-performance perovskite solar cells: review of recent advances in organo-metal halide perovskites for photovoltaic applications. *Journal of Photonics for Energy* **2016**, *6*, 022001.

[15] Cui, Y.; Wang, Y.; Bergqvist, J.; Yao, H.; Xu, Y.; Gao, B.; Yang, C.; Zhang, S.; Inganäs, O.; Gao, F.; Hou, J. Wide-gap non-fullerene acceptor enabling high-performance organic photovoltaic cells for indoor applications. *Nature Energy* **2019**, *4*, 768–775.

[16] Zimmermann, E.; Ehrenreich, P.; Pfadler, T.; Dorman, J. A.; Weickert, J.; Schmidt-Mende, L. Erroneous efficiency reports harm organic solar cell research. *Nature Photonics* **2014**, *8*, 669–672.

[17] Alagna, N.; Han, J.; Wollscheid, N.; Lustres, J. L. P.; Herz, J.; Hahn, S.; Koser, S.; Paulus, F.; Bunz, U. H. F.; Dreuw, A.; Buckup, T.; Motzkus, M. Tailoring Ultrafast Singlet Fission by the Chemical Modification of Phenazinothiadiazoles. *Journal of the American Chemical Society* **2019**, *141*, 8834–8845.

[18] Congreve, D. N.; Lee, J.; Thompson, N. J.; Hontz, E.; Yost, S. R.; Reusswig, P. D.; Bahlke, M. E.; Reineke, S.; Van Voorhis, T.; Baldo, M. A. External Quantum Efficiency Above 100% in a Singlet-Exciton-Fission-Based Organic Photovoltaic Cell. *Science* **2013**, *340*, 334–337.

[19] Bakulin, A. A.; Rao, A.; Pavelyev, V. G.; van Loosdrecht, P.

H. M.; Pshenichnikov, M. S.; Niedzialek, D.; Cornil, J.; Beljonne, D.; Friend, R. H. The Role of Driving Energy and Delocalized States for Charge Separation in Organic Semiconductors. *Science* **2012**, *335*, 1340–1344.

[20] Feron, K.; Zhou, X.; Belcher, W. J.; Dastoor, P. C. Exciton transport in organic semiconductors: Förster resonance energy transfer compared with a simple random walk. *Journal of Applied Physics* **2012**, *111*, 044510.

[21] Köhler, A.; Bässler, H. *Electronic Processes in Organic Semiconductors*; Wiley-VCH Verlag GmbH & Co. KGaA: Weinheim, Germany, 2015; pp 87–191.

[22] Ostroverkhova, O. Organic Optoelectronic Materials: Mechanisms and Applications. *Chemical Reviews* **2016**, *116*, 13279–13412.

[23] Hedley, G. J.; Ruseckas, A.; Samuel, I. D. W. Light Harvesting for Organic Photovoltaics. *Chemical Reviews* **2017**, *117*, 796–837.

[24] Shepherd, W. E. B.; Platt, A. D.; Kendrick, M. J.; Loth, M. A.; Anthony, J. E.; Ostroverkhova, O. Energy Transfer and Exciplex Formation and Their Impact on Exciton and Charge Carrier Dynamics in Organic Films. *The Journal of Physical Chemistry Letters* **2011**, *2*, 362–366.

[25] Scully, S. R.; Armstrong, P. B.; Edder, C.; Frechet, J. M. J.; McGehee, M. D. Long-Range Resonant Energy Transfer for Enhanced Exciton Harvesting for Organic Solar Cells. *Advanced Materials* **2007**, *19*, 2961–2966.

[26] Zhang, C.; Zhao, Y. S.; Yao, J. Organic composite nanomaterials: energy transfers and tunable luminescent behaviors. *New Journal of Chemistry* **2011**, *35*, 973.

[27] Mikhnenko, O. V.; Blom, P. W. M.; Nguyen, T.-Q. Exciton diffusion in organic semiconductors. *Energy & Environmental Science* **2015**, *8*, 1867–1888.

[28] Sajjad, M. T.; Zhang, Y.; Geraghty, P. B.; Mitchell, V. D.; Ruseckas, A.; Blaszczyk, O.; Jones, D. J.; Samuel, I. D. W. Tailoring exciton diffusion and domain size in photovoltaic small molecules by annealing. *Journal of Materials Chemistry C* **2019**, *7*, 7922–7928.

[29] Mikhnenko, O. V.; Cordella, F.; Sieval, A. B.; Hummelen, J. C.; Blom, P. W. M.; Loi, M. A. Temperature Dependence of Exciton Diffusion in Conjugated Polymers. *The Journal of Physical Chemistry B* **2008**, *112*, 11601–11604.

[30] Xia, J.; Sanders, S. N.; Cheng, W.; Low, J. Z.; Liu, J.; Campos, L. M.; Sun, T. Singlet Fission: Progress and Prospects in Solar Cells. *Advanced Materials* **2017**, *29*, 1601652.

[31] Huang, J.-S.; Goh, T.; Li, X.; Sfeir, M. Y.; Bielinski, E. A.; Tomasulo, S.; Lee, M. L.; Hazari, N.; Taylor, A. D. Polymer bulk heterojunction solar cells employing Förster resonance energy transfer. *Nature Photonics* **2013**, *7*, 479–485.

[32] Ward, A. J.; Ruseckas, A.; Samuel, I. D. W. A Shift from Diffusion Assisted to Energy Transfer Controlled Fluorescence Quenching in Polymer–Fullerene Photovoltaic Blends. *The Journal of Physical Chemistry C* **2012**, *116*, 23931–23937.

[33] Peeters, E.; van Hal, P. A.; Knol, J.; Brabec, C. J.; Sariciftci, N. S.; Hummelen, J. C.; Janssen, R. A. J. Synthesis, Photophysical Properties, and Photovoltaic Devices of Oligo(p -phenylene vinylene)-fullerene Dyads. *The Journal of Physical Chemistry B* **2000**, *104*, 10174–10190.

[34] Goris, L.; Haenen, K.; Nesládek, M.; Wagner, P.; Vanderzande, D.; De Schepper, L.; D'haen, J.; Lutsen, L.; Manca, J. V. Absorption phenomena in organic thin films for solar cell applications investigated by photothermal deflection spectroscopy. *Journal of Materials Science* **2005**, *40*, 1413–1418.

[35] Tvingstedt, K.; Vandewal, K.; Gadisa, A.; Zhang, F.; Manca, J.; Inganas, O. Electroluminescence from Charge Transfer States in Polymer Solar Cells. *Journal of the American Chemical Society* **2009**, *131*, 11819–11824.

[36] Herrmann, D.; Niesar, S.; Scharsich, C.; Köhler, A.; Stutzmann, M.; Riedle, E. Role of Structural Order and Excess Energy on Ultrafast Free Charge Generation in Hybrid Polythiophene/Si Photovoltaics Probed in Real Time by Near-Infrared Broadband Transient Absorption. *Journal of the American Chemical Society* **2011**, *133*, 18220–18233.

[37] Grancini, G.; Maiuri, M.; Fazzi, D.; Petrozza, A.; Egelhaaf, H.-J.; Brida, D.; Cerullo, G.; Lanzani, G. Hot exciton dissociation in polymer solar cells. *Nature Materials* **2013**, *12*, 29–33.

[38] Wang, T.; Kafle, T. R.; Kattel, B.; Chan, W.-L. A Multidimensional View of Charge Transfer Excitons at Organic Donor–Acceptor Interfaces. *Journal of the American Chemical Society* **2017**, *139*, 4098–4106.

[39] Unger, T.; Wedler, S.; Kahle, F.-J.; Scherf, U.; Bässler, H.; Köhler, A. The Impact of Driving Force and Temperature on the Electron Transfer in Donor–Acceptor Blend Systems. *The Journal of Physical Chemistry C* **2017**, *121*, 22739–22752.

[40] Etzold, F.; Howard, I. A.; Forler, N.; Cho, D. M.; Meister, M.; Mangold, H.; Shu, J.; Hansen, M. R.; Müllen, K.; Laquai, F. The Effect of Solvent Additives on Morphology and Excited-State Dynamics in PCPDTBT:PCBM Photovoltaic Blends. *Journal of the American Chemical Society* **2012**, *134*, 10569–10583.

[41] Marcus, R. A. Chemical and Electrochemical Electron-Transfer Theory. *Annual Review of Physical Chemistry* **1964**, *15*, 155–196.

[42] Ward, A. J.; Ruseckas, A.; Kareem, M. M.; Ebenhoch, B.; Serrano, L. A.; Al-Eid, M.; Fitzpatrick, B.; Rotello, V. M.; Cooke, G.; Samuel, I. D. W. The Impact of Driving Force on Electron Transfer Rates in Photovoltaic Donor-Acceptor Blends. *Advanced Materials* **2015**, *27*, 2496–2500.

[43] Shih, C.; Museth, A. K.; Abrahamsson, M.; Blanco-Rodriguez, A. M.; Di Bilio, A. J.; Sudhamsu, J.; Crane, B. R.; Ronayne, K. L.; Towrie, M.; Vlcek, A.; Richards, J. H.; Winkler, J. R.; Gray, H. B. Tryptophan-accelerated electron flow through proteins. *Science (New York, N.Y.)* **2008**, *320*, 1760–2.

[44] Isied, S. S.; Vassilian, A.; Wishart, J. F.; Creutz, C.; Schwarz, H. A.; Sutin, N. The distance dependence of intramolecular electron-transfer rates: importance of the nuclear factor. *Journal of the American Chemical Society* **1988**, *110*, 635–637.

[45] Marcus, R.; Sutin, N. Electron transfers in chemistry and biology. *Biochimica et Biophysica Acta (BBA) - Reviews on Bioenergetics* **1985**, *811*, 265–322.

[46] Fox, L. S.; Kozik, M.; Winkler, J. R.; Gray, H. B. Gaussian free-energy dependence of electron-transfer rates in iridium complexes. *Science (New York, N.Y.)* **1990**, *247*, 1069–71.

[47] Closs, G. L.; Miller, J. R.; Winkler, J. R.; Gray, H. B. Intramolecular long-distance electron transfer in organic molecules. *Science (New York, N.Y.)* **1988**, *240*, 440–7.

[48] Kuss-Petermann, M.; Wenger, O. S. Unusual distance dependences of electron transfer rates. *Physical Chemistry Chemical Physics* **2016**, *18*, 18657–18664.

[49] Zhu, X.-Y.; Yang, Q.; Muntwiler, M. Charge-Transfer Excitons at Organic Semiconductor Surfaces and Interfaces. *Accounts of Chemical Research* **2009**, *42*, 1779–1787.

[50] Drori, T.; Sheng, C.-X.; Ndobe, A.; Singh, S.; Holt, J.; Vardeny, Z. V. Below-Gap Excitation of π -Conjugated Polymer-Fullerene Blends: Implications for Bulk Organic Heterojunction Solar Cells. *Physical Review Letters* **2008**, *101*, 037401.

[51] Hallermann, M.; Haneder, S.; Da Como, E. Charge-transfer states in conjugated polymer/fullerene blends: Below-gap weakly bound excitons for polymer photovoltaics. *Applied Physics Letters* **2008**, *93*, 053307.

[52] Jailaubekov, A. E.; Willard, A. P.; Tritsch, J. R.; Chan, W.-L.; Sai, N.; Gearba, R.; Kaake, L. G.; Williams, K. J.; Leung, K.; Rossky, P. J.; Zhu, X.-Y. Hot charge-transfer excitons set the time limit for charge separation at donor/acceptor interfaces in organic photovoltaics. *Nature Materials* **2013**, *12*, 66–73.

[53] Hodgkiss, J. M.; Campbell, A. R.; Marsh, R. A.; Rao, A.; Albert-Seifried, S.; Friend, R. H. Subnanosecond Geminate Charge Recombination in Polymer-Polymer Photovoltaic Devices. *Physical Review Letters* **2010**, *104*, 177701.

[54] Howard, I. A.; Mauer, R.; Meister, M.; Laquai, F. Effect of Morphology on Ultrafast Free Carrier Generation in Polythiophene:Fullerene Organic Solar Cells. *Journal of the American Chemical Society* **2010**, *132*, 14866–14876.

[55] Morteani, A. C.; Sreearunothai, P.; Herz, L. M.; Friend, R. H.; Silva, C. Exciton Regeneration at Polymeric Semiconductor Heterojunctions. *Physical Review Letters* **2004**, *92*, 247402.

[56] Benson-Smith, J. J.; Ohkita, H.; Cook, S.; Durrant, J. R.; Bradley, D. D.; Nelson, J. Charge separation and fullerene triplet formation in blend films of polyfluorene polymers with [6,6]-phenyl C61 butyric acid methyl ester. *Journal of the Chemical Society. Dalton Transactions* **2009**, , 10000–10005.

[57] Hwang, I. W.; Moses, D.; Heeger, A. J. Photoinduced carrier generation in P3HT/PCBM bulk heterojunction materials. *Journal of Physical Chemistry C* **2008**, *112*, 4350–4354.

[58] Hedley, G. J.; Ward, A. J.; Alekseev, A.; Howells, C. T.; Martins, E. R.; Serrano, L. A.; Cooke, G.; Ruseckas, A.; Samuel, I. D. W. Determining the optimum morphology in high-performance polymer-fullerene organic photovoltaic cells. *Nature Communications* **2013**, *4*, 2867.

[59] Savoie, B. M.; Rao, A.; Bakulin, A. A.; Gelinas, S.; Movaghar, B.; Friend, R. H.; Marks, T. J.; Ratner, M. A. Unequal Partnership: Asymmetric Roles of Polymeric Donor and Fullerene Acceptor in Generating Free Charge. *Journal of the American Chemical Society* **2014**, *136*, 2876–2884.

[60] Savoie, B. M.; Jackson, N. E.; Chen, L. X.; Marks, T. J.; Ratner, M. A. Mesoscopic Features of Charge Generation in Organic Semiconductors. *Accounts of Chemical Research* **2014**, *47*, 3385–3394.

[61] Kurpiers, J.; Ferron, T.; Roland, S.; Jakoby, M.; Thiede, T.; Jaiser, F.; Albrecht, S.; Janietz, S.; Collins, B. A.; Howard, I. A.; Neher, D. Probing the pathways of free charge generation in organic bulk heterojunction solar cells. *Nature Communications* **2018**, *9*, 2038.

[62] Vandewal, K. et al. Efficient charge generation by relaxed charge-transfer states at organic interfaces. *Nature Materials* **2014**, *13*, 63–68.

[63] Lee, J.; Vandewal, K.; Yost, S. R.; Bahlke, M. E.; Goris, L.; Baldo, M. A.; Manca, J. V.; Van Voorhis, T. Charge Transfer State Versus Hot Exciton Dissociation in Polymer-Fullerene Blended Solar Cells. *Journal of the American Chemical Society* **2010**, *132*, 11878–11880.

[64] Vithanage, D. A.; Devižis, A.; Abramavičius, V.; Infahsaeng, Y.; Abramavičius, D.; MacKenzie, R. C. I.; Keivanidis, P. E.; Yartsev, A.; Hertel, D.; Nelson, J.; Sundström, V.; Gulbinas, V. Visualizing charge separation in bulk heterojunction organic solar cells. *Nature Communications* **2013**, *4*, 2334.

[65] Burke, T. M.; McGehee, M. D. How High Local Charge Carrier Mobility and an Energy Cascade in a Three-Phase Bulk Heterojunction Enable >90% Quantum Efficiency. *Advanced Materials* **2014**, *26*, 1923–1928.

[66] van der Hofstad, T. G. J.; Di Nuzzo, D.; van den Berg, M.; Janssen, R. A. J.; Meskers, S. C. J. Influence of Photon Excess Energy on Charge Carrier Dynamics in a Polymer-Fullerene Solar Cell. *Advanced Energy Materials* **2012**, *2*, 1095–1099.

[67] McMahon, D. P.; Cheung, D. L.; Troisi, A. Why Holes and Electrons Separate So Well in Polymer/Fullerene Photovoltaic Cells. *The Journal of Physical Chemistry Letters* **2011**, *2*, 2737–2741.

[68] Falke, S. M.; Rozzi, C. A.; Brida, D.; Maiuri, M.; Amato, M.; Sommer, E.; De Sio, A.; Rubio, A.; Cerullo, G.; Molinari, E.; Lienau, C. Coherent ultrafast charge transfer in an organic photovoltaic blend. *Science* **2014**, *344*, 1001–1005.

[69] Nenashev, A.; Wiemer, M.; Jansson, F.; Baranovskii, S. Theory to exciton dissociation at the interface between a conjugated polymer and an electron acceptor. *Journal of Non-Crystalline Solids* **2012**, *358*, 2508–2511.

[70] Arkhipov, V. I.; Heremans, P.; Bässler, H. Why is exciton dissociation so efficient at the interface between a conjugated polymer and an electron acceptor? *Applied Physics Letters* **2003**, *82*, 4605–4607.

[71] Köhler, A.; Bässler, H. *Electronic Processes in Organic Semiconductors*; Wiley-VCH Verlag GmbH & Co. KGaA: Weinheim, Germany, 2015; pp 193–305.

[72] Kepler, R. G. Charge Carrier Production and Mobility in Anthracene Crystals. *Physical Review* **1960**, *119*, 1226–1229.

[73] Horowitz, G. Organic Field-Effect Transistors. *Advanced Materials* **1998**, *10*, 365–377.

[74] Blom, P. W. M.; De Jong, M. J. M.; Vleggaar, J. J. M. Electron and hole transport in poly(p-phenylene vinylene) devices. *Applied Physics Letters* **1996**, *68*, 3308–3310.

[75] Coropceanu, V.; Cornil, J.; da Silva Filho, D. A.; Olivier, Y.; Silbey, R.; Brédas, J.-L. Charge Transport in Organic Semiconductors. *Chemical Reviews* **2007**, *107*, 926–952.

[76] Brédas, J.-L.; Sargent, E. H.; Scholes, G. D. Photovoltaic concepts inspired by coherence effects in photosynthetic systems. *Nature Materials* **2017**, *16*, 35–44.

[77] Gill, W. D. Drift mobilities in amorphous charge-transfer complexes of trinitrofluorenone and poly-n-vinylcarbazole. *Journal of Applied Physics* **1972**, *43*, 5033–5040.

[78] Langevin, M. Recombinaison et diffusion des ions gazeux. *J. Phys. Theor. Appl* **1905**, *4*.

[79] Lakhwani, G.; Rao, A.; Friend, R. H. Bimolecular Recombination in Organic Photovoltaics. *Annual Review of Physical Chemistry* **2014**, *65*, 557–581.

[80] Liu, Y.; Zojer, K.; Lassen, B.; Kjelstrup-Hansen, J.; Rubahn, H.-G.; Madsen, M. Role of the Charge-Transfer State in Reduced Langevin Recombination in Organic Solar Cells: A Theoretical Study. *The Journal of Physical Chemistry C* **2015**, *119*, 26588–26597.

[81] Burke, T. M.; Sweetnam, S.; Vandewal, K.; McGehee, M. D. Beyond Langevin Recombination: How Equilibrium Between Free Carriers and Charge Transfer States Determines the Open-Circuit Voltage of Organic Solar Cells. *Advanced Energy Materials* **2015**, *5*, 1500123.

Chapter 2

Stability of organic solar cells

A detailed understanding of the mechanisms which lead to the deterioration of OSCs is of utmost importance for the development of novel devices with application outside the laboratory. In this chapter the main processes contributing to the degradation of OPV devices are reviewed. The degradation patterns are separated into external factors, such as the influence of oxygen and water onto the operational stability, and intrinsic factors, namely heat- and light-induced processes. After a detailed consideration of the various degradation mechanisms, mitigation strategies to improve the stability are proposed. This chapter concludes with recommending design rules for future, more stable devices. For further reading, I recommend the reviews by W. Mateker[1] and by E. Speller[2], the latter particularly on the role of non-fullerene acceptors (NFAs), which are only briefly addressed in this review.

2.1 Intrinsic degradation

Intrinsic degradation occurs even when the devices are operated in an inert atmosphere, without exposure to oxygen or water. The main contributions are degradation due to elevated temperatures and chemical degradation caused by the interaction with light. Heat-induced processes usually involve structural reorganisation of the blend materials, altering the finely mixed nano-morphology, while light-induced processes are related to photochemical reactions in the absorber layer.

2.1.1 Heat-induced degradation

The stability of organic material systems under the influence of heat is closely related to the glass transition temperature T_g of the components which defines the temperature range where the organic molecules change from a rigid glass to a more flexible and soft state. Temperatures above T_g allow molecules and polymer chains to easily diffuse through the active layer, causing changes in the bulk or interfacial properties.

Interfacial effects

A common observation in BHJ films exposed to high temperatures is the accumulation of a polymer-rich layer at the top surface (~ 10 nm). In standard architecture devices, where electrons are collected through the top electrode, this leads to the formation of a blocking layer for charge extraction, reducing FF and V_{OC}.[3,4] The performance can be restored by peeling off and re-evaporating the electrodes. In inverted architecture solar cells, where holes are extracted through the top electrode, the accumulation of a polymer-rich phase does not inhibit charge extraction.

Also heat-induced diffusion of metal atoms from the interlayers or electrodes into the bulk of the active layer has been observed, for example in devices employing indium, aluminium, or lithium.[5–9] Greenbank et al. used Rutherford backscattering spectroscopy and XPS depth profiling on inverted P3HT:PC_{60}BM and PCDTBT:PC_{70}BM devices with the commonly used extraction layers MoO_3 and Ag to demonstrate diffusion of silver atoms into the bulk.[10,11] The diffused atoms act as quenching sites for excitons, traps for charges, or lead to doping of the active layer, thereby leading to increased recombination which in turn decreases all photovoltaic parameters.[12–17] Additionally, high temperatures can lead to delamination of the evaporated electrodes which has been shown for thin (10 - 20 nm) silver layers.[18]

Bulk effects

At elevated temperatures fullerenes, which have been primarily employed as electron acceptors, start to aggregate, forming micrometer-sized clusters (Figure 2.1, top row).[19] This is caused by the low miscibility between donor and acceptor components, for example in PTB7-Th:PC_{60}BM[20] or PffBT4T-2OD:fullerene[21,22] films. It was shown in Section 1.2 that a finely mixed microstructure with well defined percolation pathways is essential for charge gen-
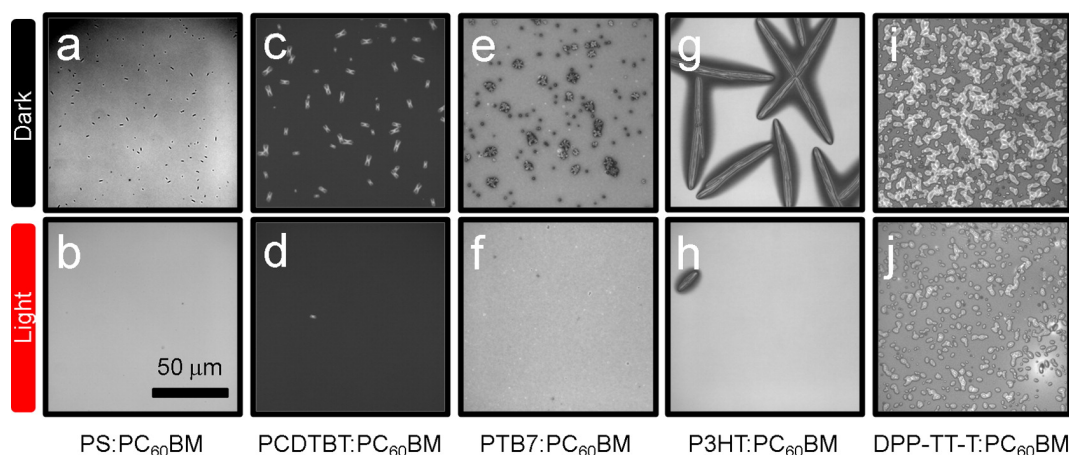
Figure 2.1: Optical microscopy images showing annealed morphologies of polymer:$PC_{60}BM$ blend films on SiO_x substrates with (bottom row) and without (top row) prior light exposure. Films at the bottom panel were exposed to fluorescent light (10 mW/cm2) for 165 min prior to annealing. Reproduced with permission from Ref.[19] Copyright 2014, American Chemical Society.

eration and extraction in a BHJ. Phase separation and formation of large, crystalline phases deteriorates charge generation since excitons may not be able to diffuse to an interface and separate within their lifetime, resulting in strong, initial degradation (*burn-in*).[23–25]

In PTB7 solar cells, high temperatures lead to side-chain cleavage or breaking of the aromatic chain; the resulting fragments decrease the mobility of the films by increasing recombination.[26,27]

Preventing heat-induced degradation

To suppress those structural changes, several strategies have been proposed. The choice and thickness of the electrode material can prevent diffusion of metal atoms into the bulk. Replacing the hole extraction layers MoO_3/Ag with WO_3/Al improves the thermal stability considerably, as silver atoms were found to diffuse into the layer in the former combination.[10,11] Greenbank et al. showed that a thin layer of WO_3 on top of the silver electrode increased the thermal stability significantly.[18] Additionally, thicker electrodes act as a heat sink and should thus be employed when the applications allow it (considering costs, flexibility, and semi-transparency).

Replacing low T_g polymers with high T_g variants is a main route to improve

stability, as this will decrease the diffusivity of the components in the active layer. Exposure to small light doses leads to increased thermal stability in some polymer:fullerene systems, as cross-linking between the components stabilises the nano-morphology against heat-induced reorganisation (Figure 2.1).[19,28,29] Furthermore, the synthesis of novel acceptors with matching miscibility is a critical step towards more stable devices.[20] The advent of NFAs could potentially achieve this requirement by replacing the heat-sensitive fullerenes.[30–32]

Another possibility is to introduce a third component into the blend to stabilise the morphology.[33,34] The crystallisation of $PC_{70}BM$ in many polymer blends can be suppressed by adding additional fullerene derivatives to the solution to form alloy acceptors.[35–37] Also adding a second polymer stabilises the domains in PTB7-Th:$PC_{60}BM$ and PTB7:$PC_{60}BM$ solar cells.[38] In polymers or small molecules containing fluorine atoms, the common chemical 4,4'-biphenol (BPO) can be employed as a *molecular lock* to freeze the morphology by forming hydrogen bonds between donor and BPO.[39] Such crosslinking is also reported for other polymer systems.[40–42]

2.1.2 Light-induced degradation

When operating the solar cells under light, a significant and fast reduction in the efficiency is often observed, even in inert atmospheres. This burn-in strongly depends on the materials used and its origin remains widely debated; a general consensus has not yet been achieved to date. The temperature of the devices in operating conditions can reach up to 80°C which can lead to structural changes which were described above.[20,43] Additionally, under certain conditions illumination can lead to dimerisation of fullerenes which impedes the dissociation of acceptor excitons and causes loss in J_{SC}. Formation of defects within the bandgap increase the energetic disorder and negatively affects charge transport.

Fullerene degradation

A common observation in many polymer:fullerene OPVs is the dimerisation of fullerenes upon illumination in inert atmospheres.[44,45] Heumueller et al. could accurately reproduce the JV-curves of degraded devices by blending $PC_{60}BM$ dimers with regular fullerenes (Figure 2.2a).[45] The dimerisation of fullerenes is mostly observed in $PC_{60}BM$ while other derivatives, such as bis$PC_{60}BM$ or $PC_{70}BM$, are less prone to oligomerise.[19,44,46,47] This process depends strongly
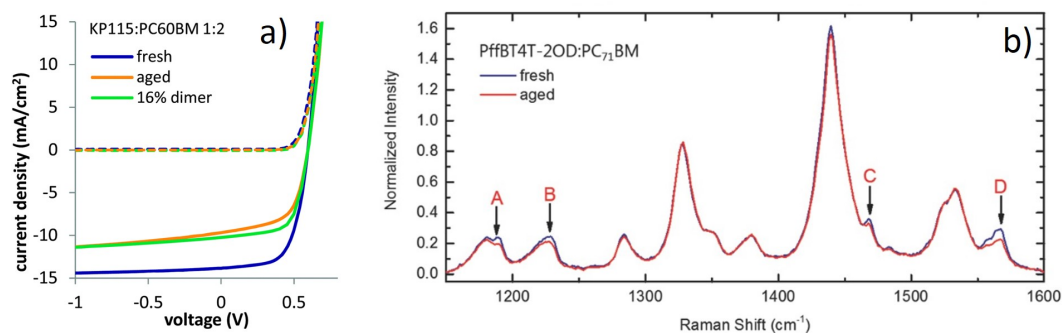
Figure 2.2: (a) Blending regular $PC_{60}BM$ with the corresponding dimer reproduces JV-curves of devices degraded under illumination. Dimerisation mainly affects the J_{SC}. Reproduced with permission.[45] Copyright 2016, The Royal Society of Chemistry. (b) Raman spectra of fresh and light-aged PffBT4T-2OD:$PC_{70}BM$ devices. Peaks labeled A–D are signatures of $PC_{70}BM$, showing negligible dimerisation. Reproduced with permission from Ref.[52] Copyright 2017, Wiley.

on the light intensity[48] and film morphology; when donor and acceptor are intimately mixed, the formation of dimers is suppressed.[45] The oligomers cause trapping of excitons in the fullerene phase due to a decreased diffusion length and influence exciton splitting at the donor-acceptor interface.[45,49] Since the effects of dimerisation are strongest when the devices are kept at V_{OC} conditions, it has been suggested that the reaction occurs via triplet excitons on the fullerene.[45] The chemical mechanism, by which these dimers form, is a [2+2] cycloaddition between two parallel double bonds on adjacent fullerenes.[44,47,50,51]

Devices based on PCDTBT blended with fullerene derivatives containing nitrogen show strong degradation when exposed to sunlight by formation of radical species on the fullerene cage, while dimerisation is not a main problem.[53] Also in PffBT4T-2OD:$PC_{70}BM$ no formation of oligomers is observed, and the degradation is caused by cleavage at the site of the solubilising side group attachment to the C_{70} cage (Figure 2.2b).[52] In PTB7:$PC_{70}BM$ devices, UV light is responsible for photochemical reactions between donor and acceptor resulting in trap states deteriorating the electron transport.[54]

Polymer degradation

Due to their interaction with high-energy photons, polymers are prone to degrade under illumination. In P3HT films illuminated under 1 sun conditions

an absorption loss was observed which is caused by photochemical reactions at the alkyl side chain of the polymer.[55] The addition of $PC_{60}BM$ can stabilise the P3HT by UV-screening, radical scavenging, and by quenching the polymer excited state.[43] Minor reductions in the optical density are also reported for other polymers.[56] The destruction of the chromophores and the resulting loss of absorption leads to fewer generated charge carriers, and hence to a reduction of J_{SC}.

In many organic systems, the loss of J_{SC} under constant illumination is accompanied by a strong, initial reduction in V_{OC}.[56–58] In P3HT:$PC_{60}BM$ devices, increased recombination and an increased trap density was observed.[58] Formation of defect states in the bandgap was further observed in devices with PCDTBT[57,59], PTB7[60], and PTB7-Th[56]. Those gap state can have several consequences for the solar cell performance: firstly, defects impede charge transport by increasing trap-assisted recombination, resulting in lower J_{SC} and FF. Additionally, the trapping reduces the average occupation of the frontier molecular orbitals and therefore the V_{OC}.[61,62] Secondly, trapped charges can create space charge regions and thus obstruct charge extraction which results in poor J_{SC} and FF.[57,63,64] Finally, defect states broaden the DOS which causes voltage losses (Figure 2.3).[65–67] The magnitude of the latter effect depends on the charge carrier density in the material and thus is lower for crystalline polymers.[68] The chemical origins for light-induced defect formation and broadening of the DOS are manifold. Impurities left over from synthesis[69–71], etching of the ITO by PSS in standard architecture solar cells[58], breaking of N-C or H-C bonds in the case of PCDTBT[29,59], trace amounts of oxygen[57], or solvent additives[56] have been proposed.

Preventing light-induced degradation

Although the origins of photo-induced burn-in are manifold and not yet fully understood, many strategies have been proposed to improve the stability of optoelectronic devices. The dimerisation of acceptor molecules is primarily a process occurring in C_{60} derivatives. Using higher-adduct fullerenes, like $PC_{70}BM$, which is commonly employed in high-efficiency systems, helps reducing this loss channel.[45] Also employing highly crystalline donor materials suppresses oligomerisation of the fullerenes.[67,68] Yan et al. showed that low levels of piperazine doping can improve the stability of polymer:$PC_{60}BM$ blends with P3HT, PTB7-Th and PffBT4T-2OD. They concluded that photon-induced charge transfer between the fullerene and piperazine leads to quenching
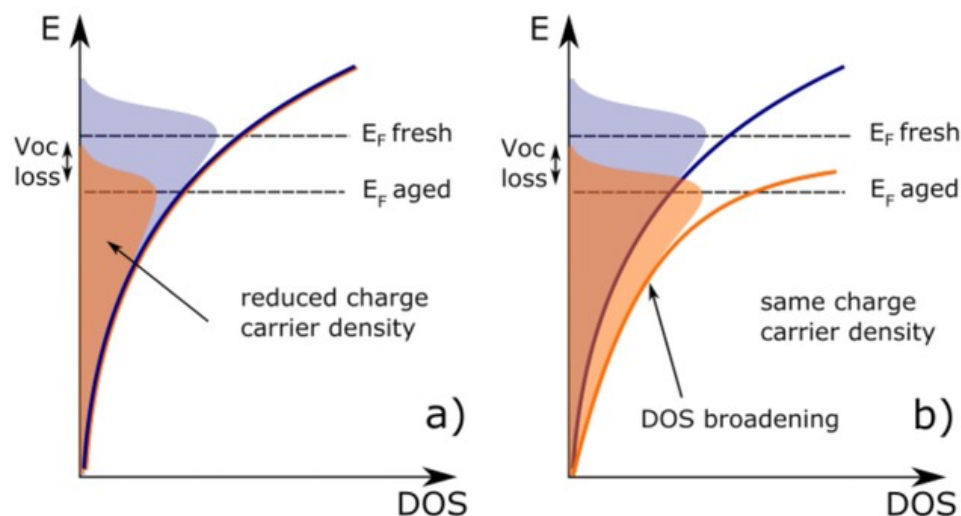
Figure 2.3: Decrease of the V_{OC} can be caused by (a) increased recombination that lowers the charge carrier density or by (b) a broadening of the DOS with unchanged charge carrier density. Reproduced with permission from Ref.[67] Copyright 2015, Wiley.

of $PC_{60}BM$ excitons, decreasing the rate of fullerene dimerisation.[72] Zhang et al. demonstrated that the addition of piperazine is able to fully eliminate the burn-in for PffBT4T-2OD:$PC_{70}BM$ devices due to its ability to form hydrogen bonds with the active components.[20] The advent of NFAs can potentially further increase stability, but more research of light-induced degradation is needed.[73,74] A recent study by Doumon et al. showed that the promising NFA ITIC is photochemically much less stable than the fullerene alternative $PC_{70}BM$.[75]

Removing impurities such as halides, metals, or oxygen from the production process reduces the formation of defects and thus decreases the burn-in in OPVs.[69,71,76,77] Additionally, avoiding low-boiling point solvent additives, such as DIO, further increases the blend stability.[56] Furthermore, donors with higher crystallinity are chemically more stable; their application reduces the energetic disorder in the system, leading to reduced voltage losses.[68] Finally, the employment of UV-filters effectively increases the device stability, as most problems arise from the high-energy part of the spectrum.[54]

2.2 Extrinsic degradation

This section covers the stability of organic solar cells under the influence of extrinsic factors like oxygen. Exposed to ambient conditions OPVs show rapid loss of performance, even in dark conditions. Oxidation of the active components or the electrodes in the presence of light is a major loss channel which is addressed in detail. The effects of humidity are only briefly covered, and I refer to other excellent literature reviews.[1,78]

2.2.1 Oxygen doping

When OPV devices are operated in oxygen atmospheres, strong degradation can be observed for some systems, even when kept under dark conditions. Schafferhans et al. reported that the performance loss of P3HT:PC$_{60}$BM solar cells, degraded in oxygen under no illumination, is mainly mediated by a strong reduction in J$_{SC}$. By using CELIV measurement techniques, they identified an increased charge carrier density to be responsible for the loss of short-circuit current which was backed-up by simulations.[79] Seemann et al. found that this effect is caused by oxygen-induced p-doping of the active layer, which is reversible upon annealing and significantly enhanced upon illumination.[80] The doping leads to an increase in mobile holes which form a space charge region at the electron extraction layer and thus hinder charge extraction by shielding the electric field inside the active layer. The reversibility under heat and vacuum or nitrogen shows that chemical oxidation of the active components is not the origin of this effect. It was rather shown that a metastable charge-transfer-complex (CTC) between P3HT and molecular oxygen, leading to mobile holes being delocalised over the polymer backbone, is responsible for the observed doping effect.[81,82] This process was also observed in PCPDTBT films,[83] organic photodetectors using PBDTTT-C,[84] and was confirmed in band-structure calculations.[85]

2.2.2 Photo-oxidation

The strongest efficiency losses are observed in the presence of both oxygen and light. The oxidation of polymers leads to the destruction of the chromophores resulting in a loss of absorption. This process is called *photo-bleaching* and depends strongly on the materials which are employed. When fullerenes oxidise, deep traps are created which impede the electron transport and increase recombination in the devices.

Photo-bleaching

Irreversible bleaching of the absorber layer is commonly observed in many OPV systems, resulting in a strong decrease of J_{SC} since less photons can be converted to excitons. A complete loss of absorption was shown for neat P3HT after 700 hours in air and light.[86] Similar developments were reported for PCDTBT[87], PTB7[88] and Si-PCPDTBT.[89] For all these polymers, infrared spectroscopy showed a loss of conjugated bonds and a growth of carbonyl, ester, and alkoxy bonds, indicating that the materials chemically reacted with oxygen. The mechanisms for this photo-oxidation are often initiated by free-radical reactions at the side chains of the molecules which can than proceed by diffusion or reaction and lead to scission of the conjugated bonds and thus destruction of the chromophores. This process has been extensively studied for P3HT[90,91] and PCDTBT.[87] An alternative mechanism is the oxidation via singlet oxygen $^1O_2$ which can be generated by polymer or fullerene triplet states.[92,93] In PTB7 this leads to a rapid oxidation of the benzodithiophene unit.[88,94]

The rate at which the organic components oxidise can vary substantially.[95] It was found that more crystalline and dense films are more resistant to photo-oxidation compared to amorphous materials.[92,95,96] In some systems, the addition of an acceptor reduces the rate of photo-oxidation of the polymer by removing the excited electron from the donor and competing with electron transfer to molecular oxygen.[86] However, in most systems the fullerene acceptor introduces additional loss channels, as is explained in the next section.[88]

Fullerene oxidation

Karuthedath et al. investigated the charge carrier dynamics in P3HT and Si-PCPDTBT solar cells with the fullerene acceptor $PC_{60}BM$. They found that the charge generation as well as the absorption is mainly unaffected by the degradation; instead the charge carrier mobility is greatly reduced with strong influence on the charge extraction.[98] Lee et al. showed that small amounts of oxidised $PC_{60}BM$ are responsible for drastic performance losses in PCDTBT solar cells (Figure 2.4).[97] Reese et al. observed formation of deep traps by oxidation of $PC_{60}BM$.[86] The generation of such trap states is suggested by the red-shifted photo- and electroluminescence upon ageing, consistent with DFT calculations of defect states, showing deeper LUMO levels compared to neat $PC_{60}BM$.[97,99]

The light-induced oxidation in $PC_{70}BM$ was shown to originate from the
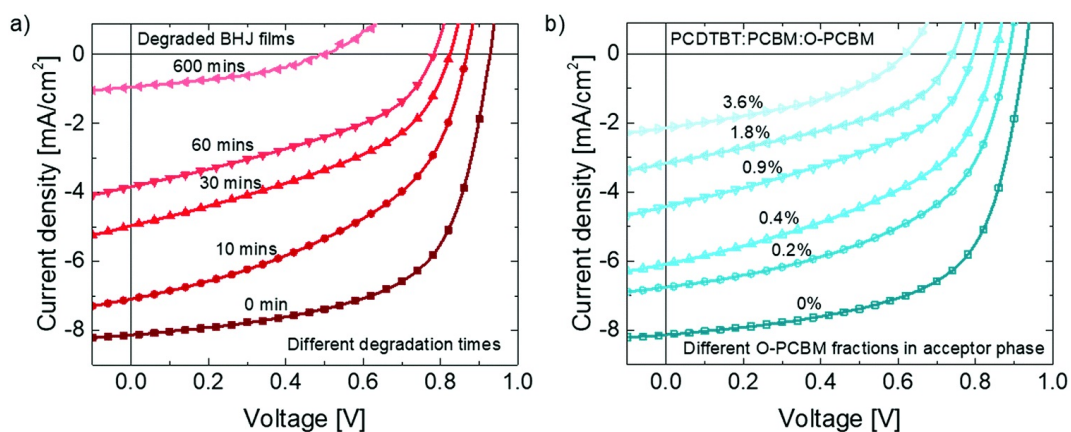
Figure 2.4: Impact of fullerene photo-oxidation on OPV devices behaviour. (a) JV characteristic of PCDTBT:PC_{60}BM devices with different degradation times under simulated AM 1.5G illumination in air. (b) JV characteristic of PCDTBT:PC_{60}BM blend devices made with different fractions of degraded PC_{60}BM, the percentages indicating the mass fraction of O-PC_{60}BM in the fullerene phase. Reproduced with permission from Ref.[97] Copyright 2018, The Royal Society of Chemistry.

formation of carbonyl groups which act as electron traps and increase non-radiative recombination and energetic disorder.[100] Two mechanisms for the oxidation of fullerenes have been proposed. Firstly, the triplet-mediated creation of highly-reactive singlet oxygen ($^1O_2$), which can oxidise the acceptor component[93,99] and, secondly, the generation of radical superoxide (O_2^-) by electron transfer from low lying excited fullerene states.[74,101] The latter process depends strongly on the electron affinity of the acceptors which should influence the design rules for the synthesis of new acceptor materials, e.g. non-fullerene acceptors.[74,101] It is thus clear that fullerene acceptors have a dramatic impact on the stability of organic electronic devices, not only by formation of traps, impeding electron transport and increasing recombination, but also by producing highly-reactive oxygen species, which are able to attack the donor component as well.

Preventing Photo-oxidation

The most principal way to prevent oxidation of the active materials is to apply a glass- or plastic-based encapsulation layer to act as a physical barrier,

impeding the ingress of oxygen and water. However, glass encapsulation is incompatible with flexible devices and furthermore substantially increases fabrication costs.[102] On the other hand, plastic encapsulation layers provide only partial blocking of atmospheric gasses. It is therefore an essential task to improve the intrinsic stability of the materials towards oxygen degradation. More dense and crystalline films proved to be more resistant against oxidation compared to amorphous polymers.[92,95,96] Since oxidation of organic compounds often starts with a radical reaction at the side chain, removing those can be a general method to improve stability. Manceau et al. showed that polymers with thermally cleaved sidechains retain most of their absorption properties after degradation under photo-oxidative conditions.[103]

It was shown that acceptors act as sensitisers for the formation of singlet oxygen ($^1O_2$) or superoxide radicals (O_2^-) and that the latter process depends on the electron affinity of the material. Acceptors with shallow LUMO energy levels can facilitate electron transfer to molecular oxygen forming the superoxides.[74,101] Consequently, the synthesis of new acceptor molecules, possibly NFAs, should consider deeper LUMO levels to improve the environmental stability, if the resulting lower V_{OC} can be compensated. However, many current non-fullerene acceptors suffer more severely from oxidative processes.[74] To delay oxidation of the active components, getter materials are employed in many OLED devices which preferentially react with water or oxygen.[104] Li et al. used a thin layer of TiO_2 on top of the active layer which acted as oxygen scavenger and UV filter.[105]

2.2.3 Contact and interlayer degradation

Not only the active layer but also the electrodes and charge collection layers are prone to degrade under the influence of extrinsic factors. Low work function metals readily oxidise, giving rise to charge extraction barriers. Water and oxygen can diffuse through pinholes in the electrodes or through hygroscopic interlayers into the device.

Electrode degradation

In the presence of oxygen or water, low work function metals such as aluminium or calcium, which are commonly used in standard architecture devices, are highly reactive. By employing TOF-SIMS in conjunction with isotopically labelled $H_2^{18}O$ and $^{18}O_2$ in small molecule solar cells, Hermenau et al. could
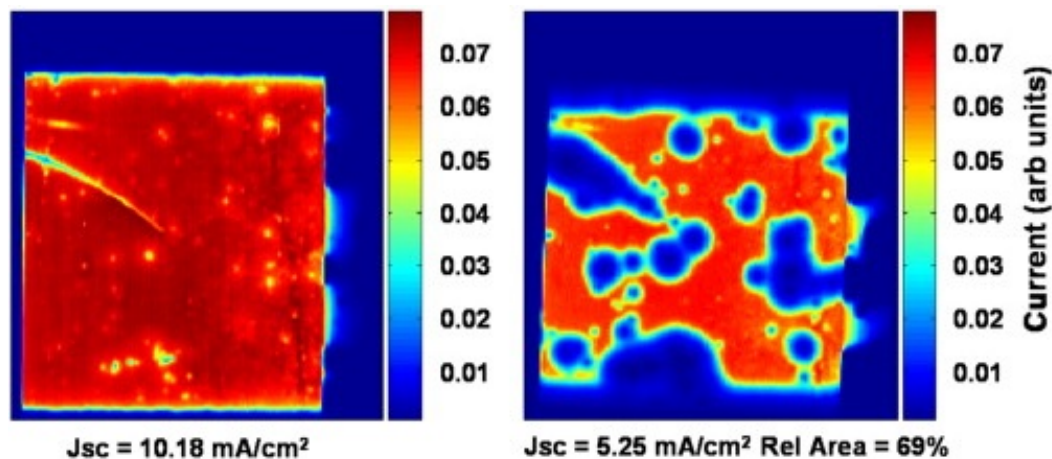
Figure 2.5: Laser beam induced current (LBIC) maps for an inverted device with silver electrode and PEDOT:PSS HTL before (left) and after ageing in air under constant illumination for 168 hours (right). Water ingress through pinholes and edges leads to loss in J_{SC}. Reproduced with permission from Ref.[108] Copyright 2011, Elsevier.

show that water primarily diffuses into the device between grains in the aluminium electrode, while molecular oxygen is mainly diffusing through pinholes in the contacts. At the interface to the hole transport layer, the water reacts with the electrode forming aluminium oxide.[106] Guerrero et al. reported oxidation of the calcium contact which leads to irreversible degradation of the devices.[81] These metal oxide layers are electrically insulating and thus create a transport barrier which hinders charge extraction through the electrodes and often leads to appearance of S-shaped JV-curves, equivalent to a strong loss of FF.[107] Formation of a dipole layer can also cause a voltage drop across the interface which has a direct impact on V_{OC}.[81]

Employing high work function silver electrodes in inverted devices significantly enhances device stability, since they are less prone to corrode. However, Lloyd et al. showed by laser beam induced current (LBIC) maps that significant amounts of water and oxygen can diffuse through a silver electrode in a inverted device and degrade the underlying PEDOT:PSS hole transport layer (Figure 2.5).[108]

Interlayer degradation

The above mentioned study (Figure 2.5) shows that also the interlayers in the device stack play an important role during degradation in ambient conditions. The impact of the common hole transport layer PEDOT:PSS onto the environmental stability of organic photovoltaic devices has been widely regarded as detrimental. The acidic nature of some formulations in conjunction with water is a possible source of corrosion of the electrodes.[8] Voroshazi et al. investigated the role of PEDOT:PSS in the oxidation of the electrodes and found that it greatly accelerates oxidation due to its hygroscopic nature.[109] Züfle et al. used capacitance and transient photocurrent measurements along with drift-diffusion simulations to identify the main causes of aluminium oxidation in standard architecture devices. They found that water ingress through the hygroscopic PEDOT:PSS and subsequent diffusion through the active layer is the main culprit, and replacing the HTL significantly improved the stability.[110] Isotopic labelling of water and oxygen during the degradation of inverted solar cells was used by Norrman et al. They found that reactions take place at the interface between PEDOT:PSS and the active layer which were caused by oxidation of phase separated PEDOT.[111]

The commonly used electron transport layer ZnO shows variable conductance which can be changed by exposure to UV light.[112,113] In the natural state, the surface layer of ZnO is doped with bound oxygen radicals, causing a low conductivity. Upon illumination these radicals are removed on a time scale of minutes, therefore increasing the conductance. In the dark this process is reverted by slow uptake of oxygen.[114]

Preventing contact and interlayer degradation

As described above, oxidation of the contacts and the interlayers is a serious problem of OPVs operated in ambient conditions. Hence, the most important step for improving the stability is to prevent oxygen and water diffusing through the electrode to the inter- and active layers. Regardless of different encapsulation techniques, the choice of electrode has a huge impact on the stability. High work function metals like silver or gold are less prone to oxidise, therefore inverted structure devices are usually much more stable compared to standard devices.[8,78,106,115,116] Furthermore, increasing the thickness of the electrodes reduces the amount of oxygen or water that can diffuse through the contacts. However, this approach is often incompatible with cheap, flexible, or semi-transparent devices.

Regardless of the architecture, replacing the HTL PEDOT:PSS is a necessary step for the realisation of long-lasting solar cells. Due to its acidic and hygroscopic nature, it readily oxidises and acts as a precursor for many loss channels in the device. Replacing PEDOT:PSS with MoO_3 increases the stability significantly. However, as was described above, the material combination MoO_3/Ag is thermally unstable, and thus a substitution by WO_3 might yield the best results.[11] In standard architecture, surface engineering of the ITO electrode with P3HT has been reported as a more stable alternative, due to its hydrophobic nature.[117]

2.3 Summary and outlook

In this chapter the influence of different environmental conditions on the operational stability of organic electronic devices was reviewed. It was shown that many systems are intrinsically unstable under the influence of heat which causes diffusion of metal atoms into the bulk[10] and phase separation of donor and acceptor domains.[21] The former process promotes trap formation, while the latter leads to the reorganisation of the finely mixed nano-morphology, increasing recombination and inhibiting charge separation. When exposed to light, often a dramatic decrease in performance (burn-in) is observed. Organic systems containing fullerene acceptors show dimerisation which adversely affects the exciton dynamics.[45] Additionally, large amounts of trap states in the bandgap are detected which impede charge transport by increased recombination, resulting in space charge regions due to trapped charges in deep states,[57] and broaden the density of states.[67] Also extrinsic factors, such as water or oxygen, have great influence on the stability of the devices. Even when kept in the dark, exposure to oxygen can lead to reversible p-type doping of the blend which results in an increased density of mobile holes, giving rise to extraction barriers at the electron extracting contact.[79] Likewise, the interlayers and contacts are prone to oxidise, particularly when low work function metals are employed.[106] The application of the hole transport layer PEDOT:PSS has been proven exceptionally harmful, due to its acidic and hygroscopic nature.[109] When the solar cells are exposed to both ambient conditions and illumination, photo-oxidation of the materials usually occurs. Commonly, this proceeds via a radical reaction involving a superoxide attack on the side chain of the polymers which results in loss of optical absorption.[87] Oxidation of the fullerenes has been proven to yield deep trap states, which massively increase recombination in the cells.[97] Based on these observations, the following guidelines can

be proposed.

A general strategy to improve the environmental stability of organic electronic devices is to apply a glass- or plastic-based encapsulation layer which impedes the diffusion of oxygen or water into the device. In inert atmospheres some systems show remarkable stability.[95,118] With glass-on-glass techniques, lifetimes of over ten thousand hours have been experimentally realised.[119] However, glass encapsulation is incompatible with flexible devices and significantly increase the fabrication costs.[102] On the other hand, flexible techniques, which are still responsible for a large amount of the total module costs, offer only an insufficient barrier to oxygen ingress thus far. Getter materials, which act as oxygen scavengers, might further delay oxidation of the active components.[104] If chosen carefully, e.g. a thin layer of TiO_2, those materials can act as a UV filter simultaneously.[105] Nonetheless, the enhancement of the intrinsic resistance of the devices to internal or external degradation is of principal importance.

The inverted architecture devices have proven to be most stable, due to the use of high work function metals which do not corrode as quickly.[106] Additionally, the aggregation of the polymer rich layer on top during fabrication does not impede charge extraction in this configuration. If the application allows it, thick electrodes can be employed which both act as a heat sink and delay diffusion of oxygen or water into the device. As a hole extraction layer, PEDOT:PSS should be avoided, for the reasons which were discussed at length above. Also the commonly used material combination MoO_3/Ag was reported to be unstable under heat; thus, the application of WO_3 together with Ag seems to be more promising, particularly when an additional thin layer of WO_3 is put on top of the electrode.[10,11,18] As electron transport layer, ZnO is best suited,[114] although its conductivity can change during illumination.[112,113]

To reduce reorganisation of the active materials, high T_g components should be employed. Additionally, crosslinking with common chemicals or fabrication of ternary structures with three active components can stabilise the morphology.[34,39,41] Annealing of the blend with small light doses may also be an option for fixing the nano-network.[19] Using highly crystalline donors with high molecular weight and purity increases the stability in light or oxygen; careful removal of impurities during synthesis is of paramount importance to reduce trap-mediated performance loss.[76,77] Since the oxidation of organic molecules often initiates at the solubilising side chain, heat- or light-induced cleavage of those groups has been suggested.[103] The application of small molecules over polymers as donor materials has shown promising lifetimes[118,120] and is successfully employed in OLEDs.[121]

The role of fullerenes has been discussed at length. High-order derivatives like PC$_{70}$BM are less prone to dimerise,[44] however, generally this type of acceptor tends to form aggregates if not crosslinked and is also easily oxidised by reactive oxygen species like $^1O_2$ or O_2^-.[21,52] The recent trend of developing NFAs has the potential to improve the environmental stability of OPVs while increasing the initial performance at the same time, although further research is required.[73–75,122,123] Its synthesis should consider creating acceptors with deep lying LUMO levels which stabilises against oxidation and formation of superoxides.[101]

Clearly, more work is needed if the environmental stability of organic photovoltaics is to reach the standard required for commercial application. This work demonstrates a further step towards this goal by investigating the photophysics and degradation mechanisms of current state-of-the-art material systems.

Bibliography

[1] Mateker, W. R.; McGehee, M. D. Progress in Understanding Degradation Mechanisms and Improving Stability in Organic Photovoltaics. *Advanced Materials* **2017**, *29*, 1603940.

[2] Speller, E. M.; Clarke, A. J.; Luke, J.; Lee, H. K. H.; Durrant, J. R.; Li, N.; Wang, T.; Wong, H. C.; Kim, J.-S.; Tsoi, W. C.; Li, Z. From fullerene acceptors to non-fullerene acceptors: prospects and challenges in the stability of organic solar cells. *Journal of Materials Chemistry A* **2019**,.

[3] Sachs-Quintana, I. T.; Heumüller, T.; Mateker, W. R.; Orozco, D. E.; Cheacharoen, R.; Sweetnam, S.; Brabec, C. J.; McGehee, M. D. Electron Barrier Formation at the Organic-Back Contact Interface is the First Step in Thermal Degradation of Polymer Solar Cells. *Advanced Functional Materials* **2014**, *24*, 3978–3985.

[4] Synooka, O.; Eberhardt, K.-R.; Singh, C. R.; Hermann, F.; Ecke, G.; Ecker, B.; von Hauff, E.; Gobsch, G.; Hoppe, H. Influence of Thermal Annealing on PCDTBT:PCBM Composition Profiles. *Advanced Energy Materials* **2014**, *4*, 1300981.

[5] Nguyen, T.; Ip, J.; Jolinat, P.; Destruel, P. XPS and sputtering study of the Alq3/electrode interfaces in organic light emitting diodes. *Applied Surface Science* **2001**, *172*, 75–83.

[6] Bulle-Lieuwma, C.; van Gennip, W.; van Duren, J.; Jonkheijm, P.; Janssen, R.; Niemantsverdriet, J. Characterization of polymer solar cells by TOF-SIMS depth profiling. *Applied Surface Science* **2003**, *203-204*, 547–550.

[7] Lee, S. T.; Gao, Z. Q.; Hung, L. S. Metal diffusion from electrodes in organic light-emitting diodes. *Applied Physics Letters* **1999**, *75*, 1404–1406.

[8] de Jong, M.; Simons, D.; Reijme, M.; van IJzendoorn, L.; Denier van der Gon, A.; de Voigt, M.; Brongersma, H.; Gymer, R. Indium diffusion in model polymer light-emitting diodes. *Synthetic Metals* **2000**, *110*, 1–6.

[9] Jeon, S. O.; Lee, J. Y. Improved lifetime in organic solar cells using

a bilayer cathode of organic interlayer/Al. *Solar Energy Materials and Solar Cells* **2012**, *101*, 160–165.

[10] Greenbank, W.; Hirsch, L.; Wantz, G.; Chambon, S. Interfacial thermal degradation in inverted organic solar cells. *Applied Physics Letters* **2015**, *107*, 263301.

[11] Greenbank, W.; Rolston, N.; Destouesse, E.; Wantz, G.; Hirsch, L.; Dauskardt, R.; Chambon, S. Improved mechanical adhesion and electronic stability of organic solar cells with thermal ageing: the role of diffusion at the hole extraction interface. *Journal of Materials Chemistry A* **2017**, *5*, 2911–2919.

[12] Gwinner, M. C.; Pietro, R. D.; Vaynzof, Y.; Greenberg, K. J.; Ho, P. K. H.; Friend, R. H.; Sirringhaus, H. Doping of Organic Semiconductors Using Molybdenum Trioxide: a Quantitative Time-Dependent Electrical and Spectroscopic Study. *Advanced Functional Materials* **2011**, *21*, 1432–1441.

[13] Nyman, M.; Dahlström, S.; Sandberg, O. J.; Österbacka, R. Unintentional Bulk Doping of Polymer-Fullerene Blends from a Thin Interfacial Layer of MoO 3. *Advanced Energy Materials* **2016**, *6*, 1600670.

[14] Sevinchan, Y.; Hopkinson, P. E.; Bakulin, A. A.; Herz, J.; Motzkus, M.; Vaynzof, Y. Improving Charge Separation across a Hybrid Oxide/Polymer Interface by Cs Doping of the Metal Oxide. *Advanced Materials Interfaces* **2016**, *3*, 1500616.

[15] Hofstetter, Y. J.; Hopkinson, P. E.; Bakulin, A. A.; Vaynzof, Y. Simultaneous enhancement in open circuit voltage and short circuit current of hybrid organic–inorganic photovoltaics by inorganic interfacial modification. *Journal of Materials Chemistry C* **2016**, *4*, 1111–1116.

[16] Pachoumi, O.; Bakulin, A. A.; Sadhanala, A.; Sirringhaus, H.; Friend, R. H.; Vaynzof, Y. Improved Performance of ZnO/Polymer Hybrid Photovoltaic Devices by Combining Metal Oxide Doping and Interfacial Modification. *The Journal of Physical Chemistry C* **2014**, *118*, 18945–18950.

[17] Vaynzof, Y.; Bakulin, A. A.; Gélinas, S.; Friend, R. H. Direct observation of photoinduced bound charge-pair states at an organic-inorganic semiconductor interface. *Physical Review Letters* **2012**, *108*, 246605.

[18] Greenbank, W.; Hirsch, L.; Chambon, S. Electrode de-wetting as a failure mechanism in thermally-aged OPV devices. *Solar Energy Materials and Solar Cells* **2018**, *178*, 8–14.

[19] Wong, H. C.; Li, Z.; Tan, C. H.; Zhong, H.; Huang, Z.; Bronstein, H.; McCulloch, I.; Cabral, J. T.; Durrant, J. R. Morphological stability and performance of polymer-fullerene solar cells under thermal stress: The impact of photoinduced PC60BM oligomerization. *ACS Nano* **2014**, *8*, 1297–1308.

[20] Zhang, C.; Heumueller, T.; Leon, S.; Gruber, W.; Burlafinger, K.; Tang, X.; Perea, J. D.; Wabra, I.; Hirsch, A.; Unruh, T.; Li, N.; Brabec, C. J. A top-down strategy identifying molecular phase stabilizers to overcome microstructure instabilities in organic solar cells. *Energy & Environmental Science* **2019**, *12*, 1078–1087.

[21] Li, N.; Perea, J. D.; Kassar, T.; Richter, M.; Heumueller, T.; Matt, G. J.; Hou, Y.; Güldal, N. S.; Chen, H.; Chen, S.; Langner, S.; Berlinghof, M.; Unruh, T.; Brabec, C. J. Abnormal strong burn-in degradation of highly efficient polymer solar cells caused by spinodal donor-acceptor demixing. *Nature Communications* **2017**, *8*, 14541.

[22] Yang, X.-Y.; Niu, M.-S.; Qin, C.; Bi, P.-Q.; Chen, Z.-H.; Feng, L.; Liu, J.-Q.; Hao, X.-T. Unraveling the unstable amorphous phase evolution effect on burn-in loss in polymer-fullerene solar cells. *Organic Electronics* **2019**, *71*, 156–163.

[23] Campoy-Quiles, M.; Ferenczi, T.; Agostinelli, T.; Etchegoin, P. G.; Kim, Y.; Anthopoulos, T. D.; Stavrinou, P. N.; Bradley, D. D. C.; Nelson, J. Morphology evolution via self-organization and lateral and vertical diffusion in polymer:fullerene solar cell blends. *Nature Materials* **2008**, *7*, 158–164.

[24] Motaung, D. E.; Malgas, G. F.; Arendse, C. J. Insights into the stability and thermal degradation of P3HT:C60 blended films for solar cell applications. *Journal of Materials Science* **2011**, *46*, 4942–4952.

[25] Yang, X.; Van Duren, J. K.; Janssen, R. A.; Michels, M. A.; Loos, J. Morphology and thermal stability of the active layer in poly(p-phenylenevinylene)/methanofullerene plastic photovoltaic devices. *Macromolecules* **2004**, *37*, 2151–2158.

[26] Savikhin, V.; Jagadamma, L. K.; Purvis, L. J.; Robertson, I.; Oosterhout, S. D.; Douglas, C. J.; Samuel, I. D.; Toney, M. F. Morphological, Chemical, and Electronic Changes of the Conjugated Polymer PTB7 with Thermal Annealing. *iScience* **2018**, *2*, 182–192.

[27] Fernandes, L.; Gaspar, H.; Tomé, J. P. C.; Figueira, F.; Bernardo, G. Thermal stability of low-bandgap copolymers PTB7 and PTB7-Th and their bulk heterojunction composites. *Polymer Bulletin* **2018**, *75*, 515–532.

[28] Li, Z.; Wong, H. C.; Huang, Z.; Zhong, H.; Tan, C. H.; Tsoi, W. C.; Kim, J. S.; Durrant, J. R.; Cabral, J. T. Performance enhancement of fullerene-based solar cells by light processing. *Nature Communications* **2013**, *4*, 2227.

[29] Tournebize, A.; Rivaton, A.; Gardette, J.-L.; Lombard, C.; Pépin-Donat, B.; Beaupré, S.; Leclerc, M. How Photoinduced Crosslinking Under Operating Conditions Can Reduce PCDTBT-Based Solar Cell Efficiency and then Stabilize It. *Advanced Energy Materials* **2014**, *4*, 1301530.

[30] Zhao, W.; Qian, D.; Zhang, S.; Li, S.; Inganäs, O.; Gao, F.; Hou, J. Fullerene-Free Polymer Solar Cells with over 11% Efficiency and Excellent Thermal Stability. *Advanced Materials* **2016**, *28*, 4734–4739.

[31] Li, S.; Liu, W.; Shi, M.; Mai, J.; Lau, T.-K.; Wan, J.; Lu, X.; Li, C.-Z.; Chen, H. A spirobifluorene and diketopyrrolopyrrole moieties based non-fullerene acceptor for efficient and thermally stable polymer solar cells with high open-circuit voltage. *Energy & Environmental Science* **2016**, *9*, 604–610.

[32] Holliday, S. et al. High-efficiency and air-stable P3HT-based polymer solar cells with a new non-fullerene acceptor. *Nature Communications* **2016**, *7*, 11585.

[33] Gasparini, N.; Salleo, A.; McCulloch, I.; Baran, D. The role of the third component in ternary organic solar cells. *Nature Reviews Materials* **2019**, *4*, 229–242.

[34] Baran, D. et al. Reducing the efficiency–stability–cost gap of organic photovoltaics with highly efficient and stable small molecule acceptor ternary solar cells. *Nature Materials* **2017**, *16*, 363–369.

[35] Santo, Y.; Jeon, I.; Sheng Yeo, K.; Nakagawa, T.; Matsuo, Y. Mixture of [60] and [70]PCBM giving morphological stability in organic solar cells. *Applied Physics Letters* **2013**, *103*, 073306.

[36] Lindqvist, C.; Bergqvist, J.; Bäcke, O.; Gustafsson, S.; Wang, E.; Olsson, E.; Inganäs, O.; Andersson, M. R.; Müller, C. Fullerene mixtures enhance the thermal stability of a non-crystalline polymer solar cell blend. *Applied Physics Letters* **2014**, *104*, 153301.

[37] Cheng, P.; Yan, C.; Wu, Y.; Wang, J.; Qin, M.; An, Q.; Cao, J.; Huo, L.; Zhang, F.; Ding, L.; Sun, Y.; Ma, W.; Zhan, X. Alloy Acceptor: Superior Alternative to PCBM toward Efficient and Stable Organic Solar Cells. *Advanced Materials* **2016**, *28*, 8021–8028.

[38] Landerer, D.; Mertens, A.; Freis, D.; Droll, R.; Leonhard, T.; Schulz, A. D.; Bahro, D.; Colsmann, A. Enhanced thermal stability of organic solar cells comprising ternary D-D-A bulk-heterojunctions. *npj Flexible Electronics* **2017**, *1*, 11.

[39] Cheng, P.; Yan, C.; Lau, T.-K.; Mai, J.; Lu, X.; Zhan, X. Molecular Lock: A Versatile Key to Enhance Efficiency and Stability of Organic Solar Cells. *Advanced Materials* **2016**, *28*, 5822–5829.

[40] Derue, L.; Dautel, O.; Tournebize, A.; Drees, M.; Pan, H.; Berthumeyrie, S.; Pavageau, B.; Cloutet, E.; Chambon, S.; Hirsch, L.; Rivaton, A.; Hudhomme, P.; Facchetti, A.; Wantz, G. Thermal Stabilisation of Polymer-Fullerene Bulk Heterojunction Morphology for Efficient Photovoltaic Solar Cells. *Advanced Materials* **2014**, *26*, 5831–5838.

[41] Rumer, J. W.; Ashraf, R. S.; Eisenmenger, N. D.; Huang, Z.; Meager, I.; Nielsen, C. B.; Schroeder, B. C.; Chabinyc, M. L.; McCulloch, I. Dual Function Additives: A Small Molecule Crosslinker for Enhanced Efficiency and Stability in Organic Solar Cells. *Advanced Energy Materials* **2015**, *5*, 1401426.

[42] Chao, Y.-C.; Chuang, C.-H.; Hsu, H.-L.; Wang, H.-J.; Hsu, Y.-C.; Chen, C.-P.; Jeng, R.-J. Enhanced thermal stability of organic photovoltaics via incorporating triphenylamine derivatives as additives. *Solar Energy Materials and Solar Cells* **2016**, *157*, 666–675.

[43] Manceau, M.; Rivaton, A.; Gardette, J.-L.; Guillerez, S.; Lemaître, N.

Light-induced degradation of the P3HT-based solar cells active layer. *Solar Energy Materials and Solar Cells* **2011**, *95*, 1315–1325.

[44] Distler, A.; Sauermann, T.; Egelhaaf, H.-J.; Rodman, S.; Waller, D.; Cheon, K.-S.; Lee, M.; Guldi, D. M. The Effect of PCBM Dimerization on the Performance of Bulk Heterojunction Solar Cells. *Advanced Energy Materials* **2014**, *4*, 1300693.

[45] Heumueller, T.; Mateker, W. R.; Distler, A.; Fritze, U. F.; Cheacharoen, R.; Nguyen, W. H.; Biele, M.; Salvador, M.; Von Delius, M.; Egelhaaf, H. J.; McGehee, M. D.; Brabec, C. J. Morphological and electrical control of fullerene dimerization determines organic photovoltaic stability. *Energy and Environmental Science* **2016**, *9*, 247–256.

[46] Rao, A.; Menon, M.; Wang, K.-A.; Eklund, P.; Subbaswamy, K.; Cornett, D.; Duncan, M.; Amster, I. Photoinduced polymerization of solid C70 films. *Chemical Physics Letters* **1994**, *224*, 106–112.

[47] Eklund, P.; Rao, A.; Zhou, P.; Wang, Y.; Holden, J. Photochemical transformation of C60 and C70 films. *Thin Solid Films* **1995**, *257*, 185–203.

[48] Wang, J.; Enevold, J.; Edman, L. Photochemical Transformation of Fullerenes. *Advanced Functional Materials* **2013**, *23*, 3220–3225.

[49] Burlingame, Q.; Tong, X.; Hankett, J.; Slootsky, M.; Chen, Z.; Forrest, S. R. Photochemical origins of burn-in degradation in small molecular weight organic photovoltaic cells. *Energy & Environmental Science* **2015**, *8*, 1005–1010.

[50] Stepanian, S. G.; Karachevtsev, V. A.; Plokhotnichenko, A. M.; Adamowicz, L.; Rao, A. M. IR Spectra of Photopolymerized C60 Films. Experimental and Density Functional Theory Study. *The Journal of Physical Chemistry B* **2006**, *110*, 15769–15775.

[51] Adams, G. B.; Page, J. B.; Sankey, O. F.; O'Keeffe, M. Polymerized C 60 studied by first-principles molecular dynamics. *Physical Review B* **1994**, *50*, 17471–17479.

[52] Cha, H.; Wu, J.; Wadsworth, A.; Nagitta, J.; Limbu, S.; Pont, S.; Li, Z.;

Searle, J.; Wyatt, M. F.; Baran, D.; Kim, J.-S.; McCulloch, I.; Durrant, J. R. An Efficient, "Burn in" Free Organic Solar Cell Employing a Nonfullerene Electron Acceptor. *Advanced Materials* **2017**, , 1701156.

[53] Inasaridze, L. N.; Shames, A. I.; Martynov, I. V.; Li, B.; Mumyatov, A. V.; Susarova, D. K.; Katz, E. A.; Troshin, P. A. Light-induced generation of free radicals by fullerene derivatives: an important degradation pathway in organic photovoltaics? *Journal of Materials Chemistry A* **2017**, *5*, 8044–8050.

[54] Bartesaghi, D.; Ye, G.; Chiechi, R. C.; Koster, L. J. A. Compatibility of PTB7 and [70]PCBM as a Key Factor for the Stability of PTB7:[70]PCBM Solar Cells. *Advanced Energy Materials* **2016**, *6*, 1502338.

[55] Manceau, M.; Chambon, S.; Rivaton, A.; Gardette, J.-L.; Guillerez, S.; Lemaître, N. Effects of long-term UV–visible light irradiation in the absence of oxygen on P3HT and P3HT:PCBM blend. *Solar Energy Materials and Solar Cells* **2010**, *94*, 1572–1577.

[56] Pearson, A. J.; Hopkinson, P. E.; Couderc, E.; Domanski, K.; Abdi-Jalebi, M.; Greenham, N. C. Critical light instability in CB/DIO processed PBDTTT-EFT:PC71BM organic photovoltaic devices. *Organic Electronics* **2016**, *30*, 225–236.

[57] Peters, C. H.; Sachs-Quintana, I. T.; Mateker, W. R.; Heumueller, T.; Rivnay, J.; Noriega, R.; Beiley, Z. M.; Hoke, E. T.; Salleo, A.; McGehee, M. D. The Mechanism of Burn-in Loss in a High Efficiency Polymer Solar Cell. *Advanced Materials* **2012**, *24*, 663–668.

[58] Khelifi, S.; Voroshazi, E.; Spoltore, D.; Piersimoni, F.; Bertho, S.; Aernouts, T.; Manca, J.; Lauwaert, J.; Vrielinck, H.; Burgelman, M. Effect of light induced degradation on electrical transport and charge extraction in polythiophene:Fullerene (P3HT:PCBM) solar cells. *Solar Energy Materials and Solar Cells* **2014**, *120*, 244–252.

[59] Street, R. A.; Davies, D. M. Kinetics of light induced defect creation in organic solar cells. *Applied Physics Letters* **2013**, *102*, 043305.

[60] Upama, M. B.; Wright, M.; Puthen-Veettil, B.; Elumalai, N. K.; Mahmud, M. A.; Wang, D.; Chan, K. H.; Xu, C.; Haque, F.; Uddin, A. Analysis of burn-in photo degradation in low bandgap polymer PTB7 using

photothermal deflection spectroscopy. *RSC Advances* **2016**, *6*, 103899–103904.

[61] Mandoc, M. M.; Kooistra, F. B.; Hummelen, J. C.; de Boer, B.; Blom, P. W. M. Effect of traps on the performance of bulk heterojunction organic solar cells. *Applied Physics Letters* **2007**, *91*, 263505.

[62] Cowan, S. R.; Leong, W. L.; Banerji, N.; Dennler, G.; Heeger, A. J. Identifying a Threshold Impurity Level for Organic Solar Cells: Enhanced First-Order Recombination Via Well-Defined PC84BM Traps in Organic Bulk Heterojunction Solar Cells. *Advanced Functional Materials* **2011**, *21*, 3083–3092.

[63] Yan, H.; Manion, J. G.; Yuan, M.; García de Arquer, F. P.; McKeown, G. R.; Beaupré, S.; Leclerc, M.; Sargent, E. H.; Seferos, D. S. Increasing Polymer Solar Cell Fill Factor by Trap-Filling with F4-TCNQ at Parts Per Thousand Concentration. *Advanced Materials* **2016**, *28*, 6491–6496.

[64] Wang, J.; Ren, X.; Shi, S.; Leung, C.; Chan, P. K. Charge accumulation induced S-shape J–V curves in bilayer heterojunction organic solar cells. *Organic Electronics* **2011**, *12*, 880–885.

[65] Blakesley, J. C.; Neher, D. Relationship between energetic disorder and open-circuit voltage in bulk heterojunction organic solar cells. *Physical Review B* **2011**, *84*, 075210.

[66] Garcia-Belmonte, G.; Boix, P. P.; Bisquert, J.; Lenes, M.; Bolink, H. J.; La Rosa, A.; Filippone, S.; Martín, N. Influence of the Intermediate Density-of-States Occupancy on Open-Circuit Voltage of Bulk Heterojunction Solar Cells with Different Fullerene Acceptors. *The Journal of Physical Chemistry Letters* **2010**, *1*, 2566–2571.

[67] Heumueller, T.; Burke, T. M.; Mateker, W. R.; Sachs-Quintana, I. T.; Vandewal, K.; Brabec, C. J.; McGehee, M. D. Disorder-Induced Open-Circuit Voltage Losses in Organic Solar Cells During Photoinduced Burn-In. *Advanced Energy Materials* **2015**, *5*, 1500111.

[68] Heumueller, T.; Mateker, W. R.; Sachs-Quintana, I. T.; Vandewal, K.; Bartelt, J. A.; Burke, T. M.; Ameri, T.; Brabec, C. J.; McGehee, M. D. Reducing burn-in voltage loss in polymer solar cells by increasing the

polymer crystallinity. *Energy Environ. Sci.* **2014**, *7*, 2974–2980.

[69] Bracher, C.; Yi, H.; Scarratt, N. W.; Masters, R.; Pearson, A. J.; Rodenburg, C.; Iraqi, A.; Lidzey, D. G. The effect of residual palladium catalyst on the performance and stability of PCDTBT:PC70BM organic solar cells. *Organic Electronics* **2015**, *27*, 266–273.

[70] Susarova, D. K.; Piven, N. P.; Akkuratov, A. V.; Frolova, L. A.; Polinskaya, M. S.; Ponomarenko, S. A.; Babenko, S. D.; Troshin, P. A. ESR spectroscopy as a powerful tool for probing the quality of conjugated polymers designed for photovoltaic applications. *Chemical Communications* **2015**, *51*, 2239–2241.

[71] Kong, J.; Song, S.; Yoo, M.; Lee, G. Y.; Kwon, O.; Park, J. K.; Back, H.; Kim, G.; Lee, S. H.; Suh, H.; Lee, K. Long-term stable polymer solar cells with significantly reduced burn-in loss. *Nature Communications* **2014**, *5*, 5688.

[72] Yan, L.; Wang, Y.; Wei, J.; Ji, G.; Gu, H.; Li, Z.; Zhang, J.; Luo, Q.; Wang, Z.; Liu, X.; Xu, B.; Wei, Z.; Ma, C.-Q. Simultaneous performance and stability improvement of polymer:fullerene solar cells by doping with piperazine. *Journal of Materials Chemistry A* **2019**, *7*, 7099–7108.

[73] Du, X.; Heumueller, T.; Gruber, W.; Classen, A.; Unruh, T.; Li, N.; Brabec, C. J. Efficient Polymer Solar Cells Based on Non-fullerene Acceptors with Potential Device Lifetime Approaching 10 Years. *Joule* **2019**, *3*, 215–226.

[74] Speller, E. M. et al. Toward Improved Environmental Stability of Polymer:Fullerene and Polymer:Nonfullerene Organic Solar Cells: A Common Energetic Origin of Light- and Oxygen-Induced Degradation. *ACS Energy Letters* **2019**, *4*, 846–852.

[75] Doumon, N. Y.; Dryzhov, M. V.; Houard, F. V.; Le Corre, V. M.; Rahimi Chatri, A.; Christodoulis, P.; Koster, L. J. A. Photostability of Fullerene and Non-Fullerene Polymer Solar Cells: The Role of the Acceptor. *ACS Applied Materials & Interfaces* **2019**, *11*, 8310–8318.

[76] Ashraf, R. S.; Schroeder, B. C.; Bronstein, H. A.; Huang, Z.; Thomas, S.; Kline, R. J.; Brabec, C. J.; Rannou, P.; Anthopoulos, T. D.; Durrant, J. R.; McCulloch, I. The Influence of Polymer Purification on Pho-

tovoltaic Device Performance of a Series of Indacenodithiophene Donor Polymers. *Advanced Materials* **2013**, *25*, 2029–2034.

[77] Mateker, W. R.; Douglas, J. D.; Cabanetos, C.; Sachs-Quintana, I. T.; Bartelt, J. A.; Hoke, E. T.; El Labban, A.; Beaujuge, P. M.; Fréchet, J. M. J.; McGehee, M. D. Improving the long-term stability of PBDTTPD polymer solar cells through material purification aimed at removing organic impurities. *Energy & Environmental Science* **2013**, *6*, 2529.

[78] Jørgensen, M.; Norrman, K.; Krebs, F. C. Stability/degradation of polymer solar cells. *Solar Energy Materials and Solar Cells* **2008**, *92*, 686–714.

[79] Schafferhans, J.; Baumann, A.; Wagenpfahl, A.; Deibel, C.; Dyakonov, V. Oxygen doping of P3HT:PCBM blends: Influence on trap states, charge carrier mobility and solar cell performance. *Organic Electronics* **2010**, *11*, 1693–1700.

[80] Seemann, A.; Sauermann, T.; Lungenschmied, C.; Armbruster, O.; Bauer, S.; Egelhaaf, H.-J.; Hauch, J. Reversible and irreversible degradation of organic solar cell performance by oxygen. *Solar Energy* **2011**, *85*, 1238–1249.

[81] Guerrero, A.; Boix, P. P.; Marchesi, L. F.; Ripolles-Sanchis, T.; Pereira, E. C.; Garcia-Belmonte, G. Oxygen doping-induced photogeneration loss in P3HT:PCBM solar cells. *Solar Energy Materials and Solar Cells* **2012**, *100*, 185–191.

[82] Abdou, M. S.; Orfino, F. P.; Son, Y.; Holdcroft, S. Interaction of oxygen with conjugated polymers: Charge transfer complex formation with poly(3-alkylthiophenes). *Journal of the American Chemical Society* **1997**, *119*, 4518–4524.

[83] Aguirre, A.; Meskers, S.; Janssen, R.; Egelhaaf, H.-J. Formation of metastable charges as a first step in photoinduced degradation in π-conjugated polymer:fullerene blends for photovoltaic applications. *Organic Electronics* **2011**, *12*, 1657–1662.

[84] Euvrard, J.; Revaux, A.; Cantarano, A.; Jacob, S.; Kahn, A.; Vuillaume, D. Impact of unintentional oxygen doping on organic photodetectors. *Organic Electronics* **2018**, *54*, 64–71.

[85] Lu, C.-K.; Meng, H.-F. Hole doping by molecular oxygen in organic semiconductors: Band-structure calculations. *Physical Review B* **2007**, *75*, 235206.

[86] Reese, M. O.; Nardes, A. M.; Rupert, B. L.; Larsen, R. E.; Olson, D. C.; Lloyd, M. T.; Shaheen, S. E.; Ginley, D. S.; Rumbles, G.; Kopidakis, N. Photoinduced Degradation of Polymer and Polymer-Fullerene Active Layers: Experiment and Theory. *Advanced Functional Materials* **2010**, *20*, 3476–3483.

[87] Tournebize, A.; Bussière, P.-O.; Wong-Wah-Chung, P.; Thérias, S.; Rivaton, A.; Gardette, J.-L.; Beaupré, S.; Leclerc, M. Impact of UV-Visible Light on the Morphological and Photochemical Behavior of a Low-Bandgap Poly(2,7-Carbazole) Derivative for Use in High-Performance Solar Cells. *Advanced Energy Materials* **2013**, *3*, 478–487.

[88] Razzell-Hollis, J.; Wade, J.; Tsoi, W. C.; Soon, Y.; Durrant, J.; Kim, J. S. Photochemical stability of high efficiency PTB7:PC70BM solar cell blends. *Journal of Materials Chemistry A* **2014**, *2*, 20189–20195.

[89] Fraga Domínguez, I.; Topham, P. D.; Bussière, P.-O.; Bégué, D.; Rivaton, A. Unravelling the Photodegradation Mechanisms of a Low Bandgap Polymer by Combining Experimental and Modeling Approaches. *The Journal of Physical Chemistry C* **2015**, *119*, 2166–2176.

[90] Hintz, H.; Egelhaaf, H.-J.; Peisert, H.; Chassé, T. Photo-oxidation and ozonization of poly(3-hexylthiophene) thin films as studied by UV/VIS and photoelectron spectroscopy. *Polymer Degradation and Stability* **2010**, *95*, 818–825.

[91] Manceau, M.; Rivaton, A.; Gardette, J.-L.; Guillerez, S.; Lemaître, N. The mechanism of photo- and thermooxidation of poly(3-hexylthiophene) (P3HT) reconsidered. *Polymer Degradation and Stability* **2009**, *94*, 898–907.

[92] Soon, Y. W.; Shoaee, S.; Ashraf, R. S.; Bronstein, H.; Schroeder, B. C.; Zhang, W.; Fei, Z.; Heeney, M.; McCulloch, I.; Durrant, J. R. Material Crystallinity as a Determinant of Triplet Dynamics and Oxygen Quenching in Donor Polymers for Organic Photovoltaic Devices. *Advanced Functional Materials* **2014**, *24*, 1474–1482.

[93] Yamane, S.; Mizukado, J.; Suzuki, Y.; Sakurai, M.; Chen, L.; Suda, H. MALDI-TOF MS Study of the Photooxidation of PCBM and Its Suppression by P3HT. *Chemistry Letters* **2015**, *44*, 339–341.

[94] Soon, Y. W.; Cho, H.; Low, J.; Bronstein, H.; McCulloch, I.; Durrant, J. R. Correlating triplet yield, singlet oxygen generation and photochemical stability in polymer/fullerene blend films. *Chemical Communications* **2013**, *49*, 1291.

[95] Mateker, W. R.; Heumueller, T.; Cheacharoen, R.; Sachs-Quintana, I. T.; McGehee, M. D.; Warnan, J.; Beaujuge, P. M.; Liu, X.; Bazan, G. C. Molecular Packing and Arrangement Govern the Photo-Oxidative Stability of Organic Photovoltaic Materials. *Chemistry of Materials* **2015**, *27*, 6345–6353.

[96] Dupuis, A.; Wong-Wah-Chung, P.; Rivaton, A.; Gardette, J.-L. Influence of the microstructure on the photooxidative degradation of poly(3-hexylthiophene). *Polymer Degradation and Stability* **2012**, *97*, 366–374.

[97] Lee, H. K. H. et al. The role of fullerenes in the environmental stability of polymer:fullerene solar cells. *Energy & Environmental Science* **2018**, *11*, 417–428.

[98] Karuthedath, S.; Sauermann, T.; Egelhaaf, H.-J.; Wannemacher, R.; Brabec, C. J.; Lüer, L. The effect of oxygen induced degradation on charge carrier dynamics in P3HT:PCBM and Si-PCPDTBT:PCBM thin films and solar cells. *Journal of Materials Chemistry A* **2015**, *3*, 3399–3408.

[99] Speller, E. M.; McGettrick, J. D.; Rice, B.; Telford, A. M.; Lee, H. K. H.; Tan, C.-H.; De Castro, C. S.; Davies, M. L.; Watson, T. M.; Nelson, J.; Durrant, J. R.; Li, Z.; Tsoi, W. C. Impact of Aggregation on the Photochemistry of Fullerene Films: Correlating Stability to Triplet Exciton Kinetics. *ACS Applied Materials & Interfaces* **2017**, *9*, 22739–22747.

[100] Wang, Y.; Jafari, M. J.; Wang, N.; Qian, D.; Zhang, F.; Ederth, T.; Moons, E.; Wang, J.; Inganäs, O.; Huang, W.; Gao, F. Light-induced degradation of fullerenes in organic solar cells: A case study on TQ1:PC71BM. *Journal of Materials Chemistry A* **2018**, *6*, 11884–11889.

[101] Hoke, E. T.; Sachs-Quintana, I. T.; Lloyd, M. T.; Kauvar, I.; Mateker, W. R.; Nardes, A. M.; Peters, C. H.; Kopidakis, N.; McGehee, M. D. The Role of Electron Affinity in Determining Whether Fullerenes Catalyze or Inhibit Photooxidation of Polymers for Solar Cells. *Advanced Energy Materials* **2012**, *2*, 1351–1357.

[102] Weerasinghe, H. C.; Vak, D.; Robotham, B.; Fell, C. J.; Jones, D.; Scully, A. D. New barrier encapsulation and lifetime assessment of printed organic photovoltaic modules. *Solar Energy Materials and Solar Cells* **2016**, *155*, 108–116.

[103] Manceau, M.; Helgesen, M.; Krebs, F. C. Thermo-cleavable polymers: Materials with enhanced photochemical stability. *Polymer Degradation and Stability* **2010**, *95*, 2666–2669.

[104] Buseman-Williams, J.; Frischknecht, K. D.; Hubert, M. D.; Saafir, A. K.; Tremel, J. D. Flat-plate encapsulation solution for OLED displays using a printed getter. *Journal of the Society for Information Display* **2007**, *15*, 103.

[105] Li, J.; Kim, S.; Edington, S.; Nedy, J.; Cho, S.; Lee, K.; Heeger, A. J.; Gupta, M. C.; Yates, J. T. A study of stabilization of P3HT/PCBM organic solar cells by photochemical active TiOx layer. *Solar Energy Materials and Solar Cells* **2011**, *95*, 1123–1130.

[106] Hermenau, M.; Riede, M.; Leo, K.; Gevorgyan, S. A.; Norrman, K. Water and oxygen induced degradation of small molecule organic solar cells. *Solar Energy Materials and Solar Cells* **2011**, *95*, 1268–1277.

[107] Glatthaar, M.; Riede, M.; Keegan, N.; Sylvester-Hvid, K.; Zimmermann, B.; Niggemann, M.; Hinsch, A.; Gombert, A. Efficiency limiting factors of organic bulk heterojunction solar cells identified by electrical impedance spectroscopy. *Solar Energy Materials and Solar Cells* **2007**, *91*, 390–393.

[108] Lloyd, M. T.; Peters, C. H.; Garcia, A.; Kauvar, I. V.; Berry, J. J.; Reese, M. O.; McGehee, M. D.; Ginley, D. S.; Olson, D. C. Influence of the hole-transport layer on the initial behavior and lifetime of inverted organic photovoltaics. *Solar Energy Materials and Solar Cells* **2011**, *95*, 1382–1388.

[109] Voroshazi, E.; Verreet, B.; Buri, A.; Müller, R.; Di Nuzzo, D.; Heremans, P. Influence of cathode oxidation via the hole extraction layer in polymer:fullerene solar cells. *Organic Electronics* **2011**, *12*, 736–744.

[110] Züfle, S.; Neukom, M. T.; Altazin, S.; Zinggeler, M.; Chrapa, M.; Offermans, T.; Ruhstaller, B. An Effective Area Approach to Model Lateral Degradation in Organic Solar Cells. *Advanced Energy Materials* **2015**, *5*, 1500835.

[111] Norrman, K.; Madsen, M. V.; Gevorgyan, S. A.; Krebs, F. C. Degradation Patterns in Water and Oxygen of an Inverted Polymer Solar Cell. *Journal of the American Chemical Society* **2010**, *132*, 16883–16892.

[112] Manor, A.; Katz, E. A.; Tromholt, T.; Krebs, F. C. Electrical and Photo-Induced Degradation of ZnO Layers in Organic Photovoltaics. *Advanced Energy Materials* **2011**, *1*, 836–843.

[113] Kam, Z.; Wang, X.; Zhang, J.; Wu, J. Elimination of Burn-in Open-Circuit Voltage Degradation by ZnO Surface Modification in Organic Solar Cells. *ACS Applied Materials & Interfaces* **2015**, *7*, 1608–1615.

[114] Lilliedal, M. R.; Medford, A. J.; Madsen, M. V.; Norrman, K.; Krebs, F. C. The effect of post-processing treatments on inflection points in current–voltage curves of roll-to-roll processed polymer photovoltaics. *Solar Energy Materials and Solar Cells* **2010**, *94*, 2018–2031.

[115] Krebs, F. C.; Norrman, K. Analysis of the failure mechanism for a stable organic photovoltaic during 10000 h of testing. *Progress in Photovoltaics: Research and Applications* **2007**, *15*, 697–712.

[116] Wong, K. W.; Yip, H. L.; Luo, Y.; Wong, K. Y.; Lau, W. M.; Low, K. H.; Chow, H. F.; Gao, Z. Q.; Yeung, W. L.; Chang, C. C. Blocking reactions between indium-tin oxide and poly (3,4-ethylene dioxythiophene):poly(styrene sulphonate) with a self-assembly monolayer. *Applied Physics Letters* **2002**, *80*, 2788–2790.

[117] Awada, H.; Mattana, G.; Tournebize, A.; Rodriguez, L.; Flahaut, D.; Vellutini, L.; Lartigau-Dagron, C.; Billon, L.; Bousquet, A.; Chambon, S. Surface engineering of ITO electrode with a functional polymer for PEDOT:PSS-free organic solar cells. *Organic Electronics* **2018**, *57*, 186–193.

[118] Burlingame, Q.; Huang, X.; Liu, X.; Jeong, C.; Coburn, C.; Forrest, S. R. Intrinsically stable organic solar cells under high-intensity illumination. *Nature* **2019**, *573*, 394–397.

[119] Sapkota, S. B.; Spies, A.; Zimmermann, B.; Dürr, I.; Würfel, U. Promising long-term stability of encapsulated ITO-free bulk-heterojunction organic solar cells under different aging conditions. *Solar Energy Materials and Solar Cells* **2014**, *130*, 144–150.

[120] Burlingame, Q.; Song, B.; Ciammaruchi, L.; Zanotti, G.; Hankett, J.; Chen, Z.; Katz, E. A.; Forrest, S. R. Reliability of Small Molecule Organic Photovoltaics with Electron-Filtering Compound Buffer Layers. *Advanced Energy Materials* **2016**, *6*, 1601094.

[121] Burrows, P. E.; Forrest, S. R.; Zhou, T. X.; Michalski, L. Operating lifetime of phosphorescent organic light emitting devices. *Applied Physics Letters* **2000**, *76*, 2493–2495.

[122] Cui, Y.; Wang, Y.; Bergqvist, J.; Yao, H.; Xu, Y.; Gao, B.; Yang, C.; Zhang, S.; Inganäs, O.; Gao, F.; Hou, J. Wide-gap non-fullerene acceptor enabling high-performance organic photovoltaic cells for indoor applications. *Nature Energy* **2019**, *4*, 768–775.

[123] Gasparini, N.; Salvador, M.; Strohm, S.; Heumueller, T.; Levchuk, I.; Wadsworth, A.; Bannock, J. H.; de Mello, J. C.; Egelhaaf, H.-J.; Baran, D.; McCulloch, I.; Brabec, C. J. Burn-in Free Nonfullerene-Based Organic Solar Cells. *Advanced Energy Materials* **2017**, *7*, 1700770.

Chapter 3

Ultrafast spectroscopy

Shortly after the first demonstration of a laser in 1960,[1] ultrashort pulses were generated from a Nd:glass source by De Maria and co-workers.[2] Since then the ultrafast laser technology has developed rapidly which led to uncountable applications in academia or everyday life. High repetition rates enable efficient communication technologies[3], while the broad spectrum of ultrashort pulses is used as a frequency comb in modern metrology as a means to measure unknown frequencies with high precision.[4,5] Shorter pulses also increase the peak power compared to cw-laser sources which is required for damage-free optical surgery[6,7] or micro-machining.[8] Very high intensities additionally give rise to non-linear effects, such as high-order harmonic generation or optical parametric amplification, which unlocked completely new fields of science.[9,10] Finally, femtosecond and attosecond laser pulses enable researchers to investigate processes which occur on the ultrashort timescale. Using pulsed lasers, the dissociation dynamics of molecules have been measured which led to the Nobel prize in Chemistry in 1999.[11] This thesis focuses on the dynamics of excitons and charges on the ps timescale and, therefore, a basic understanding of the fundamentals of ultrashort laser pulses is obligatory.

This chapter briefly explains the principles of fs laser pulses, their generation by mode-locking, their amplification by chirped pulse amplification (CPA) and their tunability by optical parametric amplification (OPA). Afterwards, the technique of fs-transient absorption (TA) spectroscopy is introduced and its application for the investigation of the photophysics of organic systems explained. After the working principle and setup of TA spectroscopy, the chapter concludes with the data processing which is performed with a global analysis algorithm to identify different processes in the materials.

3.1 Principles of short laser pulses

For the study of molecular systems using ultrafast spectroscopy, fs-laser pulses of variable wavelength are required. Therefore, in this section the basic operations to create such pulses are outlined. A train of pulsed light is generated via a technique called *mode-locking*. In order to use those pulses in complex experiments they need to be amplified which is performed via *chirped pulse amplification*. Finally, to study the dynamics of a system it needs to be excited with specific wavelengths resonant with certain optical transitions. Hence, the laser pulses must be tuned to variable photon energies which is achieved by *optical parametric amplification*.

3.1.1 Mode-locked lasers

In order to create fs or ps pulses from a cw-laser source, a technique called mode-locking is employed.[12] Depending on the size of the optical cavity and the wavelength of the light inside, discrete standing waves or modes form by constructive interference of the light wave (Figure 3.1a). The frequency separation $\Delta\nu$ between two such longitudinal modes in a linear resonator is given by

$$\Delta\nu = \frac{c}{2L} \tag{3.1}$$

where c is the speed of light and L is the distance between the mirrors of the cavity. Thus, in a typical broad bandwidth gain medium, e.g. Ti:sapphire, hundreds of thousand of modes are supported. When there is no fixed relationship between the modes, the random phases result in a near-constant output of the laser. However, when the phases of the modes are synchronised (mode-locked or phase-locked) they can interfere constructively at certain times, resulting in a train of short pulses.

The pulse duration depends on the number of available modes. Therefore, in order to create ultrashort pulses, gain media with large bandwidth such as Ti:sapphire are used. Mode-locking can be achieved by active or passive modulation of the resonator losses inside the cavity (Figure 3.1b). Active mode-locking uses an acousto-optical or electro-optical modulator which is synchronised with the round-trip time of the resonator. Pulses will freely pass the modulator at times when the loss is minimal, but are attenuated otherwise which leads to a higher gain for mode locked pulses.[13] As a result the phases between neighbouring modes are synchronised. In passive mode-locking often
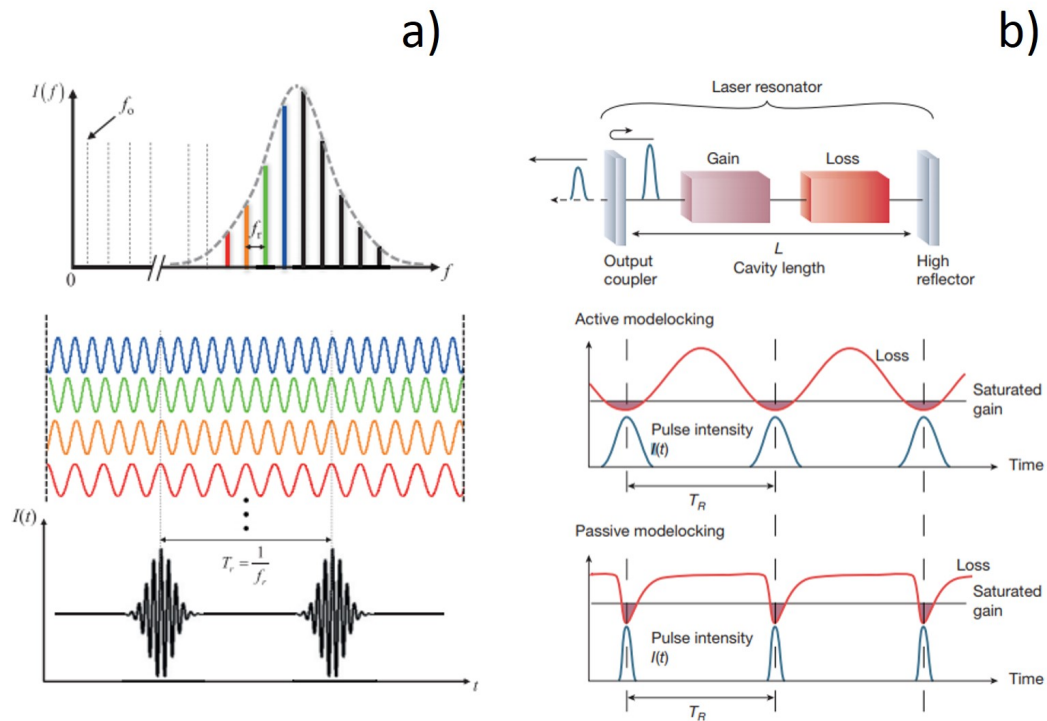
Figure 3.1: Principle of a mode locked laser. (a) The available longitudinal modes inside the cavity are determined by the gain bandwidth of the optical medium and the geometry of the resonator. If a phase relationship exists between the different modes, they periodically interfere constructively which results in the generation of ultra-short pulses. Reproduced with permission from Ref.[5] Copyright 2016, IOP Publishing. (b) Realisation of mode locking by active or passive loss modulation. Adapted with permission from Ref.[12] Copyright 2013, Springer Nature.

a saturable absorber is used which attenuates long, low-intensity pulses, but is saturated by high-intensity pulses. Thus, pulses with high intensity can pass and are shortened in the process, since their low-intensity wings are further attenuated, whereas pulses with lower intensity experience more loss than gain and eventually die out.[14] In modern applications the Kerr lens mode-locking (KLM) effect is used to generate ultrashort pulses.[15,16] In this non-linear effect, high-intensity light experiences self-focussing due to the intensity-dependence of the refractive index of the medium.[17] This effect reduces the mode area in the gain medium which improves for a short time the overlap with the (strongly focused) pump beam and therefore the effective gain.[12] Commercially available Ti:sapphire lasers provide typical pulse durations of 10 - 100 fs. The shortest pulses measured, however, are only 43 attoseconds long.[18] The repetition rate of the pulsed train of light is given by the dimensions of the cavity, typically 80 MHz in case of commercial Ti:sapphire lasers.

Depending on the application, light with narrow bandwidth is required. However, the uncertainty principle demands that bandwidth and duration of a light pulse are fundamentally connected. The relationship between pulse duration Δt and bandwidth $\Delta \nu$ for Gaussian-shaped pulses is given by

$$\Delta \nu \, \Delta t = \frac{4 \, \ln(2)}{2\pi} \approx 0.441 \tag{3.2}$$

The time-bandwidth product demands that the pulse duration and bandwidth cannot be infinitesimal small at the same time. For a 100 fs pulse from a Ti:sapphire laser with typical central wavelength of 800 nm this results already in a bandwidth of $\sim$9 nm which consequently increases to $\sim$90 nm for 10 fs pulses. Depending on the experiment, this trade-off between spectral bandwidth and pulse duration must be considered.

3.1.2   Chirped pulse amplification

A multitude of modern applications require high-intensity pulses, such as laser wakefield acceleration[19], laser micro-surgery[20], laser-driven electron diffraction[21], or micro-machining.[22] If the intensity of light is high enough, nonlinear optical phenomena, such as second-harmonic generation or optical parametric generation, can occur. Those phenomena are the basis for ultrafast spectroscopy which will be discussed in the next section. Therefore, the low energy fs-pulses from the mode-locked laser source (with energies usually in the pJ to nJ range) need to be amplified in order to reach the powers required for

those non-linear processes. However, regular amplification in a laser medium is eventually limited by the Kerr effect (see above). The self-focussing of the beam leads to ever higher intensities and eventual laser-induced damage of the optical medium or optical elements, like mirrors and lenses. The solution to this limitation was the development of chirped pulse amplification (CPA) which was in 2018 rewarded with the Nobel Prize for Physics.[23] In general, CPA works by the following three steps (Figure 3.2):

1. *Pulse stretching* In the first step the initial pulse is stretched in time. This is accomplished by using a dispersive element, such as a grating, which spatially separates the spectrum of the pulse. The shorter wavelengths are then forced to travel a longer path compared to the longer wavelengths which results in a temporally stretched pulse with reduced peak power. Thus, the pulse can be amplified without causing damage to the active medium.

2. *Pulse amplification* From the stretched (80 MHz) pulse train, one pulse at a typical rate of 4 kHz is selected to be amplified. The pulse is directed into the amplifier, often a Ti:sapphire crystal. Shortly before the pulse arrives in the optical medium, the crystal is excited to population inversion by a high-power, separate pump laser. The laser pulse passes the cavity multiple times, until the resulting stimulated emission eliminates the population inversion and amplification stops. Then the pulse is ejected out of the cavity. Capture and release of individual pulses in the cavity is realised by Pockels cells which change the polarisation of light when a voltage is applied.

3. *Pulse compression* The last step is the re-compression of the amplified pulses in a setup similar to the stretcher in the first step. During this process the red part of the spectrum is forced on a longer path compared to the blue part which results in the shortening of the stretched pulse to its original length.

In a typical regenerative amplifier used for transient absorption spectroscopy, input pulses with energies of a few nJ are thus amplified to energies on the order of mJ. Following this procedure, high-energy pulses are created and non-linear optical methods, such as optical parametric amplification which is needed to generate pulses with desired wavelength, are possible.
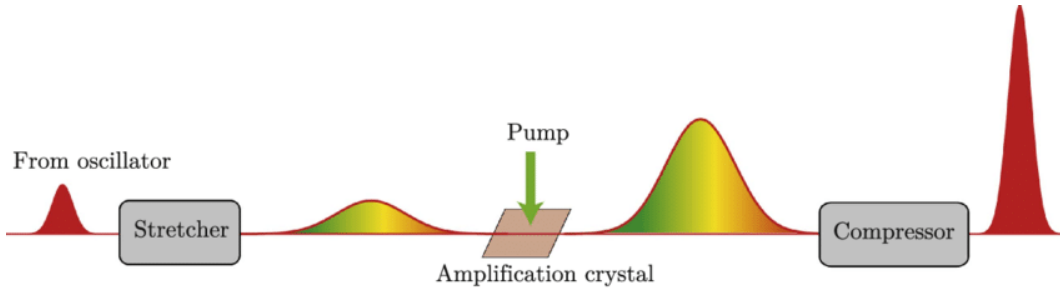
Figure 3.2: Principle of chirped pulse amplification (CPA). The ultra-short, low intensity input pulse is temporally stretched, thereby reducing its peak intensity. The stretched pulse is then amplified in a gain medium and recompressed to yield a high intensity, short pulse. Reprinted with permission from Ref.[24] Copyright 2017, IOP Publishing.

3.1.3   Optical parametric amplification

In ultrafast spectroscopy often different optical transitions in the system under study need to be excited which requires a broad tunable range of the light source from the IR to the UV part of the spectrum.[25] According to Equation 3.2, the typical pulse width of a 100 fs pulse centred around 800 nm from a Ti:sapphire laser is $\sim$9 nm which is often not sufficient to cover the spectral region of interest. Optical parametric amplification (OPA) uses second-order effects in non-linear crystals to transfer energy from a high-intensity, small bandwidth pump pulse to a signal pulse of variable frequency (Figure 3.3).[26–29] When two pulses of frequencies ω_1 and ω_3, called seed and pump pulse, respectively, are incident on a suitable crystal with $\chi^{(2)}$-non-linearity, the energy of the pump pulse can be transferred to the seed pulse. This process requires high intensities and the temporal and spacial overlap of the two pulses. Due to energy conservation, photons with frequency ω_2 are generated, the so-called idler photons

$$\hbar\omega_3 = \hbar\omega_1 + \hbar\omega_2 \tag{3.3}$$

This process can also be seen as stimulated emission from a virtual energy level, excited by photons with frequency ω_3. Thus, the amplified pulse of frequency ω_1 retains the coherent properties of the incident seed pulse. In practice the amplified light from the laser source (see above) is split into two beams: one with high intensity is used as the pump, the other is used to generate the broadband seed pulse. The latter is achieved by white-light continuum generation
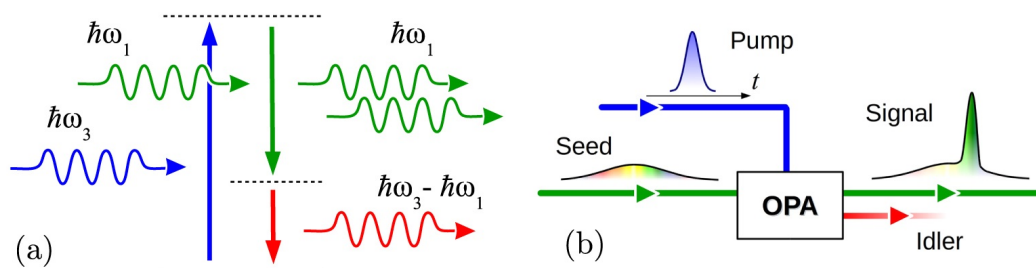
Figure 3.3: Principle of the optical parametric amplification (OPA). (a) In a non-linear process, energy from a pump pulse with frequency ω_3 is transferred to a 'signal' pulse with frequency ω_1. An additional 'idler' beam with frequency $\omega_2 = \omega_3 - \omega_1$ is generated due to energy conservation. (b) Using a broadband seed pulse together with a short and high-intensity pump pulse leads to the amplification of a narrow part of the signal pulse by changing the phase-matching condition. Reproduced with permission from Ref.[28] Copyright 2016, IOP Publishing.

(WLC) in a transparent dielectric medium (typically a sapphire plate) with $\chi^{(3)}$-non-linearity. WLC is a complex optical process which results in the spectral broadening of the pulse.[30–33] Pump and seed pulse are then focussed on a suitable crystal (often beta barium borate (BBO)) where the above-mentioned parametric amplification occurs. The process works most efficiently, when the phase-matching condition

$$\Delta \vec{k} = \vec{k_1} - \vec{k_2} - \vec{k_3} = 0 \qquad (3.4)$$

is satisfied, where $\vec{k_1}, \vec{k_2}, \vec{k_3}$ are the wave vectors of the interacting beams. By changing the angle between $\vec{k_3}$ and the optical axis of the crystal, usually achieved by rotation of the latter, the relative phases are adjusted and thus the ratio of the frequencies of signal and idler in Equation 3.3.[28] Therefore, a narrow portion of the seed beam can be amplified to yield a high-intensity, narrow bandwidth signal pulse of desired frequency.

3.2 Transient absorption spectroscopy

Transient absorption (TA) is a powerful tool to study the dynamics of organic systems on the fs to ns timescale. Many relevant processes in organic solar cells occur on this timescale, including exciton diffusion, formation of CT states,

charge separation, and recombination mechanisms. For the study of charge generation in novel OPV devices it is therefore imperative to investigate the early time dynamics of those systems. This section will give an overview of the working principle of the technique and describe necessary steps in the analysis of the datasets.

3.2.1   Working principle

Acrshortta is based on the change of the absorption properties of a molecule after its excitation. The measurement is a *pump-probe* experiment and requires two temporarily separated pulses: one high energy *pump* beam to excite the sample and one low energy *probe* beam to measure the change in absorption. By changing the time delay between the two pulses, the temporal evolution of the ground and excited states in the system can be monitored.

Transient absorption setup

The principle setup to record transient absorption data is depicted in Figure 3.4. A train of pulsed laser light with a typical wavelength of 800 nm (in the case of Ti:sapphire) and pulse width (typically 80 fs) is split into two portions, hereafter referred to as pump and probe beams. The pump beam is directed into the optical parametric amplifier, where the pulse is spectrally broadened and the desired wavelength amplified, according to the aforementioned method. To cut out unwanted contributions from the fundamental laser mode, a shortpass filter can be used which does not transmit wavelengths higher than the desired pump wavelength. Afterwards, the beam passes a continuously adjustable neutral density filter with which the intensity of the light can be regulated. If the intensity is too high, higher order contributions like exciton-exciton annihilation become dominant and change the dynamics at early times (see Chapter 1). If the intensity is too low, small signal-to-noise ratios make a meaningful data analysis difficult. It is therefore important to find a right balance between the two; typically a signal of the order of 10 mOD is considered optimal. Additionally, changing the intensity allows to study different recombination mechanisms in the system, as the dynamics of bimolecular processes depend on the number of created charges, whereas monomolecular processes, like geminate recombination, do not. After passing the filters, the pump is focussed onto the sample (spot size usually 200 - 500 μm) where it locally excites the film. After it passes the film, the beam is no longer needed and is directed into a beam dump where it is converted into heat.
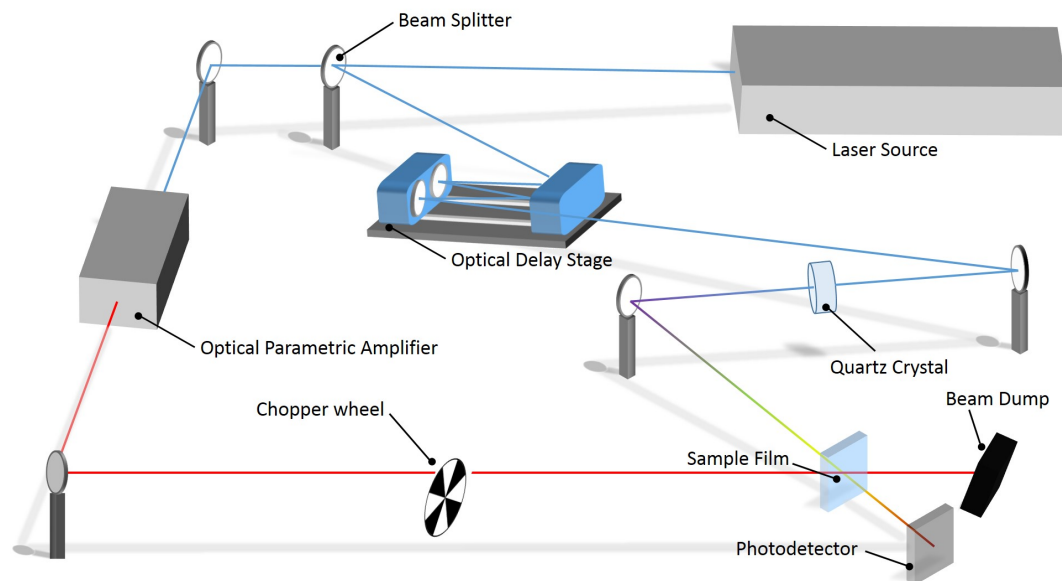
Figure 3.4: TA setup. The short pulses from the laser source are split into two beams, the pump and the probe. The wavelength of the pump beam is changed in the OPA and then modulated and focused onto the sample film. The probe beam passes a mechanical delay stage before it is directed at a quartz crystal, where a white-light continuum (either in the visible or near IR region) is generated. The beam is then focussed onto the sample, where pump and probe beam spatially overlap. The time-correlated absorption of the sample is recorded by a photodiode array.

After separation of the beams, the probe beam passes a mechanical delay stage, consisting of several mirrors on an adjustable stage. Thereby, the optical path of the light is increased stepwise which leads to a temporal delay of the two beams. With typical step sizes of 0.1 μm and length of the delay line of around 60 cm (which corresponds to a light path of 4 times 60 cm, because the light passes the delay stage multiple times), time delays up to 8 ns with a temporal resolution of 0.5 fs can be achieved. The probe beam is then focussed onto a crystal (which may be sapphire, calcium flouride, quartz, etc.) to generate a white-light continuum (see Section 3.1.3). Depending on the crystal and wavelength of the light, a broadband pulse in the visible ($\sim$400 - 800 nm) or in the NIR ($\sim$800 - 1600 nm) region can be generated. This white-light probe beam is then focussed onto the sample where it spatially overlaps with the pump beam with a diameter slightly smaller than the former. The intensity of the probe pulse must be weak so that it does not influence the population of the excited states by an appreciable amount. The sample absorbs part of the beam and the transmitted VIS or NIR light is then collimated and detected by respective photodetector arrays which measure the absorption spectrum. To account for intensity fluctuations, the probe beam is often divided into a *probe* and a *reference* beam, the latter being detected separately which improves the signal quality.

In a dense optical medium, such as the glass substrates of the samples, the group velocity of a light pulse is a function of the frequency. This group velocity dispersion leads to a wavelength-dependent stretch of the pulse and consequently shorter wavelengths arrive at the detector at earlier time delays than higher wavelengths. This *laser chirp* can stretch over several picoseconds and needs to be corrected during data analysis. Additional effects occur when pump and probe pulses interfere in the sample which leads to *coherent artefacts* at early times.[34–36]

Transient absorption data

In the pump path, the train of pulsed light is modulated by a chopper wheel with a typical repetition rate of 0.5 - 2 kHz. When the pump pulse passes through the sample it excites a certain amount of molecules, depending on the intensity and the absorption cross section by means of a vertical Franck-Condon transition. For a fixed time delay, the broadband probe beam, therefore, passes an alternately excited or unexcited sample, and the detector measures the spectral intensities of the pumped and unpumped probe pulse, $I(\lambda)_{pumped}$ and
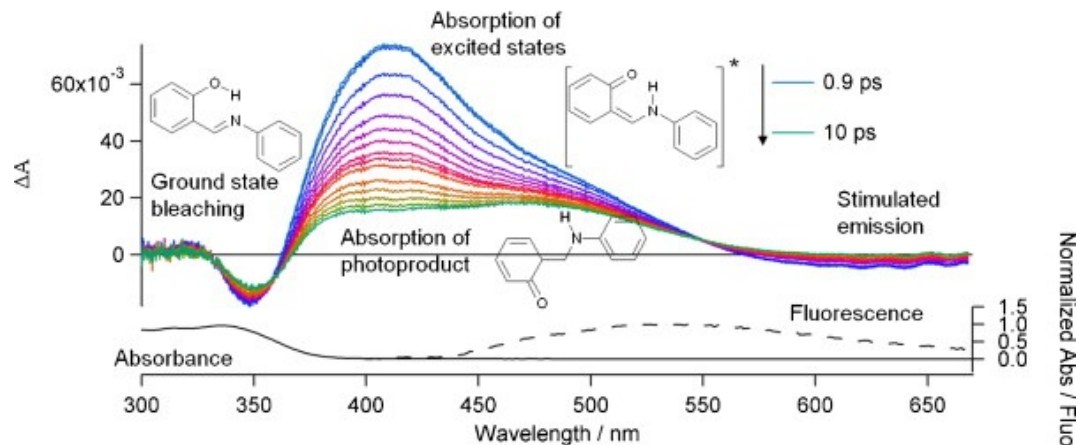
Figure 3.5: Observed contributions in fs-TA. Ultrafast intramolecular proton transfer of salicylidene aniline after 390 nm excitation is taken as example. Depicted are the ground state bleach (GSB), excited state absorption (ESA), and contributions from stimulated emission. Normalised absorption and emission spectra below. Adapted with permission from Ref.[37] Copyright 2012, Elsevier.

$I(\lambda)_{unpumped}$, respectively. These intensities are then used to calculate the absorbance difference

$$\Delta A(\lambda) = -\log\left(\frac{I(\lambda)_{pumped}}{I(\lambda)_{unpumped}}\right) \tag{3.5}$$

Afterwards, the delay line is moved to the next time step and thus a complete two-dimensional dataset $\Delta A(\lambda, t)$ over a broad spectral ($\sim$400 - 1600 nm) and temporal (fs to ns) range is recorded. Usually, some spectra are collected before the pump pulse excites the sample (*time zero*) to determine the baseline. Around time zero the temporal resolution is highest to accurately measure the instrument response function and dynamics at early times; larger time steps are used at later times where less changes are expected.

Processes occurring in the organic materials after light absorption change the optical properties of the excited sample which are measured with this method. Therefore, $\Delta A(\lambda, t)$ contains information of the dynamics of these processes, e.g. exciton generation and decay, CT formation, charge separation, or recombination mechanisms. These processes can be identified by different contributions to the transient spectra (Figure 3.5):

1. *Ground state bleach (GSB).* When the pump pulse reaches the sample,

a fraction of the molecules is promoted to excited states. Consequently, the population of the ground state decreases, and hence the absorption of the ground state is lower in the pumped sample, compared to the unpumped sample. According to Equation 3.5, this leads to a negative signal of ΔA in the region of ground state absorption of the molecules.

2. *Stimulated emission.* When the probe pulse passes through the excited sample, stimulated emission to the ground state occurs for optically allowed transitions. It thus appears in the spectral region of fluorescence of the excited chromophores, i.e. Stokes-shifted with respect to the absorption. Note that stimulated emission scales linearly with the emission frequency, whereas spontaneous emission scales with the cube of the emission frequency; consequently, contributions from stimulated emission are observable at wavelengths longer than the spontaneous emission of the molecules.[37] Since the emitted and the probe photon have the same direction, both are detected and a negative contribution to ΔA is observed. The intensity of the probe pulse is sufficiently low, so that the population of the excited states is not seriously affected.

3. *Excited state absorption (ESA).* After excitation with the pump pulse, optically allowed transitions to even higher lying states exist in some parts of the spectrum. These states are populated by absorption of the probe pulse which adds a positive contribution to ΔA. This also includes absorption of product states, such as triplets or separated charges.

Thus, for every time delay a ΔA spectrum is obtained which contains information about the molecular states in the system. Analysing those spectral traces for all available pump-probe delays allows the experimentalist to identify and determine the dynamics of the different processes. A semi-3D representation of such transient datasets is depicted in Figure 3.5a. Henceforth, a column vector of the matrix ΔA is called *spectrum* at a certain time, whereas a row vector is called *kinetics* at a certain wavelength.

3.2.2   Data analysis

Analysing the datasets is not trivial, as they contain hundreds of thousands of individual points. A general procedure to determine the various processes which occur after light absorption is called global- or target analysis. It is based on the separability of the signal into spectrally independent species with
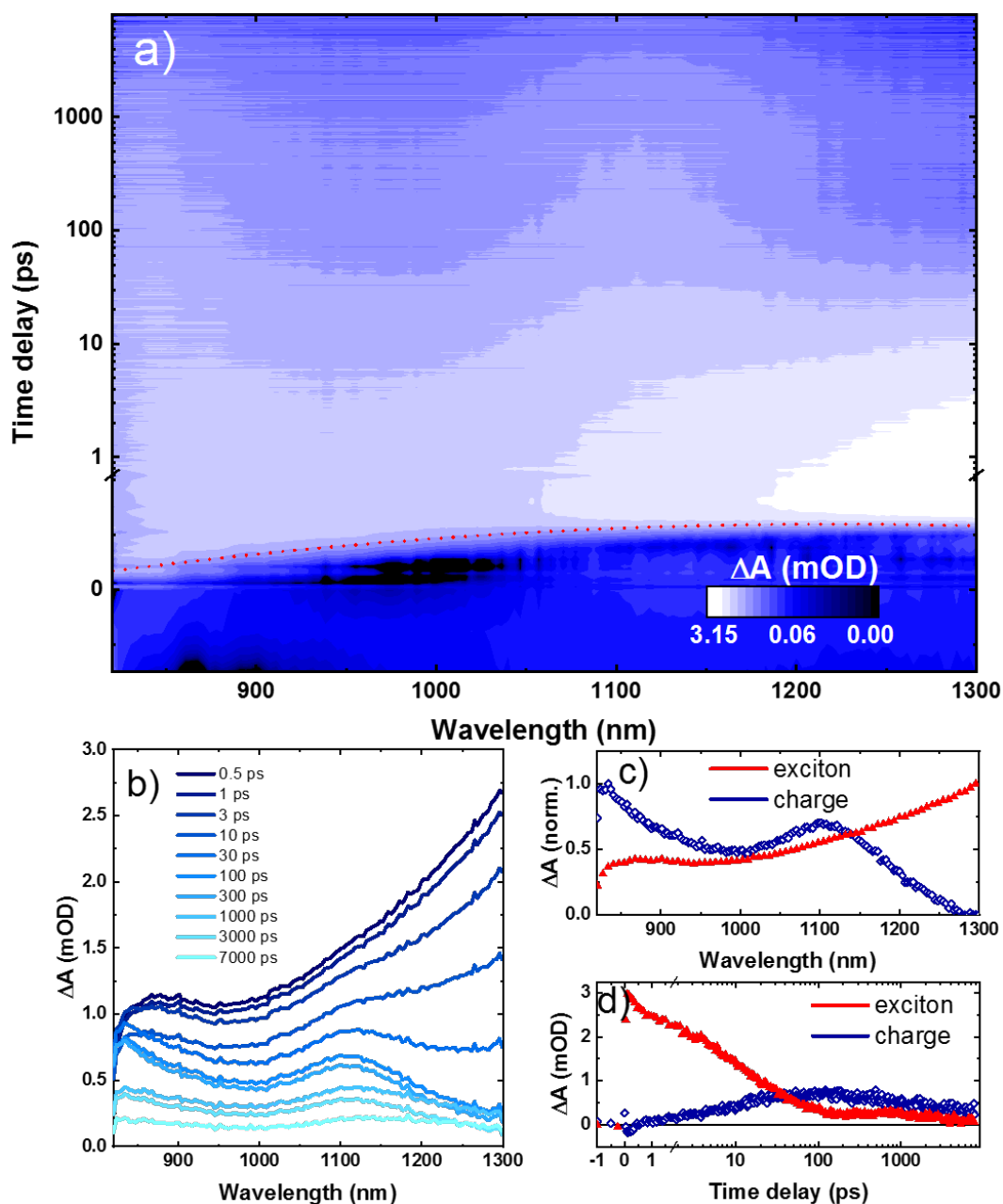
Figure 3.6: Analysis of transient datasets for an example of PffBT4T-2OD. (a) Contour map representation of the dataset. The laser chirp (red dots) is visible at times < 1 ps. (b) Difference spectra at different delay times. The spectra change in time, indicating the formation of another species. (c)+(d) Result of the global analysis with two components; spectra and corresponding kinetics which best fit the dataset.

their evolving concentrations.[37,38] Before such tools can be applied, however, preprocessing of the data is required. During this thesis a powerful engine for the manipulation and analysis of transient absorption datasets has been developed; documentation and source code of the most important functions can be found in Appendix B.

Interpolation

Due to fluctuations of the laser intensity, momentary saturation of the detectors can occur which results in an unusable data point. Those data points are saved as NaN *(Not a Number)* by the used data acquisition software (HELIOS, Ultrafast Systems) and lead to 'holes' in the two dimensional matrix. In order to obtain a continuous dataset, a simple interpolation around these points is performed as a first step of data processing. Thereby, the missing data points are replaced with the mean value of their surrounding neighbours.

Chirp correction

Due to the group velocity dispersion, which was discussed above, the blue part of the spectrum arrives earlier at the detector compared to the longer wavelengths. This leads to a wavelength dependence of time zero, $t_0(\lambda)$, on the sub-picosecond timescale which has to be corrected before any fitting algorithms can be applied. The procedure which was developed here, calculates the maximum of the first derivative of the kinetics for all wavelengths to obtain $t_0(\lambda)$. In the next step a second order polynomial is fitted to the acquired data points, representing an analytical expression of the laser chirp. Finally, the wavelength columns are shifted in time according to the polynomial which results in a dispersion-free dataset. Figure 3.6a shows the laser chirp, indicated by the red dots, which is corrected in the subsequent data analysis.

Baseline correction

To account for the stationary absorption of the molecules, the baseline is subtracted from the entire dataset. Therefore, the mean value of all data points with $t < t_0$ for all wavelengths is calculated and then subtracted from the matrix ΔA.

Singular value decomposition

In order to estimate the rank of ΔA, i.e. the number of independent components needed to describe the data, a singular value decomposition (SVD) is applied.[39] This information can be used to determine the number of different species which evolve during the measurement. Singular value decomposition of the matrix ΔA is written as

$$\Delta A = U \cdot S \cdot V^T \qquad (3.6)$$

where U and V are orthogonal matrices of dimensions $m \times m$ and $n \times n$, respectively, with m being the number of wavelengths columns and n being the number of time rows in ΔA. S is a diagonal $m \times n$ matrix which contains the singular values in descending order. The number of components needed to describe the data can be estimated from the significant singular values of S, i.e. those values clearly different from noise. By projecting the data onto the most significant entries from S, random noise in ΔA can be suppressed.

Global analysis

After the data has been preprocessed as described above, and the number of components has been estimated by SVD or an educated guess, the fitting of the dataset is performed. Approaches based on species associated difference spectra (SADS), are often used and described in detail.[37,38] They assume a homogeneous system which can be modelled with a discrete set of parameters and the separability into individual components weighted by their concentration. However, in many physical systems no precise model of the processes is known a priori, so that a model-free, nonparametric approach is used. One of those approaches is the *genetic algorithm*.[40–42] Here, an implementation developed by S. Gélinas (Optoelectronics group, Cambridge) was used. The time-resolved spectrum ΔA can be estimated in a Beer-Lambert way as a linear superposition of n_{comp} different components

$$\Delta A(t, \lambda) = \sum_{l=1}^{n_{comp}} c_l(t)\epsilon_l(\lambda) \qquad (3.7)$$

where $c_l(t)$ denotes the concentration and $\epsilon_l(\lambda)$ the spectrum of component l. The idea of the genetic algorithm is to start with a population of non-identical species, breed the strongest together and mutate them slightly over time. This allows the populations to evolve towards the best species. This is applied to

TA data analysis by starting with initial guesses of the spectra of different species, e.g. exciton ESA at early times or charge ESA at later times. Then, to build a population, replicas of those spectra are generated and random noise or Gaussians are added to differentiate them. The kinetics that best fit those spectra are calculated, as well as the weighted residuals. This allows to choose the best species (with the lowest residuals) and mix part of their spectra together to generate children, for which this procedure is repeated. After a set number of evolutionary steps, the spectra and corresponding kinetics which best fit the dataset ΔA are chosen.

The results of a exemplary data analysis are shown in Figure 3.6 for the model system of PffBT4T-2OD:PC$_{70}$BM. Panel a shows the contour representation of the ΔA dataset in the NIR before chirp correction. This picture allows a first glance at the processes occurring in the sample. It is often more convenient, however, to look at spectral traces at specific times, as depicted in Panel b. The change of the spectral features from 0.5 ps to 8 ns indicates the formation of other species in time. Panels c and d show the results of the global analysis with two components. The algorithm fitted two spectra and the corresponding kinetics to the dataset which show one species forming instantly after light absorption and a second species evolving on a timescale of 10 - 100 ps. The kinetics indicate the ultrafast formation and subsequent decay of excitons, and the concomitant formation and recombination of free charge carriers in the system which shall be discussed in Chapter 6.

Bibliography

[1] Maiman, T. H. Stimulated optical radiation in Ruby. *Nature* **1960**, *187*, 493–494.

[2] Demaria, A. J.; Stetser, D. A.; Heynau, H. Self mode-locking of lasers with saturable absorbers. *Applied Physics Letters* **1966**, *8*, 174–176.

[3] Mollenauer, L. F.; Mamyshev, P. V.; Gripp, J.; Neubelt, M. J.; Mamysheva, N.; Grüner-Nielsen, L.; Veng, T. Demonstration of massive wavelength-division multiplexing over transoceanic distances by use of dispersion-managed solitons. *Optics Letters* **2000**, *25*, 704.

[4] Holzwarth, R.; Udem, T.; Hänsch, T. W.; Knight, J. C.; Wadsworth, W. J.; Russell, P. S. J. Optical Frequency Synthesizer for Precision Spectroscopy. *Physical Review Letters* **2000**, *85*, 2264–2267.

[5] Jin, J. Dimensional metrology using the optical comb of a mode-locked laser. *Measurement Science and Technology* **2016**, *27*, 022001.

[6] Kymionis, G. D.; Kankariya, V. P.; Plaka, A. D.; Reinstein, D. Z. Femtosecond Laser Technology in Corneal Refractive Surgery: A Review. *Journal of Refractive Surgery* **2012**, *28*, 912–920.

[7] Loesel, F.; Fischer, J.; Götz, M.; Horvath, C.; Juhasz, T.; Noack, F.; Suhm, N.; Bille, J. Non-thermal ablation of neural tissue with femtosecond laser pulses. *Applied Physics B: Lasers and Optics* **1998**, *66*, 121–128.

[8] Liu, X.; Du, D.; Mourou, G. Laser ablation and micromachining with ultrashort laser pulses. *IEEE Journal of Quantum Electronics* **1997**, *33*, 1706–1716.

[9] Lewenstein, M.; Balcou, P.; Ivanov, M. Y.; L'Huillier, A.; Corkum, P. B. Theory of high-harmonic generation by low-frequency laser fields. *Physical Review A* **1994**, *49*, 2117–2132.

[10] Murnane, M. M.; Kapteyn, H. C.; Rosen, M. D.; Falcone, R. W. Ultrafast X-ray pulses from laser-produced plasmas. *Science* **1991**, *251*, 531–536.

[11] Zewail, A. H. Femtochemistry: Atomic-Scale Dynamics of the Chemical Bond Using Ultrafast Lasers (Nobel Lecture). *Angewandte Chemie International Edition* **2000**, *39*, 2586–2631.

[12] Keller, U. Recent developments in compact ultrafast lasers. *Nature* **2003**, *424*, 831–838.

[13] Hargrove, L. E.; Fork, R. L.; Pollack, M. A. Locking of hene laser modes induced by synchronous intracavity modulation. *Applied Physics Letters* **1964**, *5*, 4–5.

[14] Ippen, E.; Shank, C.; Dienes, A. Passive mode locking of the cw dye laser. *Applied Physics Letters* **1972**, *21*, 348–350.

[15] Ell, R.; Morgner, U.; Kärtner, F. X.; Fujimoto, J. G.; Ippen, E. P.; Scheuer, V.; Angelow, G.; Tschudi, T.; Lederer, M. J.; Boiko, A.; Luther-Davies, B. Generation of 5-fs pulses and octave-spanning spectra directly from a Ti:sapphire laser. *Optics Letters* **2001**, *26*, 373.

[16] Paradis, C.; Modsching, N.; Wittwer, V. J.; Deppe, B.; Kränkel, C.; Südmeyer, T. Generation of 35-fs pulses from a Kerr lens mode-locked Yb:Lu_2O_3 thin-disk laser. *Optics Express* **2017**, *25*, 14918.

[17] Brabec, T.; Spielmann, C.; Curley, P. F.; Krausz, F. Kerr lens mode locking. *Optics Letters* **1992**, *17*, 1292.

[18] Gaumnitz, T.; Jain, A.; Pertot, Y.; Huppert, M.; Jordan, I.; Ardana-Lamas, F.; Wörner, H. J. Streaking of 43-attosecond soft-X-ray pulses generated by a passively CEP-stable mid-infrared driver. *Optics Express* **2017**, *25*, 27506.

[19] Tajima, T.; Dawson, J. M. Laser Electron Accelerator. *Physical Review Letters* **1979**, *43*, 267–270.

[20] Chamberlain, W. D. Femtosecond laser-assisted deep anterior lamellar keratoplasty. *Current Opinion in Ophthalmology* **2019**, *30*, 256–263.

[21] Meckel, M.; Comtois, D.; Zeidler, D.; Staudte, A.; Pavicic, D.; Bandulet, H. C.; Pépin, H.; Kieffer, J. C.; Dörner, R.; Villeneuve, D. M.; Corkum, P. B. Laser-induced electron tunneling and diffraction. *Science (New York, N.Y.)* **2008**, *320*, 1478–82.

[22] Bonse, J.; Baudach, S.; Krueger, J.; Kautek, W. Femtosecond laser micro-machining of technical materials. Proceedings of SPIE. 2000; pp 161–172.

[23] Strickland, D.; Mourou, G. Compression of amplified chirped optical pulses. *Optics Communications* **1985**, *55*, 447–449.

[24] Heyl, C. M.; Arnold, C. L.; Couairon, A.; L'Huillier, A. Introduction to macroscopic power scaling principles for high-order harmonic generation. *Journal of Physics B: Atomic, Molecular and Optical Physics* **2017**, *50*, 013001.

[25] Lanin, A. A.; Voronin, A. A.; Fedotov, A. B.; Zheltikov, A. M. Time-domain spectroscopy in the mid-infrared. *Scientific reports* **2014**, *4*, 6670.

[26] Kroll, N. M. Parametric Amplification in Spatially Extended Media and Application to the Design of Tuneable Oscillators at Optical Frequencies. *Physical Review* **1962**, *127*, 1207–1211.

[27] Baumgartner, R.; Byer, R. Optical parametric amplification. *IEEE Journal of Quantum Electronics* **1979**, *15*, 432–444.

[28] Manzoni, C.; Cerullo, G. Design criteria for ultrafast optical parametric amplifiers. *Journal of Optics* **2016**, *18*, 103501.

[29] Arisholm, G.; Paschotta, R.; Südmeyer, T. Limits to the power scalability of high-gain optical parametric amplifiers. *Journal of the Optical Society of America B* **2004**, *21*, 578.

[30] Alfano, R. R.; Shapiro, S. L. Emission in the Region 4000 to 7000 Å Via Four-Photon Coupling in Glass. *Physical Review Letters* **1970**, *24*, 584–587.

[31] Brodeur, A.; Chin, S. L. Ultrafast white-light continuum generation and self-focusing in transparent condensed media. *Journal of the Optical Society of America B* **1999**, *16*, 637.

[32] Goulielmakis, E.; Koehler, S.; Reiter, B.; Schultze, M.; Verhoef, A. J.; Serebryannikov, E. E.; Zheltikov, A. M.; Krausz, F. Ultrabroadband, coherent light source based on self-channeling of few-cycle pulses in helium. *Optics Letters* **2008**, *33*, 1407.

[33] Putnam, W. P.; Keathley, P. D.; Cox, J. A.; Liehl, A.; Leitenstorfer, A.; Kärtner, F. X. Few-cycle, carrier–envelope-phase-stable laser pulses from a compact supercontinuum source. *Journal of the Optical Society of America B* **2019**, *36*, A93.

[34] Dietzek, B.; Pascher, T.; Sundström, V.; Yartsev, A. Appearance of coherent artifact signals in femtosecond transient absorption spectroscopy in dependence on detector design. *Laser Physics Letters* **2007**, *4*, 38–43.

[35] Hamm, P. Coherent effects in femtosecond infrared spectroscopy. *Chemical Physics* **1995**, *200*, 415–429.

[36] Palfrey, S. L.; Heinz, T. F. Coherent interactions in pump–probe absorption measurements: the effect of phase gratings. *Journal of the Optical Society of America B* **1985**, *2*, 674.

[37] Ruckebusch, C.; Sliwa, M.; Pernot, P.; de Juan, A.; Tauler, R. Comprehensive data analysis of femtosecond transient absorption spectra: A review. *Journal of Photochemistry and Photobiology C: Photochemistry Reviews* **2012**, *13*, 1–27.

[38] van Stokkum, I. H.; Larsen, D. S.; van Grondelle, R. Global and target analysis of time-resolved spectra. *Biochimica et Biophysica Acta (BBA) - Bioenergetics* **2004**, *1657*, 82–104.

[39] Blanchet, L.; Ruckebusch, C.; Huvenne, J. P.; de Juan, A. Hybrid hard- and soft-modeling applied to difference spectra. *Chemometrics and Intelligent Laboratory Systems* **2007**, *89*, 26–35.

[40] Keszei, E. In *Handbook of Genetic Algorithms: Model-Free Deconvolution of Transient Signals Using Genetic Algorithms*, hardcover ed.; Munoz, A., Rodriguez, I., Eds.; New York: Nova Science Publishers Inc., 2012; pp 33–52.

[41] Ghannadian, F.; Alford, C.; Shonkwiler, R. Application of random restart to genetic algorithms. *Information Sciences* **1996**, *95*, 81–102.

[42] Fogel, D. B. Asymptotic convergence properties of genetic algorithms and evolutionary programming: analysis and experiments. *Cybernetics and Systems* **1994**, *25*, 389–407.

Part III

Materials and Methods

Chapter 4

Fabrication of films and devices

In this chapter the fabrication of films and devices is explained. Detailed information on the investigated materials are shown in Table 4.1 and the molecular structures can be found in Figure 4.2. A brief description of the experimental methods is given in the next chapter.

The fabrication of films and devices was, unless otherwise noted, carried out in a nitrogen-filled glovebox with minimal oxygen and humidity levels ($O_2 < 3$ ppm, $H_2O < 2$ ppm). Deposition of thin films was performed by spin coating, a technique in which the organic materials are dissolved in suitable solvents and then dispensed onto the rotating substrate. During the rotation the solvent evaporates, leaving a film of thickness $d \sim c/\sqrt{\Omega}$, where c is the concentration of the dissolved material and Ω the rotational speed of the substrate. Spin coating was performed statically (film covered with solution before rotation) and dynamically (solution dispensed on the rotating substrate). To eliminate residual solvent in the layer and to promote crystallisation of the films, the substrates were annealed on a hotplate after film deposition. Organic solar cells (OSCs) were fabricated in standard and inverted architectures which are depicted along with the structure of the bottom-gate top-contact organic field effect transistors (OFETs) in Figure 4.1. For films, unless otherwise noted, the active layer was directly deposited onto the substrate, without any additional layers.

4.1 Substrates

The solar cells were fabricated on pre-cut sodalime glass substrates patterned with indium tin oxide (ITO), bought from PsiOTec Ltd. with a sheet resistance
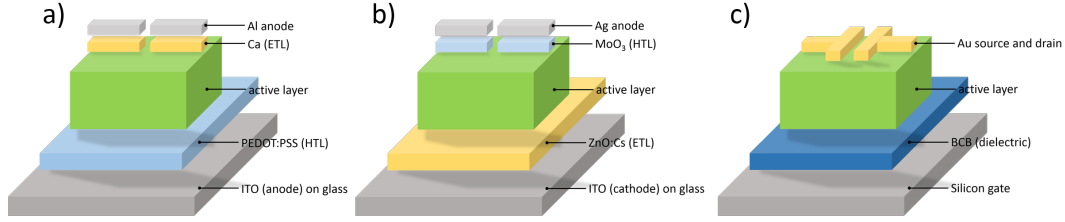
Figure 4.1: (a) Standard architecture device with PEDOT:PSS as HTL and Ca as ETL. ITO and Al serve as anode and cathode. (b) Inverted architecture device with ZnO:Cs as ETL and MoO_3 as HTL. ITO and Ag serve as anode and cathode. (c) OFET with highly-doped silicon as gate, BCB as gate dielectric, and Au as source and drain contacts.

of 15 Ωsq^{-1}. The single substrates were 12×12 mm^2 in size, with the ITO stripe (7×12 mm^2) positioned centrally. For the field-effect transistors highly doped silicon substrates were cut from a wafer (Active Business Company) in the same dimensions. The wafer was covered with a 250 nm thick layer of insulating thermal silicon oxide. For PDS measurements, high-purity fused-silica substrates (*Spectrosil*, UQG Optics) with a diameter of 12 mm were used, exhibiting high transmission in the UV. Films were prepared on microscope slides (Thermo Scientific) which were cut into the required size.

4.2   Cleaning

In a first step the samples were rinsed with acetone to remove dust and any protective layers on the substrates. Next, the substrates were loaded onto a self-made Teflon sample holder and submerged in a glass beaker filled with acetone for sonication in a water bath for 5 minutes. This step was repeated with isopropanol; afterwards the substrates were dried using a nitrogen gun and covered in a clean Petri dish. Following sonication, the samples were transferred to an oxygen plasma cleaner (Atto, Diener electronic) for surface treatment with an oxygen plasma (0.5 bar, 100 W) for 10 minutes.

4.3 Transport layer

4.3.1 Standard architecture

Standard architecture devices use PEDOT:PSS as hole transport/electron blocking layer (HTL), which is well studied and regularly employed as extraction layer in organic solar cells. The solution was briefly sonicated and filtered through a 0.45 μm PVDF filter, before spin coating (static) at 4000 rotations per minute (rpm) for 45 s and annealing at 140°C for 30 min on a hotplate. This step was performed outside the glovebox.

4.3.2 Inverted architecture

For inverted architecture solar cells, a 50 nm layer of two percent caesium-doped zinc oxide (ZnO:Cs) was deposited onto the cleaned substrates. ZnO is a commonly used electron transport/hole blocking layer (ETL) for inverted solar cells. Doping the layer with caesium leads to enhanced performance due to passivation of trap states at the metal oxide surface.[1–3] The layer was spin coated from solution (60 s at 2000 rpm, followed by 5 s at 4000 rpm, static), which was prepared from zinc acetate di-hydrate, caesium carbonate, monoethanolamine, and 2-methoxyethanol, following procedures which are described elsewhere.[1–3] After deposition of the ZnO:Cs layer, the films were annealed at 300°C for 30 min before being transferred to the glovebox.

The fabrication of ZnO nanoparticles dissolved in methanol, which are used in Chapter 6, followed the master's thesis of B. Rivkin.[4] A film was obtained from a filtered 10 mg ml^{-1} solution which was spin coated at 2500 rpm for 45 s. This step was repeated 3 times to yield a 45 nm thick layer after annealing at 80°C on a hotplate for some minutes.

4.3.3 Field-effect transistors

Field-effect transistors were directly transferred into the glovebox after the cleaning of the Si-substrates. A 40 nm thick layer of bisbenzocyclobutene (BCB) (provided by Michael Töpper, Fraunhofer IZM, Berlin), serving as the dielectric layer between gate contact and active layer, was filtered through a 0.45 μm HPLC syringe filter with PTFE membrane (Cronus, Altmann Analytik GmbH) and spin coated (500 rpm for 3 s and 5000 rpm for 60 s, dynamic) from a mesitylene-diluted solution (1:7). Afterwards the films were annealed at 290°C for 5 min.

4.4 Active layer

4.4.1 PffBT4T-2OD

The active layer solution for PffBT4T-2OD films and devices was prepared by combining the polymer PffBT4T-2OD and the fullerene $PC_{70}BM$ with concentrations of 16 and 19.2 mg ml^{-1}, respectively. The materials were dissolved in a chlorobenzene:di-chlorobenzene (1:1 volume ratio) mixture to which 3 vol.% DIO was added. The solution was heated on a hotplate inside the glovebox at 90°C for at least 3 hours until the organics were completely dissolved. After transfer to the glovebox, the substrates were pre-heated on a hotplate at 90°C. For layer deposition by dynamic spin coating (800 rpm for 45 s and 2000 rpm for 3 s) a plastic chuck was used to avoid cooling of the substrates which resulted in uniform films of 300 nm thickness. After the spin coating step, the substrates were directly placed on a hotplate and annealed for 5 min at 80°C. Polymer-only and fullerene-only films were prepared similarly with a concentration of 32 mg ml^{-1} and 38.4 mg ml^{-1}, respectively, yielding films of 420 nm and 170 nm thickness.

4.4.2 DRCN5T

The precursor solution for small molecule (SM) films and devices was prepared by dissolving 15 mg ml^{-1} DRCN5T and 12.4 mg ml^{-1} $PC_{70}BM$ in chloroform. The films were spin coated dynamically for 20 s at 1700 rpm and 5 s at 2500 rpm using a metallic chuck which yielded ∼50 nm thin films. Directly after layer deposition, the substrates were put onto a hotplate for thermal annealing at 120°C for 10 min. A second solvent vapour annealing step has proven to be beneficial for layer morphology.[5,6] Thus, after thermal treatment on the hotplate, the substrates were placed in a covered Petri dish for 60 s to which 150 μl of chloroform were added. SM-only and fullerene-only films were prepared similarly with a concentration of 30 mg ml^{-1} and 25 mg ml^{-1}, respectively, which yielded films of 340 nm and 115 nm thickness.

For all-SM devices in Chapter 8, the non-fullerene acceptor IDIC is blended with DRCN5T with concentrations of 15 mg ml^{-1}:15 mg ml^{-1}. The other processing steps are similar. Additionally, a ternary device was tested in the configuration PBDB-T-2Cl:DRCN5T:$PC_{70}BM$ with corresponding ratios of 30:20:50. The PBDB-T-2Cl solution (15 mg ml^{-1} each, in chlorobenzene) was prepared by J. Butscher, details will be found in his master's thesis.

4.5 Metal electrodes

The last step in the device fabrication is the evaporation of metal oxide extraction layers and contacts. Therefore, the samples are loaded into a thermal evaporation chamber (MICO, tectra GmbH) in which the metals are evaporated with slow rates (< 0.04 nm s^{-1}) and under high vacuum ($\approx 10^{-6}$ mbar) through a shadow mask onto the substrates. To ensure uniform coverage, the substrates were rotating during the evaporation process. This resulted in 8 solar cells ('pixels') on a single substrate, each with a device area of 4.5 mm^2.

Standard architecture PffBT4T-2OD:PC$_{70}$BM devices were fabricated with 17 nm Ca serving as ETL and 80 nm Al as the electrode. Inverted architecture PffBT4T-2OD:PC$_{70}$BM solar cells were fabricated with 17 nm MoO$_3$ as HTL and 80 nm of Ag as contacting electrode. For devices containing DRCN5T 10 nm MoO$_3$ was used as HTL instead, before evaporating 80 nm Ag. Source and drain contacts for the field-effect transistors were made from 60 nm Au.

4.6 Encapsulation

Depending on the experiment, films and devices were encapsulated with epoxy 2-component glue (UHU) and precut glass substrates (PsiOTec Ltd.) in the glovebox. The samples were kept in the glovebox overnight to ensure the glue hardened.

Material	Full name	Company
PffBT4T-2OD (PCE-11)	poly[(5,6-difluoro-2,1,3-benzothiadiazol-4,7-diyl)-alt-(3,3"'-di(2-octyldodecyl)-2,2',5',2",5",2"'-quaterthiophen-5,5"'-diyl)]	1-Material
DRCN5T	2,2'-[(3,3"',3"",4'-tetraoctyl [2,2':5',2":5",2"':5"',2""-quinquethiophene]-5,5""-diyl)bis[(Z)-methylidyne(3-ethyl-4-oxo-5,2-thiazolidinediylidene)]]bis-propanedinitrile	Ossila
PTB7	poly[[4,8-bis[(2-ethylhexyl)oxy]benzo[1,2-b:4,5-b']dithiophene-2,6-diyl][3-fluoro-2-[(2-ethylhexyl)carbonyl]thieno[3,4-b]thiophenediyl]]	Ossila
PBDB-T-2Cl (PCE-14)	Poly[(2,6-(4,8-bis(5-(2-ethylhexyl-3-chloro)thiophen-2-yl)-benzo[1,2-b:4,5-b']dithiophene))-alt-(5,5-(1',3'-di-2-thienyl-5',7'-bis(2-ethylhexyl)benzo[1',2'-c:4',5'-c']dithiophene-4,8-dione)]	Ossila
$PC_{70}BM$	[6,6]-phenyl C71-butyric acid methyl ester	Ossila
IDIC	2,2'-((2Z,2'Z)-((4,4,9,9-tetrahexyl-4,9-dihydro-s-indaceno[1,2-b:5,6-b']dithiophene-2,7-diyl)bis(methanylylidene))bis(3-oxo-2,3-dihydro-1H-indene-2,1-diylidene))dimalononitrile	1-Material
ZAD	zinc acetat dihydrate	Sigma-Aldrich
Cs_2CO_3	caesium carbonate	Sigma-Aldrich
PEDOT:PSS	poly(3,4-ethylenedioxythiophene):poly(styrenesulfonate)	Heraeus
Solvent	**Full name**	**Company**
CF	chloroform	Sigma-Aldrich
CB	chlorobenzene	Sigma-Aldrich
DCB	1,2-dichlorobenzene	Sigma-Aldrich
DIO	1,8-diiodooctane	Sigma-Aldrich
MEA	monoethanolamine	Sigma-Aldrich
2-ME	2-methoxyethanol	Sigma-Aldrich

Table 4.1: Materials and solvents used in this thesis.
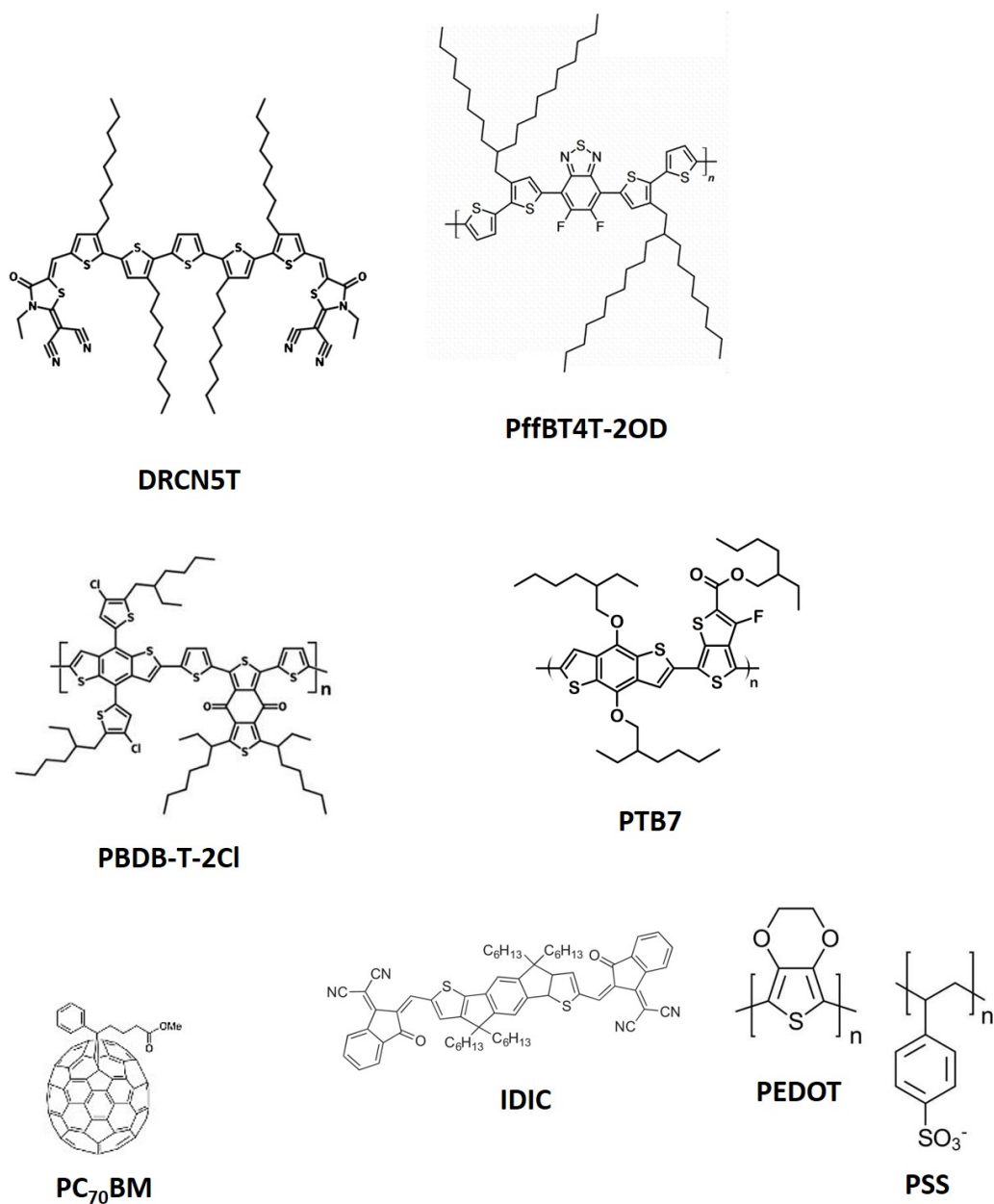
Figure 4.2: Molecular structures of the used materials. Courtesy Osilla Ltd. IDIC reproduced with permission from Ref.[7] Copyright 2017, Elsevier.

Bibliography

[1] Sevinchan, Y.; Hopkinson, P. E.; Bakulin, A. A.; Herz, J.; Motzkus, M.; Vaynzof, Y. Improving Charge Separation across a Hybrid Oxide/Polymer Interface by Cs Doping of the Metal Oxide. *Advanced Materials Interfaces* **2016**, *3*, 1500616.

[2] Hofstetter, Y. J.; Hopkinson, P. E.; Bakulin, A. A.; Vaynzof, Y. Simultaneous enhancement in open circuit voltage and short circuit current of hybrid organic–inorganic photovoltaics by inorganic interfacial modification. *J. Mater. Chem. C* **2016**, *4*, 1111–1116.

[3] Hinzmann, C.; Magen, O.; Hofstetter, Y. J.; Hopkinson, P. E.; Tessler, N.; Vaynzof, Y. Effect of Injection Layer Sub-Bandgap States on Electron Injection in Organic Light-Emitting Diodes. *ACS Applied Materials & Interfaces* **2017**, *9*, 6220–6227.

[4] Rivkin, B. Semiconducting nanoparticles for hybrid electronic devices. master thesis, Universität Heidelberg, 2017.

[5] Long, G. et al. New Insights into the Correlation between Morphology, Excited State Dynamics, and Device Performance of Small Molecule Organic Solar Cells. *Advanced Energy Materials* **2016**, *6*, 1600961.

[6] Kan, B. et al. A Series of Simple Oligomer-like Small Molecules Based on Oligothiophenes for Solution-Processed Solar Cells with High Efficiency. *Journal of the American Chemical Society* **2015**, *137*, 3886–3893.

[7] Vogelbaum, H. S.; Sauvé, G. Recently developed high-efficiency organic photoactive materials for printable photovoltaic cells: a mini review. *Synthetic Metals* **2017**, *223*, 107–121.

Chapter 5

Methods

In this chapter a brief description of the techniques which are used to characterise the films and devices is given. This includes electrical and optical, steady-state and time-resolved methods as well as experimental details of the sample degradation.

5.1 JV - measurements

Characterisation of the solar cell performance was carried out under standard AM 1.5 G illuminating conditions which specify solar radiation passing through 1.5x earth's atmosphere, representing an integrated power of 100mW cm^{-2} (1 sun). As light source an Abet Technologies SunLite™class A solar simulator with a 100 W Xe arc lamp was used. Its intensity was adjusted using a reference Si cell (NIST traceable, VLSI) to compensate for the spectral mismatch between the simulator output and the response from the measured solar cells.

The current density-voltage (J-V) measurements were performed using a Keithley 2450 source measure unit (SMU) which was controlled by a Labview program written by P. Hopkinson. The current output of the solar cells was measured while linearly sweeping the applied voltage from -1 V to +1 V in steps of 0.05 V. A self-built Arduino-based multiplexer provided the logic to measure different solar cells on several substrates in the sample holder (see Section 5.3) individually.

Figure 5.1:   Cut-away view of the Xenon arc lamp solar simulator used to measure characteristics of solar cells and OFETs. Courtesy Newport Cooperation.[1]
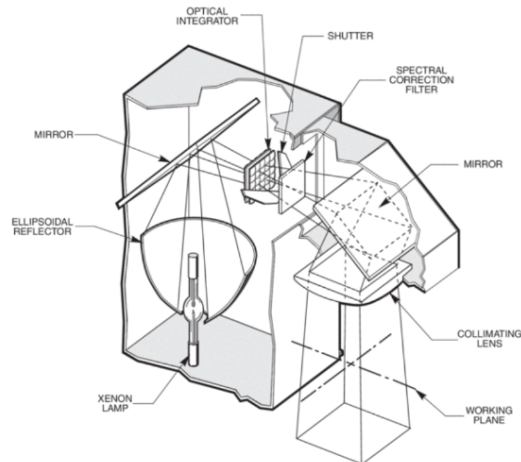
5.2   External quantum efficiency

The external quantum efficiency (EQE) is given by the number of extracted charge pairs per incident photon on the device. Measuring the EQE over a broad range of wavelengths thus gives valuable information about absorption, charge generation, transport, and extraction of charge carriers (see Chapter 1 for details).

Figure 5.2 depicts the setup, which was used to measure the EQEs throughout this thesis. A halogen lamp (Newport/Oriel Simplicity Series QTH 250 W) provided a broad spectrum in the visible range. The light exited the lamp housing through a filter wheel (Newport/Oriel), which removed harmonic wavelengths, into a software-controlled monochromator (Oriel Cornerstone 130), equipped with a grating (320 - 1070 nm, Newport). A beamsplitter (Thorlabs EBP1) directed 30% of the light onto a reference Si-diode (Thorlabs PDA36A) which provided a current that was converted to the number of photons incident on the device. The remaining light was focussed onto the solar cell with the incident light spot being smaller than the device area). The resulting photocurrent was measured by a Keithleigh 2450 SMU; a Labview program by P. Hopkinson calculated the EQE from the number of photons measured by the reference diode and the generated current measured by the SMU for each wavelength.
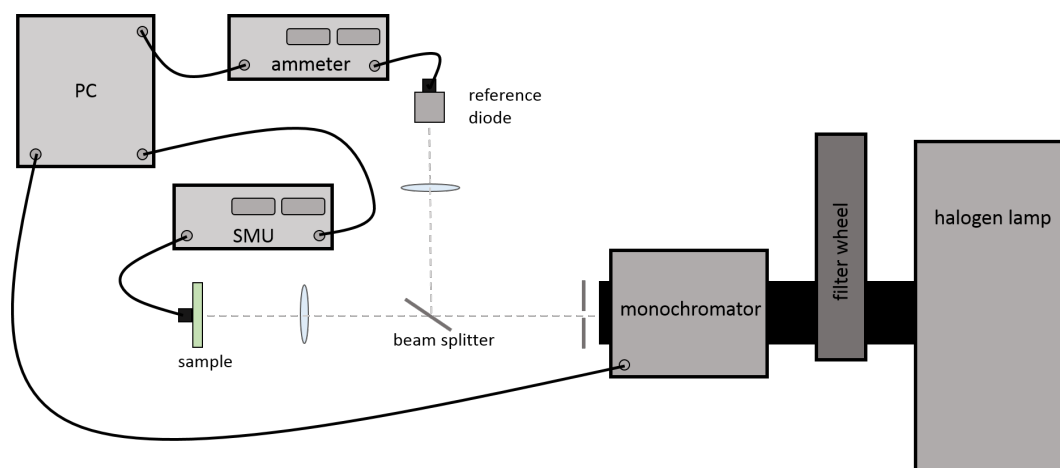
Figure 5.2: Setup used to measure the EQE of solar cells. Monochromated light is measured by a reference diode and focussed on the device area. The resulting current is measured by a SMU. A Labview program calculates the EQE from the incident photons and the extracted charge pairs for each wavelength. Adapted from Ref.[2]

5.3 Degradation rig and sample holder

For degradation of films and devices in a controlled environment, a specially designed sample holder was built (Figure 5.3a). It can hold up to 4 films/devices which are illuminated through a glass window and can be measured individually. The sample holder seals the films/devices from the outside environment; two gas connectors allow for a steady flow of a predefined atmosphere.

The environmental rig, designed in the course of our previous work,[3] is schematically depicted in Figure 5.3b. It allows for the precise control of the atmosphere by adding oxygen (99.99%) to the steady flow of ultrapure nitrogen (99.999%). A second circuit enables the control of relative humidity by adding the flow of nitrogen through a water filled bubbler. The oxygen and humidity content can thus be seamlessly controlled; the adjusted values remain stable over long-term experiments (see the aforementioned master's thesis for details).[3] The concentrations of oxygen and humidity are constantly measured (Cambridge Sensotec 2100 and EasyDew humidity, Michell instruments), while the temperature is determined by a Type K thermocouple.
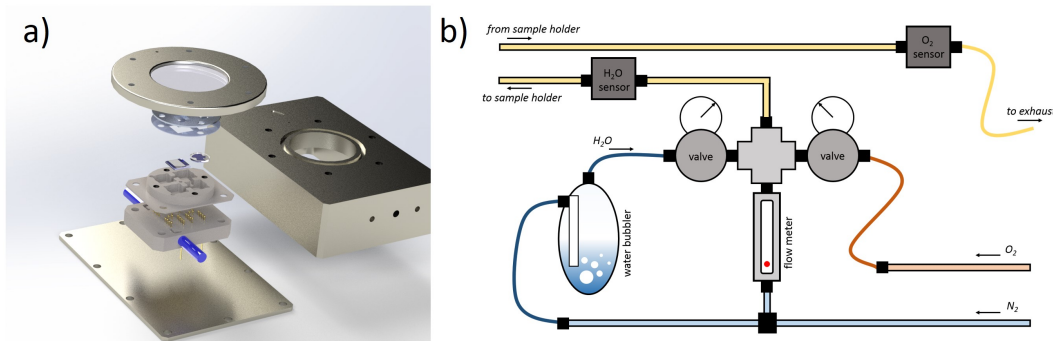
Figure 5.3: (a) Illustrative view of the sample holder. Courtesy T. Weu. (b) Schematic illustration of the environmental control. Nitrogen and oxygen are provided by gas bottles (200 bar, controlled by pressure regulators to ∼1 bar).

5.4   Transient absorption spectroscopy

Transient absorption spectroscopy (TA) measurements are used to investigate the dynamics of excitons and charge carriers on the fs - ns timescale. For details on the working principle see Chapter 3. The TA results in Chapter 6 have been obtained at the Imperial College in London, all other measurements were performed in Heidelberg.

In the London setup, seed pulses (800 nm, <100 fs) were generated at a repetition rate of 1 kHz by a Ti:sapphire regenerative amplifier (Spectra-Physics Solstice, Newport Corporation), and routed toward an optical parametric amplifier (TOPAS, Light Conversion) coupled to a frequency mixer (NIRUVis, Light Conversion) to provide the 700 nm pump. The seed pulses were also routed toward a mechanical delay stage and then directed to a commercially available femtosecond transient absorption spectrometer (HELIOS, Ultrafast Systems) to record spectra up to 6.5 ns, with an average 200 fs instrument response function. Therein, the pump (modulated at 500 Hz) and the broad-band near-infrared (∼850 - 1350 nm) probe were focused onto a ∼0.5 mm^2 spot on the sample, which was housed in a glass cuvette purged with nitrogen gas during the measurements. To ensure no additional degradation took place during the TA measurements, after the samples were degraded under a controlled environment, they were encapsulated prior to TA measurements. Additionally, the data from 10 independent scans throughout the experiment were compared, and no differences were observed.

In the Heidelberg setup, seed pulses (800 nm, <100 fs) were generated at

a repetition rate of 4 kHz by a Ti:Sapphire regenerative amplifier (Coherent Astrella), and routed towards an optical parametric amplifier (TOPAS Prime, Light Conversion) to provide the pump. The seed pulses were directed to a commercially available femtosecond transient absorption spectrometer (HE-LIOS, Ultrafast Systems), wherein a mechanical delay stage is included. The pump (modulated at 2 kHz) and the broadband near-infrared ($\sim$800-1450 nm) probe were focused onto a $\sim$0.1 mm^2 spot on the sample.

Analyses were executed in a MATLAB program which was developed during this thesis. Documentation and source code can be found in Appendix B. Fitting of the kinetic traces was performed with XYYCalc (Foppe de Haan, University of Groningen) which fits the data with a convolution of a Gaussian (instrument response of the setup) and exponential functions for ingrowing and decaying components, according to

$$F(x) = \int_{-\infty}^{+\infty} \frac{\exp\left(-\dfrac{t^2}{2\sigma^2}\right)}{\sigma\sqrt{2\pi}} \left[\sum_{i=1}^{NrDecExps} A_i e^{-((x-x_0)-t)/\tau_i} \right.$$
$$\left. + \sum_{j=1}^{NrIngrExps} A_j \left(1 - e^{-((x-x_0)-t)/\tau_j}\right) \right] dt + Base$$

where σ is the standard deviation of a normal distribution, $NrDecExps$ the number of decaying components, $NrIngrExps$ the number of ingrowing components, τ_i and τ_j the corresponding lifetimes, and $Base$ the baseline.

5.5 Pump-push photocurrent

Pump-push photocurrent (PPPC) measurements are used to study the dynamics of bound states in OPV devices. A visible pump pulse excites the system, creating bound excitons which diffuse to a donor:acceptor interface where they form intermolecular charge pairs (CT states). Those bound species can be dissociated by a time-delayed, modulated IR push pulse which leads to the creation of free charges and thus to a push-induced increase in the photocurrent, measured by a lock-in amplifier. The technique is depicted in Figure 5.4, further information can be found elsewhere.[4] The measurements in this thesis were performed at the Imperial College, London.

A 4 kHz Ti:sapphire regenerative amplifier (Astrella, Coherent) was used to seed two optical parametric amplifiers (TOPAS-Prime, Coherent) with 800
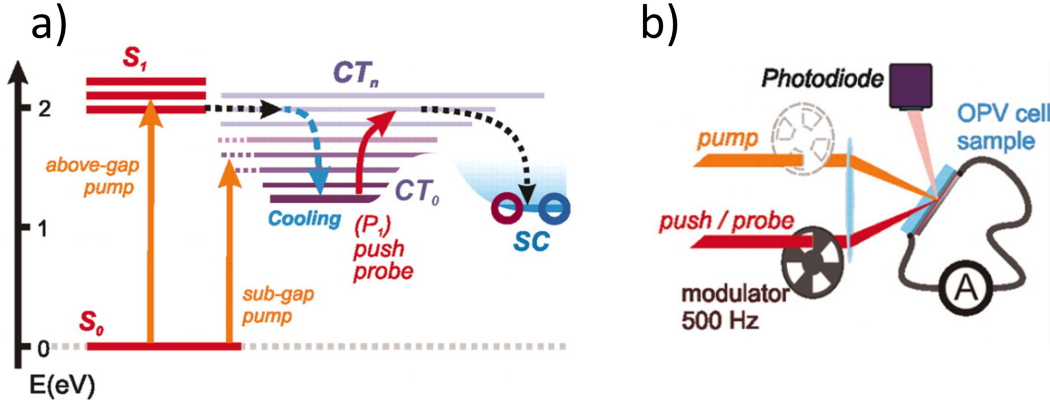
Figure 5.4: (a) Principle of PPPC, showing pump-induced formation of bound states and push-induced separation of the latter into free charges. (b) The resulting push-induced photocurrent is measured by a lock-in amplifier coupled to a mechanical chopper which modulates the pump pulses. Adapted with permission from Ref.[4] Copyright 2012, American Association for the Advancement of Science.

nm, $\sim$35 fs pulses. The 1300 nm signal output of TOPAS 1 was converted to a 650 nm pump by second harmonic generation in a β-barium borate crystal and then directed toward a mechanical delay stage. The 1300 nm signal output of TOPAS 2, modulated by an optical chopper at $\sim$1.2 kHz, was used as the push. The pump (<1 μJ cm^{-2}) and push (<0.1 μJ cm^{-2}) were focused onto a $\sim$0.5 mm^2 spot on the device. A lock-in amplifier (SR-830, Stanford Research Systems), synchronized to the modulation frequency of the pump (4 kHz) and push ($\sim$1.2 kHz), recorded the photocurrent output of the pixel attributed to each beam.

5.6 Absorption spectra

To measure the absorption spectrum of films, light between $\sim$200 - 1200 nm was monochromated (through a grating) and focussed onto the sample. A photosensitive detector recorded the transmitted light I_t behind the film to determine the absorbance A

$$A = \log\left(\frac{I_0}{I_t}\right) \tag{5.1}$$
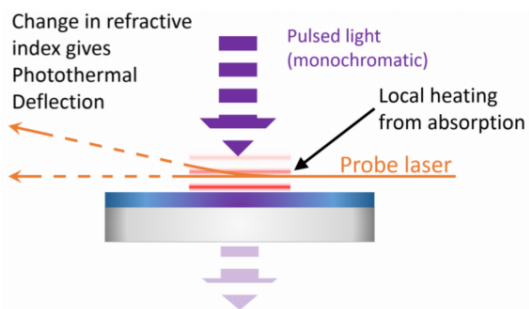
Figure 5.5: Working principle of PDS. Pulsed light is absorbed by the sample film. The resulting heat gradient causes a gradient in refractive index which deflects a probe laser parallel to the surface. The modulated deflection is measured by a photodiode. Figure courtesy of P. Hopkinson.

The sensitivity of the system is limited, thus, the measured spectra were mostly used to determine the optical bandgap of the systems, and to compare the spectral changes of pristine and degraded films qualitatively. The absorption of films was measured at room temperature with a JASCO UV–vis V670 spectrometer.

5.7 Photothermal deflection spectroscopy

Photothermal deflection spectroscopy (PDS) is a pump-probe technique used to measure the optical absorption of thin films with high sensitivity. It is based on the change of the local refractive index caused by heating of the film after light has been absorbed. With this technique optically active states within the bandgap can be measured. The system that was used in this thesis is described in detail elsewhere;[5] a schematic drawing is depicted in Figure 5.5. Pulsed, monochromated light (from a 150 W xenon short arc lamp with a Cornerstone monochromator) is focussed onto the sample that absorbs the photons which are partially converted into heat. This heat, radiating from the surface of the film, results in a temperature gradient in the perflourocarbon (Fluorinert FC-770) solution surrounding the sample. The gradient in temperature, on the other hand, leads to a gradient of refractive index which deflects a laser beam (633 nm He-Ne laser from REO) parallel to the surface. This modulated deflection is measured by a position-sensitive detector (Thorlabs, PDP90A) connected to a lock-in amplifier (Amatec SR7230). Thus, the absorption a of the film is proportional to the deflection angle ϕ and the intensity of the absorbed light I_0 via $a(\lambda) \sim \phi/I_0$. The PDS measurements in this thesis were performed by D. Becker-Koch.

5.8   Photoluminescence

To measure the emission spectra of the samples, the films are illuminated with a laser to excite optical transitions in the materials. The excited states quickly relax to the lowest unoccupied molecular orbitals (according to Kasha's rule[6]) and spontaneously recombine to the ground state which results in the emission of photons of higher wavelengths (Stokes shift). The measurements of the photoluminescence (PL) were carried out at Heidelberg University and at the Imperial College London (only for the results in Chapter 6).

In the Heidelberg setup, spectra were collected following excitation with a 447 nm diode laser (Dragon Lasers), with a power density of approximately 3 mW cm^{-1}. The intensity of both the laser and the PL were measured with a fibre coupled scientific spectrometer equipped with thermoelectric cooling (QE65000, Ocean Optics). The spectral response of the fibre and spectrometer was calibrated with a NIST traceable calibration light source (HL-2000-CAL-EXT, Ocean Optics). A Labview program from P. Hopkinson was used for data acquisition. For measurements of complete devices, the laser spot ($\sim$1 mm^2) could be focussed onto the solar cell pixel or between the pixels for film measurements.

PL spectra of the films and devices in London were obtained using a Fluorolog-3 spectrofluorometer (Jobin Yvon, HORIBA). The excitation source was set to 600 nm, and the spectra were collected between 650 and 850 nm with an integration time of 0.2 s. Both the excitation and emission slit widths were 10 nm. A 665 nm long-pass filter was used to remove scattering contributions from the excitation light. For measurements of complete solar cells, a mask with a 1$\times$1 mm^2 window was secured to the films and devices, allowing the pixels or space between pixels to be targeted in the latter case. Individual pixels were connected to a circuit outside the instrument in the short-circuit configuration. Measurements in London were performed by T. Hopper.

5.9   Time-correlated single photon counting

Time-correlated single photon counting (TCSPC) is used to determine the lifetime of excited emitting states. The PL decay in polymer solar cells contains information about exciton diffusion and/or charge transfer states. Figure 5.6 shows the working principle of this method: a pulsed LED creates short, monochromatic light pulses which are focussed onto a sample film that is absorbing the light. Depending on the processes involved, part of the absorbed
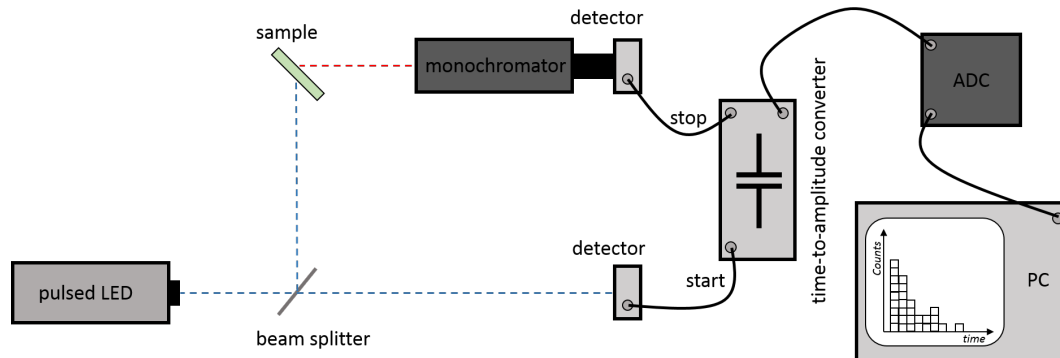
Figure 5.6: TCSPC setup used to measure the PL decay of films. A pulsed LED excites a sample film, which emits PL light after the excited states return radiatively to the ground state. The time difference between excitation and emission is recorded by a time-to-amplitude converter.

photons are spontaneously re-emitted at higher wavelengths (due to Stokes shift) after some time. The desired wavelength and corresponding bandwidth are chosen in a monochromator before the PL is amplified and measured by a detector. The signal from the pulsed LED starts the charging of a capacitor in a time-to-amplitude converter and the signal from the detected PL discharges the capacitor. The measured voltage is thus proportional to the time difference between the two signals which is converted to a digital signal in an analogue-to-digital (ADC) converter. The measurement software collects the determined lifetimes and arranges them in a histogram.

The measurements in Chapter 6 were performed on both films and devices using a DeltaFlex TCSPC instrument (Jobin Yvon IBH, HORIBA) equipped with a NanoLED excitation source (λ_{ex} = 635 nm, intensity ~1 mW cm^{-2}, <200 ps pulse duration, 1 MHz repetition rate). A mask with a ~1×1 mm^2 window was secured to the top face of the devices to selectively illuminate a particular pixel or the space between pixels. Individual pixels were connected to a circuit outside of the instrument in the short-circuit configuration. The devices were oriented in the instrument to maximize collection of the photoluminescence by the detection module, consisting of a monochromator (λ_{det} = 735 nm, 32 nm bandpass) coupled to an air-cooled detector. A 665 nm long-pass filter was placed in front of the detection module to eliminate the scattering contribution from the excitation light. The instrument response function (IRF) was obtained by measuring the scattered excitation light. All

measurements were acquired until a peak of 10,000 counts was attained. The decay curves were fitted using a mono- or biexponential decay convoluted with a Gaussian function. The calculated lifetimes reported herein are representative of measurements on at least three different pixels. Measurements in London were performed by T. Hopper.

5.10   Photoelectron emission spectroscopy

Both X-ray photoelectron spectroscopy (XPS) and ultra-violet photoelectron spectroscopy (UPS) are surface sensitive techniques that are based on the photoelectric effect (Figure 5.7). XPS uses X-ray illumination which is absorbed by core level electrons. The binding energies of the electrons is material specific, therefore, detection of the photoelectrons yields information about the chemical composition of the samples. UPS uses UV light which is used to probe the electrons in the valence band. Measuring the onset of the valence band and the photoemission onset caused by inelastically scattered (secondary) electrons allows to determine the work function and ionisation potential of the material.

The measurements were performed in an ESCALAB 250Xi from ThermoFisher in ultra-high vacuum (10^{-10} mbar). XPS used an XR6 monochromated Al K_α X-ray source ($h\nu = 1486.6$ eV) with a pass energy of -10 V and a 650 mm spot size. Due to the inelastic mean free path of the photoelectrons excited with this energy, XPS probes the top $\sim$10 nm of the samples. UPS was performed using a double differentially pumped He discharge lamp ($h\nu = 21.22$ eV) with a pass energy of 2 eV and a bias of -5 V. Due to the lower excitation energy, UPS probes the top $\sim$2 nm of the layers. To measure material properties in the bulk, Argon clusters with a kinetic energy of 4000 eV were used to etch the organic material in a controlled and damage-free way. Details can be found elsewhere.[7] The XPS and UPS measurements in this thesis were performed by V. Lami.

5.11   Transient photocurrent

Transient photocurrent (TPC) is used to measure the extraction dynamics of OPV devices. Therefore, the solar cells are excited with a pulsed laser and the corresponding dynamics of the photocurrent measured with an oscilloscope. The extraction time is influenced by the presence of trap states which retard the charge collection, resulting in an exponentially decaying photocurrent.[8,9]
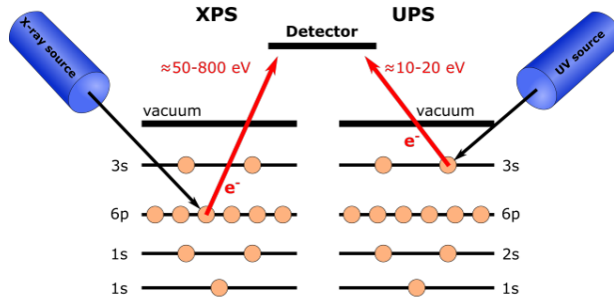
Figure 5.7: Working principle of photoelectron emission spectroscopy (PES). XPS probes the core electron levels with X-rays. UPS uses UV light to probe the electrons in the valence band. Figure courtesy of P. Fassl.[2]

For the measurements in this thesis, the light of an inorganic LED (Thorlabs TO-1 ¾, $\lambda = 465$ nm) was pulsed by a function generator (Agilent/Keysight 33510B) and focused on the solar cell. An oscilloscope (Picoscope 5443A) with a 50 Ω terminator placed across the oscilloscope input was used to measure the transient photocurrent.

5.12   X-ray diffraction

X-ray diffraction (XRD) measurements are performed to investigate the crystal structure and atomic spacing of thin films. It is based on the constructive interference of X-rays in the crystalline lattice of the material, following Bragg's law

$$n\lambda = 2d \sin\theta \tag{5.2}$$

where n is a positive integer, λ the wavelength of the X-rays, d the subatomic spacing, and θ the scattering angle. X-rays are generated in an evacuated cathode ray tube where electrons are accelerated towards a target material in which the electrons interact with the atoms. The resulting deceleration of the charges leads to a broad electromagnetic spectrum (Bremsstrahlung) and the excitation of core electrons leads to a spectrum characteristic to the material. X-rays of the desired wavelength are then selected, focussed onto the film, and the diffracted beams detected. By rotating the sample, or X-ray source and detector, constructive interference at certain θ according to Equation 5.2 occurs which is used to study the crystalline properties of the film.

   In the setup used for this thesis, XRD measurements were conducted on ITO-patterned glass substrates (see solar cell substrates, Section 4.1) on a Rigaku SmartLab diffractometer with a 9 kW rotating copper anode, equipped with a 0.5 mm ϕ-collimator. The 2D-diffraction pattern was collected with a

HyPix3000 detector at a sample-detector distance of 110 mm in a coupled $\theta/2\theta$ scan from 0 - 15°. The background was corrected by subtracting a diffraction measurement of the bare substrate. The measurements in this thesis were performed by F. Paulus.

Bibliography

[1] Newport Cooperation, Simulation of Solar Irradiation. https://www. newport.com/n/simulation-of-solar-irradiation.

[2] Fassl, P. Exploration of Properties, Stability and Reproducibility of Perovskite Solar Cells. Dissertation, Universität Heidelberg, 2018.

[3] Weu, A. Identifying Degradation Mechanisms in P3HT:PCBM Organic Solar Cells. Master thesis, Universität Heidelberg, 2016.

[4] Bakulin, A. A.; Rao, A.; Pavelyev, V. G.; van Loosdrecht, P. H. M.; Pshenichnikov, M. S.; Niedzialek, D.; Cornil, J.; Beljonne, D.; Friend, R. H. The Role of Driving Energy and Delocalized States for Charge Separation in Organic Semiconductors. *Science* **2012**, *335*, 1340–1344.

[5] Becker-Koch, D. Exploring sub-bandgap states in organic and hybrid photovoltaic materials using photothermal deflection spectroscopy. Master thesis, Universität Heidelberg, 2016.

[6] Kasha, M. Characterization of electronic transitions in complex molecules. *Discussions of the Faraday Society* **1950**, *9*, 14.

[7] Lami, V. Visualising the Energetic Landscape in Organic Photovoltaics. PhD thesis, Universität Heidelberg, 2019.

[8] Pearson, A. J.; Hopkinson, P. E.; Couderc, E.; Domanski, K.; Abdi-Jalebi, M.; Greenham, N. C. Critical light instability in CB/DIO processed PBDTTT-EFT:PC71BM organic photovoltaic devices. *Organic Electronics* **2016**, *30*, 225–236.

[9] Yan, W.; Huo, M.-M.; Hu, R.; Wang, Y. Working area effects on the energetic distribution of trap states and charge dynamics of dye-sensitized solar cells. *RSC Advances* **2019**, *9*, 1734–1740.

Part IV

Results

Chapter 6

Field-assisted charge generation

This chapter is based the publication "Field-Assisted Exciton Dissociation in Highly Efficient PffBT4T-2OD:Fullerene Organic Solar Cells" published in Chemistry of Materials, 2018.[1] It focuses on the mechanisms of exciton dissociation into free charges in PffBT4T-2OD:PC$_{70}$BM films and solar cells. It is shown that the separation of electron-hole pairs at the donor:acceptor interface is field-dependent in this material system which is unusual for high-efficiency materials where charge transfer commonly proceeds with unity efficiency. As a consequence, generation of free charges is observed in complete devices, but is suppressed in blend films without a built-in electric field. These results are important for future research on novel high-efficiency systems with low driving force for charge generation, for example in the field of non-fullerene acceptors (NFAs).

The first part introduces the materials and reviews the effects of electric fields on the charge generation process in organic solar cells. A detailed analysis of the steady-state and time-resolved photoluminescent properties and the investigation of ultrafast time scales using pump-probe and pump-push techniques follows. Finally, this chapter concludes with a model based on the observed results and an outlook for future research.

6.1 Introduction

Since its first synthesis in 2014, the polymer PffBT4T-2OD has received enormous attention as a high-efficiency donor material in organic solar cells.[2] Together with the fullerene acceptor PC$_{70}$BM, and after much research on improving the processing conditions and morphology of the active layer, this

material combination has reached almost 11% PCE, leading to the common abbreviation 'PCE-11'.[3–7] While most of the reports address the optimisation of fabrication procedures and their influence on the nano-structure of this material system, little attention has been paid to the process of charge generation which is the basis for the exceptional performance of PffBT4T-2OD:PC$_{70}$BM solar cells. As was detailed in Chapter 1, charge generation in OPVs generally involves the following steps:

1. Exciton creation and diffusion

2. Charge transfer at the donor:acceptor interface and formation of a bound CT state

3. Dissociation of the CT state into free, separated charge carriers

4. Charge transport through the layers and extraction at the electrodes

The field-assisted dissociation of relaxed CT states (CT$_1$) has been extensively studied, and can be well described by the Onsager-Braun model or more advanced theories (see Section 1.2). Usually the separation of CT$_1$ into free carriers is slightly enhanced by the application of electric fields, for example in PTB7:PC$_{70}$BM,[8] P3HT:PC$_{60}$BM,[9] PPVs,[10] and other systems.[11–13]

In contrast to the separation of CT states, exciton dissociation by charge transfer at an interface is generally unaffected by external fields. After diffusion of the electron-hole pair, excitons are quenched with near-unity efficiency due to the large energy offsets of donor and acceptor in conventional material systems which provide the required driving force for charge transfer.[14] The rate of electron transfer can be described by Marcus theory (see Section 1.2) which predicts a material-dependent optimal driving force to separate the charges (*activationless region*), whereas smaller driving forces entail a potential barrier for charge transfer (*normal region*).[15] Therefore, traditional material combinations with large energy offsets between the molecular orbitals have often been used, while systems with low driving forces showed expectedly low charge generation yields.[16–19] Exceptions to this trend emerged[20–22] and material design has shifted to systems with minimal energetic differences, particularly in the field of NFAs.[23–26] Out of those new systems, the material combination PffBT4T-2OD:PC$_{70}$BM can be used as a model system for high-performance OPVs despite small driving forces. An understanding of the fundamental processes leading to charge generation in such systems is therefore highly relevant.

6.2 Results

In the investigation of the photophysics of this material system, we observed an unusual field-effect on the dissociation of excitons the active layer. In the following sections, the steady-state and time-reolved optical properties of PffBT4T-2OD:$PC_{70}BM$ films are compared to those of complete OPV devices, comprising interlayers and electrodes. Unless stated otherwise, all measurements were performed on the same substrates (Figure 6.2d). PL, TCSPC, and ultrafast measurements in this joint project were performed partly in Heidelberg and partly at the Imperial College, London. Thomas R. Hopper assisted with the measurements and in the design of the figures and models.

6.2.1 The material system

The chemical structures of both PffBT4T-2OD and $PC_{70}BM$ are depicted in Figure 6.1a. UV-vis absorption (Figure 6.1b) and UPS measurements (Figure 6.1c) were used to obtain the bandgaps and HOMO energy levels of the materials. By fitting the absorption onsets, the optical gaps were determined to be 1.65 eV and 1.85 eV for polymer and fullerene, respectively. These values agree with previously reported bandgaps.[2,7,27] The ionisation potentials were estimated to be 5.35 eV for PffBT4T-2OD and 5.90 eV for $PC_{70}BM$. Bandgaps and ionisation potentials together were used to construct the energy level diagram in Figure 6.1d. It can be seen that the driving force for charge separation (LUMO-LUMO offset) is quite small ($\sim$0.35 eV) in comparison with other material systems.[28–32] The two used solar cell architectures (standard and inverted) are shown in Figure 6.1e and f. In the former electrons are extracted by calcium and aluminium layers, while holes are transported and collected through the PEDOT:PSS and ITO contact. In the inverted architecture, electrons are extracted by ZnO and ITO layers, while the holes are transported and collected through a MoO_3 and silver contact. In agreement with previous reports, the solar cells show excellent performance, with PCEs reaching 10.75% (Figure 6.1g).[2,5–7,27,33–35]

6.2.2 PL emission spectra

To investigate the electron transfer from donor to acceptor in this system, steady-state PL measurements were conducted (Figure 6.2). For this purpose, the polymer was excited with 600 nm light and its emission spectrum measured by a spectrometer. $PC_{70}BM$ does not exhibit a strong absorption at this
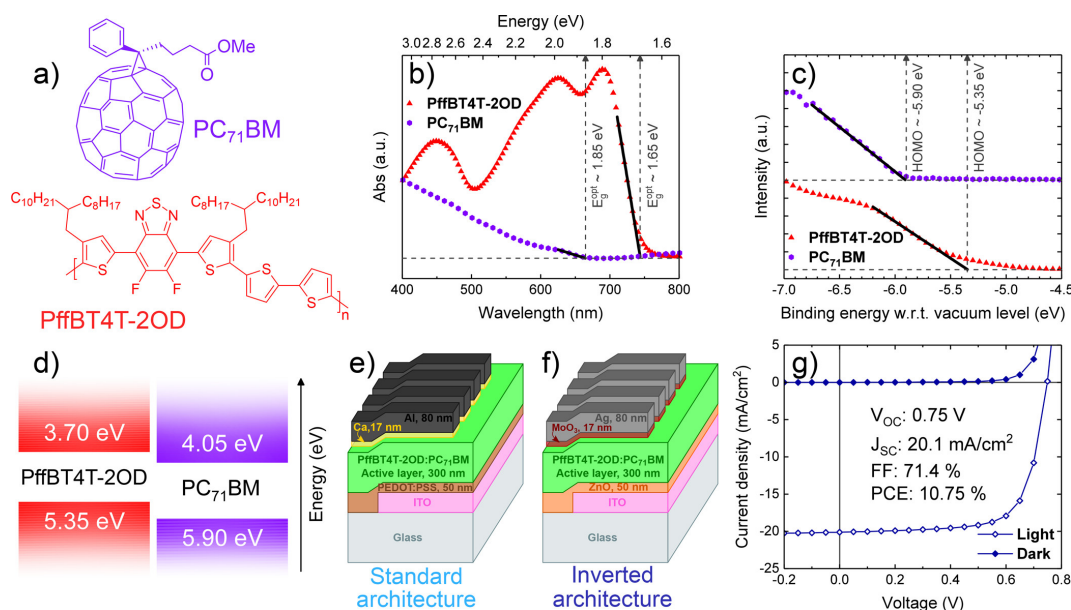
Figure 6.1: (a) Chemical structures of PffBT4T-2OD and PC$_{70}$BM. (b) UV–vis absorption spectra of pristine PffBT4T-2OD and PC$_{70}$BM films used to determine the optical bandgap of each component (1.65 and 1.85 eV, respectively). (c) UPS data for PffBT4T-2OD and PC$_{70}$BM used to estimate the HOMO energy level of each component (5.35 and 5.90 eV with respect to the vacuum level). (d) Band diagram of the PffBT4T-2OD:PC$_{70}$BM blend. (e) Standard and (f) inverted architecture devices. (g) JV characteristic of the best-performing (inverted architecture) solar cell with efficiency of 10.75%. Reproduced with permission from Ref.[1] Copyright 2018, American Chemical Society.

wavelength and, thus, its excitation and contribution to the emission can be neglected.

Figure 6.2a shows the PL spectra of the neat polymer, polymer blended with the fullerene acceptor, and complete devices in standard and inverted architectures. The maximum emission at $\sim$730 nm and general shape of the spectra are similar to those found in literature.[2,3,27] When comparing the emission of the neat polymer to the blend film, an unusually weak quenching of the polymer PL by only $\sim$20% is detected which is in contrast to the commonly observed near-unity quenching of the donor excited state when donor and acceptor are in close contact.[14] This small reduction indicates incomplete charge transfer at the donor:acceptor interface which seemingly contradicts the high efficiency of PffBT4T-2OD:PC$_{70}$BM solar cells, with J$_{SC}$'s over 20 mA cm^{-2}. However, when the emission of complete devices is measured (where the excitation light passes the active layer twice due to reflection off the back electrode), a $\sim$90% reduction of the PL intensity is observed with respect to the neat polymer film. This PL reduction is insensitive to the choice of electrodes or interlayers, indicated by the similarly effective quenching in normal and inverted architecture devices.

Previously, interactions between polymers and metal oxide layers have been reported in the context of doping or bound charge pairs across the organic-inorganic interface.[36–41] To exclude any effects of the interlayers on the polymer excited state, control experiments with PffBT4T-2OD in contact with ZnO, MoO$_3$, and in a complete, inverted polymer-only device were performed (Figure 6.2b). Only minor quenching of the donor exciton is observed in either configuration, excluding a strong effect of the interlayers or electrodes on the efficient quenching in complete devices. The small reduction of PL intensity can be attributed to some interfacial charge transfer or slight morphological changes compared to neat polymer films on glass. Nevertheless, the quenching of the polymer excited state is much weaker when compared to the blend in complete devices.

It is also possible that the observed effects originate from the internal electric field generated by the work function difference of the interlayers/electrodes. To test this hypothesis, a blend film sandwiched between two ZnO layers was fabricated and its PL measured (Figure 6.2c). To avoid high temperatures during annealing or dissolving of the blend, the top layer was deposited from ZnO nanoparticles in butanol.[42] The additional quenching in the film with equal electrodes is much weaker when compared to the device with different contacts which convincingly demonstrates a field-dependence of the charge separation
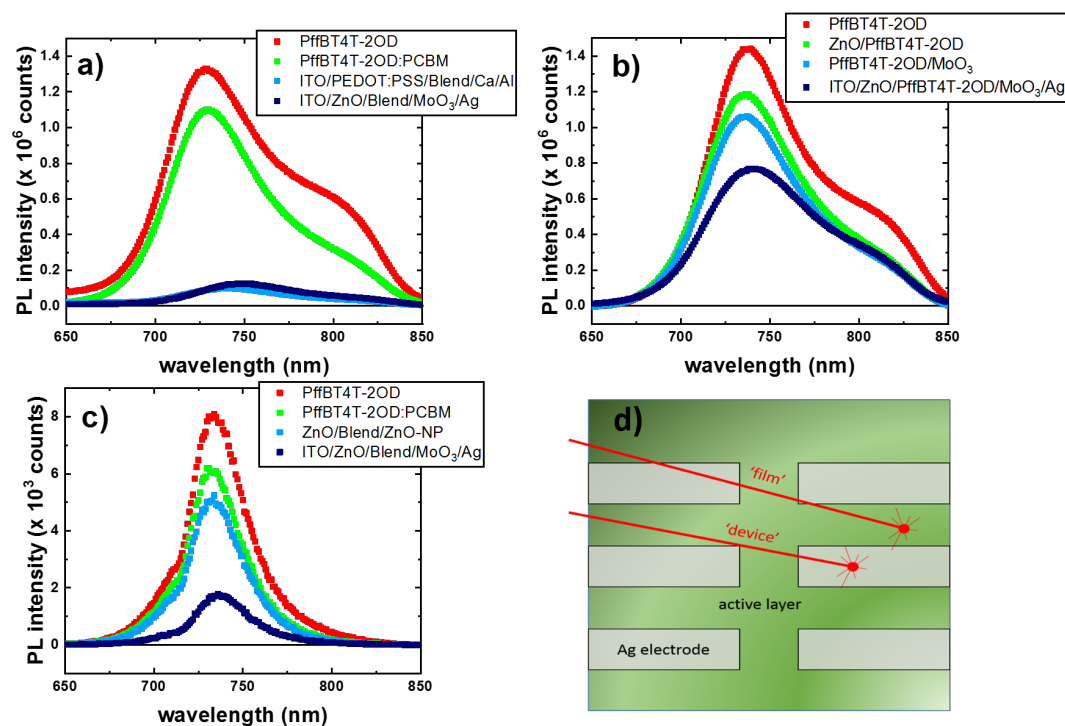
Figure 6.2: PL emission of PffBT4T-2OD and PC$_{70}$BM. Shown are spectra of (a) neat polymer, blend film and devices in normal and inverted architecture, (b) neat polymer with different interlayers or electrodes, and (c) symmetric device with equal work functions. (d) Schematic of 'film' and 'device' measurements on the same substrate. Differences in the emission spectra result from different experimental setups in Heidelberg (Panels a and b) and London (Panel c). Adapted with permission from Ref.[1] Copyright 2018, American Chemical Society.

dynamics in PffBT4T-2OD:PC$_{70}$BM solar cells. The differences in spectral shape compared to previous experiments result from different experimental setups in Heidelberg and London (Section 5.8).

6.2.3   PL lifetime

To investigate the dynamics of the charge transfer process, time-resolved PL (TCSPC) measurements were conducted (Figure 6.3). Again, the polymer was selectively excited with a 635 nm pulsed laser. Similarly to the steady-state emission discussed above, Figure 6.3a compares the excited state dynamics of neat PffBT4T-2OD with those of a blend film or complete devices. A modest decrease of the polymer exciton lifetime from 1.3 ± 0.1 ns to 1.1 ± 0.1 ns is observed when mixed with PC$_{70}$BM. This corresponds to a quenching efficiency of ∼16%, in agreement with the aforementioned reduction in PL emission. The small differences may be caused by subtle morphological changes after blending the polymer with the fullerene. Nevertheless, the lifetimes of neat and blended polymer films decay mono-exponentially, showing no additional quenching contribution from CT formation by charge transfer between donor and acceptor. However, when the blend film is integrated into a complete device, a second process at early times with a lifetime of 0.13 ± 0.07 ns is observed. This initial process dominates the early dynamics and is followed by a slower decay of ∼1 ns, similar to that observed in the blend film. This additional early component, concurrent with the strong reduction of the PL emission, is attributed to charge transfer from the excited donor to the acceptor.

Similar to the previous experiments, additional measurements with different interlayers or electrodes were performed (Figure 6.3b). No change in lifetime is observed when the polymer is brought into contact with either ZnO or MoO$_3$, disproving any strong effect of the metal oxides on the CT process. In a polymer-only device, the polymer lifetime is slightly reduced, but maintains a mono-exponential character. This is in agreement with the steady-state results, and the effects are mainly attributed to morphological changes of the polymer film when fabricated with different layers.

To strengthen the idea of a field-assisted charge transfer, the lifetime of the aforementioned device with identical electrodes was measured (Figure 6.3c). No changes in the excited state dynamics can be observed when compared to a blend film. In contrast, bi-exponential decay is measured when the electrodes exhibit different work functions, as is the case for the inverted device. These results imply that an internal electric field, provided by the different energy
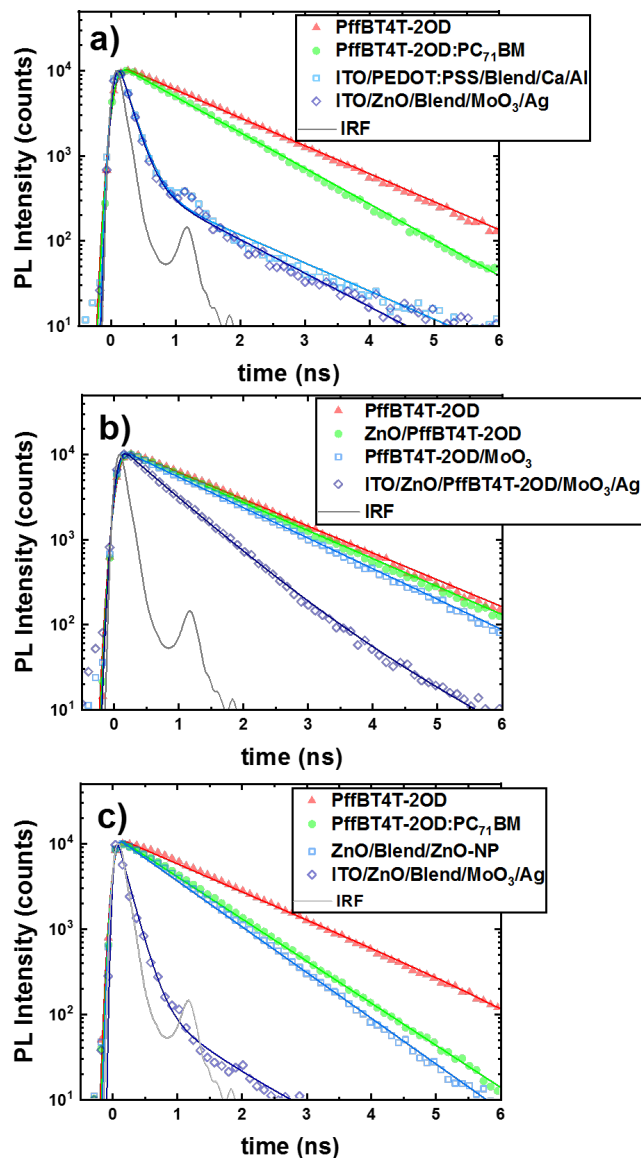
Figure 6.3: TCSPC measurements of PffBT4T-2OD and PC$_{70}$BM. (a) Lifetime of the neat polymer, the blend film and devices in normal and inverted architecture. (b) Dynamics of the neat polymer with different interlayers or electrodes. (c) Time-resolved PL of a symmetric device with equal work functions compared to films and inverted device. Lifetimes were fitted with mono -or bi-exponential fits, where appropriate. IRF denotes the instrument response function. Adapted with permission from Ref.[1] Copyright 2018, American Chemical Society.

levels of the transport layers/electrodes, is required to efficiently dissociate excitons at a donor-acceptor interface.

6.2.4 Transient absorption spectroscopy

Since charge separation processes occur on the sub-ns timescale, fs-TA spectroscopy was employed to investigate the ultrafast dynamics of the system. A low pump power of 2.5 μJ cm^{-2} was chosen to minimize additional ultrafast contributions from exciton-exciton annihilation processes (see Section 1.2.1, and Figure A.1 in the appendix); the excitation wavelength of 700 nm was selected to exclusively study the dynamics of the polymer excited states. Figure 6.4 shows the resulting TA spectra in the NIR after excitation of PffBT4T-2OD in a neat polymer film, a blend film, and an inverted device. The spectra show a broad excited state absorption (ESA) in the near-infrared (NIR) region. Expectedly, the spectral shape and evolution in time are similar in the neat polymer and blend film, indicating equally similar exciton dynamics in agreement with the TCSPC results. The spectral shape of the inverted architecture device is markedly different which is attributed to interference effects of the incoming probe beam with the part of the beam reflected off the silver electrode. In contrast to measurements in films, the signal at late times in the device does not disappear on the timescale of several nanoseconds, indicating the formation of a long-lived species. This is furthermore suggested by the gradual change of the spectral profile with time.

To further investigate the excited state dynamics in films and devices, the normalised kinetics at probe wavelengths of 1100 $\pm$ 10 nm are depicted in Figure 6.5a. During the first 50 ps all three transients show similar dynamics. After light absorption, donor excitons are created within the time resolution of the setup ($\sim$80 fs) and subsequently decay with a time constant of $\sim$200 ps due to radiative and non-radiative recombination. In the neat polymer and blend film this decay continues into the ns-regime, until all excitons eventually decay. The lifetime is comparable to other literature reports on PffBT4T-2OD excitons.[27] As mentioned above for the spectra, a long-lived component emerges after 50 ps in the device, regardless of the architecture (Figure A.2 in the appendix).

To understand the origin of this long-lived ESA component, a global analysis algorithm was applied to the dataset which decomposes the 2D-matrix into independent components, each with spectra and kinetics (see Section 3.2.2 for details). Two distinct species can be extracted by the algorithm (Figure 6.5b).
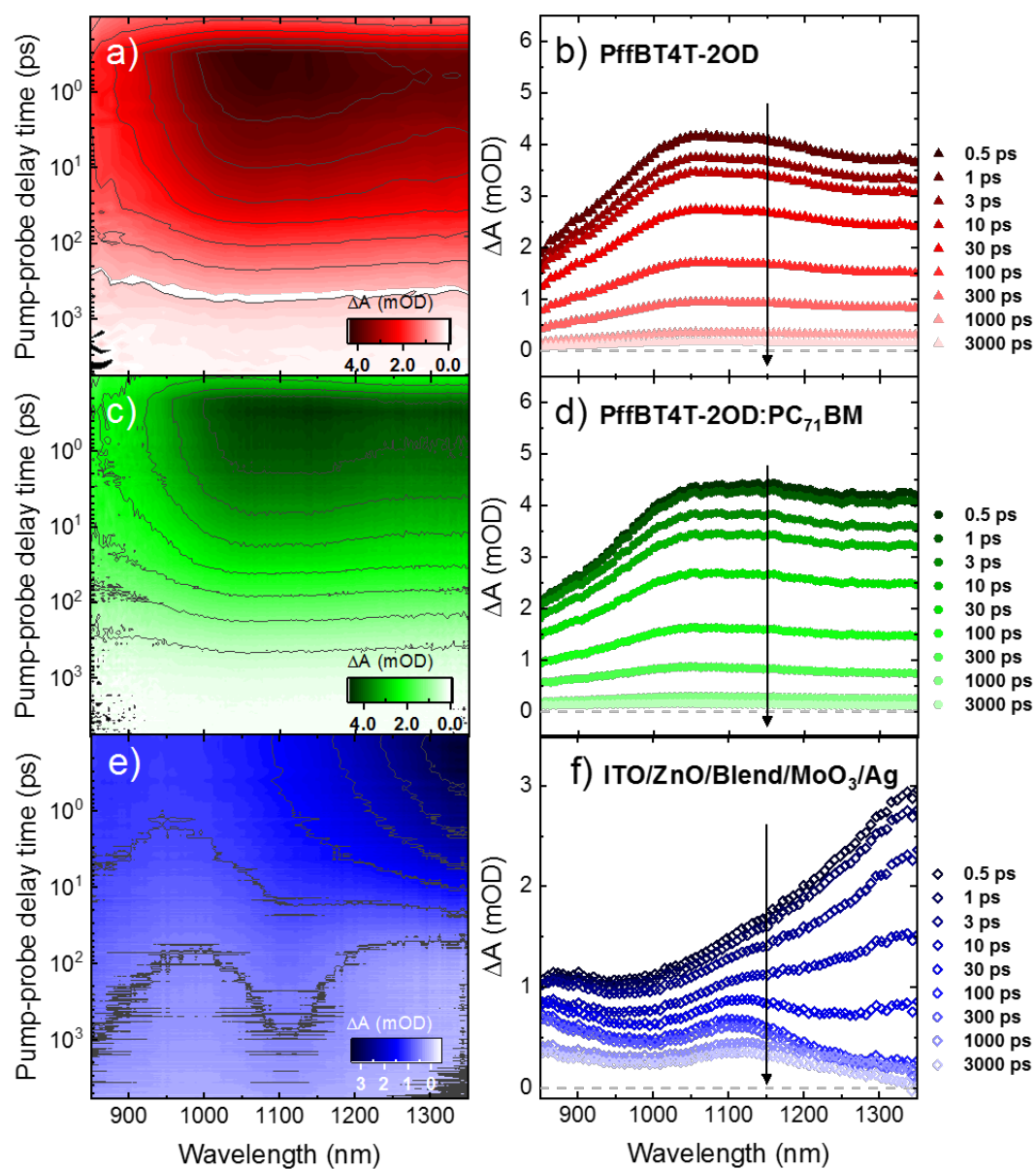
Figure 6.4: TA maps (left) and corresponding time-resolved TA spectra (right) for the polymer film (a-b), blend film (c-d) and inverted architecture blend device (e-f). Pump: 700 nm, 2.5 μJ cm^{-2}. The different spectral profile in the device is attributed to optical interference resulting from the standing wave formed by the incident probe beam and the probe beam reflected from the metal electrode. Adapted with permission from Ref.[1] Copyright 2018, American Chemical Society.
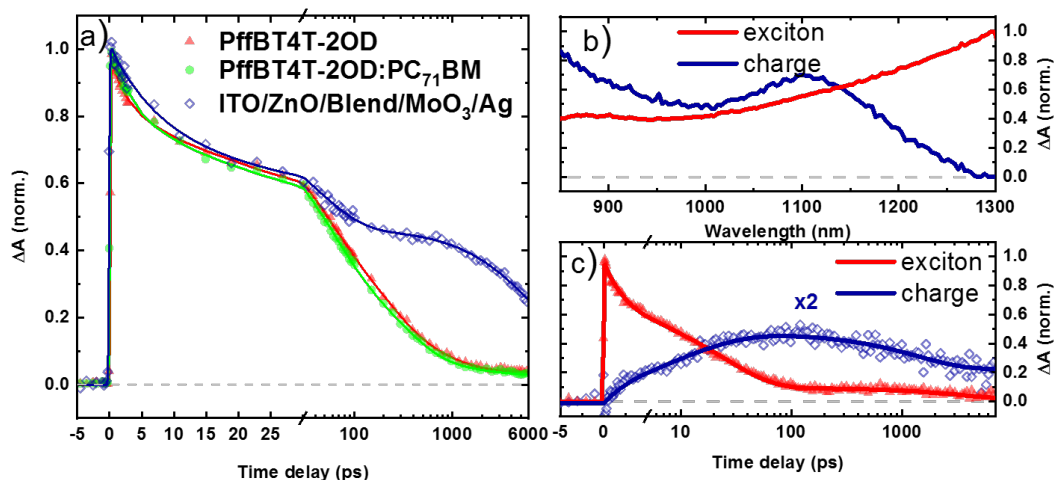
Figure 6.5: TA kinetics in films and devices. (a) Temporal evolution of the signal at 1100 ± 10 nm. (b) Resulting spectra from global analysis of the data. (c) Kinetics of the two species obtained from global analysis. Multiexponential fits serve as guide to the eye. Adapted with permission from Ref.[1] Copyright 2018, American Chemical Society.

Comparing the spectral shape of the two components with the raw signal in Figure 6.4f shows that the first component (red) resembles the TA signal at early times, while the second component (blue) is similar to the spectra at late times. After absorption of the 700 nm pulse, singlet donor excitons are generated as the only species in the active layer. These excitons undergo recombination or charge transfer, and thus should decay after some 100 ps, according to the lifetime measurements shown above. At late times, long-lived charges are expected to be the only species contributing to the signal. There-fore, the two components from the analysis can be assigned to the populations of excitons and free charge carriers. Figure 6.5c shows the kinetics associ-ated with the two components. After initial formation, the excitons exhibit a small, ultrafast decay <1 ps, most likely due to exciton-exciton-annihilation[43] or immediate charge transfer of excitons directly created at the donor-acceptor interface. Subsequently, the excitons decay by recombination or charge transfer to the acceptor on a timescale of $\sim$100 ps. The latter process is supported by comparing this timescale to the kinetics of neat or blend films in Figure 6.5a, where the decay is an order of magnitude slower due to missing charge transfer. The second species, resembling free charges in the device, emerges on a $\sim$10 ps timescale, concomitantly to the decay of the first signal, showing charge
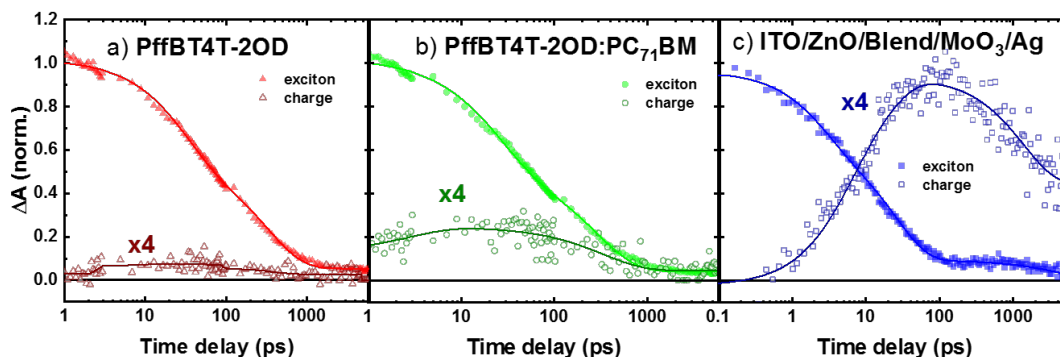
Figure 6.6: Global analysis results for films and devices. (a) The neat PffBT4T-2OD film exhibits only polymer excitons. (b) In the blend film some charges are generated, albeit with a markedly lower amplitude compared to a full device in (c). Multiexponential fits serve as guide to the eye. Adapted with permission from Ref.[1] Copyright 2018, American Chemical Society.

creation after exciton diffusion through the bulk. After 100 ps the charges exhibit slow recombination behaviour that extends beyond the time limit of the setup (> 7 ns). The long lifetime suggests that this process occurs mainly due to bimolecular recombination, in agreement with previous experiments on this system.[27]

Application of the global analysis on the films is shown in Figure 6.6. In the neat polymer film, excitons are excited and decay due to recombination until $\sim$1 ns, similar to the raw data in Figure 6.5a. The blend film shows similar exciton kinetics, indicating that no additional quenching mechanism occurs in the blend compared to the neat polymer. A minor amount of charges is formed after exciton dissociation in both films. The magnitude of the charge signal is markedly lower compared to the device structure; differences in the dynamics can be caused by space-charge effects from accumulated charges in the device with electrodes which can influence charge transport and recombination rates.[44] Since a small amount of this second species is also detected in neat polymer, where the probability for formation of free charges is very low, the signal is more likely the result of trapped charges which can be caused by oxygen, introduced during the production process. The degradation of films and devices of this material system will be the content of Chapter 7. These results show clearly that excitons are acting as precursors for charge generation in PffBT4T-2OD:PC_{70}BM devices, while charge transfer is suppressed in simple films.

6.2.5 Pump-push photocurrent

To further investigate the behaviour of excitons and charges in polymer and blend devices, pump-push photocurrent (PPPC) spectroscopy was employed. After excitation of the polymer with a 650 nm pump pulse creating donor excitons, a time-displaced NIR push pulse separates the bound electron-hole pairs. The resulting additional photocurrent dJ/J (where dJ is the push-induced current and J is the pump-induced current) is measured and plotted over time. A push wavelength of 1300 nm was selected to dissociate the bound excitons which mainly absorb at high wavelengths (Figure 6.5b). Figure 6.7a shows the PPPC transient for a polymer-only device in inverted architecture where mostly excitons reside due to lack of an acceptor component for charge separation. After absorption of the push pulse, an increased current is measured which is associated with the push-induced separation of the bound electron-hole pairs into free charge carriers.[28] This argument is strongly supported by comparing the PPPC transient with the kinetics of the exciton population in the device measured by regular TA spectroscopy. The dynamics of both resemble each other, showing that the separation of excitons leads to the improvement of photocurrent, instead of other bound species. Contrarily, applying the NIR push to the regular blend device does not yield substantial photocurrent (Figure 6.7b); the additional current is 2 - 3 orders of magnitude lower compared to the pure polymer device. Furthermore, the dynamics are completely different from the exciton kinetics, and push-induced charge generation only occurs at late times (>100 ps), when charge generation through electron transfer at the donor-acceptor interface is already complete and charge transport occurs. This late increase of the photocurrent can be interpreted as the push-induced depopulation of trap states.[45] The PPPC technique is often used to study geminate recombination in polymer:fullerene systems, by separating bound, interfacial CT states.[14,29,46] From these observations and previous TA results it is apparent that geminate recombination has only a minor effect on the charge generation and that bimolecular recombination is far more significant, as has been concluded by previous studies.[27,47]

6.3 Discussion

Considering the steady-state and time-resolved PL, TA, and PPPC results, a model describing the field-dependent exciton dissociation in PffBT4T-2OD:PC$_{70}$BM solar cells is developed (Figure 6.8). As was detailed in Section 1.2, charge gen-
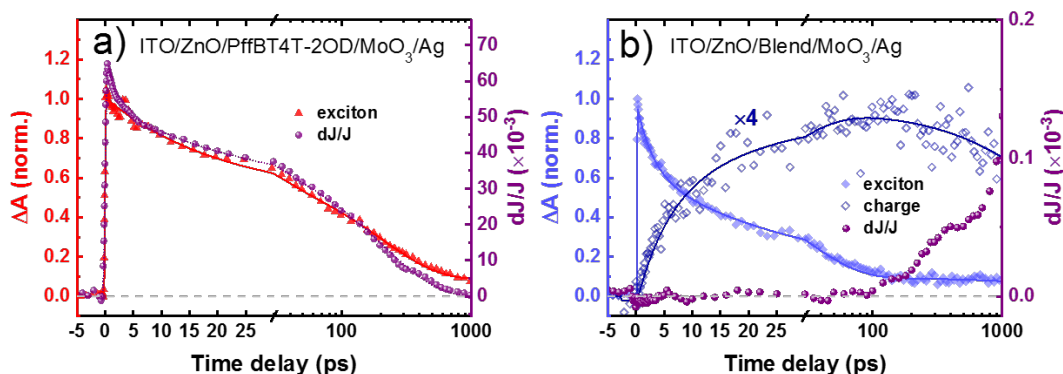
Figure 6.7: Pump-push photocurrent experiment on polymer and blend devices. (a) PffBT4T-2OD exciton dynamics of film from TA compared to change in photocurrent of device from PPPC. (b) Exciton and charge dynamics in a blend device compared to additional push-induced photocurrent. Amplitude in the blend device is much smaller compared to the polymer device, indicating the absence of bound charge pairs. Multiexponential fits serve as guide to the eye. Adapted with permission from Ref. [1] Copyright 2018, American Chemical Society.

eration through field-enhanced separation of CT states is often described by Onsager-Braun or hopping models.[8,10,13,48–51] However, for the system which was investigated here, a clear correlation between exciton dissociation into CT states and electric field is observed, as opposed to field-assisted CT separation into free charges. The former process occurs usually with unity efficiency and is seemingly insensitive to external fields in most polymer:fullerene systems.[14] According to Section 1.2, charge transfer from a neutral state into an intermolecular CT state is typically described by classical Marcus theory. While this formalism does not account for electric fields and mainly depends on the driving force between the excitonic and the CT state, it can provide an intuitive picture of the charge transfer process in the investigated system. Whereas conventional OSC blends, in which excitons dissociate into interfacial geminate pairs with high efficiency, are described by the *activationless* region of the theory, involving temperature- and field-independent exciton splitting, the PffBT4T-2OD:PC$_{70}$BM blend can be described by the *Marcus-normal* region where a potential barrier $\Delta G^{\#}$ between the two states prevents efficient charge transfer.

Light absorption in the active layer leads to creation of a donor exciton
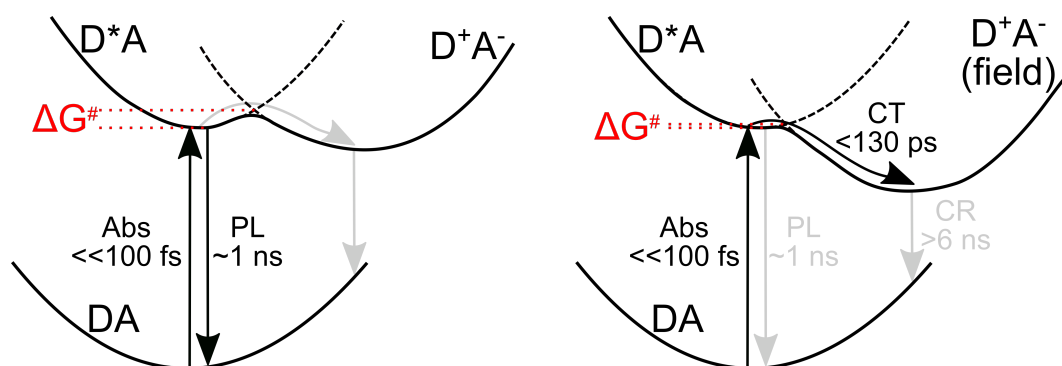
Figure 6.8: Model describing the exciton dissociation in PffBT4T-2OD:PC$_{70}$BM films (left) and solar cells (right), labelled with the timescales for absorption (Abs), photoluminescence (PL), charge transfer (CT) and charge recombination (CR). DA, D*A, and D$^+$A$^-$ represent the ground, singlet exciton, and CT state manifolds, respectively. $\Delta G^{\#}$ denotes the potential barrier between the D*A, and D$^+$A$^-$ manifolds. Reproduced with permission from Ref.[1] Copyright 2018, American Chemical Society.

within the time resolution of the setup (<80 fs). This exciton diffuses through the polymer domain until it reaches an interface with the acceptor. The small energetic offset between the molecular orbitals of donor and acceptor results in a small driving force ΔG^0 and thus a potential barrier $\Delta G^{\#}$ between the excited donor D*A and the CT state manifold D$^+$A$^-$, according to the Marcus-normal region. In the blend this $\Delta G^{\#}$ suppresses spontaneous charge transfer between donor and acceptor and thus the polymer excited state relaxes via PL to the groundstate on a timescale of ~1 ns. When the blend is integrated into a complete device, the built-in electric field provided by the interlayers/electrodes effectively lowers the energetic barrier $\Delta G^{\#}$ which leads to exciton quenching on the ps timescale. This charge transfer yields long-lived free charges with very little geminate recombination, while bimolecular recombination occurring at later times (>6 ns).

It must be noted that while the ultrafast observations are consistent with the aforementioned steady-state and time-resolved PL results, the absence of charge transfer in the blend film is in contrast with previously reported studies.[2,27] Differences in the fabrication of the films can be a possible cause for those discrepancies, as this system is particularly sensitive to preparation conditions.[7] Nevertheless, the devices prepared according to our protocol exhibit excellent photovoltaic performance.

6.4   Conclusion

In conclusion, an unusual field-effect in the high-efficiency system PffBT4T-2OD:PC$_{70}$BM was observed. For blend films, an energetic barrier seemingly prevents exciton dissociation at the donor:acceptor interface, in agreement with Marcus theory, but untypical for conventional OPV systems. As a consequence neither charge transfer nor free, separated charges are observed in these films. Investigation of complete photovoltaic devices showed efficient charge transfer and formation of free charges, as expected in high-performance systems. These findings are rationalised by a field-assisted lowering of the energetic barrier between donor exciton and intermolecular charge pair. The observed photophysics are independent of the choice of interlayers or electrodes, excluding quenching effects from other materials. These results are highly relevant for other systems with low driving forces, particularly to the field of non-fullerene acceptors which exhibit high device performance despite small energetic offsets between the materials.[23,52] Finally, this work emphasises the need to investigate OPV systems in complete devices rather than films to gain a more accurate understanding of the photophysics under operating conditions.

Bibliography

[1] Weu, A.; Hopper, T. R.; Lami, V.; Kreß, J. A.; Bakulin, A. A.; Vaynzof, Y. Field-Assisted Exciton Dissociation in Highly Efficient PffBT4T-2OD:Fullerene Organic Solar Cells. *Chemistry of Materials* **2018**, *30*, 2660–2667.

[2] Liu, Y.; Zhao, J.; Li, Z.; Mu, C.; Ma, W.; Hu, H.; Jiang, K.; Lin, H.; Ade, H.; Yan, H. Aggregation and morphology control enables multiple cases of high-efficiency polymer solar cells. *Nature Communications* **2014**, *5*, 5293.

[3] Zhang, Y.; Parnell, A. J.; Pontecchiani, F.; Cooper, J. F. K.; Thompson, R. L.; Jones, R. A. L.; King, S. M.; Lidzey, D. G.; Bernardo, G. Understanding and controlling morphology evolution via DIO plasticization in PffBT4T-2OD/PC71BM devices. *Scientific Reports* **2017**, *7*, 44269.

[4] Masters, R. C.; Wan, Q.; Zhang, Y.; Dapor, M.; Sandu, A. M.; Jiao, C.; Zhou, Y.; Zhang, H.; Lidzey, D. G.; Rodenburg, C. Novel organic photovoltaic polymer blends: A rapid, 3-dimensional morphology analysis using backscattered electron imaging in the scanning electron microscope. *Solar Energy Materials and Solar Cells* **2017**, *160*, 182–192.

[5] Ro, H. W.; Downing, J. M.; Engmann, S.; Herzing, A. A.; DeLongchamp, D. M.; Richter, L. J.; Mukherjee, S.; Ade, H.; Abdelsamie, M.; Jagadamma, L. K.; Amassian, A.; Liu, Y.; Yan, H. Morphology changes upon scaling a high-efficiency, solution-processed solar cell. *Energy & Environmental Science* **2016**, *9*, 2835–2846.

[6] Zhao, J.; Zhao, S.; Xu, Z.; Qiao, B.; Huang, D.; Zhao, L.; Li, Y.; Zhu, Y.; Wang, P. Revealing the Effect of Additives with Different Solubility on the Morphology and the Donor Crystalline Structures of Organic Solar Cells. *ACS Applied Materials & Interfaces* **2016**, *8*, 18231–18237.

[7] Ma, W.; Yang, G.; Jiang, K.; Carpenter, J. H.; Wu, Y.; Meng, X.; McAfee, T.; Zhao, J.; Zhu, C.; Wang, C.; Ade, H.; Yan, H. Influence of Processing Parameters and Molecular Weight on the Morphology and Properties of High-Performance PffBT4T-2OD:PC$_{71}$BM Organic Solar Cells. *Advanced Energy Materials* **2015**, *5*, 1501400.

[8] Gerhard, M.; Arndt, A. P.; Bilal, M.; Lemmer, U.; Koch, M.; Howard, I. A. Field-induced exciton dissociation in PTB7-based organic solar cells. *Physical Review B* **2017**, *95*, 195301.

[9] Marsh, R. A.; Hodgkiss, J. M.; Friend, R. H. Direct Measurement of Electric Field-Assisted Charge Separation in Polymer:Fullerene Photovoltaic Diodes. *Advanced Materials* **2010**, *22*, 3672–3676.

[10] Inal, S.; Schubert, M.; Sellinger, A.; Neher, D. The Relationship between the Electric Field-Induced Dissociation of Charge Transfer Excitons and the Photocurrent in Small Molecular/Polymeric Solar Cells. *The Journal of Physical Chemistry Letters* **2010**, *1*, 982–986.

[11] Bakulin, A. A.; Xia, Y.; Bakker, H. J.; Inganäs, O.; Gao, F. Morphology, Temperature, and Field Dependence of Charge Separation in High-Efficiency Solar Cells Based on Alternating Polyquinoxaline Copolymer. *The Journal of Physical Chemistry C* **2016**, *120*, 4219–4226.

[12] Tvingstedt, K.; Vandewal, K.; Zhang, F.; Inganäs, O. On the Dissociation Efficiency of Charge Transfer Excitons and Frenkel Excitons in Organic Solar Cells: A Luminescence Quenching Study. *The Journal of Physical Chemistry C* **2010**, *114*, 21824–21832.

[13] Veldman, D.; İpek, Ö.; Meskers, S. C. J.; Sweelssen, J.; Koetse, M. M.; Veenstra, S. C.; Kroon, J. M.; van Bavel, S. S.; Loos, J.; Janssen, R. A. J. Compositional and Electric Field Dependence of the Dissociation of Charge Transfer Excitons in Alternating Polyfluorene Copolymer/-Fullerene Blends. *Journal of the American Chemical Society* **2008**, *130*, 7721–7735.

[14] Savoie, B. M.; Rao, A.; Bakulin, A. A.; Gelinas, S.; Movaghar, B.; Friend, R. H.; Marks, T. J.; Ratner, M. A. Unequal Partnership: Asymmetric Roles of Polymeric Donor and Fullerene Acceptor in Generating Free Charge. *Journal of the American Chemical Society* **2014**, *136*, 2876–2884.

[15] Marcus, R. A. Chemical and Electrochemical Electron-Transfer Theory. *Annual Review of Physical Chemistry* **1964**, *15*, 155–196.

[16] Vezie, M. S.; Azzouzi, M.; Telford, A. M.; Hopper, T. R.; Sieval, A. B.; Hummelen, J. C.; Fallon, K.; Bronstein, H.; Kirchartz, T.; Bakulin, A. A.;

Clarke, T. M.; Nelson, J. Impact of Marginal Exciton–Charge-Transfer State Offset on Charge Generation and Recombination in Polymer:Fullerene Solar Cells. *ACS Energy Letters* **2019**, *4*, 2096–2103.

[17] Li, W.; Hendriks, K. H.; Furlan, A.; Wienk, M. M.; Janssen, R. A. J. High Quantum Efficiencies in Polymer Solar Cells at Energy Losses below 0.6 eV. *Journal of the American Chemical Society* **2015**, *137*, 2231–2234.

[18] Dimitrov, S. D.; Durrant, J. R. Materials Design Considerations for Charge Generation in Organic Solar Cells. *Chemistry of Materials* **2014**, *26*, 616–630.

[19] Vandewal, K.; Ma, Z.; Bergqvist, J.; Tang, Z.; Wang, E.; Henriksson, P.; Tvingstedt, K.; Andersson, M. R.; Zhang, F.; Inganäs, O. Quantification of Quantum Efficiency and Energy Losses in Low Bandgap Polymer:Fullerene Solar Cells with High Open-Circuit Voltage. *Advanced Functional Materials* **2012**, *22*, 3480–3490.

[20] Unger, T.; Wedler, S.; Kahle, F.-J.; Scherf, U.; Bässler, H.; Köhler, A. The Impact of Driving Force and Temperature on the Electron Transfer in Donor–Acceptor Blend Systems. *The Journal of Physical Chemistry C* **2017**, *121*, 22739–22752.

[21] Kawashima, K.; Tamai, Y.; Ohkita, H.; Osaka, I.; Takimiya, K. High-efficiency polymer solar cells with small photon energy loss. *Nature Communications* **2015**, *6*, 10085.

[22] Menke, S. M.; Sadhanala, A.; Nikolka, M.; Ran, N. A.; Ravva, M. K.; Abdel-Azeim, S.; Stern, H. L.; Wang, M.; Sirringhaus, H.; Nguyen, T.-Q.; Brédas, J.-L.; Bazan, G. C.; Friend, R. H. Limits for Recombination in a Low Energy Loss Organic Heterojunction. *ACS Nano* **2016**, *10*, 10736–10744.

[23] Hou, J.; Inganäs, O.; Friend, R. H.; Gao, F. Organic solar cells based on non-fullerene acceptors. *Nature Materials* **2018**, *17*, 119–128.

[24] Baran, D. et al. Reducing the efficiency–stability–cost gap of organic photovoltaics with highly efficient and stable small molecule acceptor ternary solar cells. *Nature Materials* **2017**, *16*, 363–369.

[25] Liu, J.; Chen, S.; Qian, D.; Gautam, B.; Yang, G.; Zhao, J.; Bergqvist, J.;

Zhang, F.; Ma, W.; Ade, H.; Inganäs, O.; Gundogdu, K.; Gao, F.; Yan, H. Fast charge separation in a non-fullerene organic solar cell with a small driving force. *Nature Energy* **2016**, *1*, 16089.

[26] Baran, D. et al. Reduced voltage losses yield 10% efficient fullerene free organic solar cells with >1 V open circuit voltages. *Energy and Environmental Science* **2016**, *9*, 3783–3793.

[27] Cha, H.; Wu, J.; Wadsworth, A.; Nagitta, J.; Limbu, S.; Pont, S.; Li, Z.; Searle, J.; Wyatt, M. F.; Baran, D.; Kim, J.-S.; McCulloch, I.; Durrant, J. R. An Efficient, "Burn in" Free Organic Solar Cell Employing a Nonfullerene Electron Acceptor. *Advanced Materials* **2017**, *29*, 1701156.

[28] Köhler, A.; dos Santos, D. A.; Beljonne, D.; Shuai, Z.; Brédas, J.-L.; Holmes, A. B.; Kraus, A.; Müllen, K.; Friend, R. H. Charge separation in localized and delocalized electronic states in polymeric semiconductors. *Nature* **1998**, *392*, 903–906.

[29] Bakulin, A. A.; Rao, A.; Pavelyev, V. G.; van Loosdrecht, P. H. M.; Pshenichnikov, M. S.; Niedzialek, D.; Cornil, J.; Beljonne, D.; Friend, R. H. The Role of Driving Energy and Delocalized States for Charge Separation in Organic Semiconductors. *Science* **2012**, *335*, 1340–1344.

[30] Gelinas, S.; Rao, A.; Kumar, A.; Smith, S. L.; Chin, A. W.; Clark, J.; van der Poll, T. S.; Bazan, G. C.; Friend, R. H. Ultrafast Long-Range Charge Separation in Organic Semiconductor Photovoltaic Diodes. *Science* **2014**, *343*, 512–516.

[31] Jailaubekov, A. E.; Willard, A. P.; Tritsch, J. R.; Chan, W.-L.; Sai, N.; Gearba, R.; Kaake, L. G.; Williams, K. J.; Leung, K.; Rossky, P. J.; Zhu, X.-Y. Hot charge-transfer excitons set the time limit for charge separation at donor/acceptor interfaces in organic photovoltaics. *Nature Materials* **2013**, *12*, 66–73.

[32] Grancini, G.; Maiuri, M.; Fazzi, D.; Petrozza, A.; Egelhaaf, H.-J.; Brida, D.; Cerullo, G.; Lanzani, G. Hot exciton dissociation in polymer solar cells. *Nature Materials* **2013**, *12*, 29–33.

[33] Sprau, C.; Buss, F.; Wagner, M.; Landerer, D.; Koppitz, M.; Schulz, A.; Bahro, D.; Schabel, W.; Scharfer, P.; Colsmann, A. Highly efficient poly-

mer solar cells cast from non-halogenated xylene/anisaldehyde solution. *Energy & Environmental Science* **2015**, *8*, 2744–2752.

[34] Zhang, X.; Zheng, D.; Xing, S.; Wang, H.; Huang, J.; Yu, J. Precisely control the morphology and crystallization of temperature-dependent aggregation bulk heterojunction by using co-solvent system for optimized light intensity distribution and its effect on thick active layer polymer solar cells. *Solar Energy* **2017**, *147*, 106–112.

[35] Li, N.; Perea, J. D.; Kassar, T.; Richter, M.; Heumueller, T.; Matt, G. J.; Hou, Y.; Güldal, N. S.; Chen, H.; Chen, S.; Langner, S.; Berlinghof, M.; Unruh, T.; Brabec, C. J. Abnormal strong burn-in degradation of highly efficient polymer solar cells caused by spinodal donor-acceptor demixing. *Nature Communications* **2017**, *8*, 14541.

[36] Gwinner, M. C.; Pietro, R. D.; Vaynzof, Y.; Greenberg, K. J.; Ho, P. K. H.; Friend, R. H.; Sirringhaus, H. Doping of Organic Semiconductors Using Molybdenum Trioxide: a Quantitative Time-Dependent Electrical and Spectroscopic Study. *Advanced Functional Materials* **2011**, *21*, 1432–1441.

[37] Nyman, M.; Dahlström, S.; Sandberg, O. J.; Österbacka, R. Unintentional Bulk Doping of Polymer-Fullerene Blends from a Thin Interfacial Layer of MoO3. *Advanced Energy Materials* **2016**, *6*, 1600670.

[38] Sevinchan, Y.; Hopkinson, P. E.; Bakulin, A. A.; Herz, J.; Motzkus, M.; Vaynzof, Y. Improving Charge Separation across a Hybrid Oxide/Polymer Interface by Cs Doping of the Metal Oxide. *Advanced Materials Interfaces* **2016**, *3*, 1500616.

[39] Hofstetter, Y. J.; Hopkinson, P. E.; Bakulin, A. A.; Vaynzof, Y. Simultaneous enhancement in open circuit voltage and short circuit current of hybrid organic–inorganic photovoltaics by inorganic interfacial modification. *Journal of Materials Chemistry C* **2016**, *4*, 1111–1116.

[40] Pachoumi, O.; Bakulin, A. A.; Sadhanala, A.; Sirringhaus, H.; Friend, R. H.; Vaynzof, Y. Improved Performance of ZnO/Polymer Hybrid Photovoltaic Devices by Combining Metal Oxide Doping and Interfacial Modification. *The Journal of Physical Chemistry C* **2014**, *118*, 18945–18950.

[41] Vaynzof, Y.; Bakulin, A. A.; Gélinas, S.; Friend, R. H. Direct Observation of Photoinduced Bound Charge-Pair States at an Organic-Inorganic Semiconductor Interface. *Physical Review Letters* **2012**, *108*, 246605.

[42] Beek, W. J.; Wienk, M. M.; Kemerink, M.; Yang, X.; Janssen, R. A. Hybrid zinc oxide conjugated polymer bulk heterojunction solar cells. *Journal of Physical Chemistry B* **2005**, *109*, 9505–9516.

[43] Nguyen, T.-Q.; Martini, I. B.; Liu, J.; Schwartz, B. J. Controlling Interchain Interactions in Conjugated Polymers: The Effects of Chain Morphology on Exciton-Exciton Annihilation and Aggregation in MEH-PPV Films. *The Journal of Physical Chemistry B* **2002**, *104*, 237–255.

[44] Chow, P. C. Y.; Bayliss, S. L.; Lakhwani, G.; Greenham, N. C.; Friend, R. H. In Situ Optical Measurement of Charge Transport Dynamics in Organic Photovoltaics. *Nano Letters* **2015**, *15*, 931–935.

[45] Bakulin, A. A.; Neutzner, S.; Bakker, H. J.; Ottaviani, L.; Barakel, D.; Chen, Z. Charge trapping dynamics in pbs colloidal quantum dot photovoltaic devices. *ACS Nano* **2013**, *7*, 8771–8779.

[46] Zhang, J.; Jakowetz, A. C.; Li, G.; Di, D.; Menke, S. M.; Rao, A.; Friend, R. H.; Bakulin, A. A. On the energetics of bound charge-transfer states in organic photovoltaics. *Journal of Materials Chemistry A* **2017**, *5*, 11949–11959.

[47] Cha, H.; Wheeler, S.; Holliday, S.; Dimitrov, S. D.; Wadsworth, A.; Lee, H. H.; Baran, D.; McCulloch, I.; Durrant, J. R. Influence of Blend Morphology and Energetics on Charge Separation and Recombination Dynamics in Organic Solar Cells Incorporating a Nonfullerene Acceptor. *Advanced Functional Materials* **2018**, *28*, 1704389.

[48] Onsager, L. Initial Recombination of Ions. *Physical Review* **1938**, *54*, 554–557.

[49] Clarke, T. M.; Durrant, J. R. Charge Photogeneration in Organic Solar Cells. *Chemical Reviews* **2010**, *110*, 6736–6767.

[50] Koster, L. J. A.; Smits, E. C. P.; Mihailetchi, V. D.; Blom, P. W. M. Device model for the operation of polymer/fullerene bulk heterojunction solar cells. *Physical Review B* **2005**, *72*, 085205.

[51] Mihailetchi, V. D.; Koster, L. J. A.; Hummelen, J. C.; Blom, P. W. M. Photocurrent Generation in Polymer-Fullerene Bulk Heterojunctions. *Physical Review Letters* **2004**, *93*, 216601.

[52] Yan, C.; Barlow, S.; Wang, Z.; Yan, H.; Jen, A. K.-Y.; Marder, S. R.; Zhan, X. Non-fullerene acceptors for organic solar cells. *Nature Reviews Materials* **2018**, *3*, 18003.

Chapter 7

Degradation through oxygen-doping

The main results of this chapter have been published in "Oxygen-Induced Doping as a Degradation Mechanism in Highly Efficient Organic Solar Cells", in ACS Applied Energy Materials, 2019.[1] In here, the influence of oxygen on the operational stability of PffBT4T-2OD:PC$_{70}$BM photovoltaic devices is investigated. Through a multitude of spectroscopic and ultrafast techniques it is shown that oxygen-induced p-doping of the active layer is responsible for the severe performance losses observed in this material system. It is found that the combination of oxygen and constant illumination does not lead to additional photo-oxidation of the active layer materials. These results have important implications for the development of new OPV materials and highlight the need to find efficient mitigation strategies.

After a brief introduction reviewing the main degradation patterns in oxygen and light, previous literature reports on the operational stability of PffBT4T-2OD:PC$_{70}$BM devices are analysed. The following results include in-situ measurements of OPV and OFET performance, photoelectron spectroscopy, ultrafast TA spectroscopy, and highly-sensitive PDS measurements of the sub-bandgap absorption. Finally, a model is proposed and the observed results are discussed in the context of strategies for more stable devices.

7.1   Introduction

As was reviewed in Chapter 2, the stability of OPVs is a critical prerequisite towards widespread application and requires further investigation. Operation

of high-efficiency material systems in ambient conditions often leads to rapid device deterioration, limiting the usability of such systems outside the laboratory.

Exposure to illumination can cause dimerisation of fullerene derivatives, particularly $PC_{60}BM$. [2–4] In other systems, for example $PffBT4T$-2OD:$PC_{70}BM$, formation of radical species on the fullerene cage is observed. [5,6] Often, the performance loss of OSCs under illumination is accompanied with an increased formation of trap states in the bandgap. [7–9] Even when stored in the dark, exposure to oxygen leads to doping of the active layer which causes an increase of the hole concentration and thus increased bimolecular recombination or space-charge effects. [10–13] This doping effect is accelerated by the presence of light and usually reversible under heat and vacuum. [14] The exposure to both oxygen and light typically leads to very severe, irreversible degradation of the materials by radical photo-oxidation processes which cause bleaching of the absorption or formation of deep traps. [15–17]

The material system $PffBT4T$-2OD:$PC_{70}BM$ is not only interesting regarding its unusual photophysics (Chapter 6) but also concerning its stability when subjected to external factors. Under continuous illumination in nitrogen, Li et al. observed a spinodal de-mixing of the donor and acceptor phases, leading to a decrease of interfacial area for charge separation and consequently strong burn-in of the short-circuit current. [18] Under similar conditions, Cha et al. found that bond disruption or cleavage at the fullerene side group are responsible for the rapid degradation of the FF. Exposure to thermal stress lead to a fast decrease of J_{SC} due to the aforementioned phase separation of the polymer and fullerene domains. [6] While these studies focussed on the degradation in nitrogen atmospheres, the stability of the devices operated in oxygen is hitherto unexplored. Nevertheless, the investigation of the stability of high-efficiency material combinations, for which $PffBT4T$-2OD:$PC_{70}BM$ can be a benchmark system, in oxygen environments is of paramount importance for future applications, as encapsulation techniques are often expensive or insufficiently effective.

7.2   Results

The degradation of $PffBT4T$-2OD:$PC_{70}BM$ solar cells is uniquely severe which will be investigated in the following sections. By analysing various spectroscopic and ultrafast measurements, we find that oxygen-induced p-doping of the active layer is the main contribution to the rapid loss of device perfor-

mance in oxygen atmospheres. For the fabrication of the films and devices see Chapter 4. Structure and energetics of the materials, as well as performance of the devices can be found in the previous Chapter 6. The fabrication and degradation of organic field effect transistors (OFETs) was performed by J. Kress, photoelectron spectroscopy experiments were carried out by V. Lami, and PDS measurements were done by D. Becker-Koch.

7.2.1   Device performance

The degradation of the solar cell parameters in various environments is depicted in Figure 7.1. A reference experiment in nitrogen under dark conditions (Figure 7.1a) exhibits a 20% reduction of the initial PCE after 15 hours. This behaviour is likely caused by subtle changes in the blend morphology which is very sensitive to external stressors like heat or light and cannot be avoided during the measurements.[18] Also the usage of the common processing additive DIO has destabilising effects on the blend structure.[7,19–21] Subjecting the devices to constant irradiation with 1 sun illumination (Figure 7.1b) considerably increases the degradation rates. V_{OC} and J_{SC} decrease to 70% and 60%, respectively, while the FF is not influenced by the additional light stress. As mentioned above, degradation of this system under nitrogen environments and light has been extensively studied before. It was shown that small-scale morphological changes in the blend and physical bond disruption at the fullerene component are responsible for the drastic performance losses.[6,18] It has to be noted that in our experiments the change in V_{OC} is much more pronounced compared to previous reports which we attribute to changes in the fabrication procedures.

Operating the solar cells in dark oxygen atmospheres (Figure 7.1c) significantly accelerates the degradation when compared to the nitrogen reference in the dark. While the FF shows no changes and remains above 90% of its initial value, V_{OC} and J_{SC} show considerable decays which lead to a 60 - 70% reduction of the device performance during 15 hours of operation. When both oxygen and light are used to degrade the OPVs, tremendous performance losses are observed in a burn-in type degradation, during which the PCE drops to ∼10% of its initial value within 15 hours (Figure 7.1d). The unusually strong degradation of the open-circuit voltage suggests massively increased recombination or changes of the frontier-molecular orbitals (see Chapter 2). This observation is in contrast to previously reported studies, where the V_{OC} was found to be more stable after degradation in air for several days.[6,18] However, in these
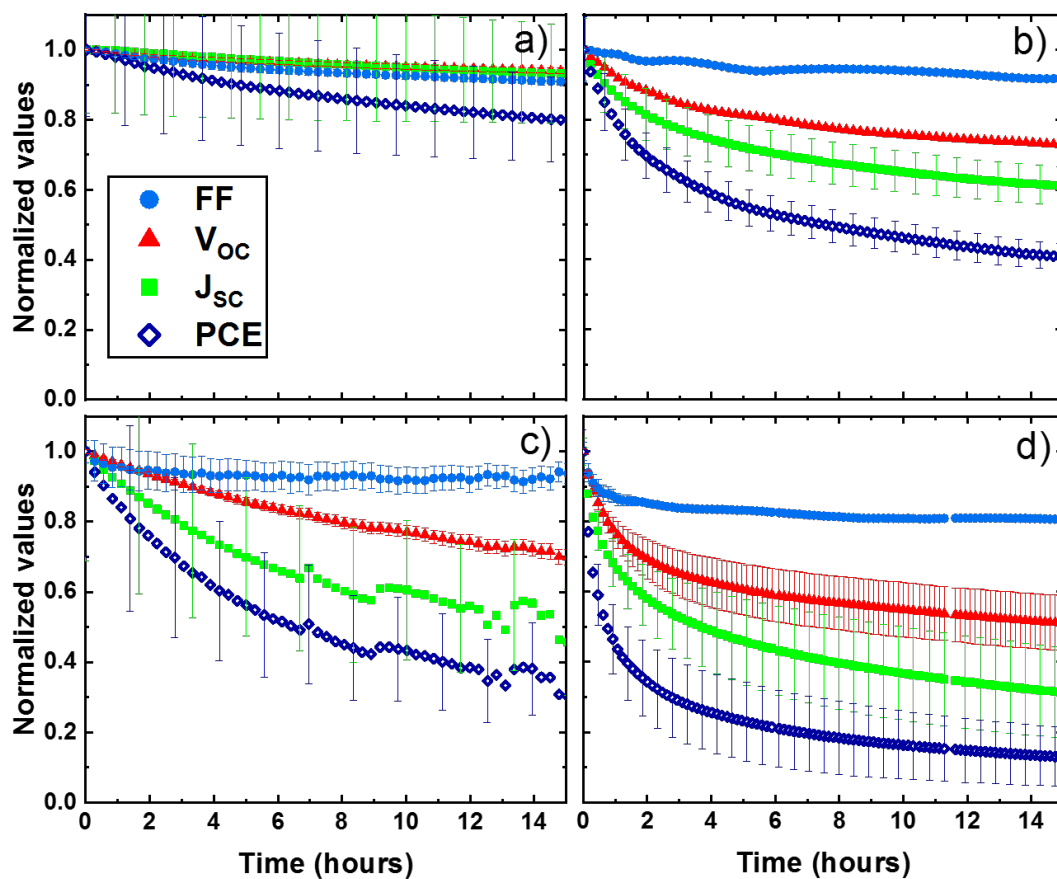
Figure 7.1: Degradation of PffBT4T-2OD:PC$_{70}$BM solar cells in various environments. (a) Degradation in nitrogen under dark conditions. (b) Degradation in nitrogen under constant illumination. (c) Degradation in 20% oxygen, without light. (d) Degradation in 20 % under continuous illumination. Data has been normalised for ease of comparison. Adapted with permission from Ref.[1] Copyright 2019, American Chemical Society.

reports the samples were stored in ambient atmospheres and not measured repeatedly, so that the absorbed light dose is much smaller compared to the experiments which were conducted here. Additionally, the effect of humidity in their measurements was neglected. Finally, as mentioned above, differences in the fabrication route can cause changes in the morphology which is critical for this material system.[22–27] Nevertheless, our OPVs perform with similar initial efficiencies (see Chapter 6).

7.2.2 PL emission

Since the behaviour of the material system in nitrogen conditions is reasonably well understood, this work focuses on the effects of oxygen exposure onto the device stability. Therefore, the PL emission of PffBT4T-2OD:PC$_{70}$BM devices was measured at different stages of degradation in 20% oxygen, with and without constant 1 sun illumination. The experiments were specifically carried out on the device area, rather than simple films, to include the complete process of charge generation (see Chapter 6). After excitation of the polymer donor with a 447 nm laser, PffBT4T-2OD excitons are created which are quenched by charge transfer to the acceptor. This quenching is not complete, giving rise to PL emission from the devices, in agreement with previous results (see Chapter 6). Degradation in oxygen and dark leads to a gradual decrease of the emission (Figure 7.2a). Approximately $\sim$80% of the remaining polymer excited state is quenched after 3 hours, with most of the changes occurring within the first 30 minutes. This quenching is more efficient in devices subjected to both oxygen and light, marked by an almost complete loss of emission after 3 hours (Figure 7.2b). Although morphological changes are observed under the influence of light,[6,18] the laser intensity used in the PL experiment ($\sim$3 mW cm^{-2}) is much lower compared to 1 sun illumination (100 mW cm^{-2}) and hence reorganisation of the active layer can be neglected. Furthermore, de-mixing of donor and acceptor phases would lead to an increase of the emission as the quenching of the polymer excited state by the fullerene is reduced. These results suggest a second decay channel for polymer excitons, competing with charge transfer to the acceptor.

7.2.3 Photoelectron spectroscopy

To investigate the origin of this oxygen-related quenching, X-ray photoelectron spectroscopy (XPS) was employed. Figure 7.3 shows the XPS spectra
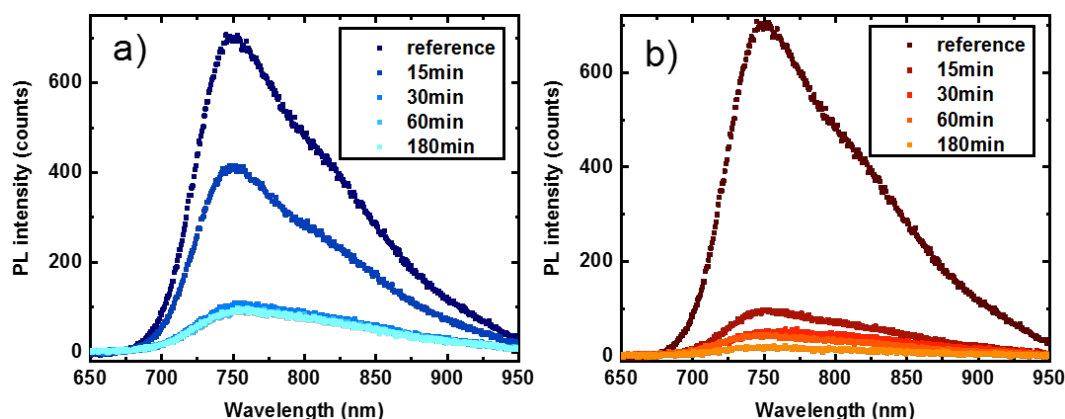
Figure 7.2: PL emission spectra of PffBT4T-2OD:PC$_{70}$BM solar cells in oxygen environments. Excitation of the donor was performed with a 447 nm laser through the glass/ITO surface onto the device area. (a) Degradation in 20 % oxygen under dark conditions. (b) Degradation in 20% oxygen under constant illumination. Adapted with permission from Ref.[1] Copyright 2019, American Chemical Society.

of sulphur (S2p), carbon (C1s), nitrogen (N1s), oxygen (O1s), and fluorine (F1s) both before and after prolonged degradation in 20% oxygen and continuous illumination for 20 hours. XPS may not be able to detect very small amounts of oxidised species, and Li et al. showed that already a few percent of oxidised PC$_{60}$BM can lead to significant reductions in device performance.[18] However, after degradation for over 20 hours the devices experienced substantial deterioration (PCE reduced by over 90%, see Figure 7.1d) and, thus, photo-oxidation products are expected to be resolvable if present. This was shown in our previous work for the model system P3HT:PC$_{60}$BM in which significant amounts of oxidised carbon and sulphur species could be detected after prolonged exposure to oxygen and light,[28] and has also been demonstrated for other materials.[29,30] For subtle changes, IR spectroscopy has been shown to be a more suitable tool.[21,31–33] Nevertheless, no changes in the chemical composition or binding energies of the components can be observed, indicating that no chemical oxidation of the materials occurred. Considering the strong effects in oxygen and light we speculate that light enhances the interaction with oxygen without inflicting additional photo-oxidation of the materials, in parallel to the previously reported light-induced impacts on active layer morphology or fullerene-mediated trap formation.
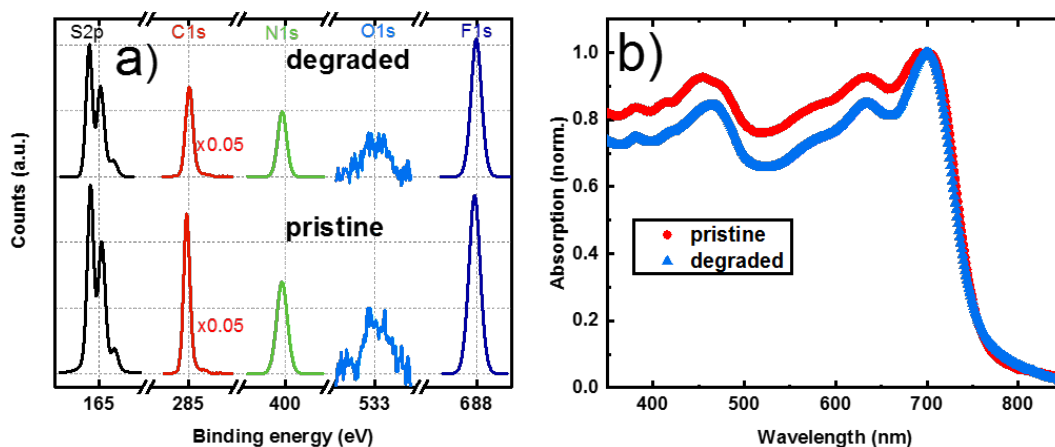
Figure 7.3: XPS spectra before and after 20 hours degradation in 20% oxygen under constant illumination. (b) Absorption spectra of PffBT4T-2OD:PC$_{70}$BM films before and after degradation in 20 % oxygen and constant illumination for 6 hours. Adapted with permission from Ref.[1] Copyright 2019, American Chemical Society.

A possible cause for the unusually strong decrease of the V$_{OC}$ in oxygen environments are changes of the bandgap or the energy levels of the materials after degradation. Therefore, absorption and ultra-violet photoelectron spectroscopy (UPS) spectra were measured. Since the effects are strongest in oxygen and continuous illumination, these conditions were used in the following experiments. Figure 7.3b shows the absorption of PffBT4T-2OD:PC$_{70}$BM films before and after degradation in 20% oxygen and constant illumination for 6 hours. The data has been normalised to specifically focus on changes of the optical gap. Apart from a more pronounced photo-bleaching at shorter wavelengths, no changes in the absorption properties of the blend can be observed; specifically, the optical gap remains unchanged.

To investigate changes in the frontier-molecular orbitals, UPS was employed to compare pristine (Figure 7.4a) and degraded (Figure 7.4b) films. The measurements were performed in the bulk of the films after etching the surface layers with an Argon cluster beam to exclude surface effects.[34] Only marginal changes of the ionisation potential of either material after storage in 20% oxygen and continuous illumination for 20 hours can be detected. Together with the absorption results, these measurements show that the energetics of the system remain unchanged even after substantial degradation. Therefore, the severe effects on the device performance must originate from increased recom-
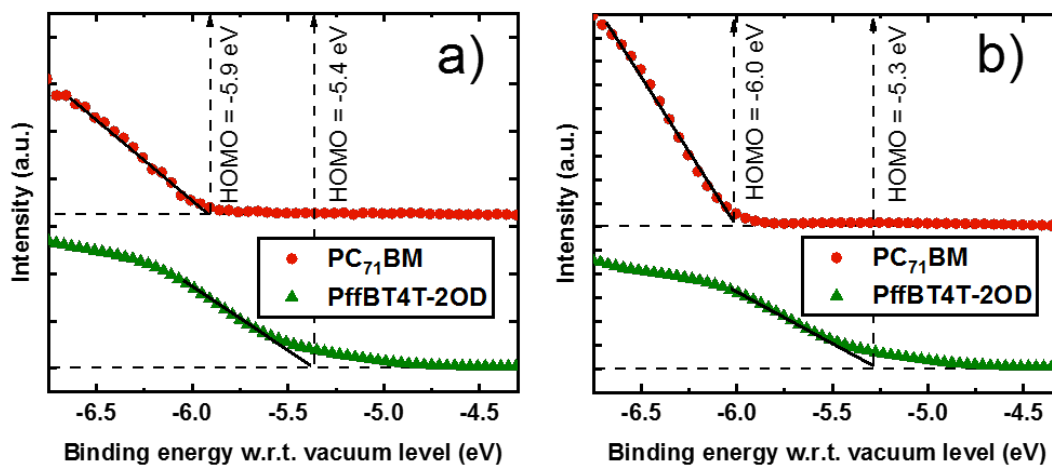
Figure 7.4: UPS spectra before (a) and after (b) 20 hours degradation in 20% oxygen under constant illumination. Adapted with permission from Ref.[1] Copyright 2019, American Chemical Society.

bination of charge carriers.

7.2.4   Transient absorption spectroscopy

To further investigate the effects of degradation on the charge generation, fs-TA was employed. Since the effects were strongest for the combined degradation in oxygen and light, and XPS measurements did not indicate any photo-oxidation of the materials, the following measurements were conducted for films and devices degraded under 20% oxygen and continuous illumination. In all measurements the polymer was exclusively excited by 700 nm pump pulses with low intensity (<10 nJ). The data analysis follows the methods detailed in Chapter 3, with the interpretation being similar to the results of Chapter 6. Global analysis for a polymer film at different stages of degradation yields two separate contributions (Figure 7.5). The dominating component is assigned to PffBT4T-2OD excitons which form instantly after absorption of the pump pulse. The decay in all films is marked by an initial fast component, corresponding to higher order exciton-exciton annihilation processes. Small differences in the dynamics compared to the previous chapter arise from the different optical setups in London and Heidelberg. In the latter, the spot size is smaller which leads to an increased intensity and therefore to increased recombination (see Chapter 5 for details of the setups). After this fast, initial
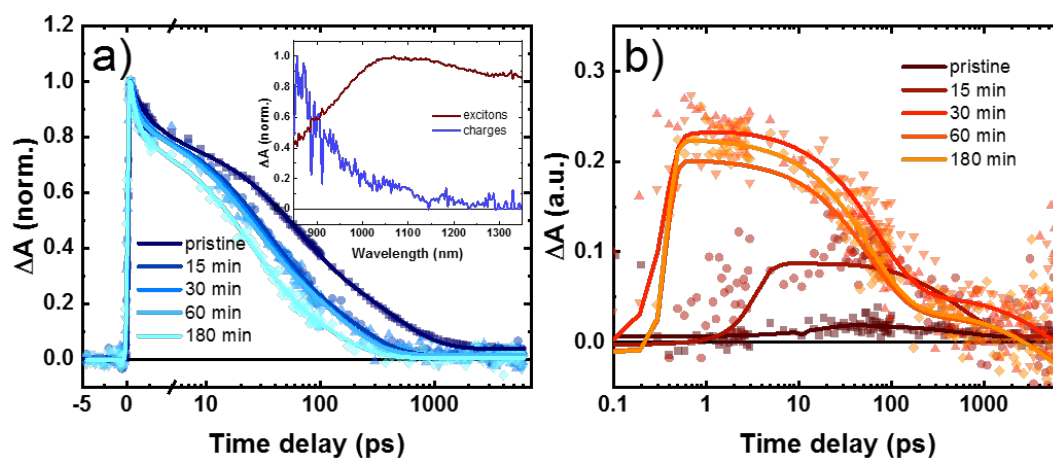
Figure 7.5: Global analysis results of TA data from neat PffBT4T-2OD films at different stages of degradation. The donor was excited with 700 nm pump pulses, with a low power of 10 nJ. (a) Exciton dynamics. (b) Trapped charges dynamics. Multi-exponential fits serve as guide to the eye.

component, the excitons decay with a slower rate towards the groundstate. In the pristine film, the charge pairs have a lifetime of ∼100 ps, and after 1 ns almost all excitons recombined, concurring with the results in Chapter 6 and previous reports.[35] With progressing degradation the exciton lifetime decreases by almost one order of magnitude after 3 hours of storage in oxygen and light.

Additionally to the exciton signal, the analysis yields a weakly absorbing second component. The inset compares the spectral profiles of the two contributions which can be assigned to donor excitons and charges when the results from the previous chapter are taken into account. A small contribution from this charge signal is measured in pristine films which can be caused by oxygen introduced during the fabrication process or residual impurities from the synthesis. With progressing degradation in oxygen and light two observations can be made: firstly, the magnitude of the second species is increasing until it saturates after 30 min of exposure to oxygen and light. Secondly, the dynamics gradually change towards early times. Both these observations in combination with the decreasing exciton lifetime indicate an oxygen-related quenching of the initial electron-hole pairs which becomes more efficient with increasing amounts of oxygen in the film.

As was detailed in Chapter 6, exciton dissociation in blend PffBT4T-2OD:PC_{70}BM films is suppressed by an energetic barrier preventing charge
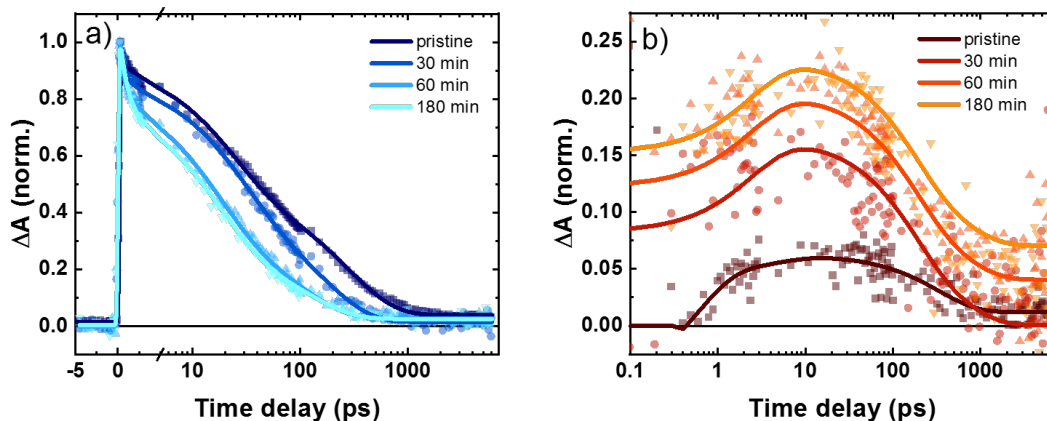
Figure 7.6: Global analysis results of TA data from blend PffBT4T-2OD:PC$_{70}$BM films at different stages of degradation. The donor was exclusively excited with 700 nm pump pulses, with a low power of 10 nJ. (a) Exciton dynamics. (b) Trapped charges dynamics. Multi-exponential fits serve as guide to the eye.

transfer from donor to acceptor, in contrast to complete devices. Therefore, the ultrafast results are expected to be similar to the polymer-only films. Figure 7.6 shows the results of the analysis of blend films at different stages of degradation.

Similar to the polymer-only films, two separate contributions are found by the algorithm (Figure 7.6a). Absorption of the 700 nm pump pulses leads to the creation of PffBT4T-2OD electron-hole pairs within the time resolution of the setup ($<$80 fs). The following exciton decay is similar to the results above, as free charge generation outside a device structure is prevented and hence no additional exciton quenching mechanism is present in blend films compared to polymer-only films. The reduced exciton lifetime during degradation is in agreement with the PL quenching in Figure 7.2 and indicates an evolving decay channel for the donor excitations.

With progressing degradation in oxygen and light, the magnitude of the second signal increases (Figure 7.6b), until after 3 hours it is comparable to free charges in a device (compare Figure 6.6 in the previous chapter). However, the dynamics of the charge signal here are markedly different from free charge carriers, with rise and decay times one order of magnitude faster in the degraded films. Additionally, with increasing oxygen uptake the second component becomes increasingly important at early times. These observations
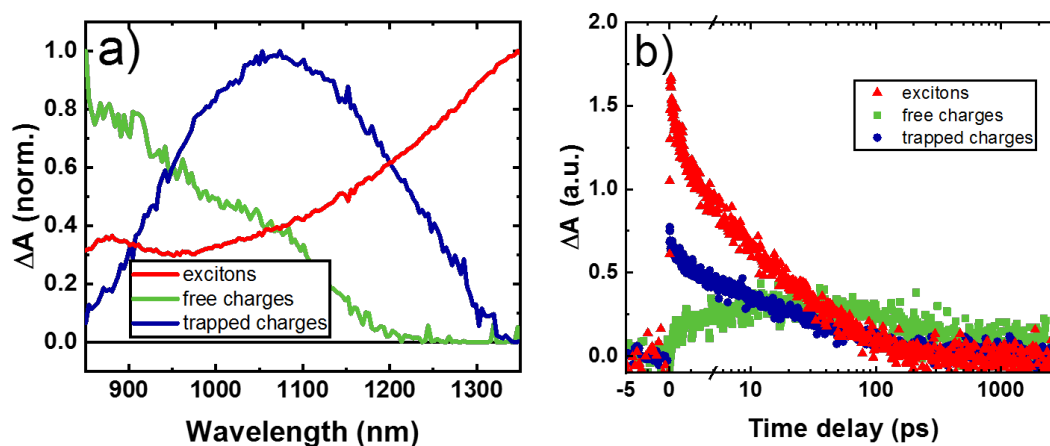
Figure 7.7: Global analysis results of TA data from PffBT4T-2OD:PC$_{70}$BM devices after 60 minutes of degradation. The donor was exclusively excited with 700 nm pump pulses, with a low power of 10 nJ. (a) Three components as a result from the analysis, corresponding to donor excitons, free charges, and trapped charges. (b) Dynamics of the three contributions. The trapped carriers primarily contribute at early times.

show that early charge separation in blend films occurs when operated in oxygen environments, demonstrated by the increased exciton quenching and the formation of short-lived charges. The analysis suggests that early charge transfer to oxygen-mediated defect states results from the exposure to oxygen and light.

Applying the bespoke methods onto a degraded, complete device, where efficient charge generation occurs, yields three distinct contributions (Figure 7.7a). The first two components represent donor excitons and free charges, agreeing spectrally with the results for pristine devices in the previous chapter (see Figure 6.5). A third species, markedly different from the other two, is found in the degraded device. The kinetics of exciton and free charges agree with the previous results in pristine devices (Figure 7.7b). The third component dominates primarily at early times (<100 ps), similarly to the trapped charges in the polymer-only and blend film. Therefore, this third contribution is assigned to trapped charges, resulting from charge transfer from the excited donor to defect states, created by the presence of oxygen. Note that analysis of a complete device, where free and trapped charges reside, is extremely difficult and the algorithm may not be able to separate all components completely
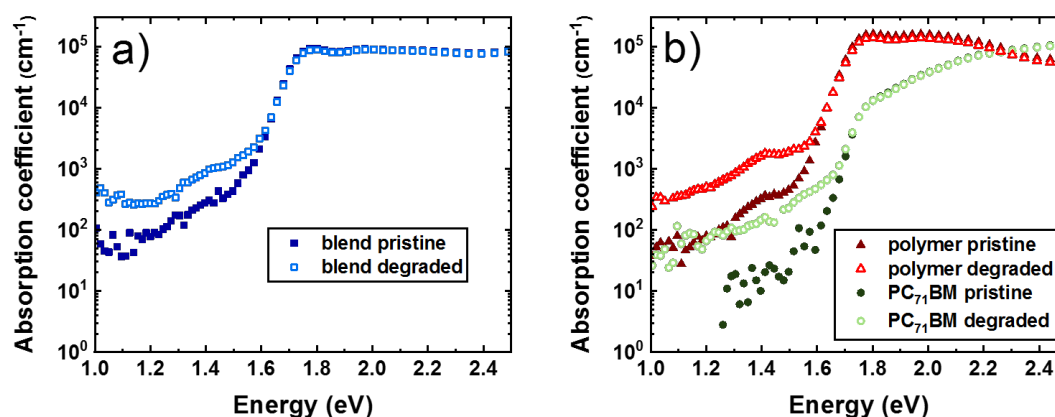
Figure 7.8: photo-thermal deflection spectroscopy (PDS) measurements of pristine and degraded films (for 6 hours in 20% and constant illumination. (a) Absorption spectra of blend films. (b) Absorption of the single materials. Absorption coefficients below $10\ cm^{-1}$ cannot be measured in this setup. Adapted with permission from Ref.[1] Copyright 2019, American Chemical Society.

which can explain the different kinetics of the trapped charges in devices and blend films. These observations suggest that additionally to the formation of free charges by CT at a donor:acceptor interface, oxygen-related exciton quenching occurs on an ultrafast timescale. The resulting unbound electron is trapped at the oxygen site where it experiences fast recombination.

7.2.5   Photothermal deflection spectroscopy

Further evidence for oxygen-induced trap formation can be obtained by photothermal deflection spectroscopy (PDS) which enables precise determination of the sub-bandgap absorption. Figure 7.8a shows the absorption spectra of blend films before and after degradation for 6 hours in 20% oxygen and continuous illumination. Only a minor reduction of the absorption is measured above the bandgap, in agreement with the UV-Vis results in Figure 7.3b. However, inside the bandgap an almost one order of magnitude increase of absorption is detected, stemming from oxygen -or light-induced formation of defect states. The distribution is seemingly uniform, indicative of shallow and deep traps below the band edge.

In both PffBT4T-2OD- and $PC_{70}BM$-only films the sub-bandgap absorption increases significantly after degradation (Figure 7.8b). Both materials exhibit similar formation of defect states, indicating that the degradation of

the blend films and devices is facilitated by each of the two components. The magnitude of the increased absorption is larger compared to the blend film, indicating a stabilising effect of the blend over the single materials.[15,36]

7.2.6 Organic field effect transistors

To further elucidate the mechanism of oxygen degradation, the material system was applied in ambipolar organic field effect transistors (OFETs). The used bottom-gate/top-contact configuration (see Chapter 4) exhibits excellent performance, low hysteresis with hole mobility of 0.3 cm^2 V^{-1} s^{-1}, and weak ambipolar behaviour with electron mobility of 0.016 cm^2 V^{-1} s^{-1}. The transistors have been degraded simultaneously with the solar cells in the sample holder described above, while their output and transfer characteristics have been measured in-situ. A reference measurement of the transfer characteristics in nitrogen over 15 hours is shown in Figure 7.9a. The curves show an increase of the threshold voltage in the p-channel with progressing operation in nitrogen under dark conditions. This shift is a common observation and is ascribed to a gradual filling of trap states in the channel by subsequent transfer measurements.[37,38] Additionally, the hole mobility increases slightly by $\sim20\%$ as a consequence of the aforementioned passivation of defect states (see Figure 7.9c).

Operation of the transistors in dark oxygen environment changes its behaviour considerably (Figure 7.9b) The threshold voltage for the hole transport shifts to more positive values, indicating a gradual increase of the charge carrier concentration in the channel. This behaviour is suggestive of a p-doping mechanism of the polymer domain which supplies mobile holes to the transport with a consequently decreasing threshold voltage, compensating the trend in pure nitrogen. The hole mobility (Figure 7.9c) remains largely unaffected by the degradation in oxygen, and increases slightly due to passivation of traps inside the channel. Throughout the experiment the injection into the active layer remains stable which can be seen by the output curves in Figure 7.9d.

7.3 Discussion

PffBT4T-2OD:PC_{70}BM solar cells show exceptionally poor device stability, even under inert conditions. The strong degradation effects have previously been attributed to small-scale morphological changes in the active layer of the devices. At elevated temperatures, which are a consequence of continuous illu-
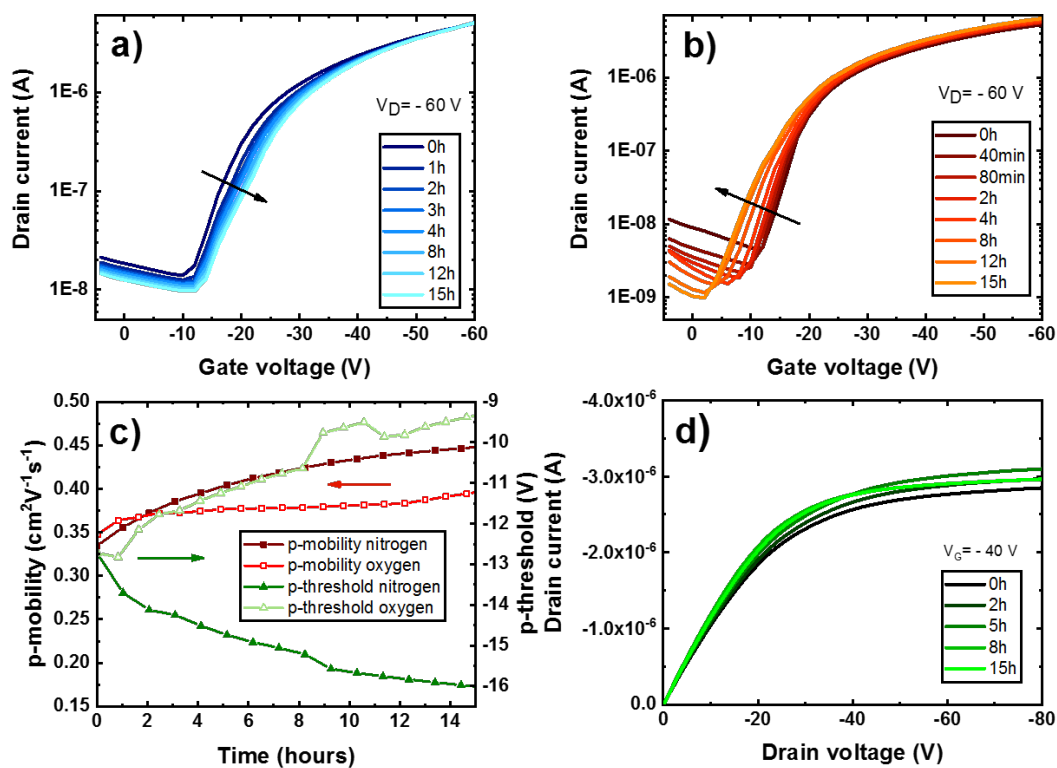
Figure 7.9: OFET measurements during operation in nitrogen or 20% oxygen without illumination. (a) Transfer curves in nitrogen. (b) Transfer curves in oxygen. (c) Extracted hole mobility and p-threshold voltage for OFETs in nitrogen or oxygen. (d) Output curves for transistors operated in oxygen atmosphere. Adapted with permission from Ref.[1] Copyright 2019, American Chemical Society.

mination, de-mixing of the donor and acceptor phases leads to a rapid decrease of interfacial area for charge generation and therefore to a significant reduction of the generated current.[18] This process is accelerated by the presence of processing additives, such as DIO.[7] Under light the fullerenes quickly degrade, leading to light-induced formation of defect states.[6] While previous reports focussed on the evolution of the microstructure in nitrogen atmospheres and on the role of the fullerene acceptor, the influence of oxygen onto the blend and particularly the polymer part was investigated in this work.

Operation of PffBT4T-2OD:PC$_{70}$BM OPVs in oxygen environments accelerates the device degradation significantly. This degradation is mainly caused by an unusually strong reduction of V$_{OC}$ together with a rapid decay of J$_{SC}$. Measurements of the optical gap and the frontier-molecular orbitals before and after excessive degradation in oxygen and light show no changes of the energy levels of the blend components, implying that massively increased recombination must be responsible for the strong effects on V$_{OC}$. Measuring the PL emission of complete devices at different stages of degradation shows efficient quenching of the donor excitons in oxygen. The dynamics of this PL quenching were investigated using ultrafast TA spectroscopy. A reduction of the exciton lifetime concurs with the steady-state results, showing oxygen-induced quenching of the electron-hole pairs. Additionally to the exciton population, a second contribution is measured in polymer-only films, which exhibits fast formation and recombination dynamics. This second component is spectrally similar to charge carriers in complete devices, albeit with markedly different kinetics. Analysing the blend film, which is photophysically similar to the pure polymer film since the generation of free charge carriers is prevented, shows the same results: the early formation of the charge species concurs with the reduction of the exciton lifetime. This observation suggests that oxygen-induced defect states cause efficient exciton dissociation by trapping and recombination of charge carriers. This suggestion is further supported by analysing complete devices in which, next to excitons and free charges, trapped charge carriers are detected as a third component which primarily influences the signal in the first 100 ps. Confirmation of the oxygen-mediated trap states is obtained by PDS measurements of the bandgap. In both the single materials as well as in the blend an increased absorption below the bandedge is detected, clearly showing the formation of defect states.

To identify the mechanism of oxygen degradation in the material system, the output and transfer characteristics of OFETs were measured during degradation. The shift of the threshold voltage to smaller values is in agreement

with p-doping of the channel. It was furthermore confirmed by XPS measurements that no photo-oxidation of the materials is occurring when the devices are degraded simultaneously in oxygen and light. The rapid device deterioration under the combined influence of oxygen and light is likely a consequence of two separate degradation mechanisms: the previously reported light-induced separation of donor and acceptor phases, and an additional oxygen-related degradation mechanism. The TA and PDS results of the single materials also confirm that the degradation is not limited to one of the blend components, but affects the entire bulk.

Considering the aforementioned results, we speculate that oxygen-induced p-doping is responsible for the severe performance loss. In contrast to irreversible photo-oxidation, which is a common observation in polymer:fullerene OPVs (see Chapter 2),[15–17,39] we propose a reversible interaction with oxygen, similar to previously reported material systems.[10–14,28,40,41] This suggestion is supported by measuring the device performance in oxygen followed by vacuum treatment (10^{-6} mbar) which is shown in the appendix (Figure A.3). The performance can be partly recovered, mainly caused by the reversibility of FF and J_{SC}, confirming that reversible oxygen degradation is a major loss channel in PffBT4T-2OD:PC$_{70}$BM solar cells. It has to be noted that with the used methods it is impossible to derive a detailed chemical mechanism for the observed results. A weakly interacting charge transfer complex between polymer and molecular oxygen is a reasonable assumption.

7.4 Conclusions

To conclude this study, it has been shown that severe performance losses are observed when PffBT4T-2OD:PC$_{70}$BM devices are operated in oxygen environments. It has been proposed that oxygen-induced p-doping of the active layer components is responsible degradation mechanism. These results highlight the need to develop efficient mitigation strategies, limiting the impact of oxygen onto the active components or preventing the diffusion of molecular oxygen into the device. This is particularly important for the new generation materials, such as systems employing NFAs, which push the device efficiencies to unprecedented levels.

Bibliography

[1] Weu, A.; Kress, J. A.; Paulus, F.; Becker-Koch, D.; Lami, V.; Bakulin, A. A.; Vaynzof, Y. Oxygen-Induced Doping as a Degradation Mechanism in Highly Efficient Organic Solar Cells. *ACS Applied Energy Materials* **2019**, *2*, 1943–1950.

[2] Heumueller, T.; Mateker, W. R.; Distler, A.; Fritze, U. F.; Cheacharoen, R.; Nguyen, W. H.; Biele, M.; Salvador, M.; Von Delius, M.; Egelhaaf, H. J.; McGehee, M. D.; Brabec, C. J. Morphological and electrical control of fullerene dimerization determines organic photovoltaic stability. *Energy and Environmental Science* **2016**, *9*, 247–256.

[3] Wang, J.; Enevold, J.; Edman, L. Photochemical Transformation of Fullerenes. *Advanced Functional Materials* **2013**, *23*, 3220–3225.

[4] Yan, L.; Wang, Y.; Wei, J.; Ji, G.; Gu, H.; Li, Z.; Zhang, J.; Luo, Q.; Wang, Z.; Liu, X.; Xu, B.; Wei, Z.; Ma, C.-Q. Simultaneous performance and stability improvement of polymer:fullerene solar cells by doping with piperazine. *Journal of Materials Chemistry A* **2019**, *7*, 7099–7108.

[5] Inasaridze, L. N.; Shames, A. I.; Martynov, I. V.; Li, B.; Mumyatov, A. V.; Susarova, D. K.; Katz, E. A.; Troshin, P. A. Light-induced generation of free radicals by fullerene derivatives: an important degradation pathway in organic photovoltaics? *Journal of Materials Chemistry A* **2017**, *5*, 8044–8050.

[6] Cha, H.; Wu, J.; Wadsworth, A.; Nagitta, J.; Limbu, S.; Pont, S.; Li, Z.; Searle, J.; Wyatt, M. F.; Baran, D.; Kim, J.-S.; McCulloch, I.; Durrant, J. R. An Efficient, "Burn in" Free Organic Solar Cell Employing a Nonfullerene Electron Acceptor. *Advanced Materials* **2017**, , 1701156.

[7] Pearson, A. J.; Hopkinson, P. E.; Couderc, E.; Domanski, K.; Abdi-Jalebi, M.; Greenham, N. C. Critical light instability in CB/DIO processed PBDTTT-EFT:PC71BM organic photovoltaic devices. *Organic Electronics* **2016**, *30*, 225–236.

[8] Khelifi, S.; Voroshazi, E.; Spoltore, D.; Piersimoni, F.; Bertho, S.; Aernouts, T.; Manca, J.; Lauwaert, J.; Vrielinck, H.; Burgelman, M. Effect of light induced degradation on electrical transport and charge extraction

in polythiophene:Fullerene (P3HT:PCBM) solar cells. *Solar Energy Materials and Solar Cells* **2014**, *120*, 244–252.

[9] Street, R. A.; Davies, D. M. Kinetics of light induced defect creation in organic solar cells. *Applied Physics Letters* **2013**, *102*, 043305.

[10] Schafferhans, J.; Baumann, A.; Wagenpfahl, A.; Deibel, C.; Dyakonov, V. Oxygen doping of P3HT:PCBM blends: Influence on trap states, charge carrier mobility and solar cell performance. *Organic Electronics* **2010**, *11*, 1693–1700.

[11] Guerrero, A.; Boix, P. P.; Marchesi, L. F.; Ripolles-Sanchis, T.; Pereira, E. C.; Garcia-Belmonte, G. Oxygen doping-induced photogeneration loss in P3HT:PCBM solar cells. *Solar Energy Materials and Solar Cells* **2012**, *100*, 185–191.

[12] Abdou, M. S.; Orfino, F. P.; Son, Y.; Holdcroft, S. Interaction of oxygen with conjugated polymers: Charge transfer complex formation with poly(3-alkylthiophenes). *Journal of the American Chemical Society* **1997**, *119*, 4518–4524.

[13] Aguirre, A.; Meskers, S.; Janssen, R.; Egelhaaf, H.-J. Formation of metastable charges as a first step in photoinduced degradation in π-conjugated polymer:fullerene blends for photovoltaic applications. *Organic Electronics* **2011**, *12*, 1657–1662.

[14] Seemann, A.; Sauermann, T.; Lungenschmied, C.; Armbruster, O.; Bauer, S.; Egelhaaf, H.-J.; Hauch, J. Reversible and irreversible degradation of organic solar cell performance by oxygen. *Solar Energy* **2011**, *85*, 1238–1249.

[15] Reese, M. O.; Nardes, A. M.; Rupert, B. L.; Larsen, R. E.; Olson, D. C.; Lloyd, M. T.; Shaheen, S. E.; Ginley, D. S.; Rumbles, G.; Kopidakis, N. Photoinduced Degradation of Polymer and Polymer-Fullerene Active Layers: Experiment and Theory. *Advanced Functional Materials* **2010**, *20*, 3476–3483.

[16] Tournebize, A.; Bussière, P.-O.; Wong-Wah-Chung, P.; Thérias, S.; Rivaton, A.; Gardette, J.-L.; Beaupré, S.; Leclerc, M. Impact of UV-Visible Light on the Morphological and Photochemical Behavior of a Low-Bandgap Poly(2,7-Carbazole) Derivative for Use in High-Performance Solar Cells. *Advanced Energy Materials* **2013**, *3*, 478–487.

[17] Lee, H. K. H. et al. The role of fullerenes in the environmental stability of polymer:fullerene solar cells. *Energy & Environmental Science* **2018**, *11*, 417–428.

[18] Li, N.; Perea, J. D.; Kassar, T.; Richter, M.; Heumueller, T.; Matt, G. J.; Hou, Y.; Güldal, N. S.; Chen, H.; Chen, S.; Langner, S.; Berlinghof, M.; Unruh, T.; Brabec, C. J. Abnormal strong burn-in degradation of highly efficient polymer solar cells caused by spinodal donor-acceptor demixing. *Nature Communications* **2017**, *8*, 14541.

[19] Li, N.; Brabec, C. J. Air-processed polymer tandem solar cells with power conversion efficiency exceeding 10%. *Energy & Environmental Science* **2015**, *8*, 2902–2909.

[20] Kim, W.; Kim, J. K.; Kim, E.; Ahn, T. K.; Wang, D. H.; Park, J. H. Conflicted effects of a solvent additive on PTB7:PC71BM bulk heterojunction solar cells. *Journal of Physical Chemistry C* **2015**, *119*, 5954–5961.

[21] Tremolet de Villers, B. J.; O'Hara, K. A.; Ostrowski, D. P.; Biddle, P. H.; Shaheen, S. E.; Chabinyc, M. L.; Olson, D. C.; Kopidakis, N. Removal of Residual Diiodooctane Improves Photostability of High-Performance Organic Solar Cell Polymers. *Chemistry of Materials* **2016**, *28*, 876–884.

[22] Umeyama, T.; Igarashi, K.; Sakamaki, D.; Seki, S.; Imahori, H. Unique cohesive nature of the β 1 -isomer of [70]PCBM fullerene on structures and photovoltaic performances of bulk heterojunction films with PffBT4T-2OD polymers. *Chemical Communications* **2018**, *54*, 405–408.

[23] Ma, W.; Yang, G.; Jiang, K.; Carpenter, J. H.; Wu, Y.; Meng, X.; McAfee, T.; Zhao, J.; Zhu, C.; Wang, C.; Ade, H.; Yan, H. Influence of Processing Parameters and Molecular Weight on the Morphology and Properties of High-Performance PffBT4T-2OD:PC$_{71}$BM Organic Solar Cells. *Advanced Energy Materials* **2015**, *5*, 1501400.

[24] Liu, Y.; Zhao, J.; Li, Z.; Mu, C.; Ma, W.; Hu, H.; Jiang, K.; Lin, H.; Ade, H.; Yan, H. Aggregation and morphology control enables multiple cases of high-efficiency polymer solar cells. *Nature Communications* **2014**, *5*, 5293.

[25] Zhang, Y.; Parnell, A. J.; Pontecchiani, F.; Cooper, J. F. K.; Thompson, R. L.; Jones, R. A. L.; King, S. M.; Lidzey, D. G.; Bernardo, G. Un-

derstanding and controlling morphology evolution via DIO plasticization in PffBT4T-2OD/PC71BM devices. *Scientific Reports* **2017**, *7*, 44269.

[26] Masters, R. C.; Wan, Q.; Zhang, Y.; Dapor, M.; Sandu, A. M.; Jiao, C.; Zhou, Y.; Zhang, H.; Lidzey, D. G.; Rodenburg, C. Novel organic photo-voltaic polymer blends: A rapid, 3-dimensional morphology analysis using backscattered electron imaging in the scanning electron microscope. *Solar Energy Materials and Solar Cells* **2017**, *160*, 182–192.

[27] Zhao, J.; Zhao, S.; Xu, Z.; Qiao, B.; Huang, D.; Zhao, L.; Li, Y.; Zhu, Y.; Wang, P. Revealing the Effect of Additives with Different Solubility on the Morphology and the Donor Crystalline Structures of Organic Solar Cells. *ACS Applied Materials & Interfaces* **2016**, *8*, 18231–18237.

[28] Weu, A. Identifying Degradation Mechanisms in P3HT:PCBM Organic Solar Cells. Master thesis, Universität Heidelberg, 2016.

[29] Kettle, J.; Ding, Z.; Horie, M.; Smith, G. XPS analysis of the chemical degradation of PTB7 polymers for organic photovoltaics. *Organic Electronics* **2016**, *39*, 222–228.

[30] Tabačiarová, J.; Mičušík, M.; Fedorko, P.; Omastová, M. Study of polypyrrole aging by XPS, FTIR and conductivity measurements. *Polymer Degradation and Stability* **2015**, *120*, 392–401.

[31] Müller, C.; Glaser, T.; Plogmeyer, M.; Sendner, M.; Döring, S.; Bakulin, A. A.; Brzuska, C.; Scheer, R.; Pshenichnikov, M. S.; Kowalsky, W.; Pucci, A.; Lovrinčić, R. Water Infiltration in Methylammonium Lead Iodide Perovskite: Fast and Inconspicuous. *Chemistry of Materials* **2015**, *27*, 7835–7841.

[32] Thomas, P. S.; Guerbois, J.-P.; Russell, G. F.; Briscoe, B. J. FTIR Study of the Thermal Degradation of Poly(vinyl Alcohol). *Journal of Thermal Analysis and Calorimetry* **2001**, *64*, 501–508.

[33] Rivaton, A.; Chambon, S.; Manceau, M.; Gardette, J.-L.; Lemaître, N.; Guillerez, S. Light-induced degradation of the active layer of polymer-based solar cells. *Polymer Degradation and Stability* **2010**, *95*, 278–284.

[34] Lami, V.; Weu, A.; Zhang, J.; Chen, Y.; Fei, Z.; Heeney, M.; Friend, R. H.; Vaynzof, Y. Visualizing the Vertical Energetic Landscape in Organic Photovoltaics. *Joule* **2019**,.

[35] Cha, H.; Wheeler, S.; Holliday, S.; Dimitrov, S. D.; Wadsworth, A.; Lee, H. H.; Baran, D.; McCulloch, I.; Durrant, J. R. Influence of Blend Morphology and Energetics on Charge Separation and Recombination Dynamics in Organic Solar Cells Incorporating a Nonfullerene Acceptor. *Advanced Functional Materials* **2018**, *28*, 1704389.

[36] Manceau, M.; Rivaton, A.; Gardette, J.-L.; Guillerez, S.; Lemaître, N. Light-induced degradation of the P3HT-based solar cells active layer. *Solar Energy Materials and Solar Cells* **2011**, *95*, 1315–1325.

[37] Sirringhaus, H. Reliability of organic field-effect transistors. *Advanced Materials* **2009**, *21*, 3859–3873.

[38] Bobbert, P. A.; Sharma, A.; Mathijssen, S. G. J.; Kemerink, M.; de Leeuw, D. M. Operational Stability of Organic Field-Effect Transistors. *Advanced Materials* **2012**, *24*, 1146–1158.

[39] Mateker, W. R.; Heumueller, T.; Cheacharoen, R.; Sachs-Quintana, I. T.; McGehee, M. D.; Warnan, J.; Beaujuge, P. M.; Liu, X.; Bazan, G. C. Molecular Packing and Arrangement Govern the Photo-Oxidative Stability of Organic Photovoltaic Materials. *Chemistry of Materials* **2015**, *27*, 6345–6353.

[40] Lu, C.-K.; Meng, H.-F. Hole doping by molecular oxygen in organic semiconductors: Band-structure calculations. *Physical Review B* **2007**, *75*, 235206.

[41] Euvrard, J.; Revaux, A.; Cantarano, A.; Jacob, S.; Kahn, A.; Vuillaume, D. Impact of unintentional oxygen doping on organic photodetectors. *Organic Electronics* **2018**, *54*, 64–71.

Chapter 8

Photoprotection by small molecules

This chapter includes results from the manuscript "Energy Transfer to a Stable Donor Suppresses Degradation in Organic Solar Cells" which has been submitted to Advanced Functional Materials.[1] The environmental stability of the small molecule donor DRCN5T in oxygen and light is investigated by fs-TA spectroscopy. Solar cells comprising blends with the fullerene acceptor $PC_{70}BM$ exhibit remarkable device stability, primarily facilitated by an almost constant short-circuit current. This exceptional degradation behaviour is attributed to two separate mechanisms: firstly, the small molecule shows high intrinsic stability towards environmental factors and, apart from minor photo-bleaching effects, no signs of degradation can be detected. Secondly, the stability of the blend is increased by ultrafast energy transfer from the acceptor to the donor, thereby preventing high-energy excitations from degrading the fullerene. This photoprotective mechanisms can be utilised in other material systems incorporating unstable components, e.g. for non-fullerene acceptors or in ternary blends.

This chapter starts by briefly reviewing the research on the small molecule DRCN5T with particular emphasis on the degradation under ambient conditions. Following the results, which mainly reflect the photophysics on the ps-timescale, this chapter concludes with the proposed model of energy transfer which can explain the high stability of the films and devices. Finally, the observed results are discussed in the context of strategies for more stable OPV devices.

8.1   Introduction

With efficiencies already on the order of commercially available conventional technologies,[2] the operational stability of OPV devices remains a major challenge en route to widespread application.[3,4] As was shown in Chapter 2, a multitude of degradation mechanisms can affect the long-term stability of OSCs. Exposure to oxygen leads to p-doping of the active layer for some polymers (see Chapter 7), the combined influence of oxygen and light often results in photo-oxidation of the components and formation of trap states within the bandgap. Particularly the fullerene acceptors are a common source for degradation, as they are easily oxidised and susceptible for cluster formation at elevated temperatures which leads to de-mixing of the active materials.[5,6]

Solution processable small molecule (SM) have received an increasing interest as active materials in OPVs, owing to their easy purification, small batch-to-batch variation, and potentially higher environmental stability compared to polymer or fullerene materials.[7–11] They are already successfully employed as non-fullerene acceptors in OSCs, yielding significantly improved performance compared to conventional fullerene derivatives, due to superb aggregation properties and complementary absorption in the visible part of the spectrum.[12–18] Although less studied, some groups have used small molecule donors together with $PC_{70}BM$ or in all-SM OSCs and achieved remarkable PCEs.[19–23] In a ternary structure with $PC_{70}BM$, small molecules recently achieved an impressive 12.84% PCE.[24]

The donor molecule DRCN5T, designed by Y. Chen and co-workers,[25] has shown impressive results both with fullerene- and non-fullerene acceptors.[26–28] However, while the degradation patterns in polymer:fullerene systems are reasonably well understood, the stability of SM-devices has gained significantly less attention.[29–32] Previous degradation studies of the material system DRCN5T:$PC_{70}BM$ focussed entirely on analysing the microstructure of encapsulated devices after heat treatment.[33,34] Morphological changes, as common for devices employing fullerenes, lead to degradation of J_{SC} and FF. The specific role of DRCN5T in the degradation under ambient conditions is, however, hitherto unreported. Yet, a detailed understanding of the degradation mechanisms is highly relevant for future research, as DRCN5T can act as a benchmark material for SM-based OPVs.

8.2 Results

This section explores the stability DRCN5T:PC_{70}BM solar cells under degradation in oxygen and light. The device performance and external quantum efficiency (EQE) are measured in-situ and compared to other polymer:fullerene systems. At the same time, the processes of charge generation are investigated by ultrafast fs-TA spectroscopy and the impact of degradation is followed in the blend and in neat films. Finally, the charge transport and extraction properties are briefly discussed.

The fabrication of films and devices is explained in Chapter 4. Degradation was conducted in the aforementioned sample holder (see Chapter 5) under 20% oxygen and continuous 1 sun illumination. In-situ TA measurements were performed in ambient conditions (rel. humidity $40 \pm 5\%$) and under continuous white light illumination (100 mW cm^{-2}, Thorlabs MWWHD3). R. Kumar from the Imperial College, London assisted with the analysis of the transient datasets.

8.2.1 Device performance

The DRCN5T:PC_{70}BM devices in inverted architecture exhibit excellent performances with a maximum PCE of 8.2% (V_{OC} 0.94 V, J_{SC} 14.7 mA cm^{-2}, FF 59.5%) which is competitive with previously reported standard architecture devices.[25,34] At the time of writing, this was the first reported attempt to employ this material system in inverted architecture devices. Figure 8.1a shows the energy level diagram of the active layer which was approximated from the optical bandgap (Figure 8.1b) and the ionisation potentials of the materials. The latter were measured by V. Lami, details can be found in his doctoral thesis.[35] The inverted architecture was specifically chosen to minimise degradation effects from the interlayers and low workfunction electrodes and to focus on the degradation of the active layer (see Chapter 2).[7,36–39]

Figure 8.1b depicts the changes in absorption of the single materials after degradation for 12 hours. Some photobleaching can be observed between 400 nm and 760 nm for the SM donor, while for the fullerene acceptor no changes occur. The optical bandgaps of both materials, given by the absorption onsets, remain unchanged after degradation.

To investigate the stability of DRCN5T:PC_{70}BM devices, the performance was monitored in-situ during degradation in nitrogen (dark) and oxygen (1 sun) over the course of 33 hours in the sample holder (Figure 8.2). The reference
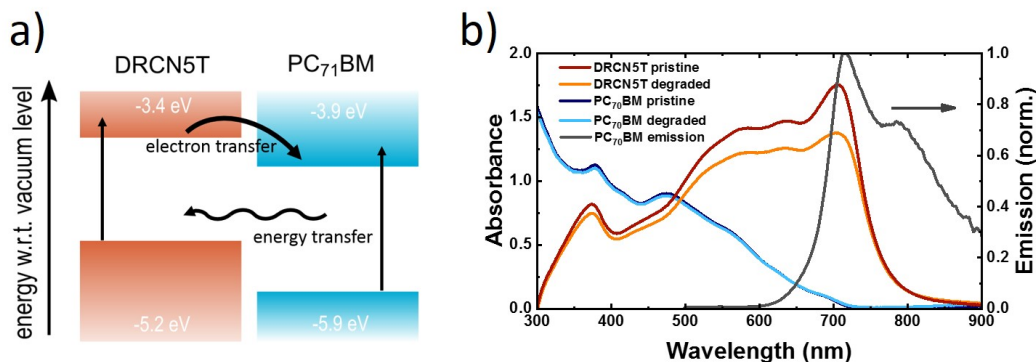
Figure 8.1: (a) Energy level diagram of DRCN5T:$PC_{70}BM$. Arrows indicate the photon absorption in the donor or acceptor, electron transfer from donor to acceptor and energy transfer from acceptor to donor. (b) Absorption and emission spectra of DRCN5T and $PC_{70}BM$ films, before and after 12 hours degradation. Emission spectrum courtesy of Edinburgh Instruments Ltd. Reproduced with permission from Ref.[1] Copyright Wiley-VCH Verlag GmbH & Co. KGaA.

experiment displays a performance drop of 20% which can mainly be attributed to the loss of FF. The V_{OC} decreases only marginally and the J_{SC} is increasing slightly which can be the result of delayed (light-induced) annealing of the active layer and subsequent improvement of the nanostructure or passivation of trap states in the ZnO ETL.[40,41] These changes are likely caused by subtle morphological reorganisation of the active layer, which has been previously observed for this material system.[33,34] Additionally, the MoO_3 hole transport layer can cause doping of the SM donor, leading to space charge effects which hinder the charge extraction.[42–45]

Operating OPVs in oxygen and light typically leads to rapid and significant degradation of the performance, foremost the J_{SC}, e.g. in the case of PffBT4T-2OD (see Chapter 7). However, the DRCN5T:$PC_{70}BM$ system shows exceptional stability with the J_{SC} retaining 90% of its initial value after 30 hours of degradation (Figure 8.2b). Simultaneously, V_{OC} and FF decrease at a slightly increased rate compared to the reference measurement in nitrogen which results in a 40% drop of PCE in the time frame of the experiment. Considering the degradation patterns in common material systems employing fullerene acceptors, DRCN5T:$PC_{70}BM$ devices exhibit remarkable operational stability. Since the apparent insensitivity of the J_{SC} towards external factors is the no-
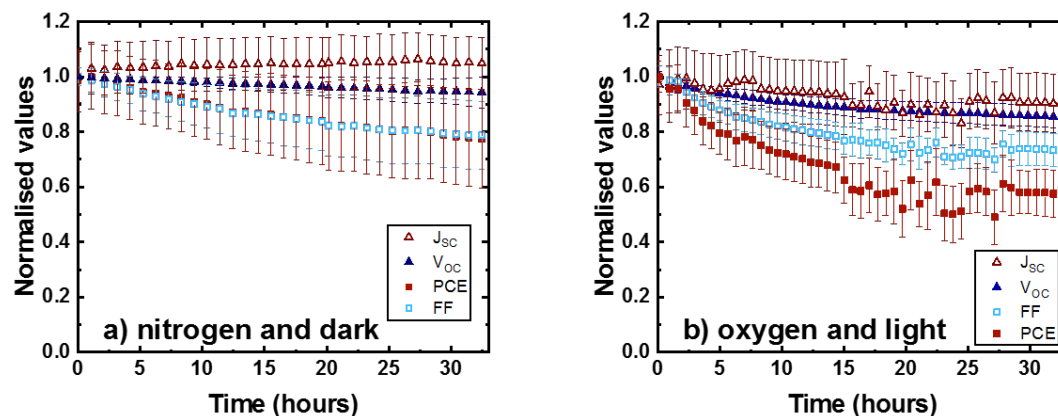
Figure 8.2: Normalised OSC parameters over time during degradation in (a) nitrogen and dark, (b) 20% oxygen and continuous 1 sun illumination. The data represents the mean and standard deviation of 10 and 11 solar cells on two substrates, respectively. Reproduced with permission from Ref.[1] Copyright Wiley-VCH Verlag GmbH & Co. KGaA.

table observation of this degradation study, the following results focus on this particular feature.

As a first step, we looked at the EQE of DRCN5T:PC_{70}BM devices during degradation (Figure 8.3a). The spectral region from 500 nm to 800 nm is predominantly governed by contributions from the donor; a minor reduction of the response in this part of the spectrum is measured, concomitantly with the loss of optical absorption of the small molecule (compare Figure 8.1b). At wavelengths below 500 nm, PC_{70}BM contributes increasingly to the current generation. The observed losses of the EQE are more pronounced in this region, but are not related to loss of optical absorption. The overall decrease of the EQE is unusually small when compared to other systems containing fullerene acceptors.[23,46,47] In devices containing PBDB-T-2Cl ('PCE-14') and PC_{70}BM, strong effects of degradation are observed which are typical for polymer:fullerene systems (Figure 8.3a).

Further indication of the unusual degradation dynamics of DRCN5T:PC_{70}BM devices during degradation is obtained by comparing the decay of the normalised J_{SC} to three high-efficiency, polymer:PC_{70}BM systems, namely PTB7, PBDB-T-2Cl, and PffBT4T-2OD (Figure 8.3b). While fast, initial degradation of the J_{SC} occurs in all three polymer systems, especially PffBT4T-2OD, the J_{SC} of the small molecule system remains almost unchanged after 18 hours
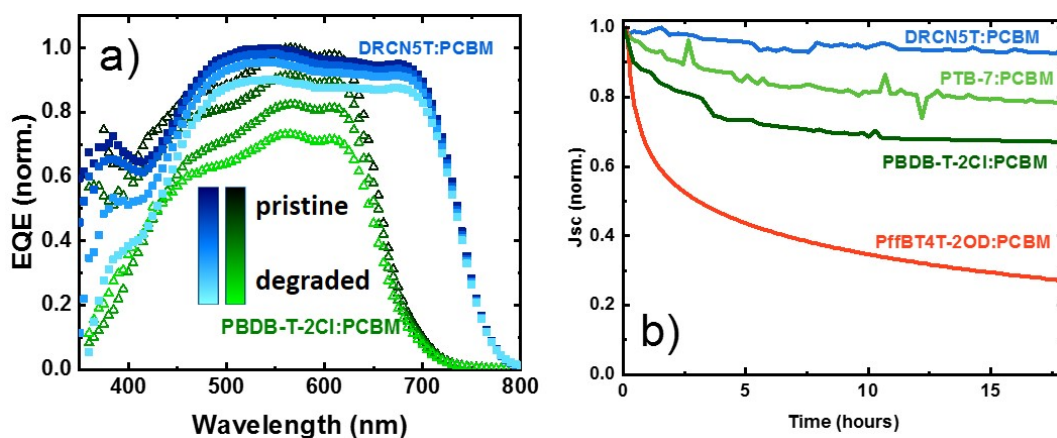
Figure 8.3: (a) Evolution of EQE spectra for DRCN5T:PC$_{70}$BM and PBDB-T-2Cl:PC$_{70}$BM solar cells upon exposure to 1 sun illumination and 20% oxygen for 22 h. (b) Reduction in J$_{SC}$ in DRCN5T:PC$_{70}$BM OSCs compared to three analogous polymer:fullerene OPV systems. Reproduced with permission from Ref.[1] Copyright Wiley-VCH Verlag GmbH & Co. KGaA.

of degradation.

8.2.2   Charge generation

In order to elucidate this unique behaviour in DRCN5T:PC$_{70}$BM devices, fs-TA spectroscopy was used to investigate the processes of charge generation on the ultrafast timescale. The transient spectra of neat donor and acceptor films in the NIR, which have been acquired after excitation with 700 nm and 350 nm pump pulses (150 nJ), respectively, exhibit a broad excited state absorption (ESA) feature representing the DRCN5T and PC$_{70}$BM exciton (Figures 8.4 a and b). The corresponding kinetics, at representative wavelengths of 1200 nm and 1350 nm, show that after absorption of the pump pulse, excitons are created within the time resolution of the setup (<80 fs) and decay subsequently by radiative and non-radiative processes to the groundstate within 8 ns (Figures 8.4 d and e).

The exciton dynamics of the neat DRCN5T films show no changes during during degradation for 9 hours (Figure 8.4d). Specifically, no additional component, e.g. from trap states (compare to PffBT4T-2OD excitons in Chapter 7) can be detected. Therefore, the donor excitons are largely unaffected by the presence of oxygen and light, demonstrating a high intrinsic stability towards
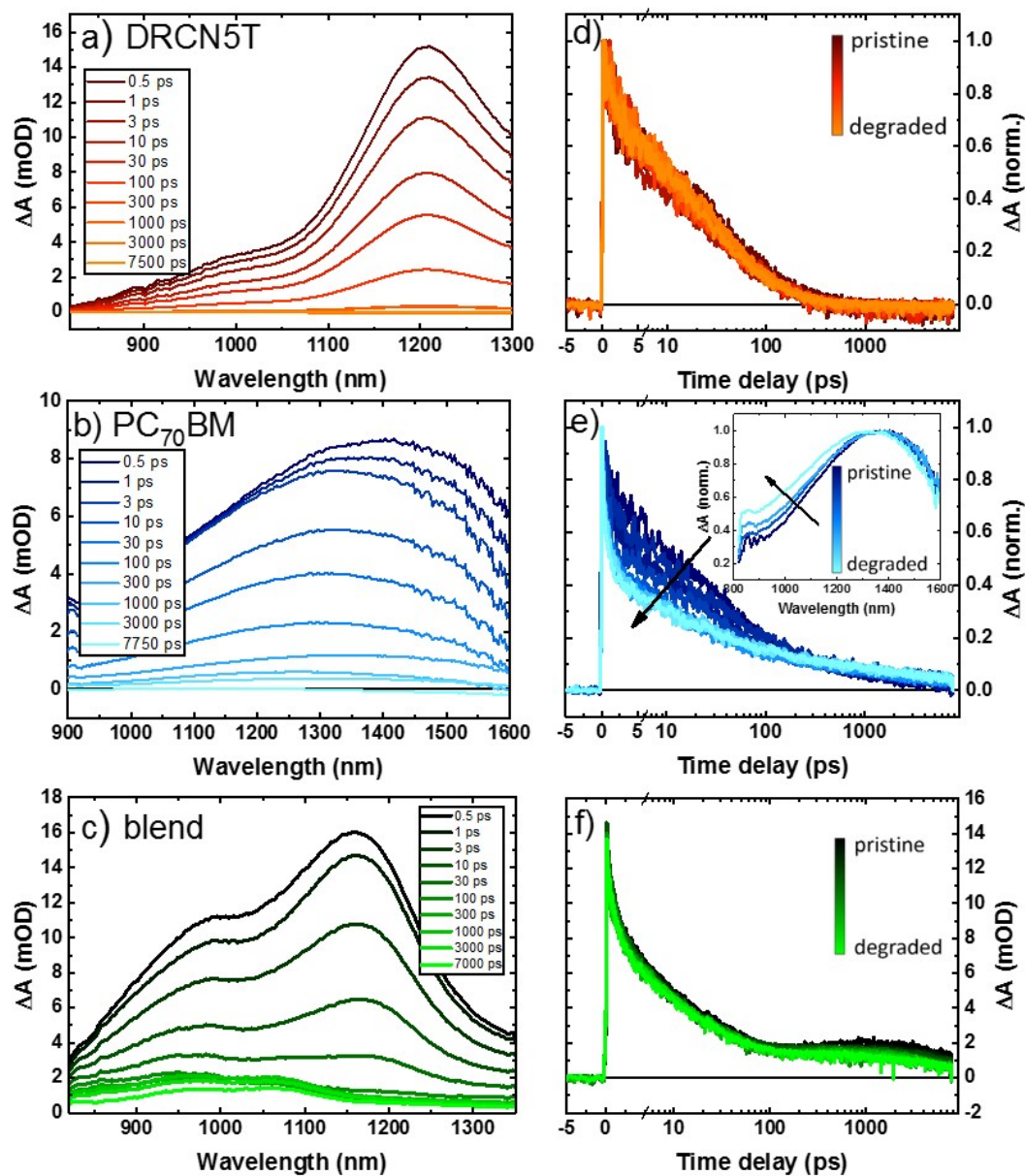
Figure 8.4: Transient absorption data for films of the single materials and blend, excited with 150 nJ pump pulses. (a) Spectra of neat DRCN5T excited at 700 nm. (b) Spectra of neat $PC_{70}BM$ excited at 350 nm. (c) Spectra of blend excited at 700 nm. (d) Kinetics of DRCN5T excitons, probed at 1200 nm, over 9 hours of degradation. (e) Kinetics of $PC_{70}BM$ excitons, probed at 1350 nm, over 7 hours of degradation. Inset: spectral change at time delay of 1 ps. (f) Kinetics of blend, probed at 1050 nm, over 5 hours of degradation. Reproduced with permission from Ref.[1] Copyright Wiley-VCH Verlag GmbH & Co. KGaA.

these factors. In contrast to the small molecule, the dynamics of the fullerene exciton are strongly affected by the degradation (Figure 8.4e). During 7 hours of degradation, the lifetime of the excited states decreases from 50 ps to 7 ps, implying an efficient initial quenching mechanism. Furthermore, the degradation leads to the formation of a long-lived species, marked by the marginally increased signal at later times. The formation of this additional component is moreover indicated by the changes of the transient spectra (inset Figure 8.4e). The signal at lower wavelengths gradually increases during degradation, concomitantly with the decrease of exciton lifetime. We speculate that the increased early quenching of the signal and formation of long-lived states can be rationalised by the generation of oxygen- or light-induced trap states, similarly to the results obtained for PffBT4T-2OD in Chapter 7. Gap states in the fullerene after degradation were also observed by PDS measurements, see Section 7.2.5, which further supports this assumption.

After investigating the single materials, we now focus on the processes occurring in the blend. Since no indication of field-dependent photophysics was observed (see Figure A.4 in the appendix) the following studies were conducted on films rather than complete devices. Figure 8.4c show the spectra of a DRCN5T:PC$_{70}$BM film, after excitation of the donor with a 700 nm pump pulse. The shape and decay of the spectra at early times follows the dynamics of the DRCN5T exciton. However, a long-lived species builds up at wavelengths below 1200 nm, which is absent in the neat film. The formation of an additional population is also indicated by the kinetics at a probe wavelength of 1050 nm (Figure 8.4f). Initially, the signal decays much faster compared to the SM-only film and a long-lived contribution prevails at later times until the end of the measurement window (> 8 ns). These observations are ascribed to the fast quenching of the donor excitons by the acceptor molecules with subsequent electron transfer to the fullerene, creating free charges in the blend films. The long lifetime of the signal suggests that recombination of the charges occurs primarily through bimolecular processes.[48] The dynamics of the signal do not change considerably during degradation. Furthermore, no photobleaching is observed which is the result of quenching the donor excited state by the acceptor, thereby removing the high-energy electron from the small molecule before it can cause degradation.[49,50]

Using the information from the raw data, a global analysis was employed to separate the dynamics of excitons and charges in the blend (Figure 8.5). The algorithm yields two separate components, corresponding to donor exci-
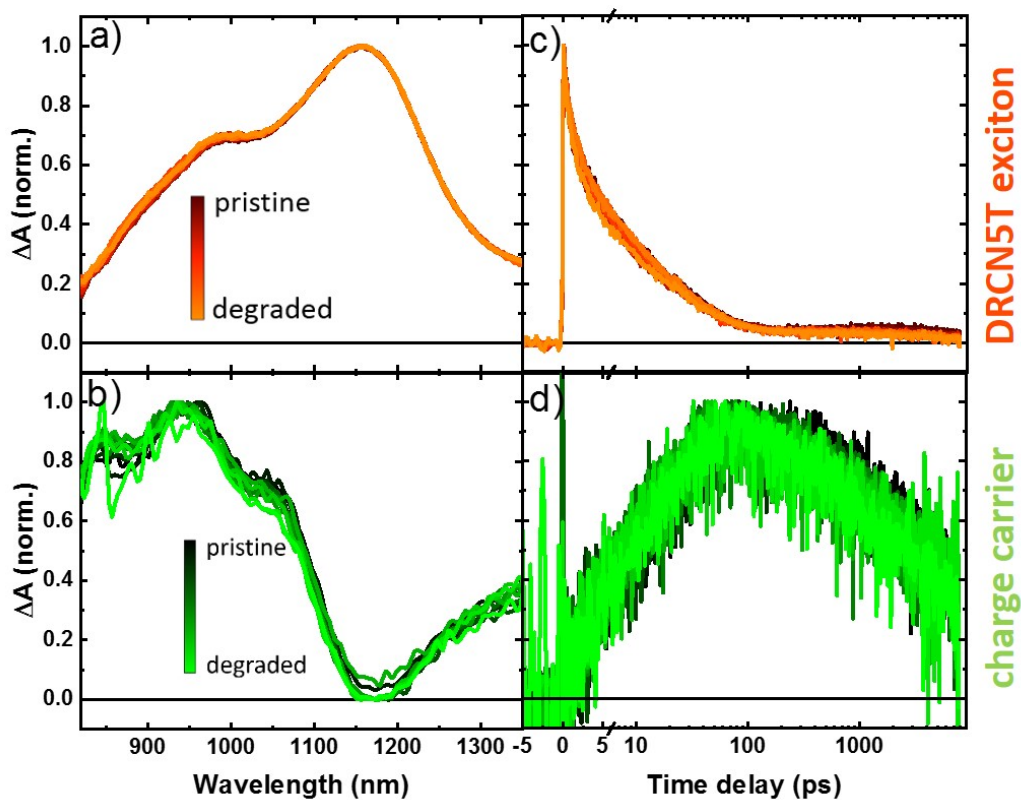
Figure 8.5: Spectra (left) and kinetics (right) of GA-derived components of the transient absorption spectrum of the DRCN5T:PC$_{70}$BM blend after 700 nm excitation (150 nJ) at selected stages of the degradation process. (a) DRCN5T exciton and (b) charge spectra show no signs of degradation. (c) Exciton and (d) charge kinetics are unchanged over 5 hours of degradation. Reproduced with permission from Ref.[1] Copyright Wiley-VCH Verlag GmbH & Co. KGaA.

tons and free charge carriers which agree spectrally with the aforementioned observations where initially excitons dominate at higher wavelengths around 1200 nm and subsequently free charges contribute to the signal for wavelengths between 800 nm and 1150 nm. The DRCN5T excitons show fast early decay, facilitated by charge transfer to the acceptor. After 100 ps the signal is almost vanished, suggesting an efficient electron transfer process. Concomitantly with the exciton dynamics, the charges are formed on a 10 ps timescale and are characterised by a long lifetime, which extends over the acquired time window of 8 ns. Note that previous reports on this system showed that in optimised blends almost no CT states are present which would contribute to the signal at wavelengths <900 nm.[51]

Comparing the transient spectra and kinetics at different stages of degradation reveals no changes after 5 hours. Some fluctuations in the fitted lifetimes are observed, but cannot be correlated to the extend of degradation (see Figure A.5 in the appendix). Concluding the results, the observations suggest that exciton creation in the DRCN5T, diffusion to the donor:acceptor interface, and subsequent electron transfer to the $PC_{70}BM$ are largely unaffected by the presence of oxygen and light. While this conclusion agrees with the experiments on the SM-only films, the EQE measurements and TA results from the fullerene-only films suggest that the degradation mainly affects the $PC_{70}BM$ part of the blend.

In order to investigate the role of the fullerene acceptor in the degradation of the system, the previous experiment on the blend film was repeated with 350 nm pump pulses which primarily excite the $PC_{70}BM$. Note that the SM donor weakly absorbs at 350 nm (Figure 8.1b), indicating that the acceptor is not exclusively excited. We compare the kinetics of the fullerene-only film with the blend film at the probe wavelength of 1300 nm which corresponds to the peak absorption of the $PC_{70}BM$ exciton (Figure 8.6). As observed before, the neat fullerene is strongly affected by degradation, resulting in an efficient quenching of the excitons at early times and simultaneous formation of trapped states. On the other hand, the signal of the blend film is seemingly unchanged during 5 hours of degradation. Considering the strong effects in the fullerene, which are usually responsible for the loss in performance in many material systems (see Chapter 2), the apparent stability of the blend is a remarkable observation. It suggests that the charge generation process which initiated by the absorption of high-energy photons in the acceptor is stabilised, similar to the previous results for absorption in the donor domains. Specifically, the early
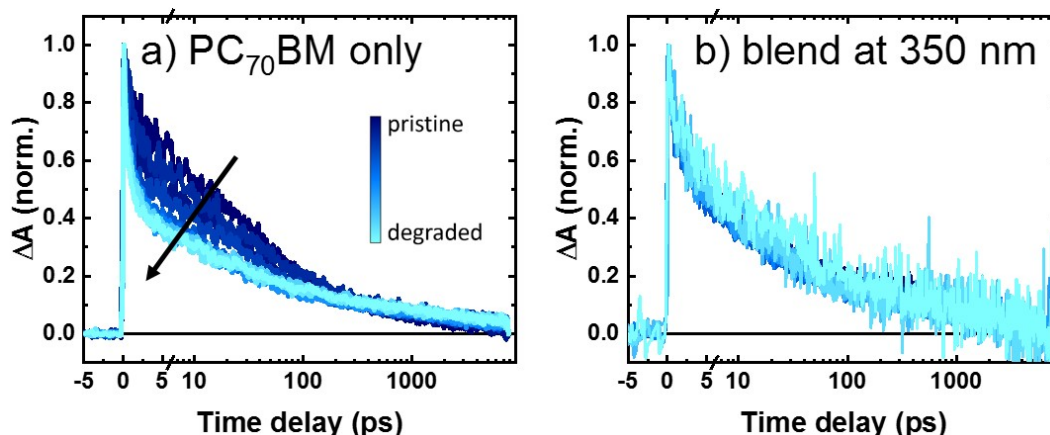
Figure 8.6: Normalised decay in amplitude of (a) neat $PC_{70}BM$ and (b) DRCN5T:$PC_{70}BM$ blend spectra excited with a 350 nm pump pulse (150 nJ) at the selected wavelength of 1300 nm at increasing extents of degradation (7 hours and 5 hours, respectively). Reproduced with permission from Ref.[1] Copyright Wiley-VCH Verlag GmbH & Co. KGaA.

quenching and formation of trapped charges in $PC_{70}BM$ is largely suppressed by the presence of the donor which implies an efficient stabilising mechanism in the blend.

To determine the mechanism behind the stabilisation of the acceptor in the blend compared to the single film, TA spectra of blend films following 250 nm excitation were recorded where the relative amount of excited $PC_{70}BM$ molecules is much larger compared to DRCN5T. The global analysis yields three separate components (Figure 8.7). The spectral profile of the first species (blue) is similar to $PC_{70}BM$ excitons from the fullerene-only films with dominating contributions at wavelengths above 1300 nm (Figure 8.4b). Following the absorption of the 250 nm pump pulses, $PC_{70}BM$ excitons are created and decay subsequently with a lifetime of ∼10 ps. Strikingly, in addition to a component representing free charges in the film (green), the analysis yields a third contribution with a spectral profile corresponding to DRCN5T excitons (red). According to the kinetics in Figure 8.7b, the donor excitons are not initially generated by the pump pulse, but form within 500 fs, concurrently with the acceptor exciton decay. Following the decay of the donor exciton population, long-lived, free charges are formed on a 10 ps timescale with subsequent bimolecular recombination. Note that the algorithm was not able to fully separate the signal of the $PC_{70}BM$ exciton from that of the free charges
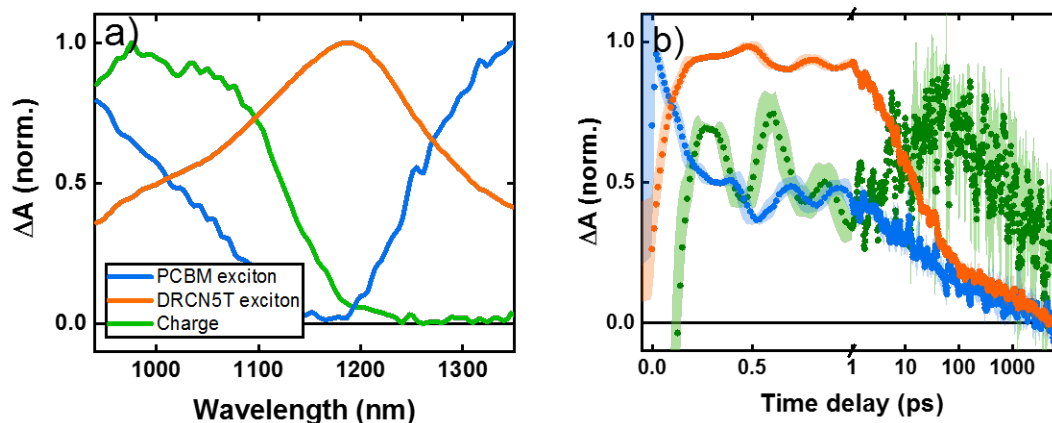
Figure 8.7: Normalised spectra (a) and kinetics (b) for the three contributions to the TA spectrum of DRCN5T:PC$_{70}$BM after 250 nm excitation (150 nJ): acceptor exciton (blue), donor exciton (red), and free charges (green). Kinetic traces are plotted as moving averages with associated errors shown. Reproduced with permission from Ref.[1] Copyright Wiley-VCH Verlag GmbH & Co. KGaA.

which results in the unphysical behaviour of the free charges at time delays <1 ps. The delayed formation of DRCN5T excitons through the decay of PC$_{70}$BM excitons is indicative of an efficient, sub-ps energy transfer from the fullerene acceptor to the SM donor. The resulting donor exciton diffuses to an interface where it dissociates via electron transfer, yielding free charges. Through this mechanism, the fullerene is protected as the high-energy excitations are efficiently removed on a sub-ps timescale. Since the small molecule is intrinsically stable, this energy transfer does not cause degradation of the donor.

8.2.3   Charge transport

The TA results show that the processes of charge generation are largely unaffected by degradation in ambient conditions which means specifically that exciton formation, its diffusion to a donor:acceptor interface, charge transfer, and subsequent formation of free charge carriers are stable. Additionally, we considered the transport characteristics of the generated charges. Since the charge transport in a donor:acceptor blend depends strongly on the morphology of the active layer, we performed X-ray diffraction (XRD) on pristine and degraded films to probe the blend morphology (Figure 8.8). The diffraction
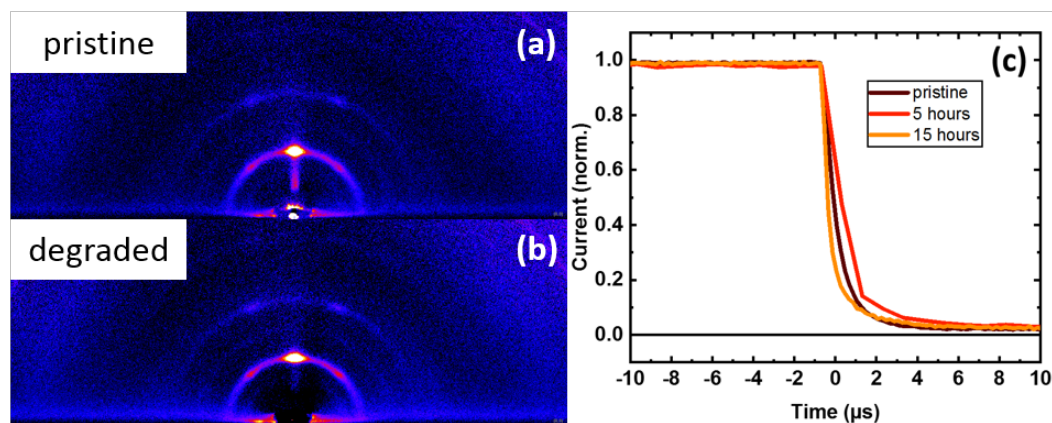
Figure 8.8: X-ray diffraction (XRD) and transient photocurrent (TPC) measurements of pristine and degraded samples. (a) XRD scan of a pristine DRCN5T:PC$_{70}$BM film. (b) The same film after 7 hours of degradation. (c) Extraction curves for DRCN5T:PC$_{70}$BM devices at different stages of degradation. The XRD measurements have been performed by F. Paulus. Reproduced with permission from Ref.[1] Copyright Wiley-VCH Verlag GmbH & Co. KGaA.

patterns agree with previously reported measurements on such films.[25] No changes in the crystallinity can be observed after degradation which shows that the large-scale morphology remains intact.

To further assess the extraction properties of the devices, transient photocurrent (TPC) measurements were performed at different stages of degradation (Figure 8.8c). Using TPC, the extraction time of the charges can be correlated to the presence of deep traps which retard the charge transport.[52,53] Here. no correlation between extraction time and degradation can be observed in the transient signals, suggesting that also the charge transport and extraction across the interfaces to the electrodes are stable during degradation.

8.3   Discussion

Based on the results discussed in the previous sections, we propose a mechanism to explain the remarkable stability of DRCN5T:PC$_{70}$BM devices (Figure 8.9). Excitation of the small molecule yields donor excitons which diffuse to an interface with the acceptor where the electron is transferred to the fullerene. This dissociation leads to the formation of long-lived free charges on a 10 ps timescale which decay bimolecularly. This process is seemingly unaffected by
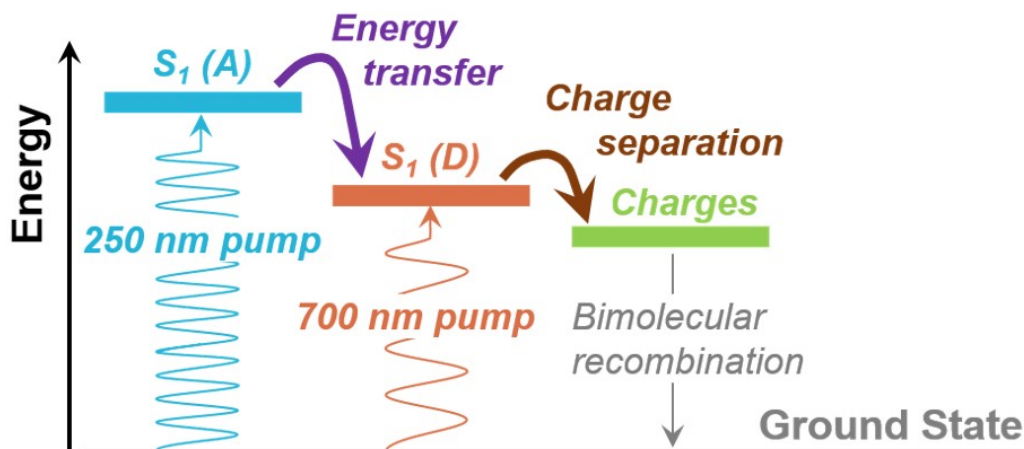
Figure 8.9: Proposed model of the energy transfer in DRCN5T:PC$_{70}$BM OSC devices. Excitation of the high-bandgap acceptor leads to sub-ps energy transfer, yielding donor excitons. These excitons undergo diffusion and electron transfer which results in long-lived charge carriers. Reproduced with permission from Ref.[1] Copyright Wiley-VCH Verlag GmbH & Co. KGaA.

the exposure to oxygen and light, because DRCN5T itself is intrinsically stable towards these conditions. Excitation of the acceptor at short wavelengths leads to the creation of high-energy fullerene excitons which, in combination with oxygen, usually cause rapid degradation in other systems (see Chapter 2). However, in the studied system efficient long-range energy transfer from the acceptor to the donor transfers the exciton to the stable small molecule, and thus, the fullerene is protected. The resulting donor exciton diffuses to a donor:acceptor interface and yields free charges by electron transfer back to the acceptor. This photoprotective process occurs on a sub-ps timescale and therefore outcompetes hole transfer from acceptor to donor which is on the order of 10 ps (after diffusion of the exciton). The energy transfer can be rationalised by a Förster-type process which is explained in Chapter 1. The Förster radius is given by

$$R_0^6 = \frac{9 \ln 10}{N_A} \frac{\kappa^2}{2^7 \pi^5 n^4} \Phi_D \int d\lambda \, \lambda^4 \cdot I_D(\lambda) \cdot \epsilon(\lambda) \tag{8.1}$$

where N_A is Avogadro's number, κ the orientation factor between the interacting dipoles, n the refractive index of the surrounding medium, Φ_D the PL quantum yield of the donating component, I_D the normalised emission of the

donating component, and ϵ the extinction coefficient of the accepting component. Assuming isotropic orientation of the dipoles ($\kappa^2 = 2/3$), a refractive index of $n = 1.5$, the photoluminescent quantum yield of $PC_{70}BM$ to be $\Phi_D = 0.01\%$, and calculating the overlap integral using the absorption and emission spectra in Figure 8.1b (by first determining the extinction coefficient using a film thickness of 340 nm), the Förster radius is on the order of $R_0 = 1.6$ nm, in agreement with similar reports in OPVs.[54–57]

In a larger sense, the observed mechanism allows to focus on the stability of one of the blend components, while the other does not limit the device stability, since it is protected by the energy transfer. Furthermore, in addition to more stable device operation, long-range energy transfer improves current generation by directed exciton transport to a donor:acceptor interface, instead of diffusion-limited exciton migration.[54,58–60] Therefore, by designing novel material systems with complementary emission and absorption, the proposed energy transfer can be utilised to focus exclusively on the electron transfer from donor to acceptor, since the limitations from inefficient hole transfer from acceptor to donor can be eliminated.[61,62]

We propose that this photoprotective mechanism can further be utilised in other systems with unstable components, such as fullerene derivatives, and should influence design rules towards more stable devices. While current research focuses on the development of novel material systems with efficient charge generation, our results demonstrate that complementary emission and absorption spectra of the constituents should also be considered. This can be particularly useful for NFAs with low electron affinity which exhibit high V_{OC} but facilitate the formation of radical oxygen species.[63–65] An example of DRCN5T blended with the non-fullerene acceptor IDIC, where the energetics prohibit energy transfer between the acceptor and the donor, is shown in Figure A.6a in the appendix.[16,66] Here, the J_{SC} drops to 10% after 25 hours of degradation which exemplifies the potential of energy transfer for the device stability. Furthermore, DRCN5T or similar molecules could be utilised as a third component in a ternary blend to increase the device stability.[24] A preliminary experiment with the system PBDB-T-2Cl:$PC_{70}BM$ shows that the stability of the J_{SC} can be significantly enhanced when 20% DRCN5T are added to the blend (Figure A.6b).

8.4   Conclusion

Photovoltaic devices comprising the material system DRCN5T:PC$_{70}$BM exhibit exceptional stability in oxygen or ambient conditions under continuous 1 sun illumination. This stability is primarily driven by the apparent insensitivity of the J$_{SC}$ towards degradation, retaining over 90% of its initial value after 30 hours in the aforementioned conditions. These observations can be rationalised by two separate conclusions: through the use of fs-TA spectroscopy it was shown that firstly, the small molecule donor is intrinsically very stable, showing no signs of degradation and secondly, the fullerene acceptor is protected by the presence of the donor through efficient, long-range, and ultrafast energy transfer from PC$_{70}$BM to DRCN5T. The latter leads to a sub-ps quenching of the fullerene excited state which would otherwise cause rapid degradation. Furthermore, the transport and extraction characteristics remain largely unchanged which together with the stable charge generation explains the robustness of the J$_{SC}$ towards the degradation conditions. We propose that this photoprotective mechanism can also be used in other systems with unstable components and should influence design rules towards more stable OSC devices, for example with non-fullerene acceptor or in ternary blends.

Bibliography

[1] Weu, A.; Kumar, R.; Butscher, J. F.; Lami, V.; Paulus, F.; Bakulin, A. A.; Vaynzof, Y. Energy Transfer to a Stable Donor Suppresses Degradation in Organic Solar Cells. *Advanced Functional Materials* **2019**, *submitted*, Sep.

[2] Cui, Y.; Yao, H.; Zhang, J.; Zhang, T.; Wang, Y.; Hong, L.; Xian, K.; Xu, B.; Zhang, S.; Peng, J.; Wei, Z.; Gao, F.; Hou, J. Over 16% efficiency organic photovoltaic cells enabled by a chlorinated acceptor with increased open-circuit voltages. *Nature Communications* **2019**, *10*, 2515.

[3] Fan, B.; Zhang, D.; Li, M.; Zhong, W.; Zeng, Z.; Ying, L.; Huang, F.; Cao, Y. Achieving over 16% efficiency for single-junction organic solar cells. *Science China Chemistry* **2019**, , 1–7.

[4] Yuan, J.; Zhang, Y.; Zhou, L.; Zhang, G.; Yip, H.-L.; Lau, T.-K.; Lu, X.; Zhu, C.; Peng, H.; Johnson, P. A.; Leclerc, M.; Cao, Y.; Ulanski, J.; Li, Y.; Zou, Y. Single-Junction Organic Solar Cell with over 15% Efficiency Using Fused-Ring Acceptor with Electron-Deficient Core. *Joule* **2019**, *3*, 1140–1151.

[5] Lee, H. K. H. et al. The role of fullerenes in the environmental stability of polymer:fullerene solar cells. *Energy & Environmental Science* **2018**, *11*, 417–428.

[6] Li, N.; Perea, J. D.; Kassar, T.; Richter, M.; Heumueller, T.; Matt, G. J.; Hou, Y.; Güldal, N. S.; Chen, H.; Chen, S.; Langner, S.; Berlinghof, M.; Unruh, T.; Brabec, C. J. Abnormal strong burn-in degradation of highly efficient polymer solar cells caused by spinodal donor-acceptor demixing. *Nature Communications* **2017**, *8*, 14541.

[7] Hermenau, M.; Riede, M.; Leo, K. *Stability and Degradation of Organic and Polymer Solar Cells*; John Wiley & Sons, Ltd: Chichester, UK, 2012; pp 109–142.

[8] Walker, B.; Kim, C.; Nguyen, T.-Q. Small Molecule Solution-Processed Bulk Heterojunction Solar Cells. *Chemistry of Materials* **2011**, *23*, 470–482.

[9] Chen, Y.; Wan, X.; Long, G. High Performance Photovoltaic Applications

Using Solution-Processed Small Molecules. *Accounts of Chemical Research* **2013**, *46*, 2645–2655.

[10] Coughlin, J. E.; Henson, Z. B.; Welch, G. C.; Bazan, G. C. Design and Synthesis of Molecular Donors for Solution-Processed High-Efficiency Organic Solar Cells. *Accounts of Chemical Research* **2014**, *47*, 257–270.

[11] Lin, Y.; Li, Y.; Zhan, X. Small molecule semiconductors for high-efficiency organic photovoltaics. *Chemical Society Reviews* **2012**, *41*, 4245.

[12] Gao, L.; Zhang, Z.-G.; Bin, H.; Xue, L.; Yang, Y.; Wang, C.; Liu, F.; Russell, T. P.; Li, Y. High-Efficiency Nonfullerene Polymer Solar Cells with Medium Bandgap Polymer Donor and Narrow Bandgap Organic Semiconductor Acceptor. *Advanced Materials* **2016**, *28*, 8288–8295.

[13] Zhao, W.; Qian, D.; Zhang, S.; Li, S.; Inganäs, O.; Gao, F.; Hou, J. Fullerene-Free Polymer Solar Cells with over 11% Efficiency and Excellent Thermal Stability. *Advanced Materials* **2016**, *28*, 4734–4739.

[14] Zhao, W.; Li, S.; Yao, H.; Zhang, S.; Zhang, Y.; Yang, B.; Hou, J. Molecular Optimization Enables over 13% Efficiency in Organic Solar Cells. *Journal of the American Chemical Society* **2017**, *139*, 7148–7151.

[15] Feng, H.; Qiu, N.; Wang, X.; Wang, Y.; Kan, B.; Wan, X.; Zhang, M.; Xia, A.; Li, C.; Liu, F.; Zhang, H.; Chen, Y. An A-D-A Type Small-Molecule Electron Acceptor with End-Extended Conjugation for High Performance Organic Solar Cells. *Chemistry of Materials* **2017**, *29*, 7908–7917.

[16] Sun, C.; Pan, F.; Bin, H.; Zhang, J.; Xue, L.; Qiu, B.; Wei, Z.; Zhang, Z.-G.; Li, Y. A low cost and high performance polymer donor material for polymer solar cells. *Nature Communications* **2018**, *9*, 743.

[17] Kan, B.; Zhang, J.; Liu, F.; Wan, X.; Li, C.; Ke, X.; Wang, Y.; Feng, H.; Zhang, Y.; Long, G.; Friend, R. H.; Bakulin, A. A.; Chen, Y. Fine-Tuning the Energy Levels of a Nonfullerene Small-Molecule Acceptor to Achieve a High Short-Circuit Current and a Power Conversion Efficiency over 12% in Organic Solar Cells. *Advanced Materials* **2018**, *30*, 1704904.

[18] Hou, J.; Inganäs, O.; Friend, R. H.; Gao, F. Organic solar cells based on non-fullerene acceptors. *Nature Materials* **2018**, *17*, 119–128.

[19] Sun, Y.; Welch, G. C.; Leong, W. L.; Takacs, C. J.; Bazan, G. C.; Heeger, A. J. Solution-processed small-molecule solar cells with 6.7% efficiency. *Nature Materials* **2012**, *11*, 44–48.

[20] Zhang, Q. et al. Small-molecule solar cells with efficiency over 9%. *Nature Photonics* **2015**, *9*, 35–41.

[21] Deng, D.; Zhang, Y.; Zhang, J.; Wang, Z.; Zhu, L.; Fang, J.; Xia, B.; Wang, Z.; Lu, K.; Ma, W.; Wei, Z. Fluorination-enabled optimal morphology leads to over 11% efficiency for inverted small-molecule organic solar cells. *Nature Communications* **2016**, *7*, 13740.

[22] Qiu, B.; Xue, L.; Yang, Y.; Bin, H.; Zhang, Y.; Zhang, C.; Xiao, M.; Park, K.; Morrison, W.; Zhang, Z.-G.; Li, Y. All-Small-Molecule Nonfullerene Organic Solar Cells with High Fill Factor and High Efficiency over 10%. *Chemistry of Materials* **2017**, *29*, 7543–7553.

[23] Duan, T.; Tang, H.; Liang, R.-Z.; Lv, J.; Kan, Z.; Singh, R.; Kumar, M.; Xiao, Z.; Lu, S.; Laquai, F. Terminal group engineering for small-molecule donors boosts the performance of nonfullerene organic solar cells. *Journal of Materials Chemistry A* **2019**, *7*, 2541–2546.

[24] Xu, C.; Wang, J.; An, Q.; Ma, X.; Hu, Z.; Gao, J.; Zhang, J.; Zhang, F. Ternary small molecules organic photovoltaics exhibiting 12.84% efficiency. *Nano Energy* **2019**, , 104119.

[25] Kan, B. et al. A Series of Simple Oligomer-like Small Molecules Based on Oligothiophenes for Solution-Processed Solar Cells with High Efficiency. *Journal of the American Chemical Society* **2015**, *137*, 3886–3893.

[26] Liang, N.; Meng, D.; Ma, Z.; Kan, B.; Meng, X.; Zheng, Z.; Jiang, W.; Li, Y.; Wan, X.; Hou, J.; Ma, W.; Chen, Y.; Wang, Z. Triperylene Hexaimides Based All-Small-Molecule Solar Cells with an Efficiency over 6% and Open Circuit Voltage of 1.04 V. *Advanced Energy Materials* **2017**, *7*, 1601664.

[27] Yamamoto, K.; Shahiduzzaman, M.; Yamada, A.; Takaya, T.; Chikamatsu, T.; Koganezawa, T.; Karakawa, M.; Kuwabara, T.; Takahashi, K.; Taima, T. Molecular orientation control of semiconducting molecules using a metal layer formed by wet processing. *Organic Electronics* **2018**, *63*, 47–51.

[28] Wang, Y.; Chang, M.; Kan, B.; Wan, X.; Li, C.; Chen, Y. All-Small-Molecule Organic Solar Cells Based on Pentathiophene Donor and Alkylated Indacenodithiophene-Based Acceptors with Efficiency over 8%. *ACS Applied Energy Materials* **2018**, *1*, 2150–2156.

[29] Hermenau, M.; Leo, K.; Riede, M. Comparison of different conditions for accelerated ageing of small molecule organic solar cells. SPIE Photonics Europe. Brussels, 2010.

[30] Lessmann, R.; Hong, Z.; Scholz, S.; Maennig, B.; Riede, M.; Leo, K. Aging of flat heterojunction zinc phthalocyanine/fullerene C60 organic solar cells. *Organic Electronics* **2010**, *11*, 539–543.

[31] Hermenau, M.; Riede, M.; Leo, K.; Gevorgyan, S. A.; Norrman, K. Water and oxygen induced degradation of small molecule organic solar cells. *Solar Energy Materials and Solar Cells* **2011**, *95*, 1268–1277.

[32] Kyaw, A. K. K.; Wang, D. H.; Gupta, V.; Zhang, J.; Chand, S.; Bazan, G. C.; Heeger, A. J. Efficient Solution-Processed Small-Molecule Solar Cells with Inverted Structure. *Advanced Materials* **2013**, *25*, 2397–2402.

[33] Cheacharoen, R.; Mateker, W. R.; Zhang, Q.; Kan, B.; Sarkisian, D.; Liu, X.; Love, J. A.; Wan, X.; Chen, Y.; Nguyen, T.-Q.; Bazan, G. C.; McGehee, M. D. Assessing the stability of high performance solution processed small molecule solar cells. *Solar Energy Materials and Solar Cells* **2017**, *161*, 368–376.

[34] Min, J.; Jiao, X.; Sgobba, V.; Kan, B.; Heumüller, T.; Rechberger, S.; Spiecker, E.; Guldi, D. M.; Wan, X.; Chen, Y.; Ade, H.; Brabec, C. J. High efficiency and stability small molecule solar cells developed by bulk microstructure fine-tuning. *Nano Energy* **2016**, *28*, 241–249.

[35] Lami, V. Visualising the Energetic Landscape in Organic Photovoltaics. PhD thesis, Universität Heidelberg, 2019.

[36] Krebs, F. C.; Norrman, K. Analysis of the failure mechanism for a stable organic photovoltaic during 10000 h of testing. *Progress in Photovoltaics: Research and Applications* **2007**, *15*, 697–712.

[37] de Jong, M. P.; van IJzendoorn, L. J.; de Voigt, M. J. A.

Stability of the interface between indium-tin-oxide and poly(3,4-ethylenedioxythiophene)/poly(styrenesulfonate) in polymer light-emitting diodes. *Applied Physics Letters* **2000**, *77*, 2255–2257.

[38] Wong, K. W.; Yip, H. L.; Luo, Y.; Wong, K. Y.; Lau, W. M.; Low, K. H.; Chow, H. F.; Gao, Z. Q.; Yeung, W. L.; Chang, C. C. Blocking reactions between indium-tin oxide and poly (3,4-ethylene dioxythiophene):poly(styrene sulphonate) with a self-assembly monolayer. *Applied Physics Letters* **2002**, *80*, 2788–2790.

[39] Jørgensen, M.; Norrman, K.; Krebs, F. C. Stability/degradation of polymer solar cells. *Solar Energy Materials and Solar Cells* **2008**, *92*, 686–714.

[40] Wong, H. C.; Li, Z.; Tan, C. H.; Zhong, H.; Huang, Z.; Bronstein, H.; McCulloch, I.; Cabral, J. T.; Durrant, J. R. Morphological stability and performance of polymer-fullerene solar cells under thermal stress: The impact of photoinduced PC60BM oligomerization. *ACS Nano* **2014**, *8*, 1297–1308.

[41] Lilliedal, M. R.; Medford, A. J.; Madsen, M. V.; Norrman, K.; Krebs, F. C. The effect of post-processing treatments on inflection points in current–voltage curves of roll-to-roll processed polymer photovoltaics. *Solar Energy Materials and Solar Cells* **2010**, *94*, 2018–2031.

[42] Euvrard, J.; Revaux, A.; Cantarano, A.; Jacob, S.; Kahn, A.; Vuillaume, D. Impact of unintentional oxygen doping on organic photodetectors. *Organic Electronics* **2018**, *54*, 64–71.

[43] Bakulin, A. A.; Xia, Y.; Bakker, H. J.; Inganäs, O.; Gao, F. Morphology, Temperature, and Field Dependence of Charge Separation in High-Efficiency Solar Cells Based on Alternating Polyquinoxaline Copolymer. *The Journal of Physical Chemistry C* **2016**, *120*, 4219–4226.

[44] Veldman, D.; İpek, Ö.; Meskers, S. C. J.; Sweelssen, J.; Koetse, M. M.; Veenstra, S. C.; Kroon, J. M.; van Bavel, S. S.; Loos, J.; Janssen, R. A. J. Compositional and Electric Field Dependence of the Dissociation of Charge Transfer Excitons in Alternating Polyfluorene Copolymer/-Fullerene Blends. *Journal of the American Chemical Society* **2008**, *130*, 7721–7735.

[45] Lu, C.-K.; Meng, H.-F. Hole doping by molecular oxygen in organic semi-

conductors: Band-structure calculations. *Physical Review B* **2007**, *75*, 235206.

[46] Katz, E.; Mescheloff, A.; Visoly-Fisher, I.; Galagan, Y. Light intensity dependence of External Quantum Efficiency of fresh and degraded organic photovoltaics. *Solar Energy Materials and Solar Cells* **2016**, *144*, 273–280.

[47] Nehm, F.; Pfeiffelmann, T.; Dollinger, F.; Müller-Meskamp, L.; Leo, K. Influence of aging climate and cathode adhesion on organic solar cell stability. *Solar Energy Materials and Solar Cells* **2017**, *168*, 1–7.

[48] Cha, H.; Wheeler, S.; Holliday, S.; Dimitrov, S. D.; Wadsworth, A.; Lee, H. H.; Baran, D.; McCulloch, I.; Durrant, J. R. Influence of Blend Morphology and Energetics on Charge Separation and Recombination Dynamics in Organic Solar Cells Incorporating a Nonfullerene Acceptor. *Advanced Functional Materials* **2018**, *28*, 1704389.

[49] Reese, M. O.; Nardes, A. M.; Rupert, B. L.; Larsen, R. E.; Olson, D. C.; Lloyd, M. T.; Shaheen, S. E.; Ginley, D. S.; Rumbles, G.; Kopidakis, N. Photoinduced Degradation of Polymer and Polymer-Fullerene Active Layers: Experiment and Theory. *Advanced Functional Materials* **2010**, *20*, 3476–3483.

[50] Manceau, M.; Rivaton, A.; Gardette, J.-L.; Guillerez, S.; Lemaître, N. Light-induced degradation of the P3HT-based solar cells active layer. *Solar Energy Materials and Solar Cells* **2011**, *95*, 1315–1325.

[51] Long, G. et al. New Insights into the Correlation between Morphology, Excited State Dynamics, and Device Performance of Small Molecule Organic Solar Cells. *Advanced Energy Materials* **2016**, *6*, 1600961.

[52] Pearson, A. J.; Hopkinson, P. E.; Couderc, E.; Domanski, K.; Abdi-Jalebi, M.; Greenham, N. C. Critical light instability in CB/DIO processed PBDTTT-EFT:PC71BM organic photovoltaic devices. *Organic Electronics* **2016**, *30*, 225–236.

[53] Yan, W.; Huo, M.-M.; Hu, R.; Wang, Y. Working area effects on the energetic distribution of trap states and charge dynamics of dye-sensitized solar cells. *RSC Advances* **2019**, *9*, 1734–1740.

[54] Hedley, G. J.; Ruseckas, A.; Samuel, I. D. W. Light Harvesting for Organic Photovoltaics. *Chemical Reviews* **2017**, *117*, 796–837.

[55] Ostroverkhova, O. Organic Optoelectronic Materials: Mechanisms and Applications. *Chemical Reviews* **2016**, *116*, 13279–13412.

[56] Menke, S. M.; Holmes, R. J. Exciton diffusion in organic photovoltaic cells. *Energy Environ. Sci.* **2014**, *7*, 499–512.

[57] Shepherd, W. E. B.; Platt, A. D.; Kendrick, M. J.; Loth, M. A.; Anthony, J. E.; Ostroverkhova, O. Energy Transfer and Exciplex Formation and Their Impact on Exciton and Charge Carrier Dynamics in Organic Films. *The Journal of Physical Chemistry Letters* **2011**, *2*, 362–366.

[58] Ward, A. J.; Ruseckas, A.; Samuel, I. D. W. A Shift from Diffusion Assisted to Energy Transfer Controlled Fluorescence Quenching in Polymer–Fullerene Photovoltaic Blends. *The Journal of Physical Chemistry C* **2012**, *116*, 23931–23937.

[59] Luhman, W. A.; Holmes, R. J. Investigation of Energy Transfer in Organic Photovoltaic Cells and Impact on Exciton Diffusion Length Measurements. *Advanced Functional Materials* **2011**, *21*, 764–771.

[60] Scully, S. R.; Armstrong, P. B.; Edder, C.; Frechet, J. M. J.; McGehee, M. D. Long-Range Resonant Energy Transfer for Enhanced Exciton Harvesting for Organic Solar Cells. *Advanced Materials* **2007**, *19*, 2961–2966.

[61] Lloyd, M. T.; Lim, Y.-F.; Malliaras, G. G. Two-step exciton dissociation in poly(3-hexylthiophene)/fullerene heterojunctions. *Applied Physics Letters* **2008**, *92*, 143308.

[62] Huang, J.-S.; Goh, T.; Li, X.; Sfeir, M. Y.; Bielinski, E. A.; Tomasulo, S.; Lee, M. L.; Hazari, N.; Taylor, A. D. Polymer bulk heterojunction solar cells employing Förster resonance energy transfer. *Nature Photonics* **2013**, *7*, 479–485.

[63] Speller, E. M.; Clarke, A. J.; Luke, J.; Lee, H. K. H.; Durrant, J. R.; Li, N.; Wang, T.; Wong, H. C.; Kim, J.-S.; Tsoi, W. C.; Li, Z. From fullerene acceptors to non-fullerene acceptors: prospects and challenges in the stability of organic solar cells. *Journal of Materials Chemistry A* **2019**,.

[64] Hoke, E. T.; Sachs-Quintana, I. T.; Lloyd, M. T.; Kauvar, I.; Mateker, W. R.; Nardes, A. M.; Peters, C. H.; Kopidakis, N.; McGehee, M. D. The Role of Electron Affinity in Determining Whether Fullerenes Catalyze or Inhibit Photooxidation of Polymers for Solar Cells. *Advanced Energy Materials* **2012**, *2*, 1351–1357.

[65] Yan, C.; Barlow, S.; Wang, Z.; Yan, H.; Jen, A. K.-Y.; Marder, S. R.; Zhan, X. Non-fullerene acceptors for organic solar cells. *Nature Reviews Materials* **2018**, *3*, 18003.

[66] Lin, Y.; He, Q.; Zhao, F.; Huo, L.; Mai, J.; Lu, X.; Su, C.-J.; Li, T.; Wang, J.; Zhu, J.; Sun, Y.; Wang, C.; Zhan, X. A Facile Planar Fused-Ring Electron Acceptor for As-Cast Polymer Solar Cells with 8.71% Efficiency. *Journal of the American Chemical Society* **2016**, *138*, 2973–2976.

Part V

Conclusions

Conclusion and Outlook

This thesis addresses two urgent subjects of present organic solar cell research, namely the understanding of charge generation in novel material systems with low driving force, and the operational stability organic photovoltaic devices in oxygen environments. The results obtained during this work demonstrate the enormous potential of femtosecond transient absorption spectroscopy for the investigation of the physics on ultrashort timescales which are governed by the dynamics of excitons and charges. To establish a physical foundation for the study of the ensuing processes, the principles of solar cell operation are explained in Chapter 1. Particular emphasis is given to the processes of charge generation which involve formation and diffusion of excitons, charge transfer at a donor:acceptor interface, dissociation of the interfacial charge pair, and transport of the separated charges through the film. It follows a detailed account of the various degradation mechanisms which have been reported for devices exposed to ambient conditions in Chapter 2. Finally, Chapter 3 gives a brief introduction into ultrafast laser spectroscopy, including the creation of high-intensity, femtosecond laser pulses and their application in transient absorption experiments.

The investigation of charge generation in the polymer system PffBT4T-2OD:PC$_{70}$BM is covered in Chapter 6. It was found that the dissociation of excitons at the interface between polymer and fullerene is field-dependent. Consequently, charge transfer in neat films is suppressed which can be rationalised by an energetic barrier following Marcus theory. This energetic barrier is reduced by the presence of a built-in electric field provided by the interlayers in a complete photovoltaic device, resulting in efficient generation of free charges. The unusual photophysics of this particular system could be representative for an entire class of novel material systems with low driving force which current research focuses upon. Notably, the emergence of non-fullerene acceptors, which enable high V$_{OC}$ through small band offsets, can benefit from the results of this study. An immediate consequence of the observed effects

is the requirement to investigate complete photovoltaic devices, in contrast to simple films, for photophysical studies in such systems.

The second part of this thesis examines the environmental stability of PffBT4T-2OD:PC_{70}BM devices (Chapter 7). When exposed to oxygen or light, those OPVs exhibit exceptionally strong degradation which results in an almost complete loss of photovoltaic performance within hours. Employing transient absorption spectroscopy, conjointly with various other techniques, led to the proposition of an oxygen-induced p-doping mechanism to explain the observed results. It was shown that exposure to oxygen promotes the formation of defect states within the bandgap, affecting the charge generation in PffBT4T-2OD:PC_{70}BM solar cells. These defects lead to efficient, initial quenching of excitons with subsequent creation of trapped charges which, consequently, leads to the severe losses of the J_{SC}, being the primary driver for the device degradation. This study highlights the need to develop effective mitigation strategies to impede the ingress of molecular oxygen into the active layer of modern OPV devices. Possible methods, such as oxygen scavengers or encapsulation layers, are discussed in Chapter 2. The latter, however, are often only insufficiently effective or incompatible with flexible device substrates, while also equating to a major part of the overall module costs. Some new ideas are needed for the design of novel, stable and high-efficient material systems for applications outside the laboratory.

One of such ideas is suggested in the last part of this thesis which investigates the environmental stability of the small molecule donor DRCN5T (Chapter 8). We demonstrate the the DRCN5T:PC_{70}BM devices exhibit unique resistance of the J_{SC} towards external factors, even after prolonged exposure to oxygen and 1 sun illumination, and in spite of the fullerene acceptor PC_{70}BM which typically causes rapid degradation in many systems, including the aforementioned system of PffBT4T-2OD:PC_{70}BM. This remarkable stabilisation of the blend is achieved by two separate mechanisms which are investigated by fs-TA spectroscopy: firstly, the small molecule donor displays impressive intrinsic stability, showing no signs of degradation on the ultrafast timescale. Secondly, the inherent weaknesses of the fullerene acceptor are negated by an efficient, sub-ps energy transfer from PC_{70}BM to DRCN5T. This process quickly transfers the high-energy excited state from the unstable acceptor to the stable donor, thereby preventing it from degrading the fullerene. Consequently, the charge generation process is largely unaffected by the presence of oxygen or light which results in the exceptional stabilisation of the short-circuit current. We propose that this photoprotective mechanism can also be exploited in novel

material systems and should influence design rules towards more stable and efficient photovoltaic devices. Choosing material combinations which support energy transfer can facilitate the development of next-generation devices, as it requires only one of the components to be stable. Additionally, energy transfer can assist in device optimisation since researchers can exclusively focus on enhancing charge transfer from one component to the other, instead of improving both electron and hole transfer at the interfaces. These effects could be particularly useful for the rapidly advancing non-fullerene acceptors and ternary blends. Finally, this study illustrates the promising properties of small molecules for organic photovoltaic devices and highlights their potentially superior stability over commonly employed polymers.

To conclude, this thesis demonstrates the tremendous potential of femtosecond transient absorption spectroscopy for the investigation of the physics on the ultrashort timescales, and should help to establish TA as an ubiquitous tool in organic electronic research. It is particularly well suited for the study of device stability since external factors, such as oxygen or continuous illumination, have a direct impact on the dynamics of photoexcited excitons and charge carriers. Future research should include the influence of humidity on the device lifetime which was beyond the scope of this work. Furthermore, it has been unambiguously shown that the application of small molecule donors can yield superior long-term stability when compared to commonly used polymers, and research of such systems should be continued. Finally, the suggested photoprotective mechanism by energy transfer should be meticulously investigated, as it has the potential to have a lasting impact on the design rules of OPV devices. This work, therefore, contributes substantially to the understanding of the elementary processes during charge generation and the long-term stability of organic solar cells which is of high relevance for future research in the field of organic photovoltaics.

Appendix A

Supplementary Data
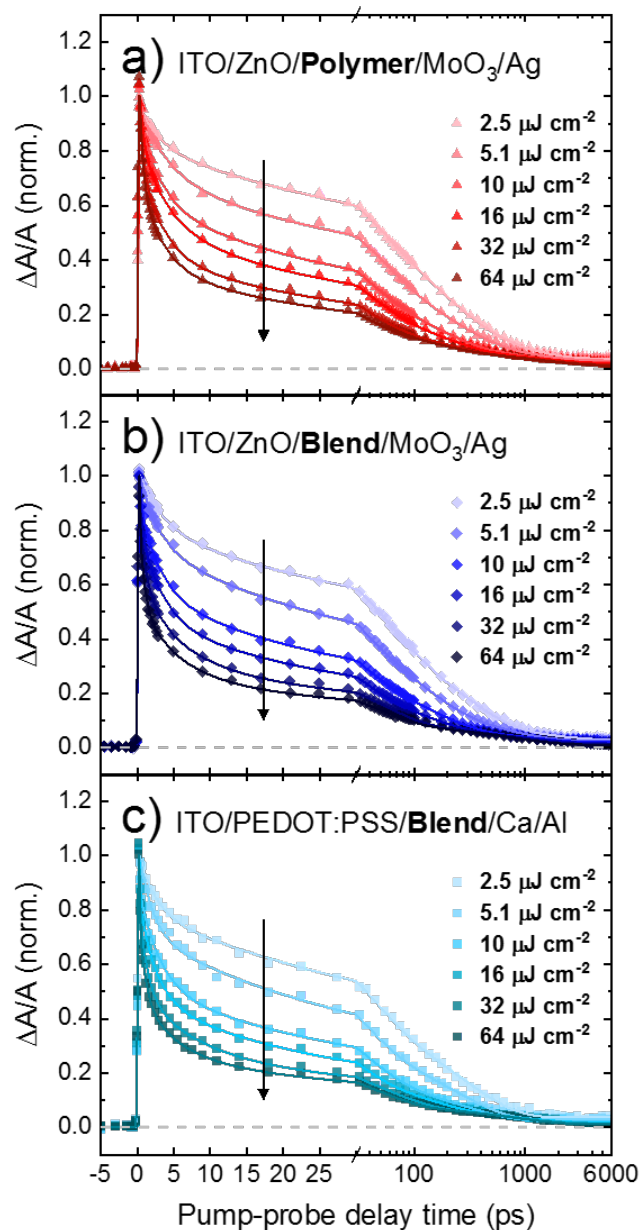
Figure A.1: Pump-intensity dependence on the normalized NIR TA kinetics for the active layer (i.e. between the bottom electrodes) of the (a) inverted architecture PffBT4T-2OD, (b) inverted architecture PffBT4T-2OD:PC$_{70}$BM and (c) standard architecture pffbt4t-2od:PC$_{70}$BM devices. Multiexponential fits are shown as a guide to the eye. Pump: 700 nm, probe: 1100 $\pm$ 10 nm. Reproduced with permission.[1] Copyright 2018, American Chemical Society.
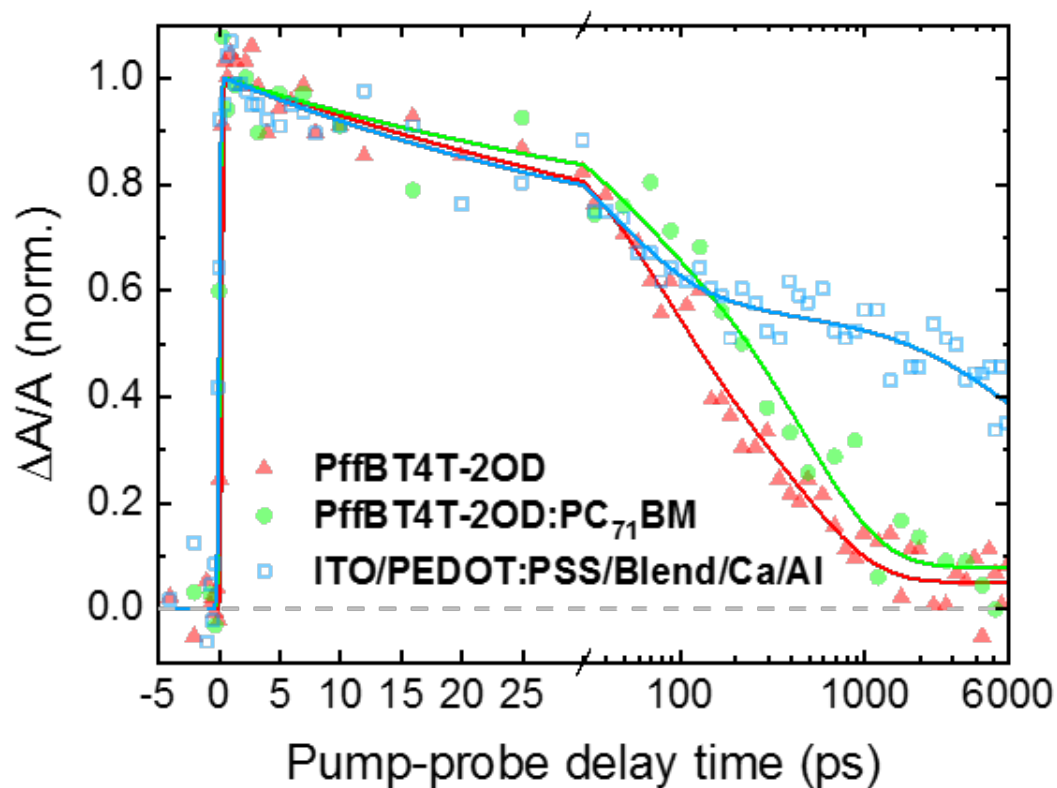
Figure A.2: NormalizedNIR TA kinetics for the polymer film, blend film and standard architecture blend device. The results demonstrate the same overall behaviour as for the inverted architecture device in Figure 6.5, in that charges contribute to the spectral response of the device at later times. Here, the kinetics and magnitude of the ESA decay are slightly different from the inverted architecture blend device in Figure S3a, which we attribute to a minor difference in the pump and probe beam profiles. Pump: 700 nm, 1.3 μJ cm^{-2}; Probe:1100 $\pm$ 10 nm. Multiexponential fits are shown as a guide to the eye. Reproduced with permission.[1] Copyright 2018, American Chemical Society.
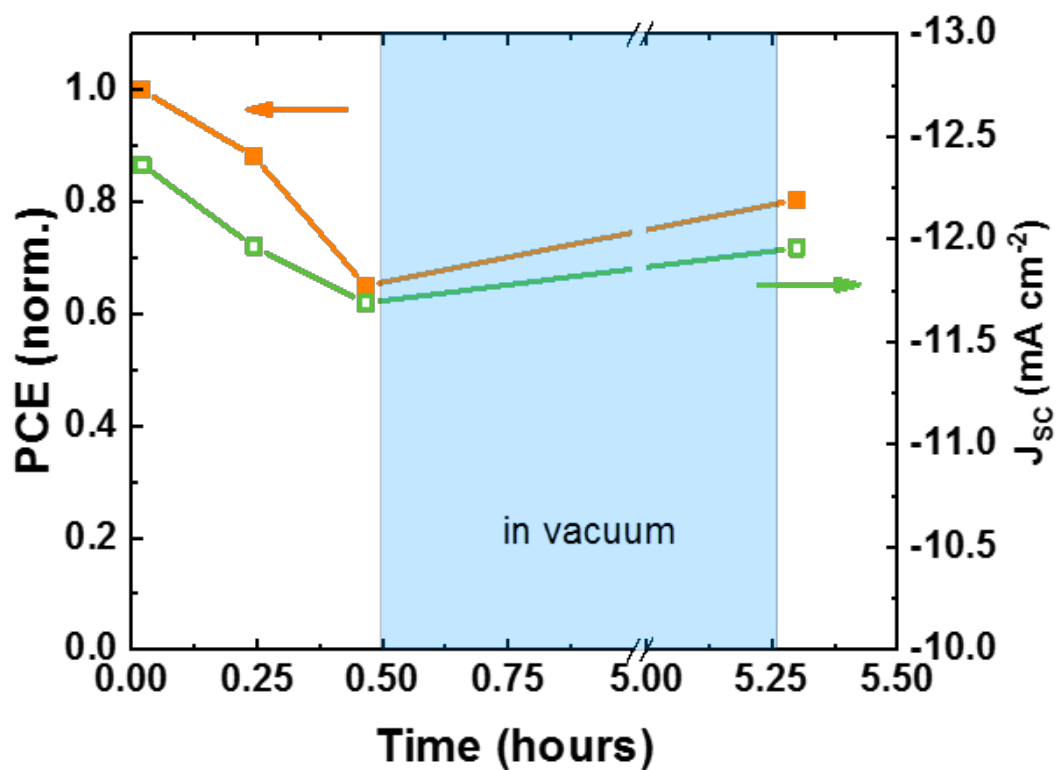
Figure A.3: Recovery of the performance of PffBT4T-2OD:PC$_{70}$BM solar cells after vacuum treatment (10^{-6} mbar) for 5 hours, following degradation in 20% oxygen in the dark. Adapted with permission.[2] Copyright 2019, American Chemical Society.
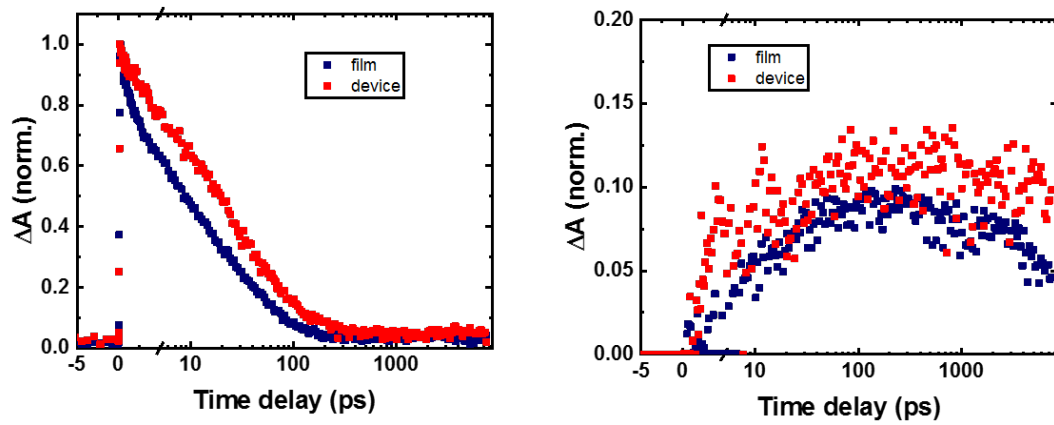
Figure A.4: (a) Exciton and (b) charge carrier dynamics of a DRCN5T film compared to a complete device after excitation with 700 nm pump (150 nJ). No field effect observable.
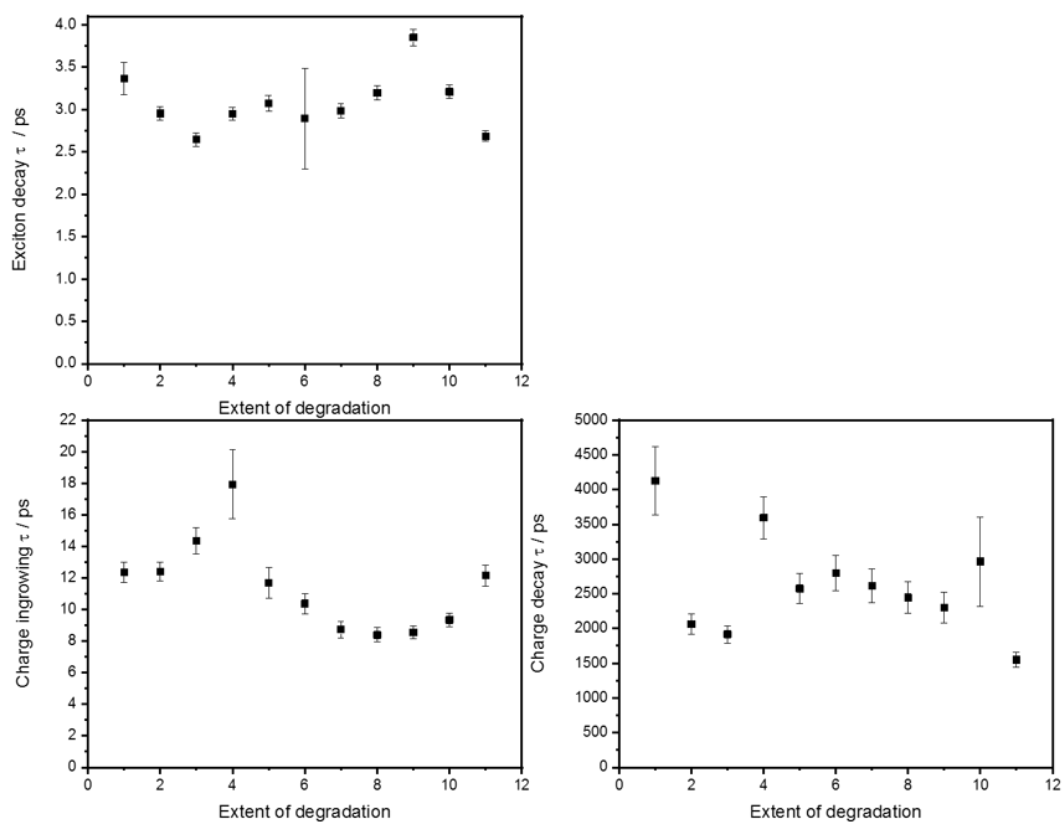
Figure A.5: Lifetimes of exciton and charge components extracted by global analysis of the blend film after excitation of the donor with 700 nm pulses. No correlation of the rates with progressing degradation can be observed. Reproduced with permission from Ref.[3] Copyright Wiley-VCH Verlag GmbH & Co. KGaA.
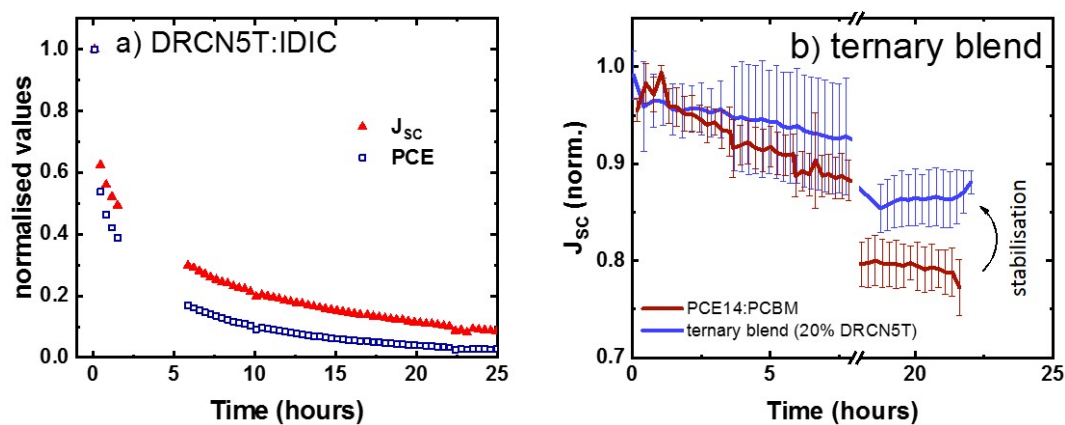
Figure A.6: (a) Blend of DRCN5T with the non-fullerene acceptor IDIC. The energetics of this system do not allow energy transfer from acceptor to donor which leads to a dramatic loss of J_{SC}. (b) Loss in J_{SC} of a blend of PBDB-T-2Cl:PC$_{70}$BM compared to a ternary blend with 20% DRCN5T. Depicted are the mean and standard deviation of 6 and 8 solar cells, respectively. During the experiment the connection to the measurement setup was lost for several hours. The ternary system was fabricated in a ratio 30:20:50 for PBDB-T-2Cl:DRCN5T:PC$_{70}$BM. Reproduced with permission from Ref.[3] Copyright Wiley-VCH Verlag GmbH & Co. KGaA.

Bibliography

[1] Weu, A.; Hopper, T. R.; Lami, V.; Kreß, J. A.; Bakulin, A. A.; Vayn-
    zof, Y. Field-Assisted Exciton Dissociation in Highly Efficient PffBT4T-
    2OD:Fullerene Organic Solar Cells. *Chemistry of Materials* **2018**, *30*, 2660–
    2667.

[2] Weu, A.; Kress, J. A.; Paulus, F.; Becker-Koch, D.; Lami, V.;
    Bakulin, A. A.; Vaynzof, Y. Oxygen-Induced Doping as a Degradation
    Mechanism in Highly Efficient Organic Solar Cells. *ACS Applied Energy
    Materials* **2019**, *2*, 1943–1950.

[3] Weu, A.; Kumar, R.; Butscher, J. F.; Lami, V.; Paulus, F.; Bakulin, A. A.;
    Vaynzof, Y. Energy Transfer to a Stable Donor Suppresses Degradation in
    Organic Solar Cells. *Advanced Functional Materials* **2019**, *submitted*, Sep.

Appendix B

Software documentation

Here the basic usage of the Matlab program to analyse transient datasets is explained. In the main window (Figure B.1) a transient dataset is selected ('File' → 'open'). The latter must be in .csv formatting, with the first column containing the wavelengths and the first row containing the time delays. This format is standard for the commercial HELIOS software which was used for data acquisition. After selection of the transient dataset the contour representation (could be enhanced in future with logarithmic color scale), the spectra at different times, and the kinetics and different wavelengths can be analysed. The handles allow a seamless navigation through the dataset. Each plot can be opened in a separate figure for plotting ('Open'), or exported in a .txt file ('Export') for further processing. Unwanted parts in the spectrum can be cutout ('Mask data') and the complexity of the dataset can be reduced by deleting every second row to decrease computational time which is sometimes necessary in visible datasets ('Reduce VIS').

The preprocessing of the data, according to the methods in Chapter 3, begins with the interpolation of the dataset over missing data points which are saved as NaN and are detrimental for later algorithms ('Edit' → 'Spline Correction'). In a next step, the laser chirp has to be accounted for as the fitting algorithms will produce unphysical results at early times (Figure B.2). This is done by navigating to 'Edit' → 'Chirp Correction'. The baseline is subtracted 'Edit' → 'Baseline Correction'.

By performing a singular value decomposition (SVD) the leading contributions to the dataset can be determined and random noise rejected (Figure B.3). It is achieved by selecting 'Edit' → 'SVD Correction'. The plots show the right- and left-hand singular vectors which represent the spectra and ki-
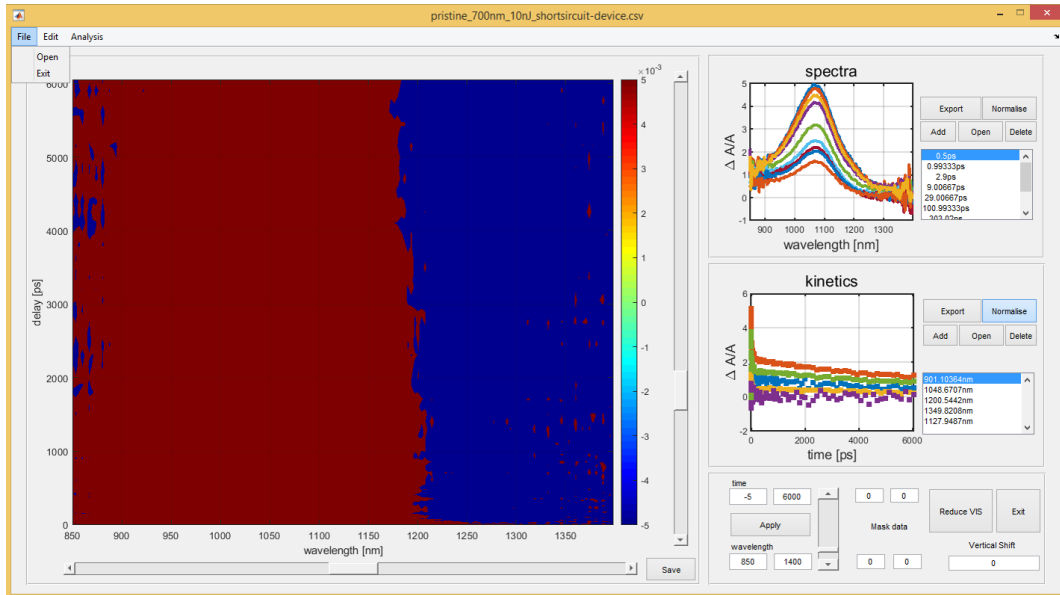
Figure B.1: Main window of the program. A contour plot, the spectra and the kinetics are depicted. The handles allow to look at specific wavelengths or times.
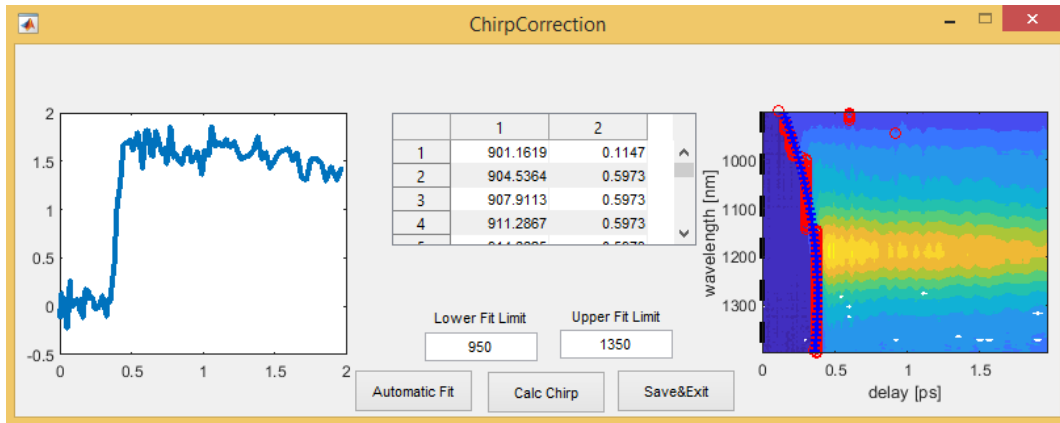
Figure B.2: Chirp correction of the dataset. The laser chirp can be calculated manually or automatically.
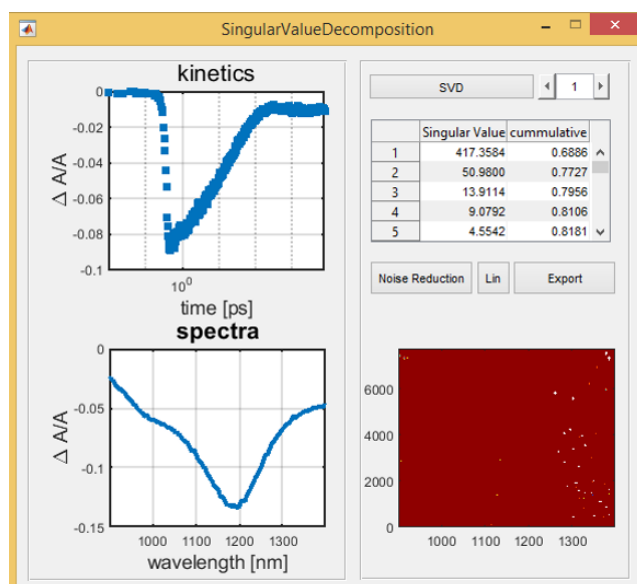
Figure B.3: Singular value decomposition of the data allow to determine the leading contributions to the transient dataset which helps to reduce random noise.

netics to the singular values. The contour plot calculates the residuals of the SVD-corrected dataset and the raw data.

The fitting of the dataset with a genetic algorithm is implemented with code from S. Gelinas (Cambridge). It is executed in a separate script ('run˙garos˙JZ.m') and requires the corrected dataset and additional files for reference spectra. For the source code ('GAros.m') contact A. Bakulin.

Listing B.1: Interpolation

```
 1  function del_A = splineCorrection(del_A_raw)
 2  %Searches the dataset for NaN and replaces it with mean of neighbouring
 3  %points. This is done for each wavelength along its time axis
 4
 5  %lengths
 6  wavelength = length(del_A_raw(:,1));
 7  time = length(del_A_raw(1,:));
 8
 9  %for all lambda
10  for l = 1:wavelength
11      %for all times
12      for t = 1:time
13          %find NaN
14          if isnan(del_A_raw(l,t))
15              %should not be at the edges
16              if t>1 && t<time
17                  del_A_raw(l,t) = (del_A_raw(l,t 1) + del_A_raw(l,t+1))/2;
18              end
19          end
20      end
21  end
22
23  %for all lambda
24  for l = 1:wavelength
25      %for all times
26      for t = 1:time
27          %find NaN
28          if isnan(del_A_raw(l,t))
29              %should not be at the edges
30              if l>1 && l<wavelength
31                  del_A_raw(l,t) = (del_A_raw(l 1,t) + del_A_raw(l+1,t))/2;
32              end
33          end
34      end
35  end
36
37  del_A = del_A_raw;
38
39  end
```

Listing B.2: Baseline correction

```
 1  function subBaseline(hObject, eventdata, handles)
 2  %substracts the baseline of the dataset
 3
 4  %get dataset
 5  del_A = getappdata(0,'del_A');
 6  time_vec = getappdata(0,'time');
 7  wavelength = getappdata(0,'wavelength');
 8
 9  %mean does not work with Inf or NaN
10  del_A(isnan(del_A)) = 0;
11  del_A(isinf(del_A)) = 0;
12
13  for l = 1:length(wavelength)
14      del_A(l,:) = del_A(l,:)    mean(del_A(l,1:time2row(time_vec, 1)));
```

```matlab
15  end
16
17  %write dataset
18  setappdata(0,'del_A',del_A);
19
20  %apply
21  BtnApply_Callback(hObject, eventdata, handles)
```

Listing B.3: Chirp correction

```matlab
1   %       Executes on button press in btnAutomFit in CHIRP CORRECTION
2   function btnAutomFit_Callback(hObject, eventdata, handles)
3   %calculates the first derivative to estimate time zero
4
5   del_A = getappdata(0,'del_A_vis');
6   time = getappdata(0,'time_vis');
7   wavelength = getappdata(0,'wavelength_vis');
8
9   contourf(handles.axes2,time',wavelength,del_A,'EdgeColor','none');
10  set(handles.axes2,'YDir','Reverse')
11  ylabel(handles.axes2,'wavelength [nm]');
12  xlabel(handles.axes2,'delay [ps]');
13  hold on;
14
15  tmp_tz=zeros(length(wavelength),2);
16  tmp_tz(:,1)=wavelength;
17
18
19  for ii=1:length(wavelength)
20      plot(handles.axes1,time,del_A(ii,:),'LineWidth', 3);
21
22      %derivative of function
23      derv = abs(diff(del_A(ii,:)));
24
25      %position
26      pos = time(find(derv==max(derv)));
27
28      tmp_tz(ii,2)= pos(1);
29      set(handles.TbChirp,'Data',tmp_tz);
30
31      scatter(handles.axes2,tmp_tz(ii,2),wavelength(ii),'r');
32
33  end
34
35  %       Executes on button press in BtnSave in CHIRP CORRECTION
36  function BtnSave_Callback(hObject, eventdata, handles)
37  % takes time_zero(lambda) and shifts the entire dataset
38
39  %get data
40  del_A = getappdata(0,'del_A');
41  time = getappdata(0,'time');
42  wavelength = getappdata(0,'wavelength');
43  wavelength_vis = getappdata(0,'wavelength_vis');
44  data = get(handles.TbChirp,'Data');
45  t0 = data(1:end,2);
46
47  %lower limit due to problems with coherent artefact
```

```matlab
48  lowLim=str2double(get(handles.edLowLim,'String'));
49  iLowLim=find(wavelength_vis>=lowLim);
50  visLim=lamda2row(wavelength_vis,wavelength(1));
51
52  %upper limit
53  upLim=str2double(get(handles.edUpperLim,'String'));
54  iUpLim=find(wavelength_vis>=upLim);
55
56  if isempty(iLowLim)
57      iLowLim=length(wavelength);
58  end
59
60  %find the chirp correction fit
61  [P,S]=polyfit(wavelength_vis(iLowLim(1):iUpLim(1)),t0(iLowLim(1):iUpLim(1)),2)
        ;
62  [t0hat,delta]=polyval(P,wavelength,S);
63
64  delay_t0l=zeros(length(wavelength),length(time));
65  mint0l=zeros(length(wavelength),1);
66  maxt0l=zeros(length(wavelength),1);
67
68  for ii=1:length(wavelength)
69      delay_t0l(ii,:)=time;
70      mint0l(ii,1)=min(time);
71      maxt0l(ii,1)=max(time);
72  end
73
74  %apply the chirp correction
75  for ii=1:length(wavelength)
76      delay_t0l(ii,:)=time t0hat(ii);
77      mint0l(ii,1)=min(delay_t0l(ii,:));
78      maxt0l(ii,1)=max(delay_t0l(ii,:));
79  end
80
81  delaycorr=time;
82
83  del_Acorr=zeros(length(wavelength),length(delaycorr));
84
85  for ii=1:length(wavelength)
86      del_Acorr(ii,:)=interp1(delay_t0l(ii,:),del_A(ii,:),delaycorr);
87  end
88
89  setappdata(0,'time',delaycorr);
90  setappdata(0,'del_A',del_Acorr);
91
92  close(handles.figure1);
```

Listing B.4: Singular value decomposition

```matlab
1  function BtnSVD_Callback(hObject, eventdata, handles)
2  %calculate the SVD correction
3
4  %calculate only the selected region
5  del_A = getappdata(0,'del_A_vis');
6  time = getappdata(0,'time_vis');
7  wavelength = getappdata(0,'wavelength_vis');
8
```

```matlab
 9  %SVD does not work with Inf or NaN
10  del_A(isnan(del_A))=0;
11  del_A(isinf(del_A))=0;
12
13  %do not calculate where masked
14  if getappdata(0,'maskedData') == 1
15      hfromWavelength = findobj('Tag','edMaskFrom');
16      huntilWavelength = findobj('Tag','edMaskUntil');
17      hfromTime = findobj('Tag','edMaskFromTime');
18      huntilTime = findobj('Tag','edMaskUntilTime');
19
20
21      maskFromWavelength = lamda2row(wavelength,str2double(get(hfromWavelength,'
              String')));
22      maskUntilWavelength = lamda2row(wavelength,str2double(get(huntilWavelength
              ,'String')));
23      maskFromTime = time2row(time,str2double(get(hfromTime,'String')));
24      maskUntilTime = time2row(time,str2double(get(huntilTime,'String')));
25
26      del_A(maskFromWavelength:maskUntilWavelength,:) = [];
27      wavelength(maskFromWavelength:maskUntilWavelength) = [];
28      time = [];
29
30      del_A(:,maskFromTime:maskUntilTime) = [];
31      time(maskFromTime:maskUntilTime) = [];
32  end
33
34  %perform the singular value decomposiotion
35  %U   represents the spectrum
36  %S   the singular values in a diagonal matrix
37  %V   represents the kinetics
38  [U,S,V] = svd(del_A);
39
40  setappdata(0,'U',U);
41  setappdata(0,'S',S);
42  setappdata(0,'V',V);
43
44  %list the singular values and add them up to indicate 80%90%
45  S = diag(S);
46  cumm = S./sum(abs(S));
47
48  for i=2:length(S)
49      cumm(i) = cumm(i) + cumm(i    1);
50  end
51
52  set(handles.TbSingularValues,'Data',[S cumm])
53  set(handles.SlSvd,'Max',length(S));
54  set(handles.SlSvd, 'SliderStep', [1/length(S) , 10/length(S) ]);
55
56  %call the plot function
57  plotSVD(handles)
58
59  %clear memory
60  clear variables
61
62  function BtnNC_Callback(hObject, eventdata, handles)
63  %applies the SVD correction up to singular value k to the dataset
64
```

```matlab
65  U = getappdata(0,'U');
66  S = getappdata(0,'S');
67  V = getappdata(0,'V');
68
69  wavelength = getappdata(0,'wavelength_vis');
70  time = getappdata(0,'time_vis');
71
72  k = str2double(get(handles.EdSVD,'String'));
73
74  %do not calculate where masked
75  hfromWavelength = findobj('Tag','edMaskFrom');
76  huntilWavelength = findobj('Tag','edMaskUntil');
77  hfromTime = findobj('Tag','edMaskFromTime');
78  huntilTime = findobj('Tag','edMaskUntilTime');
79
80  maskFromWavelength = lamda2row(wavelength,str2double(get(hfromWavelength,'
        String')));
81  maskUntilWavelength = lamda2row(wavelength,str2double(get(huntilWavelength,'
        String')));
82  maskFromTime = time2row(time(:,1),str2double(get(hfromTime,'String')));
83  maskUntilTime = time2row(time(:,1),str2double(get(huntilTime,'String')));
84
85  SVDmatrix = U(:,1:k)*S(1:k,1:k)*V(:,1:k)';
86
87  if getappdata(0,'maskedData') == 1
88      columnsWavelength = SVDmatrix(maskFromWavelength:end,:);
89      SVDmatrix(maskFromWavelength:maskUntilWavelength,:) = NaN;
90      SVDmatrix(maskUntilWavelength+1:length(wavelength),:) = columnsWavelength;
91
92      columnsTime = SVDmatrix(:,maskFromTime:end);
93      SVDmatrix(:,maskFromTime:maskUntilTime) = NaN;
94      SVDmatrix(:,maskUntilTime+1:length(time(:,1))) = columnsTime;
95  end
96
97  % time = getappdata(0,'time_vis');
98  % time = time(:,end);
99  % time = repmat(time,1,length(U));
100
101  setappdata(0,'del_A',SVDmatrix);
102  setappdata(0,'time',getappdata(0,'time_vis'));
103  setappdata(0,'wavelength',getappdata(0,'wavelength_vis'));
```

Listing B.5: Genetic algorithm

```matlab
1   clear
2
3   % Set the file name of the data you want to use.
4   %
5   % This is using the '.cor' format returned by 'chirpcorrectx.m'. For
6   % any other format, minor ajustments might be necessary but it should be
7   % fairly straightfoward.
8   %fname = 'GAros_in.cor';
9   fname = 'PCE11_01_pristine.csv';
10
11  % File output name, where the resulting spectra and time traces will be
12  % saved as a .mat file. The variable names will be:
13  %   wl: wavelength axis
```

```matlab
14  %   spe: a matrix with all the spectra (ref+init)
15  %   t: the time axis
16  %   tt: the time traces associated with each spectrum in the spe variable
17  %fOutName = 'GAros_out.mat';
18  fOutName = 'Results_PCE11.mat';
19
20  % Set the spectra in 0 Wavelength (nm) or 1 energy (eV), the variable x
21  % will be used to refer to the one selected.
22  wlE = 0;
23
24  % Set the size of the region used for smoothing on the time and wavelength
25  % (or energy) axis. use 1 for no smoothing.
26  sm_t = 1; % Time
27  sm_x = 1; % Wavelength/Energy
28
29  % Set the cutoff wavelength/energy and time. If the value is out of bounds,
30  % automatically uses the first/last value in the vector
31  t_min =  5; % Start time
32  t_max = 8000; % End time
33  x_min = 850; % Minimum value in wavelength/Energy
34  x_max = 1350; % Maximum value in wavelength/Energy
35
36  %SG001.
37  % Subsample the fitted spectra to reduce computational time and, most
38  % importantly, ensure the algorithm doesn't optimises pixel to pixel noise
39
40  % Subsampling factor
41  subsF = 1;
42
43  % Set the initial spectra file location
44  %  These spectra will be modified by the algorithm
45
46  % Use external files as initial guess? Yes(1) / No(0)
47  %   Random noise/gaussians can still be added weather an external file is
48  %   used or not. Their properties are defined in the 'is' object. Use
49  %   is.n=0 if no noise is needed, and is.p(1)=0 if no ranodm gaussians are
50  %   needed.
51  init_methd = 0;
52  % Use only if init_methd=0, sets the number of spectra to optimize
53  init_nb = 1;
54
55  %  Warning: each file must contain x and y axis in the right units.
56  init_fname = {};
57
58  % Set the reference spectra file location
59  %  These spectra are 'fixed', they will be NOT modified by the algorithm
60  %  if no references are needed, use init_fname = {};
61  %
62  %  Warning: each file must contain x and y axis in the right units.
63  ref_fname = {'LondonExFilmRef.txt'};
64
65  % Set the uncertainty estimation method
66  %  0  Uniform
67  %       Each point has the same error.
68  %  1  Proportional
69  %       The uncertainty of each point is proportional to the smoothed value
70  %       at that point. n controls the smoothing and should be bigger than
71  %       the actual smoothing used on the data.
```

```matlab
72  %   2   Singular Value Decomposition
73  %           Uses the first k terms of the SVD and uses the smoothed difference
74  %           with the TA data to estimate error. n controls the smoothing.
75  %   3   Standard Deviation
76  %           Estimates the error with the STD of the points contained in a 2*n+1
77  %           square around the point.
78  %   4   pre (t=0) standard deviation
79  %           Look at the fluctuation in the t < 0, by measuring the STD
80  %           In this case, n is the number of points before the start of the
81  %           chirp.
82  unc_methd = 3;
83  k = 10;
84  %n = 16;
85  n = 2;
86
87  % Set initialization parameters for GA.m
88  %  params = {npop; nrun; is; rr; mut; con};
89  %
90  %           gen.npop: is the number of species in the population, must be even
91  %           gen.nrun: number of runs
92  %           gen.rr: Refresh rate of the figure showing evolution
93  %
94  %           is.n: Amplitude of noise added to initial guess spectra
95  %           is.no: Offset of isn with respect to it's mean (0.5)
96  %           is.p: Parameters of the gaussians used to generate initial spectra
97  %               [Amplitude Mean Width].*rand(1,3)
98  %               Mean and Width are fraction of the total number of points.
99  %               e.g. if the wavelength vector is from 500nm to 900nm and
100 %                   there are 100 points, Width=0.5 corresponds to 50 points
101 %                   (or (900nm 500nm)*0.5 = 200nm).
102 %           is.ng: Number of gaussian used to generate initial spectra
103 %
104 %           mut.bms: Big mutation strenght (amplitude)
105 %           mut.bmr: Big mutation decay: Decrease the amplitude of big mutations
106 %               every 'bmd' step by /ceil(i/bmd)
107 %           mut.sms: Small mutations strenght (amplitude)
108 %           mut.smd: Small mutation decay Decrease the amplitude of big mutations
109 %               every 'smd' step by /ceil(i/smd)
110 %
111 %           con.nkp: Negative kinetic penalty (constrain), this is a correction
112 %               applied to the residual to penalize negative kinetics by:
113 %               1+nkp*(fraction of negative points)
114 %               Use nkp = 0 if the sign of the spectra is expected to change.
115 %           con.spes: Spectrum sign (constrain), must be defined for each spectrum
116 %               in 'init' (n by 1 vector)
117 %                   [0] no constrain
118 %                   [1] positive sectra only (GSB,SE)
119 %                   [ 1] negative spectra only (PIA)
120
121 gen.npop = 1000;
122 gen.nrun = 30;
123 gen.rr = 10;
124
125 is.n = 0.3;
126 is.no = 0.5;
127 is.p = [1 1 0.25];
128 is.ng = 5;
129
```

```matlab
130   mut.bms = 0.1;
131   mut.bmr = 120000;
132   mut.sms = 0.05;
133   mut.smr = 60000;
134   mut.e = 2;
135
136   con.nkp = 5;
137   con.spes = [1];
138
139   % Parameters controlling the iterative runs of GA
140
141   % Number of iterations performed
142   nb_of_iter = 50;
143
144   % Decrease of the random noise added to the initial guess at each iteration
145   noise_red = 1.02;
146
147   save GAros_param.mat
148   [wl,spe,t,tt] = GAros('GAros_param.mat');
```

Acknowledgements